Doctoral Dissertation
Doctoral Program in Materials Science and Technology (32th Cycle)

Elaboration of Calcium Phosphate Bioceramics with Different Architectures

Achievements by Gelcasting and Robocasting Technologies

Mehdi Mohammadi

* * * * * *

Supervisors
Prof. Paola Palmero
Prof. Jean-Marc Tulliani, Co-Supervisor

Doctoral Examination Committee:
Prof. Fabrice Rissignol, Referee, University of Limoges- IRCER – Centre Européen de la Céramique
Prof. Elisa Boanini, Referee, University of Bologna

Politecnico di Torino
April 28, 2020

I hereby declare that, the contents and organisation of this dissertation constitute my own original work and does not compromise in any way the rights of third parties, including those relating to the security of personal data.

…….....

Mehdi Mohammadi

Turin, April 28, 2020

Summary

The aim of this thesis was the elaboration of dense, porous and multi-layer hydroxyapatite (HA) ceramics to be used in biomedical applications. The production was made through two advanced methods: gelcasting and robocasting techniques, both based on the colloidal ceramic processing suitable for the production of high-performance complex geometries. Two different batches of a commercial type HA were used in production. The preliminary characterisations showed that both batches were calcium deficient HA with different Ca/P ratios, but similar particles size distribution. The dispersion process of HA powders was carried out through dry and wet ball-milling (DBM and WBM) processes, providing powders with different particle size distributions which were used in the production processes.

The optimisation of the sintering process of the powders was accomplished by conducting dilatometry tests on the samples made from DBM and WBM powders. The effect of the heating rate and the initial particle size on the sinterability and the grain growth were investigated and on the ground of these results, the sintering process was optimised. An abnormal grain refinement during the sintering process was observed for the samples made from the powder with the lower Ca/P ratio leading to a bimodal grain size distribution of the final material. Further analyses showed that the grain refinement resulting from the HA to tetracalcium phosphate (TTCP) phase transformation which took place at 1300 °C.

The gelcasting of the porous and the dense samples were conducted using agar as an environmentally friendly non-toxic gelling agent. Dense samples with densities up to 97 %TD were obtained using WBM powders. These high densities led to the high mechanical performance of the dense samples. The foaming method was used for the development of macroporosity in the porous samples. Highly porous structures in the porosity range of 63% to 87% characterised by spherical interconnected pores were obtained. The effect of different constituents of the

ceramic slurry on the porosity and pore sizes of the porous samples were investigated. The mechanical properties of dense and porous samples were studied by conducting uniaxial compression tests. Moreover, functionally graded multifunctional scaffolds, mimicking the natural bone structure, were developed using the optimised dense and porous gelcasting techniques in which the dense part had the load-bearing function and the porous layer fulfilled the biological requirements.

Dense, porous and functionally graded multilayer samples were also produced by robocasting technique. Different ink formulations were needed for successful production of each part. The samples were characterised by fully dense struts comparable to gelcast samples and the successive layers were well squeezed together. Optimisation of the paste formulation led to the production of multilayer structures with pore sizes more than 1.3 mm which is not achievable with other methods. The crack formation and propagation leading to the fracture of the porous robocast samples were studied using an environmental SEM (ESEM) equipped with the in-situ compressive device. The mechanical properties of the dense and porous robocast samples were found lower than the samples made by the gelcasting technique.

In vitro bioactivity tests were performed on the produced samples to investigate their bone formation ability. All the tested samples were found to be covered by an apatite layer confirming their osteoconductivity. However, the samples made from the powder with lower Ca/P ratio formed a thicker bioactive layer.

Polymer-ceramic composite layers were added to the multilayer robocast samples to add antibacterial functionality to the samples. Incorporation of a small amount of Ag^{+} ions in the composite materials was found as a powerful tool to prevent post-surgery infection after implantation of the orthopaedic implants.

Acknowledgements

I would like to express my special appreciation and thanks to my advisors Professor Paola Palmero and Professor Jean-Marc Tulliani, for the continuous support of my PhD study and related research, for their patience, motivation, and immense knowledge. I would like to thank them for encouraging my research and for allowing me to grow as a research scientist. Their advice on both research as well as on my career have been priceless.

My sincere thanks also go to Dr Fabrice Rossignol from the University of Limoges, IRCER, for his scientific advice and knowledge and many insightful discussions. Without his precious support, it would not be possible to conduct this research.

I am also pleased to say thank you to Dr Richard Gaignon who provided me with an opportunity to join their team in 3Dceram company, and who gave access to the laboratory and research facilities.

I am also pleased to say thank you to Professor Valleria Allizond from the University of Torino who helped me in understanding and conducting antibacterial tests.

I gratefully acknowledge financial support through the Additive Manufacturing Initiative for Transnational Innovation in Europe (AMITIE) project funded by EU H2020 Research & Innovation Programme under the Marie Skłodowska Curie Grant Agreement 734342.

I would always remember my fellow labmates too for the stimulating discussions as well as the fun-time we spent together. I am lucky to have made such great friends.

Above all, I would like to thank my wife Parisa for her love and constant support, for all the late nights and early mornings, and for keeping me sane over the past few months. Thank you for being my best friend. I owe you everything.

Contents

List of Tables

List of Figures

Chapter 1 Calcium phosphate bioceramics for biomedical applications

Abstract

Calcium phosphates are the second generation of bioceramics which have found widespread biomedical interests because of their bioactivity properties which give these materials osteoconductive and osteoinductive properties. Hydroxyapatite and β-tricalcium phosphate are the two mostly studied phases that their microstructural, mechanical and biological properties have been vastly investigated and several criteria for their different applications have been established. Due to a flexible lattice structure, several ion substitutions make it possible to introduce different functionalities and to tailor the characteristics of the used material with regard to the application demands. However, these bioceramics suffer from insufficient mechanical properties. While like other ceramics, they are characterised by brittle behaviour, the low sinterability makes it difficult to achieve a high degree of densification.

Tissue engineering is a recently emerged science which uses engineering principals in combination with life science. Tissue engineering aims at conducting bone regeneration in a reliable and physiologically acceptable manner establishing the most effective combination of mechanical and biological properties of an implant.

Gelcasting and robocasting are two advanced ceramic production techniques based on colloidal processing which guarantee high material performance combined with complex shapes. Based on the colloidal processing of ceramics, both methods result in ceramics with a high degree of microstructural homogeneity and mechanical properties.

Abbreviations

3-D	Three dimensional
3DP	3D printing
AM	Additive manufacturing
BCP	Biphasic calcium phosphate
CAD	Computer-aided design
CaP	Calcium phosphate
CD-HA	Calcium deficient hydroxyapatite
FA	Fluorapatite
HA	Hydroxyapatite
MAM	Methacrylamide
MBAM	Methylenebisacrylamide
OA	Oxyapatite
OHA	Hydroxyoxyapatite
PCL	Polycaprolactone
PLA	Polylactic acid
PMMA	Polymethylmethacrylate
RB	Robocasting
SLA	Stereolithography
SLS	Selective laser sintering
TCP	Tricalcium phosphate
TD	Theoretical density
TE	Tissue engineering
TTCP	Tetracalcium phosphate
XRD	X-ray diffractometry
α-TCP	α-tricalcium phosphate
β-TCMP	β-tricalcium magnesium phosphate
β-TCP	β-tricalcium phosphate
μSLA	Micro stereolithography

1.1 Calcium phosphate bioceramics

Bioceramics are a category of biomaterials which has a ceramic origin and due to their high biocompatibility, have been widely investigated for biomedical applications. Regarding response in the biological environment, bioceramics can be categorized in two main groups: the ones which are chemically and mechanically stable and the ones which are interesting because of their active biological responses [1].

The first generation of bioceramics is bio-inert ceramics. When implanted, these materials do not form any bond with surrounding tissues; on the contrary, they form a non-adherent fibrous layer at the interface. Therefore, the tissue response to inert bioceramics depends on fit, not chemistry, and implants made from these ceramics are clinically successful when implanted with a tight mechanical fit without any physical movements [1, 2]. High mechanical strength and chemical stability make of them excellent candidates for load-bearing biomedical applications such as the total hip replacements or dental prosthetics [1]. Alumina (Al_2O_3) and Zirconia (ZrO_2) are two main representatives of this group.

The second generation is bioactive ceramics. These materials trigger specific biological reactions at the interface of the material resulting in the formation of a bond between the tissues and the material which guarantees a complete connection and correlation of the implant to the host body [1]. A bioactive bioceramic can also be bioresorbable, designed to be gradually degraded in the body and replaced with natural tissue. A very well-known and broadly studied family of these materials are calcium phosphate (CaP) bioceramics [1].

CaPs are mainly composed of calcium cations (Ca^{2+}) together with phosphate anions in which the phosphate anions can be in three different forms of orthophosphate (PO_4^{3-}), metaphosphate (PO_3^-), or pyrophosphate ($P_2O_7^{4-}$). CaPs are chemically very similar to the natural bone composition [2]. In fact, the major constituents of the natural bone structure and tooth enamel is made from CaPs. It is also possible to synthesise CaP bioceramics in the laboratory with similar composition, structure and properties of biological ones.

The chemical similarity to natural bones makes CaPs non-toxic, biocompatible and most importantly bioactive, which accounts for their extensive uses as bone substitute materials. As an implant in the body, they support osteoblast adhesion and proliferation [3] and their integration into living tissue leads to an intimate physicochemical bonding between the implants and bone, named osteointegration. In fact, the osteointegration ability induces a strong interface between the implanted ceramic and the bone tissue. In order to tailor the biological response and osseointegration of the CaP bioceramics, various chemical compositions, architectures and microstructures have been investigated [4].

CaP family consists of several phases whose primary difference is the calcium to phosphorus ratio (Ca/P ratio). Hydroxyapatite (HA), tricalcium phosphate (TCP) and calcium-deficient hydroxyapatite (CD-HA) are the important phases which have been studied extensively. Although they have different physical and chemical

characteristics, these phases convert to each other through various thermomechanical and chemical reactions. These reactions often involve important changes in the physical and chemical characteristics of the materials and affect their performance in the application site.

CaPs have a wide range of biomedical applications as coatings to improve the biocompatibility, structural components as joint or tissue replacements, resorbable temporary structures and frameworks, as well as drug-delivery systems [5].

1.1.1 HA

HA, more precisely calcium HA, belongs to a family of CaPs called apatite. Apatites are compounds with similar structures with the Ca/P atomic ratio in the range of 1.5 to 1.67 but not necessarily identical compositions [1]. HA is considered as a compound of definite crystallography and definite composition of $Ca_{10}(PO_4)_6(OH)_2$ with calcium to phosphorous atomic ratio of 1.67 [1].

HA has been characterised as non-toxic and biocompatible, non-inflammatory and non-immunogenic, osteoconductive and bioactive [6]. The major mineral part of the bone is HA; all other phases are considered as minor or precursor phases that transfer to HA at higher pH [7]. HA is thermodynamically stable in pH, temperature and composition of the physiological fluid [6].

Although pure HA is a composition of calcium, phosphorous, oxygen and hydrogen, there would be some minor and trace elements in the composition. The trace elements may have biological origin or be introduced from the reagents used to prepare the powder. According to ASTM F1185-14 [8], commercial HA must contain at least 95% HA, as established by X-ray diffractometry (XRD) analyses. A few ppm of trace elements such as arsenic (As), cadmium (Cd), mercury (Hg) and lead (Pb) is acceptable in HA composition.

The crystallographic structure of HA is the hexagonal system with a space group P63/m which is characterised by a six-fold c-axis perpendicular to three equivalent a-axes (a_1, a_2, a_3) at angles 120° to each other [1] as shown in Figure 1-1 [9]. The atomic structure of HA is stabilised by a network of orthophosphate (PO_4) groups with all other atoms arrange around. In fact, six PO_4 tetrahedral ions stretch from levels z = 0.25 to z = 0.75 in a helical arrangement and provide the skeletal framework of the whole structure. In this crystal lattice, calcium atoms occupy two different positions of Ca(I) (columnar Ca) or Ca(II) (screw axis Ca). Four atoms are in the Ca(I) positions and six atoms are in the Ca(II) positions. The Ca(II) atoms form two triangles in two levels of z = 0.25 and z = 0.75. The OH groups arrange along the c-axis at the centre of the Ca (II) triangles and may have either upward or downward orientation. The induced strains due to this disorderliness are compensated by substitutions or ion vacancies. Therefore, at ambient temperature, the HA structure is stabilised by partial substitution of hydroxide by fluoride or chloride [1, 9].

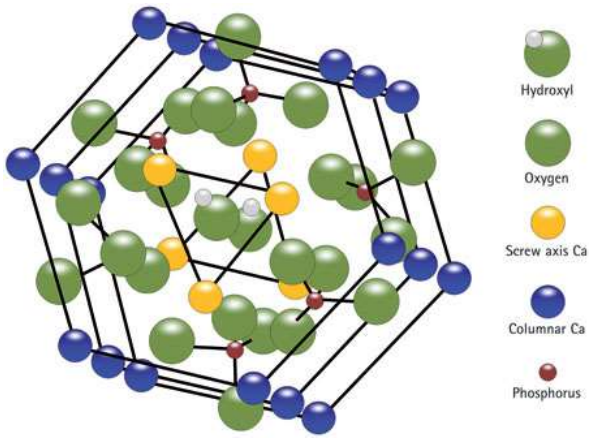

Figure 1-1: Illustration of the structure of HA. Reprinted from [10] with the permission of Nature under the license no 4774940413868.

While the Ca/P molar ratio of pure stoichiometric HA is 1.67, in the lower values the apatite is considered as calcium deficient (CD-HA). The general formula of CD-HA is $Ca_{10-x}(PO_4)_{6-x}(HPO_4)_x(OH)_{2-x}$, with $0 \leq x \leq 2$ [9]. It may be considered as HA with some ions missing (ionic vacancies) in which higher Ca deficiency is accompanied by more disorder, imperfections, and vacancies [9]. The synthesis conditions, reaction pH and/or temperature are effective factors in calcium deficiency of apatites structures [4].

The crystallinity of CD-HA crystals is poor and compared to HA, the crystal lattice of CD-HA has greater a-axis dimension (0.9438 to 0.9461 nm versus 0.9422 nm for HA), probably due to the incorporation of HPO_4 (partial HPO_4 for PO_4 substitution) [11]. On heating above 700 °C, dry CD-HA with Ca/P = 1.5 will convert to β-TCP and that with 1.5 < Ca/P < 1.67 will convert into a mixture of HA and β-TCP [7].

Calcium deficiency reduces the mechanical properties of HA. A reduction of 80% and 75% of hardness and toughness for CD-HA crystals compared to stoichiometric HA has been reported, respectively [9].

Biological apatites are not pure HA. Not only their stoichiometry, crystallinity and composition are different from pure HA, but also they have different physical, mechanical and dissolution behaviours [1]. Pure stoichiometric HA never occurs in biological systems [7]. They are always carbonate substituted and usually calcium deficient. Various elements such as Na^+, Mg^{2+}, Zn^{2+}, Si^{4+}, Sr^{2+}, etc. are incorporated in the structure of natural bone as nutrients which play an extremely vital role in the different aspects of bone formation, growth and repair [12]. It is more appropriate to refer them as carbonate apatite or carbonate-substituted apatite and not as HA [1].

Synthetic HA can be prepared using several techniques such as the solid-state reactions, wet methods, and hydrolysis of other CaPs. In all cases, to obtain the Ca/P atomic ratio equal to 1.67, the Ca- and PO_4-containing reagents must be mixed in proportion. However, even under the ideal stoichiometric conditions, the intermediate formation of precursor phases, such as amorphous calcium apatite and CD-HA generally leads to nonstoichiometric products. CD-HA can be obtained by

the precipitation method under different conditions of pH and temperature; the lower the pH, the higher the temperature required for the precipitation of apatite [4]. Hydrolysis of the non-apatitic CaPs such as α-TCP is another method of preparation of CD-HA [4]. It is also possible to derive HA from the biological origin such as coral, bovine bone or marine algae. In the synthesis of HA not only the stoichiometry of HA must be controlled but also the crystal size and shape and the agglomeration characteristics of the powder must be managed [4, 9].

HA is used in the forms of granules, blocks and scaffolds, by itself or as a composite with polymers or other ceramics or as coatings on orthopaedic (e.g. hip joint) or dental implants [4]. Its clinical usages range from augmenting atrophic alveolar ridges to repair long bone defects, ununited bone fractures, middle ear prostheses, spinal fusions, and craniofacial repair. It has also been used in dental surgery, biomolecular delivery, and drug delivery [7].

1.1.2 TCP

TCPs are another most widely used CaP compounds in the biomedical field. TCP corresponds to the chemical formula of $Ca_3(PO_4)_2$ and designates different compounds containing the orthophosphate ion PO_4^{3-} with a Ca/P atomic ratio close to 1.5 [4].

TCPs include 4 polymorphs, among them α and β-TCP are the most frequently observed in the bioceramics field [4, 13]. α- and β-TCP have the same chemical composition, but their crystal structures are different [9]. α-TCP crystal is in the monoclinic space group $P2_1/a$ and β-TCP crystallizes in the rhombohedral space group R3c. The unit cell of α and β-TCP contains 24 and 21 formula units of $Ca_3(PO_4)_2$, respectively [4, 7, 13, 14].

While both forms of crystalline TCP form only at high temperature [7], β-TCP is stable from room temperature to its transition temperature in which it transforms to the α-TCP phase [4]. In fact, α-TCP is a high-temperature polymorph of β-TCP, usually prepared by heating β-TCP above 1125 °C and quenching to prevent the reverse transformation [7]. Ion impurities such as Mg, Zn and Fe may affect the transition temperature which stabilises β-TCP [4].

Like HA, α- and β-TCP are highly biocompatible and can bond to bone easily [15]. In the human biological environment, they dissolve progressively and advance the replacement by natural bone growth. However, α-TCP has higher specific energy and is more reactive. Indeed, the resorption rate of α-TCP is usually faster than the formation of new bone which limits the application of α-TCP [9].

The Mg-substituted β-TCP (β-TCMP, β-tricalcium magnesium phosphate), which is often called whitlockite, is the only form of β-TCP that is found in biological systems. Under physiological conditions, β-TCMP is formed instead of β-TCP because of its lower solubility. In fact, whitlockite seems to be very stable suggesting that it could be a non-bioresorbable phase. It increases the densification and mechanical properties of the material [16]. It has been claimed that the addition of 1 wt% Mg in TCP prevents β- to α-TCP phase transformation. The crystal

structure of whitlockite is similar to that of β-TCP but the crystal composition is more complex and generally includes hydrogen phosphate (HPO_4^{2-}) groups in biological systems [4, 9].

Because of high-temperature stability and easiness of processing, β-TCP based ceramics have been commercialised for a long time to be used for bone substitution and repair. Many kinds of bone defects, such as augmentation of alveolar ridge defects after tooth extraction can be reconstructed by this ceramic. α-TCP has also been found limited similar applications [4]. Moreover, β-TCP can be used in combination with HA as a bone-substitution bioceramic, in the form of a biphasic CaP. β-TCP is considered to be both osteoconductive and osteoinductive, and due to its low interfacial energy with respect to apatite, it can induce the precipitation of an apatite layer upon incubation in aqueous ionic solutions [4, 7, 13].

1.1.3 Biphasic and triphasic calcium phosphates

Biphasic calcium phosphate (BCP) usually entitles a bioceramic material consisting of a mixture of HA and β-TCP [17]. If a part of β-TCP transforms to α-TCP, the resulting material will be a mixture of 3 phases and will be named as triphasic calcium phosphate. It is impossible to separate the individual phases because they are homogeneously and intimately mixed at the submicron level and are strongly integrated with each other [7]. In general, the properties of these materials depend on the fractions of these phases and are intermediate between those of the constituent compounds [18].

The main biomedical idea behind the BCP formulations is to achieve the desired balance of different and sometimes incompatible properties. Considering bioactivity, bioresorbability, osteoconductivity and osteoinductivity as major biological properties of interest in biomedical application, different CaP phases show different levels of these characteristics. For example, while HA is more stable, has superior mechanical properties and is more osteoconductive than β-TCP, the solubility and osteoinductivity of β-TCP are higher than HA. Therefore, by adjusting the HA to β-TCP ratio it is possible to produce a material with desired final properties of stability and biodegradability [7, 18].

Sintering of non-stoichiometric CaPs, such as CD-HA, at temperatures above 700-800 °C is the simplest way to prepare biphasic or triphasic calcium phosphates according to the next equation. The product of the thermal treatment is the formation of a BCP consisting of HA and TCP (usually β-TCP) [18].

$$CDHA(Ca_{10-x}(HPO_4)_x(PO_4)_{6-x}(OH)_{2-x}) \rightarrow HA(Ca_{10}(PO_4)_6(OH)_2) + \beta - TCP(Ca_3(PO_4)_2$$

Equation 1-1

The BCP composition (HA/β-TCP ratio) obtained after sintering is a function of the calcium deficiency of the primary apatite and the time and temperature of the applied thermal treatment [4]. For example, the thermal decomposition of $Ca_{10-x}(HPO_4)_x(PO_4)_{6-x}(OH)_{2-x}$ with x = 0.5 results in the formation of a BCP with HA/β-TCP ratio of 1/3 according to the following chemical equation.

$$Ca_{9.5}(HPO_4)_{0.5}(PO_4)_{5.5}(OH)_{1.5} \rightarrow Ca_{10}(PO_4)_6(OH)_2 + 3Ca_3(PO_4)_2 + H_2O \quad \text{Equation 1-2}$$

BCP ceramic may also be prepared by mechanically mixing of the desired amount of two types of synthetic apatites or commercial CaP reagents. However, in comparison with the material produced from thermal decomposition of CD-HA with the same HA/β-TCP ratio, the material prepared with mechanical mixing shows inferior sintering behaviour and less homogenous phase distribution [4, 18].

The relationship between cellular activity and the percentage of β-TCP in BCP is quite complicated. Various results were considered by different researchers as the optimum value of the HA/β-TCP ratio. Compositions such as 20% HA and 80% β-TCP [19], 15% HA and 85% β-TCP [20], 25% HA and 75% β-TCP [21], 30% HA and 70% β-TCP [22], 50% HA and 50% β-TCP [23] , 60% HA and 40% β-TCP [24], or even 100% HA [25] are reported in the literature as the ideal combination for cellular activity. These differences can be attributed to the potential applications that the authors considered in their researches which required different final properties [18].

BCP bioceramics are commercialised under various trademarks as blocks, particulates (granules), and custom-designed shapes [4]. They are utilised as bone grafts or bone substitute biomaterials for orthopaedic, maxillofacial and dental applications. Large bone defects, in some load-bearing areas, can be repaired by customized pieces of BCP which will maintain their shape over long periods. BCP is also used in sinus floor elevation for dental implant placement, to fill dental root canals and some similar applications. [7].

1.2 Ion substitutions

CaPs are considered to have very flexible structures, which allows substitutions in their lattice by many ions, almost half of the elements of the periodic system, without significant change in its hexagonal symmetry [1, 9]. The highly exchangeable nature of both HA and TCP crystalline structures represents a powerful design tool in the introduction and tailoring of different biological properties such as bone remodelling and tissue regeneration in CaP family of the bioceramics [26]. Full substitution of Sr^{2+}, Ba^{2+}, Pb^{2+} and partial substitution of ions such as Mg^{2+}, Zn^{2+}, Mn^{2+}, Na^{+} or K^{+}, for calcium (Ca^{2+}), the substitution of sulphates, vanadates, borates and acid phosphate (HPO_4^{-}) for $(PO_4)^{3-}$, and substitution of F^{-} and Cl^{-} for (OH^{-}) are some examples of the ion substitution occurring in the HA structure [1].

In general, the ion substitutions in the HA structure can be described by the following formula:

$$(Ca, M)_{10}(PO_4, CO_3Y)_6(OH, F, Cl)_2 \quad \text{Equation 1-3}$$

where M and Y represent ions substituting for Ca^{2+} and $(PO_4)^{3-}$, respectively [1].

For cations substituting Ca in the apatite structure, there is a strong correlation between substituting cations radius and their accommodation either in the site Ca(I) or in the site Ca(II). For example, when the cation radius is larger than Ca^{2+}, because

of bigger volume, Ca(II) sites are more preferred than Ca(I) sites. Furthermore, the cation distribution between the two sites Ca(I) and Ca (II) is also affected by the anion present in the channel due to the ions' charge and the strength of the corresponding bonds [9].

The substitution of monovalent anions (e.g., F^-, Cl^-) for OH groups takes place under charge balance. On the other hand, the substitution of bivalent anions (e.g., HPO_4^{2-}, CO_3^{2-}, SO_4^{2-}, SeO_3^{2-}) for the trivalent phosphate group occurs by charge imbalance. Balancing of the charge occurs by the formation of both hydroxide and calcium vacancies. In the same way, the negative charges resulting from the incorporation of a tetravalent anion (e.g., SiO_4^{4-}) within the lattice, is compensated by hydroxide vacancies [9].

Two different substitutions are possible for carbonate, CO_3^{2-}. Substitution type A that it replaces for the hydroxyl (OH^-) group and substitution type B that it replaces for the phosphate (PO_4^{3-}) group. Biological HAs are examples of Type B substitution and on the other hand, synthetic HAs are known as type A. These two types of substitution have opposite effects on the lattice parameters, a-axis and c-axis dimensions. The substitution of larger planar CO_3^{2-} groups for smaller linear OH^- groups increases the a-axis and decreases the c-axis dimensions. On the other hand, the replacement of larger tetrahedral PO_4^{3-} by smaller planar CO_3^{2-} groups decreases the a-axis and increases the c-axis dimensions [1]. It is possible to control the type of the substitution by the preparation method: Type A is obtained at high temperatures (at around 1000 °C) and Type B by precipitation or hydrolysis methods at low temperatures (25–95 °C) [4].

The physicochemical changes such as structural changes, crystal size, surface charge, and morphology caused by ion substitution, lead to important changes in the biological and mechanical performance of CaPs [4, 9]. In fact, the addition of trace elements can tailor the mechanical and biological properties of CaP scaffolds. For example, F-for-OH substitution in HA structure decreases the a-axis dimensions without changing the c-axis and is usually associated with an increase in the crystallinity and the stability of the structure [1], but it doesn't influence densification or grain growth [27]. Also, Sr-for-Ca or Mg-for-Ca substitution causes an increase in the extent of the dissolution of the apatite [1]. However, the degree of the effect depends on the size and amount of the substituting ion [4]. Furthermore, it has already been shown that the bivalent ions such as Zn^{2+}, Mg^{2+}, Sr^{2+}, Cu^{2+}, and Co^{2+} ions play a vital role in osteogenesis and angiogenesis [12]. Zinc-doped CaP materials show osteoblastic response in vitro as well as new bone formation in vivo. The positive effects of magnesium on densification and new bone formation has also been studied. It was also claimed the encouraging effect of strontium on bone formation [12].

Another important substitution in HA lattice is the silicon for phosphorous or more precisely SiO_4^{4-} for PO_4^{3-} groups. Due to the smaller radius of the silicon ion, silicon for phosphorous substitution in the HA unit cell leads to a distortion of PO_4^{3-} tetrahedra. The presence of silicon CaP materials increases the solubility of the

material therefore, stimulates the biological activity and creates finer microstructures [12] [28].

Introduction of Mn^{2+} ions in HA lattice (MnHA) is another interesting ion substitution. Manganese is an essential trace element which plays an important role in metabolism behaviour of all kinds of tissues in the human body. Mn^{2+} ions promote cellular attachment and enhance osteogenesis [29]. Mn^{2+} in the HA structure has also benefits in the repair and regeneration of damaged bones [12].

In recent years the researchers' interest in the design and development of multifunctional systems has increased. To this aim, the concept is to use the synergetic effect of various dopants or ion substitution in HA structure. In fact, the simultaneous ion substitutions in the apatite structure can have synergistic or antagonistic effects on the properties of the apatite. For example, magnesium and carbonate have synergistic effects on the crystallinity and dissolution properties of synthetic apatites; magnesium and fluoride or carbonate and fluoride have antagonistic effects, the fluoride effect being the dominant one [1, 30]. Similarly, the reported enhancement in the sinterability of HA ceramics resulting from Type B carbonate ions substitution is partially due to coupled substitution with Na^+ and subsequent formation of Na/Ca-phosphates which improves the sinterability [27].

1.3 Thermal decomposition

By submitting CaP bioceramics to thermal treatments, various decompositions and phase transformations take place which are functions of the Ca/P ratio of the starting material. The binary phase diagram of CaO and P_2O_5 which is the reference phase diagram for CaP ceramics is presented in Figure 1-2 and a simplified version of the part of the phase diagram dealing with CaPs family is presented in Figure 1-3. In these diagrams, the vertical lines correspond to Ca/P ratio of 1.5, 1.67 and 2.0, and are consistent with TCP, HA and tetracalcium phosphate (TTCP) phases, respectively. For the Ca/P ratio between 1.67 and 1.5 the material will be a combination of HA and α- or β-TCP, while when this ratio ranges between 1.67 and 2.0, CaO will be present besides the HA phase [1].

During thermal processing of stoichiometric HA, dehydroxylation is the first phenomenon that occurs. It has been suggested that during heating, HA molecules tend to lose hydroxyl groups at temperatures higher than 900 °C which results in the formation of hydroxyoxyapatite (OHA) and oxyapatite (OA) phases, according to the following equation [13, 31]:

$$Ca_{10}(PO_4)_6(OH)_2 \leftrightarrow Ca_{10}(PO_4)_6(OH)_{2-2y}O_y + yH_2O \qquad \text{Equation 1-4}$$

In this equation, if y=1 then the final material will be OA rather than OHA. Dehydroxylation proceeds without apatite decomposition. It induces the formation of hydroxide vacancies (noted V^o_{OH}), and therefore oxide ions O^{2-} ($O^{'}_{OH}$) replace hydroxide ions OH^- (OH^x_{OH}). Thus, the dehydroxylation equilibrium can be written

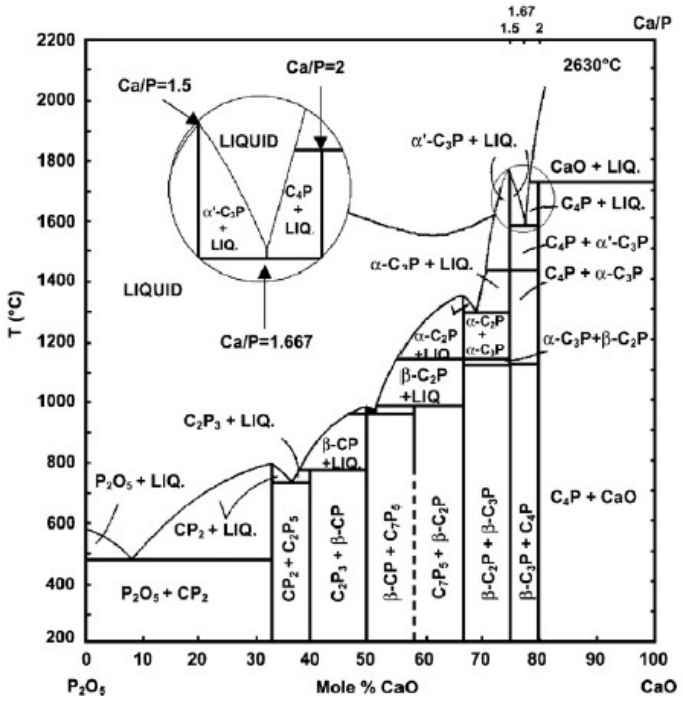

Figure 1-2: Phase diagram of the CaO-P_2O_5 system (C=CaO, P=P_2O_5). Each line represents a phase boundary. Here C_7P_5 represents $7CaO.5P_2O_5$; other abbreviations can be written out in the same manner. Reprinted from [32] with permission.

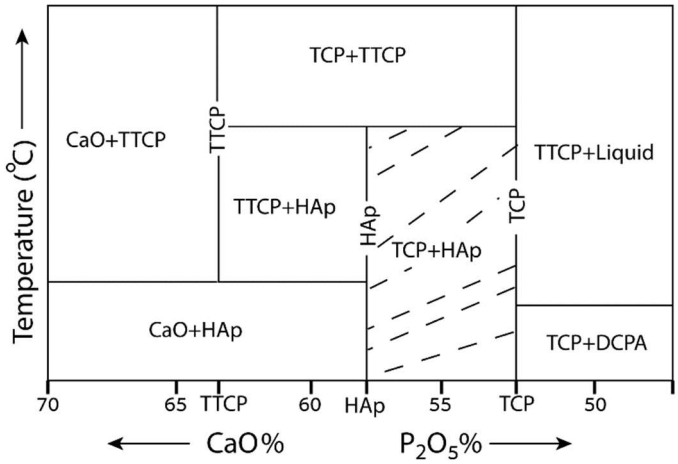

Figure 1-3: Simplified phase diagram of CaPs. Reprinted from [33] with permission.

as the following equation:

$$2OH_{OH}^{x} = O'_{OH} + V_{OH}^{0} + H_2O_{(gas)} \qquad \text{Equation 1-5}$$

In general, the dehydroxylation of HA is a reversible reaction and the water vapour released during the heating cycle can be taken up by the HA lattice during cooling. This process induces the formation of residual pores, with an adverse effect on the sintering behaviour of the material [31].

After dehydroxylation, the stoichiometric HA (Ca/P=1.67) is stable up to higher temperatures. Decomposition of HA happens at temperatures higher than

1300 °C which gives rise to the formation of TCP and TTCP according to the following equation:

$$Ca_{10}(PO_4)_6(OH)_2 \rightarrow 2Ca_3(PO_4)_2 + Ca_4P_2O_5 + H_2O \quad \text{Equation 1-6}$$

Therefore, the sequence of the phase transformations occurring during heat treatment of stoichiometric HA can be written as below [31, 34, 35]:

$$HA \rightarrow OHA \rightarrow OA \rightarrow TCP + TTCP \quad \text{Equation 1-7}$$

Both dehydroxylation and decomposition may result in volume expansions due to different theoretical densities (TD) of different phases [31].

The decomposition temperature of HA is affected by the partial water vapour pressure in the treatment atmosphere. While under vacuum the decomposition reactions can take place earlier, heat treatment in the partial water pressure may prevent those reactions. However, the sintering in the presence of water can be deleterious, since it reduces the densification rate of HA and accelerates the grain growth [27].

For HA material with Ca/P molar ratio higher than 1.67, the thermal treatment gives rise to the CaO formation. The further transformations of CaO to $Ca(OH)_2$ and $CaCO_3$ are accompanied by volume changes. The stresses associated with these last transformations decrease the strength and may cause decohesion of the whole material [27].

For HA material with Ca/P molar ratio lower than 1.67, sintering leads to the formation of β– or α–TCP phases. The allotropic transformation of β-TCP to α-TCP occurs at 1125 °C. This transformation is reversible and by performing a sufficiently slow cooling cycle, it is possible to have an almost complete phase transformation [34]. The presence of TCP decreases the mechanical properties and increases biodegradability of HA ceramics [27].

1.4 Sintering behaviour

Sintering is a controlled heat treatment considered as the last step of many ceramic processing techniques which leads to consolidation and densification of ceramic parts and plays a major role in the final properties of ceramic materials. Solid-state sintering is normally done in the temperature range of 0.5 - 0.9 respect to the ceramic melting point [37]. At these temperatures, the ceramic particles joint together to decrease their surface energy and the solid-state atomic diffusion reduces or eliminates the porosity between particles leading to the consolidation of the material. Sintering of CaP bioceramics not only affects the final microstructure (such as grain size and morphology, porosity amount and size) but also, due to several phase transformations, the final phase composition. All of these parameters affect the mechanical performance as well as the biological behaviour of CaP bioceramics [38].

In general, the sintering of CaP bioceramics is carried out in the air (conventional method) at temperatures between 950 and 1350 °C, for a few hours,

at heating and cooling rates in the range 2–20 °C/min [4]. If in the production stage, organic additives are used as binder or surfactant, a debinding cycle at intermediate temperatures is performed, to burn out these compounds. Also, all other volatile materials remaining from the synthesis stage, such as moisture, carbonates, ammonia, nitrates and any other organic compounds, are removed as gaseous products. If the elimination of these gases is accomplished before the closing of the open porosities, it will result in the production of denser ceramics. On the other hand, trapping of these gases within the ceramic structure decreases the densification and mechanical performance of the final material.

Sinterability of CaP ceramics is strictly connected to the characteristics of starting powder such as particle size distribution, agglomeration, crystallinity and chemical substitutions [29, 39]. There is a correlation between sintering temperature and time, with density, porosity, grain size, chemical composition and strength of the final ceramic [5]. The degree of densification and atomic diffusion are mainly controlled by the sintering temperature and time [5].

Upon sintering of the CaP bioceramics, like other ceramic materials, three sequential stages can be detected, as shown in Figure 1-4. Moving from the green state of the specimen (Figure 1-4a) to the first sintering stage (Figure 1-4b), the ceramic particles join together at their contact points, forming necks with increasing the strength of the material. This stage occurs with light densification until approximately 65 %TD is reached. At the end of the first stage, the ceramic body is characterised by a skeleton of weakly bounded grains crossed by a network of open pores [37, 38].

The main densification of ceramic parts occurs in the second or intermediate stage of sintering (Figure 1-4c), with the shrinkage of pores. During this stage, the microstructure of ceramic consists of a three-dimensional interpenetrating network of solid grains and continuous channel-like pores. At the end of this stage, which corresponds to about 90% relative density, the continuous pore network starts to break up into individual isolated pores.

The third sintering stage (Figure 1-4d) starts at relative densities higher than 90%. In this stage, the reduction of porosity continues, but at a slower rate, until densification stops. The isolated pores may disappear altogether, leaving a fully or nearly fully dense ceramic. The rapid grain growth can lead to the coalescence of neighbouring pores, so the average pore size often increases, even though the number of pores and the porosity decreases [37, 38]. The presence of open pores during the second sintering stage of the sintering drags the grain boundaries and limits the grain growth. In contrast, the collapse of the open pores in the last stage leads to an abrupt grain growth above 90 %TD [40].

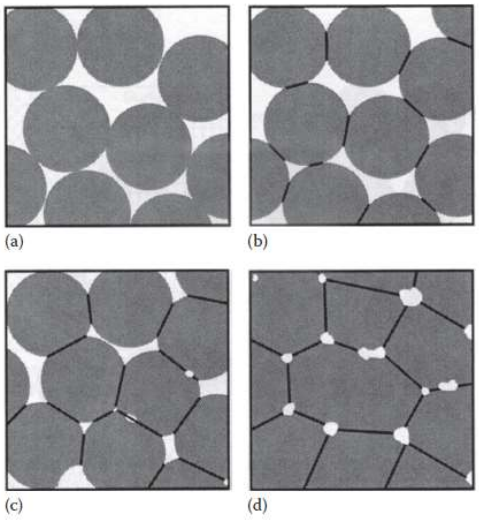

Figure 1-4: Schematic illustration of the approximate microstructure of each stage of the solid-state sintering. (a) Green sample, (b) initial stage, (c) intermediate stage, and (d) final stage [37].

At the microscopic scale, matter motion may proceed through different diffusion mechanisms involving surface, volume or grain boundary diffusion. In surface diffusion, the powder compact consolidates without noticeable densification, while volume or grain boundary diffusion is associated with densification [38]. The surface mechanism activates at lower temperatures than the two other mechanisms because of its lower activation energy. The activation energies are in the range 190-290 and about 400 kJ/mol for surface and volume/grain boundary diffusion of HA, respectively [38].

Surface diffusion of CaP bioceramics starts at low temperatures, from ≈400 ˚C and continues up to ≈700–800 ˚C. In this stage, the surface area of HA grains decreases, and the formation of strong chemical bonds between HA particles results in the development of necks between them [38]. The rate of isothermal surface area reduction (ν) due to superficial atomic diffusion in CaP apatites can be estimated by the following formula [38]:

$$\nu = dS/dt = k(T, Ca/P) \times (P_{H_2O})^{0.68} \times S^8 \qquad \text{Equation 1-8}$$

where S is the surface area, P_{H2O} is the partial pressure of water vapour, and k is a constant whose value depends on the temperature and CD-HA composition [38]. This equation shows that the water vapour available in the sintering atmosphere plays a positive role in the rate of surface area reduction. The higher the water pressure the higher the decrease of surface area. On the other hand, at a fixed temperature, the constant k decreases with increasing the Ca/P ratio of the apatite powder. For example, the value of this constant for stoichiometric HA (Ca/P ratio of 1.67) is only 9.2×10^{-3} compared to 1.35 for CD-HA with Ca/P ratio of 1.535 [38]. This difference is related to the higher concentration of calcium and hydrogen vacancies in the crystal lattice of CD-HA rather than HA, which promotes matter diffusion. In fact, the high value of *k* in CD-HA can lead to grain boundary sliding and noticeable grain binding with the surface mechanism. As a result, the total solid-gas interfacial energy reduces significantly, and the driving force for further

mechanisms decreases as well. The lower sinterability of CaP characterised by low Ca/P ratio and the final coarsened microstructure made by irregular shaped-grains are consequences of the high surface area reduction during the surface sintering stage [38, 41].

At temperatures higher than ≈ 750 ˚C, the thermal energy is enough for volume and/or grain boundary diffusions to start. With the beginning of densification, the previously formed necks grow and develop grain boundaries. The reduction of pore volume results in samples shrinkage. The onset of densification for CD-HA occurs at lower temperatures than stoichiometric HA [42].

Some authors discussed the effect of dehydroxylation on sintering. As stated in the previous part, the dehydroxylation of HA produces H_2O gas release and entrapment of this gas inside the bulk material. The establishment of a local hydrothermal environment filled with high-pressure steam inside these pores affects the sintering and grain growth behaviour of HA. Even before total porosity closing, the atomic diffusion responsible for densification may also be influenced because of the steam flows inside the sintering compact [31].

Grain growth in stoichiometric HA occurs mainly during the last sintering stage, typically when relative bulk density is >95 %TD, playing a crucial role on the final microstructure at very high sintering temperatures [38].

The crystallinity degree of the starting powder also affects the sintering densification of HA bioceramics. In fact, the activation energy for grain boundary diffusion is lower for poorly crystallized powders, and therefore densification during sintering is enhanced with respect to well-crystallized apatites [39].

The phase composition of sintered HA ceramics is affected by the Ca/P ratio of the initial powder. Different phases, such as α- and β-TCP, TTCP and CaO, can be found in the final sintered material along with HA. Apatites prepared from strong alkaline solutions, under air atmosphere, may contain CO_3^{2-} and can form CaO and HA upon sintering above 900°C. TTCP can also result from the reaction between β-TCP and CaO [1]. In fact, the Ca/P molar ratio has to be very close to the theoretical value (1.67) in order to avoid chemical substitutions which affect densification behaviour [39].

At sintering temperatures higher than 1125 ˚C, the allotropic transformation of β- to α-TCP is accompanied by a sudden volumetric expansion and induces mechanical stresses within the sample. Possible cracking due to these internal stresses leads to low mechanical reliability of TCP-containing CaP materials. Because, normally, the rate of the cooling stage does not allow the complete reverse transformation of α- to β-TCP, ceramics heated above the transformation temperature typically contain a mixture of α- and β-TCP phases [38]. It was reported that a dwelling at 900 ˚C for 24 h during cooling is needed to complete the reverse α- to β-TCP transformation [38].

In case of CaP ceramics, the important grain growth occurring during the final sintering stage and the presence of isolated residual pores at grain boundaries make the conventional sintering methods not able to provide fully dense ultra-fine-grained ceramics [40]. In order to decrease the sintering temperature, advanced

sintering methods such as hot pressing, hot isostatic pressing or hot pressing with post-sintering processes, can be used as well. As a result, higher densities and finer microstructures can be obtained, besides higher thermal stability and better mechanical properties of CaP bioceramics. Microwave and spark plasma sintering techniques are further non-conventional methods which are used to sinter CaP bioceramics [5].

1.5 Mechanical properties

Although exceptional biocompatibility makes CaP bioceramics excellent candidates for use in bone replacement and repair applications, they suffer from low mechanical properties. In fact, although CaPs have similar strength and stiffness to cortical and cancellous bone, their inherent brittleness and low reliability (i.e., low fracture toughness) limit the use of CaPs to non-load-bearing applications [7, 38, 43]. The compressive strength of CaPs is higher than that of natural bone, however, they are brittle, with low impact resistance and tensile stress [7].

A wide range of values, concerning mechanical properties, has been reported in the literature for HA and TCP ceramics [18, 44, 45]. This is due to the several parameters affecting CaPs mechanical properties. Preparation route, initial particle size, crystallinity, chemistry, sintering cycle and phase decomposition during heating are the main parameters able to affect the final properties. In general, the presence of residual amorphous phase, microporosity, and the large grain size decreases the mechanical properties of CaPs. Conversely, high crystallinity, low porosity, and fine microstructure result in higher mechanical properties [44].

In the following parts, the most important parameters affecting the mechanical properties of dense and porous CaP bioceramics are discussed in detail.

1.5.1 Porosity

Porosity shows the greatest influence on mechanical properties. Several mechanical properties decrease substantially with porosity increase [4, 13]. Pores are sites of concentrated stresses which reduce the stress need for crack initiation and propagation, leading to premature failure. In general, there is an exponential relationship between the increase of porosity and the reduction of mechanical properties of ceramic materials [7, 45, 46].

Mechanical strength is not only affected by porosity fraction but pores size and geometry play an important role, too [7, 45]. It has been found that at a fixed amount of porosity, the compressive strength of HA bioceramic increases almost linearly with decreasing the macropore sizes [46]. This effect is more important at lower porosity volumes, and when porosity increases to more than 70%, the compressive strength becomes almost insensitive to the pore size [46]. Also, the presence of sharp corners as points of flaw initiation must be taken into account. Cordell et al [47] investigated the compressive and bending strength of HA scaffolds as well as their reliability with different pore sizes. The authors found that for HA bioceramics

both bending and compressive strengths were higher for samples with smaller average pore sizes. However, the Weibull distribution showed that the reliability of the materials increased by increasing the pores sizes. Therefore, in the evaluation of the reliability of HA, pore size and pore size distribution must be considered along with the deformation mode (bending or compression) [47].

One of the most common representations of the relationship between strength and pore fraction is given by the following equation:

$$\sigma = \sigma_0 \exp(-bp) \qquad \text{Equation 1-9}$$

in which σ and σ_0 are the strength of the porous ceramic and the fully dense material, respectively, b is an experimentally determined constant related to the sensitivity to porosity, and p is the pore fraction. It can be seen that this equation considers an exponential effect of the pore fraction on the mechanical properties. However, the effect of pore size and geometry is not considered [43].

Figure 1-5 shows the biaxial flexural strength of porous HA as a function of pore fraction in a relatively high range of porosity. The experimental points are well fitted by Equation 1-9, which confirms that this equation well describes the behaviour of CaPs with relatively high pore fractions and pore sizes, over a wide range of independent studies [43].

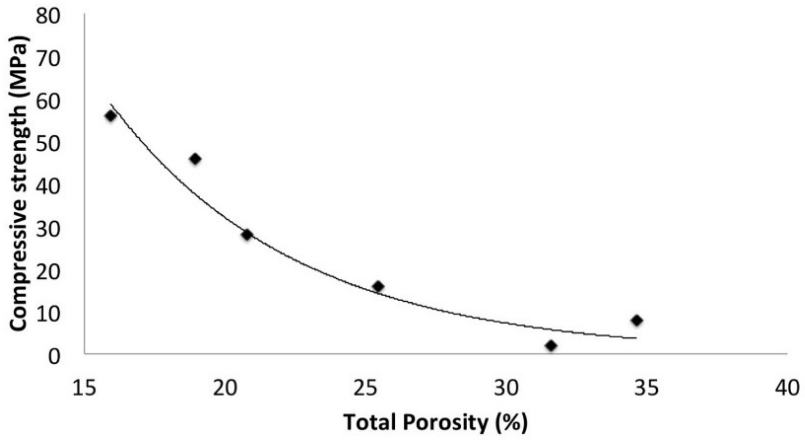

Figure 1-5: Influence of porosity on the biaxial strength of porous CaP. Reprinted from [48] with the permission of Elsevier under the license no 4782701500474.

A further study was developed by Gibson and Ashby regarding the relationship between mechanical properties and relative density. This model is valid for open-cell foams and can be summarized by the following equations:

$$\sigma^* = \sigma_s C_1 \left(\frac{\rho^*}{\rho_s}\right)^{1.5} \qquad \text{Equation 1-10}$$

$$E^* = E_s C_2 \left(\frac{\rho^*}{\rho_s}\right)^{2} \qquad \text{Equation 1-11}$$

where σ^* is the crushing strength and E^* the elastic modulus of the porous body; σ_S and E_S are the rupture modulus and the elastic modulus of the strut, respectively; (ρ^*/ρ_S) the relative density of the material; and C_1 and C_2 constants with values

close to 0.2 and 1, respectively [49]. According to these equations, with decreasing the relative density both fracture strength and elastic modulus decrease, however, porosity has a bigger effect on the elastic modulus than on the fracture strength.

1.5.2 Sintering temperature and relative density

Sintering temperature affects the mechanical properties in several ways. Density, final grain size, and final phase composition are different characteristics that are dependent on the sintering temperatures and have a substantial influence on the mechanical properties.

In general, the final density of ceramics has a direct relationship with sintering temperature, which affects the mechanical performance as well. The denser the material, the higher the mechanical properties. However, the effect of sintering temperature on the final density of CaP bioceramics should be considered along with other parameters such as powder composition, powder size, surface area and phase decompositions [50].

Grain coarsening which takes place at higher sintering temperatures has been found to reduce the mechanical properties of sintered CaPs [51]. In general, the strength of ceramics, like metals, is proportional to the inverse square root of the grain size. Smaller grains, which are also associated with smaller microstructural defects, improve the strength and hardness of materials [29, 43].

Apart from grain coarsening, which is promoted at high temperatures, the dehydroxylation and decomposition of HA can reduce the mechanical properties. Decomposition products can hinder the formation of strong inter-particle bonding, and inter-granular segregation can lead to grain boundary weakening [6]. Inhomogeneous microstructure and very fine pores generated by the decomposition of HA significantly decrease density, Young's modulus, and toughness, while the flexural strength seems to be more affected by the largest defects present in the material [29, 50].

It has been shown that different mechanical properties are affected by the sintering temperature in different ways. In other words, the maximum values of different mechanical characteristics don't occur at similar sintering temperature. For example, in the case of nano-HA sintered between 1000 and 1400 °C, the highest Young's modulus was achieved at 1200 °C, while the maximum hardness was obtained at 1300 °C [6].

1.5.3 Preparation methods and composition

The structural and mechanical properties of HA can be modified by varying the processing method and the optimisation of the synthesis processes. Different processing parameters lead to synthesized powder with different particle sizes, composition and textural properties which affect the final properties of the sintered ceramic bodies [50].

Increasing the Ca/P atomic ratio to 1.67 was found to improve the strength of the HA ceramics. In fact, the mechanical properties reach a maximum value at

Ca/P=1.67 and then decrease suddenly at higher ratios [7]. This effect is imputed to the phase decomposition of the CaP ceramics, which affects the mechanical properties [43].

Dopants show an effect on the final mechanical properties of HA ceramics, too. For example, Mn-doped HA reaches higher density (>99 %TD) compared to undoped HA. Samples containing less than 0.5 wt% MnO_2 exhibited higher mechanical properties (such as Vickers hardness, fracture toughness, and Young's modulus) than the undoped HA materials [52].

Studies have shown that β-TCP is detrimental to the mechanical properties of HA components. As a general trend, mechanical properties decrease with increasing the β-TCP phase. Due to the different theoretical densities of HA, β-TCP, and α-TCP, phase transformations are accompanied by volume changes. Microcracks formation during phase transformations occurring during sintering decreases the mechanical properties [43]. On the other hand, it has been claimed that a relatively small amount of β-TCP strengthens the HA matrix, according to the rule of composite mixtures [53]. The maximum strength was achieved at 10 [52], 20 [54] and 40 wt% β-TCP [55]. However, other studies show a decreasing trend in mechanical strength by the introduction of TCP phase [56, 57, 58].

1.5.4 Improvement of mechanical properties

Several methods have been proposed in the literature to improve the mechanical properties of CaP bioceramics. Some examples deal with the use of ceramic nanopowders, the exploitation of more advanced sintering processes, the production of hybrid structures from HA and biopolymers, and the reinforcement of HA matrix with high strength ceramics [59, 60, 61, 62, 63].

An effective approach is the development of HA-based composites. One of the mostly studied reinforcing material is zirconia. Chang et al. [59] and Miao et al. [60] showed that the incorporation of zirconia in the HA matrix yields higher mechanical properties (bending strength, microhardness, and Young's modulus) compared to pure HA. However, the higher sintering temperature of zirconia than HA promotes grain coarsening and decomposition of the HA phase.

In order to improve the fracture toughness of HA ceramics, the introduction of HA whiskers in the nano-sized HA matrix has been investigated, providing an increase of 1.5 $MPa.m^{1/2}$ [61].

Another parameter to control the mechanical properties of HA is the final grain size of near fully dense samples. Grain refinement improves strength and hardness. It is logical to expect higher mechanical performance for the nanostructured HA than conventional HA, due to a grain boundary strengthening effect, which is more important in nanosized materials. However, the control of the detrimental grain growth, for densities higher than 90 %TD, is difficult, which makes the fabrication of fully dense nanostructured ceramics a hard task [62].

The exploitation of advanced sintering processes such as hot pressing, post-hot isostatic pressing, spark plasma sintering and different microwave configurations

have also been proposed [63, 64]. The idea behind these technologies is to achieve high density without significant grain growth and/or detrimental phase transformations. Despite the advantageous consequences of these methods, sophisticated and expensive equipment are required, which limits their application [40].

Mazaheri et al. [40] proposed two-step sintering as a novel method to control the grain growth of HA nanopowders, as a simple but promising approach to obtain fully dense nanostructured ceramics. In this method, samples were firstly heated up to 900 °C (T1) for 60 s to reach uniform temperature; then the specimens were cooled down to 800 °C (T2) for 20 hours. The cooling rate between these two temperatures was as high as 60 °C/min. This approach allowed to obtain nearly full dense HA samples, with the final grain size significantly lower than the conventional sintered samples (average grain sizes of 0.19 and 1.7 μm, respectively) with almost doubled fracture toughness (0.98±0.12 to 1.92±0.20 $MPam^{1/2}$) [40]. However, depending on the material, several combinations of T1 and T2 should be tested to find the best combination of density and grain size.

As a final strategy, the production of hybrid components of HA and biopolymers (such as polycaprolactone (PCL) or polylactic acid (PLA)) is performed as well, in order to improve the mechanical and biological properties of the scaffolds. Polymer/ceramic composites help to avoid the inherent brittleness of the bioceramic and enhance the compression resistance [65].

1.6 Biological properties

1.6.1 Integration with the host tissue

By the introduction of biomaterials as an implant in a biological site, different types of implant-tissue responses can be expected which are dependent on the physical characteristics of the implant (porosity volume, size, and structure, degree of pore interconnectivity [4]) as well as on the biological properties (bioactivity, osteoconductivity, osteoinductivity, etc.). The interactions between the ceramic implant and the host tissue lead to gradual incorporation of bioceramics into the developing bone tissue [7].

The most fundamental property for an implant material is biocompatibility. This means that the implant can perform its intended function, without inducing any undesirable effects on the host tissue [43]. CaP bioceramics have shown good biocompatibility, do not elicit any inflammatory responses and must specifically provide a suitable substrate for the growth of new bone [13].

BS ISO 23317-2014 [66] defines bioactivity as the property that elicits a specific biological response at the interface of the material resulting in the formation of a bond between tissue and material. Bioactivity of CaP bioceramics has been already demonstrated: this property is due to the formation of apatite nano-crystals, similar to bone apatite, on the surfaces of HA grains after implantation in bony or non-bony sites [4].

Growing of the new bone on the implant surface is defined as osteoconduction [7]. In general, bioactive materials are also osteoconductive. CaP implants not only permit new cells of bone to attach, proliferate, and migrate through their structure, but also allow the nutrient-waste matters to be exchanged through the formation of new blood vessels [67]. The osteoconductive property of CaP implant takes place according to a sequence of physicochemical interactions at the surface of the implant. At the beginning of implantation, a local decrease of pH leads to partial dissolution of CaP in the implant surface, resulting in the release of calcium and phosphate ions into the microenvironment around the implant. Increasing the degree of saturation in their microenvironment results in the precipitation on the surface of biological apatite microcrystals that favour bone tissue apposition. Incorporation of other ions such as carbonate and magnesium, as well as organic macromolecules from biological fluids along with various proteins and growth factors in these microcrystals, subsequently may facilitate cell attachment and function [4, 7]. As the osteoconduction progresses, a direct structural and functional connection between living bone and the surface of the artificial implant takes place. This last phenomenon is known as osseointegration [68].

Osteoinduction is defined by the ability of a material to form bone in an ectopic site. CaPs by having a chemical composition similar to biological bone, stimulate bone formation and has been shown to be osteoinductive [26]. Osteoinductive materials support tissue ingrowth and allow the formation of bone even in non-bone-forming sites [4]. It has been claimed that micro and macro porosities promote osteoinductivity of CaPs because they are capable of entrapping and concentrating growth factors [69].

Among several factors that affect the osseointegration and the strength of the interface between an implant and bone, the most important ones are surface chemistry, roughness, level of crystallinity and Ca/P ratio. Surface roughness, both at the micrometre and the nanometre levels improve bone regeneration through the promotion of osteoblasts functions [7]. The surface energy affects the bone cell maturation and differentiation, as well as osseointegration. Higher surface energy leads to more rapid cell activation and differentiation [7].

Crystallinity affects proliferation mechanisms. For example, the spreading of osteoblasts is faster on better-crystallized surfaces, mainly due to the development of a more organized cytoskeleton [70].

Moreover, calcium ions in HA, having a positive charge, promote the attachment of osteoblasts and cell growth [71, 72]. In contrast, phosphate ions showed to have an inhibitory effect on cell activity [73].

The enhancement of bone formation of CaP ceramics is also dependent on the Ca/P ratio [26]. While stoichiometric HA has no osteoinductive capability and failed to show evidence of new bone formation, *in-vivo* tests have shown that β-TCP promotes bone formation [74]. Studies demonstrated that when the implant is a biphasic mixture of HA and β-TCP phases, it shows better bone regeneration properties. In fact, HA, independently from its source (natural or synthetic), forms a strong chemical bond with host bone tissue, while β-TCP plays an important role

in cell proliferation, revascularization, and osteogenesis. Therefore, the highest rate of new bone formation is achieved at a moderate combination of these two phases. For pure HA, the osteoblastic activity is weak and the ceramic particles are simply surrounded by fibrous connective tissue, with a lower formation of new bone compared to ceramics containing β-TCP. This may be due to the low dissolution rate of HA. As the proportion of β-TCP increases, the osteoclastic activity also increases, with associated ceramic resorption [74]. However, pure β-TCP shows weak bone formation ability. This is due to the high dissolution factor of this phase: in fact, β-TCP resorbs more readily than HA and most of the 100% β-TCP particles disappeared within short periods. Therefore, the ceramic does not remain in the tissue sufficiently for cell differentiation, maturation, and revascularization [74].

1.6.2 Dissolution

The core mechanism of bone formation on CaP surfaces is the partial dissolution of the CaPs due to the acidic condition produced by osteoclasts. The chemical composition and Ca/P ratio are the main determinant factors in the dissolution rate of CaPs. TCP with a Ca/P ratio of 1.5, is more soluble than HA, with the ratio of 1.67. By infiltration of cells into the scaffolds and their proliferation, the degradation of the scaffold provides further space for continued cell growth and tissue formation [75]. Implants made of pure HA often remain in body for several years after implantation. It was found that the degradation of HA did occur, but it stopped after osteo ingrowth [13]. Among all CaPs, only fluorapatite (FA) is more stable and less soluble than HA. As a general trend, the solubility of these phases decreases in the order α-TCP > β-TCP > CD-HA > HA > FA [4].

Even though the chemical composition of α-TCP is identical to β-TCP, due to its higher specific energy, it is more reactive in aqueous systems. Having a resorption rate faster than the formation of a new bone is considered as the major disadvantage for using pure α-TCP in biomedical applications [7, 76].

There are also additional factors that influence the biodegradation of CaP ceramics. By increasing the surface area, decreasing the crystallinity and grain size and increasing the ionic substitutions, the rate of biodegradation increases. Increasing porosity greatly enhances the surface area in contact with body fluids, thus leading to a faster dissolution rate. Lattice defects promote the dissolution process. Substitution in the apatite structure affects apatite solubility. For example, HA solubility increases by anionic substitution of carbonate for phosphate and on the other hand, cationic substitutions such as Mg in place of Ca, improves the biological performances by providing trace ions [7]. Substituted β-TCPs containing Zn and Mg proved to exhibit a lower solubility than non-substituted ones, depending on the substitution ratio. Furthermore, the kinetics of the dissolution of β-TCP seems very sensitive to the presence of foreign ions in the solution, especially Mg^{2+} and Zn^{2+} [4].

While the resorbability rate comparable to the formation of bone tissue can be considered as the desirable rate, other factors such as age, sex and general metabolic health of the recipient, as well as the anatomic site also affect the rate of bone formation. In general, the natural replacement of CaP implants can be in the range of 3 to 36 months [7].

1.7 Tissue engineering and scaffold production

In comparison with living tissue, all present-day orthopaedic implants are not able to provide these three critical characteristics: (1) the ability to self-repair; (2) the ability to maintain a blood supply; and (3) the ability to modify their structure and properties in response to environmental factors such as mechanical load. On the other hand, the artificial implants have a limited lifespan, and with continually increasing of life expectancy, a shift from the replacement to the regeneration of tissues seems inevitable [77]. Tissue engineering (TE) is an alternative to bone-grafting procedures. It uses engineering principals in combination with life science to find prospective solutions for bone regeneration in a reliable and physiologically acceptable manner [67]. The general practice in TE is to use scaffolds with sufficient porosity and mechanical strength as structural support for the newly formed tissue which involves cell adhesion, migration, growth, and proliferation, resulting in good integration with surrounding tissues. A suitable scaffold should be biocompatible, osteoconductive and osteoinductive. However, an ideal bone graft not only provides strength and support, but also by gradual resorption at speeds not more than the new bone formation, transfers the mechanical loads to the surrounding newly regenerated tissue and creates space for the growth of the natural bone tissue [44, 78].

1.7.1 Physical properties

Transport of nutrients, as well as metabolic waste, is crucial for the growth of new bone. To this aim, scaffolds should possess three dimensional, highly interconnected porous network together with appropriate pore size, and pore structure. The bone scaffold needs to ensure the permeability of liquids through the structure. The scaffold must be porous enough to support bonding, which means to possess at least 60 vol% porosity [67, 79]. Increasing both the specific surface area and pore volume accelerates the biological apatite deposition and enhances the bone-forming ability. Higher surface area is not only beneficial for chemical bonding between the bioceramics and bones but also provides good mechanical fixation [1, 45]. Moreover, the pores' interconnection is of uttermost importance because it guarantees the cell distribution and migration deeply throughout the implant [9].

When designing a scaffold, pores sizes are the most important factor. They must be large enough because they provide passways for cell transport. In order to allow cell attachment and vascularization, the pore size has to be in the range of 100-800

μm. [80]. *In-vivo* experiments conducted by Gauthier et al. showed a more significant bone formation for the implants with a macropore size of 565 μm than a macropore size of 300 μm [81]. Similarly, another research showed grater ingrowth in HA blocks with 260 μm pore diameter than the block with 150 μm pore diameter [82]. While the minimum pore size of 100 μm has been reported to be necessary for porous implant operation, a different range of pore sizes is beneficial for specific aspects of new bone formation [1, 9]. It has been claimed that 5 μm pores permit new vascularization, pores between 15 μm and 40 μm allow fibroblastic growth, pores between 40 μm and 100 μm favour osteoid growth, pores between 200 μm and 350 μm allow significant bone growth and pores bigger than 500 μm permit fast vascularization [83]. The vascular tissue does not appear in pores <100 μm [1]. Microporosity smaller than 10 μm can also be used in drug delivery applications. Controlled porosity allows the therapeutic agents to release on a targeted site by a slow, continuous, and controlled flux [84].

Pores in the sub-micrometre range enhance cell adhesion and proliferation and have the potential to absorb substances such as proteins and growth factors that work in the regenerative process [85]. Pores in the range of 2–5 μm, at the walls of the scaffold, improve the biological performance of the porous scaffold via facilitating of fibrovascular colonization [9, 86]. However, these improvements of the biological properties take place along with a decrease in the mechanical integrity of the struts [87, 88].

In vivo tests showed that the interconnection size of over 20 μm allows cell penetration and tissue formation inside macropores. However, an interconnection size of over 50 μm can assure mineralized bone formation.

1.7.2 Mechanical properties

The clinical success of an implant also depends on its mechanical behaviour. An ideal bone scaffold should possesses the mechanical properties similar to the replaced bone and guarantees proper load transfer. A matrix should be designed such that its mechanical properties matches the mechanical properties of the immediate surrounding tissues of the defect. While an underdesigned matrix may fail as mechanical support to the skeleton, an overdesigned matrix with high elastic modulus can lead to stress shielding, in which the implant carries nearly all the load, prevents the bone from being properly loaded and leads to the new bone formation that has not enough mechanical properties [1, 27].

In fact, the mechanical integrity of the implant with the tissue starts from its implantation to complete healing [43]. Not only the implant must provide sufficient mechanical support but also its mechanical performance should be in cooperation with biological activity. Higher mechanical behaviour is generally in contrast with the higher porosity which is an important factor in the bioactivity of the implant [13]. On the other hand, it has been shown that a certain time after implantation and ingrowth of new bone, the mechanical properties improve [76]. It has been demonstrated that the initial mechanical property of BCP increased two or three

times (2–6 MPa) in a few weeks after implantation [4, 13]. The improvement of the mechanical properties of HA scaffolds after 2 weeks of immersion in the simulated body fluid, due to the precipitation of apatite crystals, has been also reported [89].

1.8 Production of ceramic parts through gelcasting technique

Gelcasting is an advanced ceramic forming method that is based on techniques taken from the traditional ceramics industry and polymer chemistry. In gelcasting technology, an organic monomer is added to the ceramic slurry as the gelling agent and the in situ polymerization of the monomer leads to a strong cross-linked network that binds ceramic particles together, producing green bodies with high density and strength [37]. Compared to the traditional ceramic processing, an additional heat treatment is needed to burn out the organic additives before sintering, which has to be carried out with care to prevent cracking due to the induced stresses [37].

The main advantage of gelcasting is the ability to produce components with high material performance combined with complex shapes, which are not easily obtained by other methods. Gelcast green parts show high strength that results in improved machinability and allows obtaining even more complex shapes. Moreover, based on colloidal processing, the obtained microstructure shows high homogeneity, offering uniform properties through the whole part [37].

Gelcasting, in general, is based on aqueous systems using dispersant and processing methods similar to traditional slip casting. The normally required slurry properties are also similar to those for slip casting: stability against flocculation, high particle concentration (≈ 50 vol%), and suitable viscosity for casting [37].

Higher solid loading is desirable in gelcasting technique. Normally, high solid contents lead to a higher density of the final ceramic products and reduce the shrinkage during drying. However, ceramic slurries with too high solid loadings usually result in higher viscosity which makes difficult the casting into the moulds. Therefore, it is important to use effective dispersant to obtain flowable ceramic slurry with high solid loadings [11, 37, 51].

The first monomers used as gelling agents were acrylamide monomers. Nevertheless, this monomer was found to be neurotoxic and could cause cancer to humans [49]. After using methacrylamide (MAM) and methylenebisacrylamide (MBAM) as a new standard system because of their relatively low toxicity, researchers have recently explored the gelling abilities of non-toxic gelling agents such as polysaccharides, proteins, methylcellulose, albumin, starch, gelatin and agarose as environmentally friendly reagents. [90].

1.8.1 Gelcasting of porous parts

The microstructure of the final macroporous ceramic is ultimately affected by the processing route. Therefore, the microstructure needed in the final application

along with the inherent characteristics of the process such as cost, simplicity, and versatility determine the selected processing method. The three main methods in the production of macroporous ceramic structures are sacrificial template method, replica technique, and direct-foaming technique [91].

The sacrificial template method involves the addition of some organic inclusions in the green bodies that will burn out during sintering, leaving behind the corresponding pores. In this case, the porous microstructure is tailored by changing the size and amount of organic inclusions. However, the degree of interconnectivity of struts in this method is reported to be poor [92, 93].

The replica technique involves the coating of flexible open-cell polymer foams with ceramic slurry. The burning out of the polymer foam leaves behind a replica of the original foam in the sintered ceramic. In this method, the structural properties of the ceramic foams, like relative density, morphology, size, and distribution of cell walls, are controlled by the characteristics of the polymer foam, such as porosity and pore size distribution, as well as the amount of the impregnated slurry [93]. The critical step in this method is the choice of polymers. The polymer foam dictates reproducibility through its modulus of elasticity and must also burn out with minimal residue [26]. Final hollow struts are another drawback of the replica process, which reduces the ceramic mechanical properties [86].

The gelcasting of foams is another method for the production of macroporous ceramics which has been found to have several advantages over other methods. This method was developed by combining the gelcasting process with the aeration of the ceramic suspensions containing foaming and gelling agents [94]. Ceramic foams are produced by two main techniques, namely mechanical frothing and the injection of gases into ceramic suspensions. The addition of surfactants is required to stabilise the produced foams.

This process yields cellular structures with porosity varying from 40% to 90%. and sizes between 30 μm and 1 mm. Whether the pores are open or closed depends on the pore fraction [95]. One of the major advantages of this technique over other porous parts production techniques is the development of well-densified struts [86, 91]. Besides, the mechanical strengths of sintered foams are greater than that porous samples obtained by other routes thanks to the spherical pore shape associated with a fully densified matrix [96]. This process is known to yield non-cytotoxic materials with optimised strength and open spherical pores and can be applied to many raw materials.

Foaming agents or surfactants are usually organic compounds which consist of both hydrophobic and hydrophilic groups. Having this configuration, surfactants tend to adsorb onto gas-liquid interfaces, reducing the surface tension of the gas-liquid interface and making the foam films thermodynamically stable [77]. The fast gelation of organic monomers freezes the foamed ceramic slurry and provides a highly porous structure with relatively strong bodies [86].

The foam formation takes place by two consecutive assembly processes: 1- the short-chain amphiphilic molecules adsorb on the particles surfaces, and 2- the partially hydrophobized particles adsorb onto the air-water interface of freshly

incorporated bubbles. These assembly processes lead to a hierarchical structure in three levels: 1- Short-chain amphiphilic molecules, 2- partially hydrophobized particles, and 3- air bubbles [91].

By stirring the suspension, the injection of gas into the suspensions leads to the liquid to be drawn around each bubble until formation of a thin film. In the first place, the quantity of foam depends on the effectiveness of the foaming agent in reduction of the surface tension of the solution. Then, further thinning is prevented by the forces established due to the movement of the surfactant molecules from the interior of the slips toward the newly created surfaces. By attachment of the most surfactant molecules to the gas/liquid interfaces, no longer is possible to stabilise new films and the volume increase stops. The maximum foam volume is determined by the minimum film thickness that can sustain a stable foam. Above this level, the rate of bubble generation by stirring becomes equal to their almost instant disintegration and therefore, a further increase of the foam volume is hindered. [97].

Final morphology of the foamed structure is also controlled by the interval between foam generation and foam solidification. In this time period, while some bubbles may coalesce to form larger bubbles, some others may dwindle and disappear. The thinning process of the lamella surrounding the bubbles is considered as the responsible to these changes. The thinning process takes place due to the mechanisms such as gravity induced drainage, capillary induced drainage, local depression of surface tension due to hot spots and Van der Waals attraction between the surfaces of thin films. The fact that the properties such as permeability and strength of the final porous part are controlled by the final cell size distribution and wall thickness, emphasises the importance of the changes in the foam structure prior to solidification. For example, the intact remaining of the bubble surrounding films leads to closed-cell foam and the partial rupture of the films results in open celled foams. Foams collapse due to excessive film rupture in extreme cases [97].

The most critical factors in the successful production of porous bodies through gelcasting of foams comprise the selected gelling substances and the control of gelling reactions. First of all, in order to obtain homogeneous microstructures and highly dense struts, the gelling matter should not have an adverse effect on the dispersion of powder and the stability of the suspension. Furthermore, the addition of the gelling precursor should not lead to a significant increase in the slurry viscosity, which would limit the ability of foam generation. Conversely, the high viscosity of the slurry imparts higher stability to the foam and prevents it from the collapse [95]. The foaming process of the suspensions with low viscosity is easier and the produced samples contain higher porosity. However, after foam generation, the liquid drainage by capillary and gravitational forces happens faster and the gelation must be fast enough to prevent the foam to collapse. The formed polymeric network must be sufficiently strong to support the porous structure. Despite its large porosity, the gelled foams must withstand demoulding, handling, drying and machining without damage [95].

1.9 Production of ceramic parts through additive manufacturing techniques

Conventional techniques of scaffold production are dealing with a major limitation: it is not possible to control the scaffold architecture, pore size and pore network precisely enough. Additive manufacturing (AM) methods have been proposed to overcome these drawbacks because of their unique capability in the fabrication of macroporous complex parts. The discrete nature of AM methods provides the potential for spatial and temporal control of the microstructure to obtain geometrically complex components that would be very hard to fabricate using machining [98]. As a result, the number of researches on AM for TE applications has been progressively increased in recent years.

However, contrary to the polymeric and metallic materials, only a limited number of AM techniques are applicable to ceramic production, mainly due to the high melting point of the ceramic materials. Furthermore, many of the AM techniques have serious limitations in the production of dense ceramic bodies, and retention of superior physicochemical properties of produced monolithic ceramics is still challenging [79, 98, 99].

Depending on the fabrication principle, AM techniques set up for biomedical applications can be classified into four categories: 3D printing (3DP) or binder jetting, selective laser sintering (SLS), stereolithography (SLA) and slurry extrusion-based techniques. These AM methods display different advantages and limitations in terms of accuracy, surface roughness and mechanical properties [100].

1.9.1 3DP

3DP is a powder-based AM method. In this method, a liquid binder is selectively sprayed onto a powder bed and binds the particles together to shape the final design, followed by sintering to obtain the final part. 3DP is generally a fast and simple process and is capable to print parts from a wide range of materials including metal, polymer, and ceramics [99]. It has been implemented in the production of a wide variety of ceramic parts as well as CaP bioceramics [88, 100, 102, 103, 104, 105].

However, the low powder packing combined with random agglomeration makes the final parts produced from 3DP highly porous, which results in low mechanical performance. Furthermore, to maintain the appropriate flowability for the deposition of thin layers, powders needed to consist of relatively large particle sizes (indicatively 30–100 μm) which may affect the sinterability and densification behaviour after printing. In fact, the parts made by this method contain bimodal porosities, a designed porosity in the range of ~ 0.5–2 mm and an additional microporosity due to incomplete densification [97, 102, 104]. Due to very low sintered densities, which rarely exceeds 50% of the theoretical value, this technique seems not to be suitable for the production of the structural parts [101].

1.9.2 SLS

In the SLS process, a ceramic powder bed is sintered layer by layer using a high-intensity laser beam to form the 3-D object. The application of this method on CaP powders started in 1994 for the production of ceramic bone-implants [107] and continued until now with the fabrication of BCP ceramic parts [100, 108].

Poor resistance of ceramic materials to thermal shock and limited material diffusion, due to the short interaction time between laser and powder, lead to poor sintering and low mechanical properties of the ceramic bodies produced with this technique [99, 100].

1.9.3 SLA

The SLA is a 3-D printing technique based on the selective photopolymerization of a liquid resin filled with ceramic particles. After layer by layer production of the part, the green structure is cleaned to remove the unpolymerized suspension, then debound and sintered to obtain the final part. The typical slurry is a mixture of the ceramic powder, a monomer solution, a photoinitiator and a dispersant to increase the ceramic concentration between 40–60 vol% [99, 100].

Scaffolds produced by SLA possess a good surface finishing, good mechanical properties, and high accuracy even though the cleaning and debinding steps are problematic. SLA has been found to be an effective method for the production of complex HA parts [109] and the final microstructure is crack-free with controlled channel size [110].

Currently, in the market, there are different CaP scaffolds made by SLA as bone replacements. The efficiency of this technique in the production of large customized patient-specific implants from HA is demonstrated and successfully implanted on complex craniofacial bone defects [111].

Micro stereolithography (μSLA) is a similar technique which has been developed in parallel to the traditional SLA process. This technique allows the production of scaffolds with higher accuracy, approximately 10 times higher than conventional SLA. Using μSLA, the pore shape is efficiently controlled, which is hardly achievable by any other AM direct methods [100].

1.9.4 Robocasting (RB)

RB is an AM technique based on the continuous deposition of ceramic pastes through a nozzle in the form of the filament. The spacing between the filaments may be accurately controlled to achieve the desired shape. The feeding material is a typically highly concentrated ceramic paste (50-65 vol% of solid loading) and the nozzle displacement is controlled by a robotic arm moving independently in X-Y-Z directions in accordance with a computer-aided design (CAD) model. The deposition is done layer by layer at a controlled rate and each layer serves as the foundation for the next layers to build up a 3-D structure. The nozzles used for the

material extrusion typically are in the range of 100-1000 μm and almost complete densification upon sintering be achieved due to the high green density of the material after drying. Composed of fine and dense filaments, this technology is particularly attractive for the structural and functional ceramic manufacturing. The paste injection system can be pneumatic, using compressed gas, or mechanical, using screw or piston to push the material out. The control of the material flow is done more precisely by the mechanical system [112].

The original robocasting technology was developed by Cesarano at the Sandia National Laboratories in the USA [113]. In the primary formulation, the consolidation was based on the transformation from a pseudoplastic to a dilatant behaviour of high solid loaded ceramic filaments, triggered by minimal drying of the slurry after extrusion in air. Because of limitations of the original technique such as the difficulty in controlling the drying kinetics and the sensitivity to solid loading, the new formulations developed were based on the colloidal gels, named as the gel-based inks [99, 114, 115]. As illustrated in Figure 1-6, fluid inks are composed of a suspension of colloidal particles in a liquid medium, but gel-based inks are characterised by flocculated particles forming an interconnected network within the medium. Polymeric binders are used in the ink formulations to provide colloidal gels. The binder also helps to bind individual ceramic particles together so that the printed layers can support the weight of the subsequently deposited layers and remain stable [114]. Polymer binder is a relatively inert material, selected not to react with the ceramic powder or undergo chemical reactions. The binder burns out during the sintering process, as the temperature is gradually increased [116].

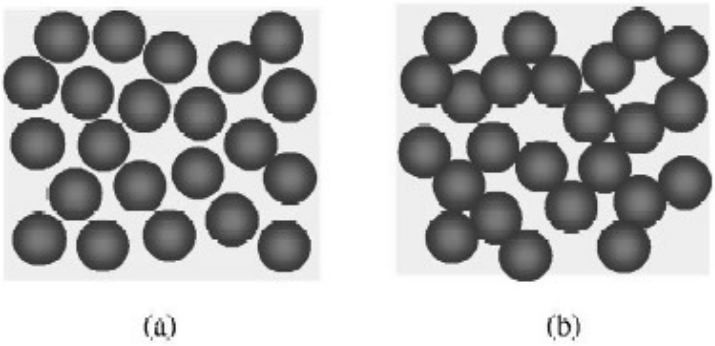

Figure 1-6: Schematic illustrations of fluid (a) and gel-based (b) colloidal inks. Reprinted from [114] with the permission of Elsevier under the license no 4775560059382.

Colloidal gels were found to be very suitable materials for the robocasting process because their viscoelastic behaviour can be tailored in a large range to facilitate flow through nozzles and produce complex 3-D structures. Furthermore, they can be designed to set immediately to maintain their shape even when they span gaps [117]. A high colloid volume fraction in the colloidal gels minimises drying induced shrinkage and allows the particle's network to resist capillary forces.

The concentration of a colloidal suspension is described by the parameter ϕ, which is the volumetric fraction of the particles in the total sample volume. Colloidal gels consist of a percolating network of attractive particles that is capable to transmit stress above ϕ_{gel}. During loading in the printing head, colloidal gels are considered as a viscous gel, but upon extrusion, the stress increases beyond their yield point (τ_y) and they exhibit shear-thinning flow behaviour and the viscosity decreases of several orders of magnitude [117].

Within the cylindrical deposition nozzle, gel-based inks flow with a three-zone velocity profile. A core which is unyielded and moves at a constant velocity, a yielded (fluid) shell which surrounds the core and experiences laminar flow, and a thin slip layer at the nozzle wall. The ink exits the nozzle as a continuous, rod-like filament with a rigid-core/fluid-shell architecture, which simultaneously promotes shape retention and allows it to fuse. Upon deposition, with the reformation of the attractive particles, the fluid shell quickly transforms into the gelled state.

One important factor to maintain the part stability after extrusion and sagging of the filaments is the rheological properties of the filament [99]. The viscosity should be optimised to build 3-D structures layer by layer which holds its shape during printing. While, very low viscosities do not facilitate 3-D printing of layers, very high viscosities require high extrusion pressures and often lead to clogging of the nozzle [116].

To ensure the suitability of the ceramic suspension feeding through deposition nozzle, the size (D_{50}) of the ceramic powder is typically kept in the submicrometer range which also ensures good sintering activity of the green parts. Furthermore, high green density (up to 60%) allows achieving almost complete densification upon sintering. Robocasting has the ability to obtain parts with considerable mechanical properties higher than the scaffolds produced by powder-based AM technologies [99].

Considering the range of printable materials, robocasting is a very flexible technique. However, there are limitations in the shapes that it can produce. The layer-wise nature of the technique always generates parts with step edges, and in the case of large overhangs, supports also must be printed. The size of the step edges is dependent on the radius of the printed filament, typically 100-250 μm, while other techniques such as SLA can achieve a fifth of that size. Robocast parts can be fully densified by conventional sintering procedures, leading to high mechanical quality [118].

Successful production of scaffolds with pore sizes ranging from 100 to 1200 μm and filament diameter of 225-1000 μm have been reported in the literature [99]. The macropore size and fraction are controlled by the combination of the rod diameter and spacing between them. It is also possible to introduce microporosity (1–30 μm) and sub-microporosity (1 μm) in the structure by incorporating polymer microspheres such as polymethylmethacrylate (PMMA) beads as fugitive porogen in the ink, and by optimising the sintering of raw scaffolds, respectively. Strict control over both the macroporosity and microporosity allows scaffold properties such as pore size, pore fraction, strength, modulus, and permeability to be varied

systematically and gives an effective tailoring possibility in the design of the scaffolds for different biomedical purposes [43, 75, 100].

The comparison of the mechanical strength of CaP scaffolds fabricated by different AM methods shows that the samples produced by RB have considerably higher mechanical properties than the other methods. For example, the strength of the scaffold fabricated by the RB technique is up to one order of magnitude higher than the strength of scaffolds made by 3DP with equal porosity [89]. The higher mechanical properties of the samples made by robocasting can be reasonably correlated to the higher density achieved by these samples, due to the fact that RB is a liquid-based process. The excellent mechanical characteristics of robocast CaP scaffolds allow them to be potentially used in load-bearing bone TE applications. However, the longer process compared to other AM techniques and the limited accuracy correlated to the nozzle size radius are two important limitations of this method [101].

In RB scaffolds, like all other porous materials, the strength is correlated to the final porosity. Increasing porosity reduces the strength. A similar decrease in strength with microporosity has been shown [43]. However, for the same macropore and micropore fraction, macroporosity is the more determining strength factor [43].

Uday et al. [116] recently showed that the average volumetric densification after sintering is related linearly to infill density such that the densification decreases by decreasing the pore percentage. This relationship can be a design factor used to scale up geometries by prediction of the shrinkage level so that the geometry of the final part be accurately determined during the post-sintering process.

Although extrusion-based AM has the potential to produce dense struts, the production of monolithic parts presents some difficulties. The high amount of organics in the formulation causes problems during the debinding stage and the textured structure, resulting from the stacking of filaments, affects the surface quality and the mechanical properties of the printed part [99].

References

[1] L. L. Hench, An introduction to bioceramics, second edition, Imperial College Press, 2013.

[2] L. L. Hench and J. R. Jones, Biomaterials, artificial organs and tissue engineering, USA: Woodhead Publishing Limited, 2005.

[3] S. V. Dorozhkin, "Nanosized and nanocrystalline calcium orthophosphates," *Acta Biomaterialia,* vol. 6, pp. 715-734, 2010.

[4] T. Kokubo, Bioceramics and their clinical applications, Woodhead Publishing in Materials, 2008.

[5] S. V. Dorozhkin, "Calcium orthophosphate bioceramics," *Ceramics International,* vol. 41, pp. 13913-13966, 2015.

[6] A. Karimzadeh, M. R. Ayatollahi, A. Bushroa and M. Herliansyahd, "Effect of sintering temperature on mechanical and tribological properties of hydroxyapatite measured by nanoindentation and nanoscratch experiments," *Ceramics International,* vol. 40, pp. 9159-9164, 2014.

[7] N. Eliaz and N. Metoki, "Calcium phosphate bioceramics: A review of their history, structure, properties, coating technologies and biomedical applications," *Materials,* vol. 10, no. 4, p. 334, 2017.

[8] American Standard for Testing and Materials, "Standard Specification for Composition of Hydroxylapatite for Surgical Implants," *ASTM F1185-03,* 2014.

[9] I. V. Antoniac, Handbook of Bioceramics and Biocomposites, Springer, 2016.

[10] M. I. Kay, R. A. Young and A. S. Posner, "Crystal structure of hydroxyapatite," *Nature,* vol. 204, pp. 1050-1052, 1964.

[11] B. Basu, D. Katti and A. Kumar, Advanced biomaterials; Fundamentals, processing and applications, New Jersey: John Willy and Sons, INC, 2009.

[12] S. Bose, G. Fielding, S. Tarafder and A. Bandyopadhyay, "Understanding of dopant-induced osteogenesis and angiogenesis in calcium phosphate ceramics," *Trends in Biotechnology,* vol. 31, no. 10, pp. 594-605, 2013 .

[13] D. Shi, Biomaterials and tissue engineering, Berlin: Springer, 2004.

[14] J. Elliot, "Structure and chemistry of the apatites and other calcium orthophosphates," in *Studies in inorganic chemistry*, Elsevier, 1994.

[15] B. Chen, D. Jiang, J. Zhang, M. Dong and Q. Lin, "Gel-casting of β-TCP using epoxy resin as a gelling agent," *Journal of the European Ceramic Society ,* vol. 28, pp. 2889-2894, 2008.

[16] W. Xue, K. Dahlquist, A. Banerjee, A. Bandyopadhyay and S. Bose, "Synthesis and characterization of tricalcium phosphate with Zn and Mg based dopants," *Journal of Materials Science Materials in Medicine,* vol. 19, no. 7, pp. 1669-1677, 2008.

[17] S. Sanchez-Salcedo, J. Werner and M. Vallet-Regi, "Hierarchical pore structure of calcium phosphate scaffolds by a combination of gel-casting and multiple tape-casting methods," *Acta Biomaterialia,* vol. 4, pp. 913-922, 2008.

[18] S. V. Dorozhkin, "Biphasic, triphasic and multiphasic calcium orthophosphates," *Acta Biomaterialia ,* vol. 8, pp. 963-977, 2018.

[19] X. Zhang, X. Li, H. Fan and X. Liu, "Bimodal porous bi-phasic calcium phosphate ceramics and its dissolution in SBF solution," *Key Engineering Materials,* Vols. 330-332, pp. 91-94, 2007.

[20] E. B. Nery, R. Z. LeGeros, K. Lynch and K. Lee, "Tissue response to biphasic calcium phosphate ceramic with different ratios," *Journal of Periodontology,* vol. 63, no. 9, pp. 729-735, 1992.

[21] Y. Tanimoto, Y. Shibata, A. Murakami, T. Miyazaki and N. Nishiyama, "Effect of varying HAp/TCP ratios in tape-cast biphasic calcium phosphate ceramics on response In vitro," *Journal of Hard Tissue Biology,* vol. 18, pp. 71-6, 2009.

[22] B. Hahn, D. Park, J. Choi, J. Ryu, W. Yoon, B. Lee and H. Kim, "Effect of the HA/β-TCP ratio on the biological performance of calcium phosphate ceramic coatings fabricated by a room-temperature powder

spray in vacuum," *Journal of the American Ceramic Society ,* vol. 92, no. 4, pp. 793-799, 2009.

[23] Y. Kong, H. Kim and H. Kim, "Phase conversion of tricalcium phosphate into Ca-deficient apatite during sintering of hydroxyapatite-tricalcium phosphate biphasic ceramics," *Journal of Biomedical Materials Research. Part B, Applied Biomaterials,* vol. 84, no. 2, pp. 334-339, 2008.

[24] J. Cho, C. Chung and S. Rhee, "Bioactivity and osteoconductivity of biphasic calcium phosphates," *Bioceramics Development and Applications 1,* vol. 1, p. Article ID D101129, 2011.

[25] S. Jalota, S. Bhaduri and A. Tas, "In vitro testing of calcium phosphate (HA, TCP, and biphasic HA-TCP) whiskers," *Journal of Biomedical Materials Research. Part A,* vol. 78, no. 3, pp. 481-490, 2006.

[26] I. Denry and L. T. Kuhn, "Design and characterization of calcium phosphate ceramic scaffolds for bone tissue engineering," *Dental Materials,* Vols. 43-53, p. 32, 2016.

[27] W. Suchanek and M. Yoshimura, "Processing and properties of hydroxyapatite-based biomaterials for use as hard tissue replacement implants," *Journal of Materials Research,* vol. 13, no. 1, pp. 94-117, 1998.

[28] A. M. Pietak, J. W. Reid, M. J. Stott and M. Sayer, "Silicon substitution in the calcium phosphate bioceramics," *Biomaterials ,* vol. 28, pp. 4023-4032, 2007.

[29] M. Zilm, S. D. Thomson and M. Wei, "A comparative study of the sintering behavior of pure and manganese-substituted hydroxyapatite," *Materials,* vol. 8, pp. 6419-6436, 2015.

[30] B. Yilmaz, A. Z. Alshemary and Z. Evisc, "Co-doped hydroxyapatites as potential materials for biomedical applications," *Microchemical Journal ,* vol. 144, pp. 443-453, 2019.

[31] Y. Liu and Z. Shen, "Dehydroxylation of hydroxyapatite in dense bulk ceramics sintered by spark plasma sintering," *Journal of the European Ceramic Society,* vol. 32, pp. 2691-2696, 2012.

[32] E. R. Kreidler and F. A. Hummel, "Phase relations in the system SrO-P_2O_5 and the influence of water vapor on the formation of $Sr_4P_2O_9$," *Inorganic Chemistry,* vol. 6, no. 5, pp. 884-891, 1967.

[33] I. Manjubala, T. P. Sastry and R. V. Suresh Kumar, "Bone in-growth induced by biphasic calcium phosphate ceramic in femoral defect of dogs," *Journal of Biomaterials Applications,* vol. 19, no. 4, pp. 341-360, 2005.

[34] T. Wanga and A. Dorner-Reisel, "Thermo-analytical investigations of the decomposition of oxyhydroxyapatite," *Materials Letters,* vol. 58, pp. 3025-3028, 2004.

[35] C.-J. Liao, F.-H. Lin, K.-S. Chen and J.-S. Sun, "Thermal decomposition and reconstitution of hydroxyapatite in air atmosphere," *Biomaterials,* vol. 20, pp. 1807-1813, 1999.

[36] S. Raynaud, E. Champion, D. Bernache-Assollant and P. Thomas, "Calcium phosphate apatites with variable Ca/P atomic ratio I. Synthesis, characterisation and thermal stability of powders," *Biomaterials ,* vol. 23, pp. 1065-1072, 2002.

[37] M. N. Rahaman, Ceramic processing, second edition, CRC Press, 2017.

[38] E. Champion, "Sintering of calcium phosphate bioceramics," *Acta Biomaterialia,* vol. 9, p. 5855–5875, 2013.

[39] E. Landi, A. Tampieri, G. Celotti and S. Sprio, "Densification behaviour and mechanisms of synthetic hydroxyapatites," *Journal of the European Ceramic Society,* vol. 20, pp. 2377-2387, 2000.

[40] M. Mazaheri, M. Haghighatzadeh, A. Zahedi and S. Sadrnezhaad, "Effect of a novel sintering process on mechanical properties of hydroxyapatite ceramics," *Journal of Alloys and Compounds ,* vol. 471, pp. 180-184, 2009.

[41] S. Raynaud, E. Champion and D. Bernache-Assollant, "Calcium phosphate apatites with variable Ca/P atomic ratio II. Calcination and sintering," *Biomaterials ,* vol. 23, pp. 1073-1080, 2002.

[42] N. Y. Mostafa, "Characterization, thermal stability and sintering of hydroxyapatite powders prepared by different routes," *Materials Chemistry and Physics,* vol. 94, pp. 333-341, 2005.

[43] A. J. Wagoner Johnson and B. A. Herschler, "A review of the mechanical behavior of CaP and CaP/polymer composites for applications in bone replacement and repair," *Acta Biomaterialia,* vol. 7, pp. 16-30, 2011.

[44] H. Liu, Nanocomposites for Musculoskeletal Tissue Regeneration, Kidlington, UK: Woodhead Publishing, 2016.

[45] S. V. Dorozhkin, "Bioceramics of calcium orthophosphates," *Biomaterials ,* vol. 31, pp. 1465-1485, 2010.

[46] D. M. Liu, "Influence of porosity and pore size on the compressive strength of porous hydroxyapatite ceramic," *Ceramics International,* vol. 23, pp. 135-139, 1997.

[47] J. M. Cordell, M. L. Vogl and A. J. Wagoner Johnson, "The influence of micropore size on the mechanical properties of bulk hydroxyapatite and hydroxyapatite scaffolds," *Journal of the Mechanical Behaviour of Biomedical Materials ,* vol. 2, pp. 560-570, 2009.

[48] M. Pujari-Palmer, C. Robo, C. Persson, P. Procter and H. Engqvist, "Influence of cement compressive strength and porosity on augmentation performance in a model of orthopedic screw pull-out," *Journal of the Mechanical Behavior of Biomedical Materials,* vol. 77, pp. 624-633, 2018.

[49] P. Sepulveda, F. Ortega, M. D. M. Innocentini and V. C. Pandolfelli, "Properties of highly porous hydroxyapatite obtained by the gelcasting of foams," *Journal of American Ceramic Society,* vol. 83, no. 12, pp. 3021-3024, 2000.

[50] S. Laasri, M. Taha, A. Laghzizil, E. Hlil and J. Chevalier, "The affect of densification and dehydroxylation on the mechanical properties of stoichiometric hydroxyapatite bioceramics," *Materials Research Bulletin,* vol. 45, pp. 1433-1437, 2010.

[51] B. Chen, T. Zhang, J. Zhang, Q. Lin and D. Jiang, "Microstructure and mechanical properties of hydroxyapatite obtained by gel-casting process," *Ceramics International,* vol. 34, pp. 359-364, 2008.

[52] S. Ramesh, C. Tan, C. Peralta and W. Teng, "The effect of manganese oxide on the sinterability of hydroxyapatite," *Science and Technology of Advanced Materials,* vol. 8, pp. 257-263, 2007.

[53] T. Shiota, M. Shibata, K. Yasuda and Y. Matsuo, "Influence of β-tricalcium phosphate dispersion on mechanical properties of hydroxyapatite ceramics," *Journal of the Ceramic Society of Japan,* vol. 116, pp. 1002-1005, 2008.

[54] P. Habibovic, M. Kruyt, M. Juhl, S. Clyens, R. Martinetti, L. Dolcini, N. Theilgaard and C. van Blitterswijk, "Comparative in vivo study of six hydroxyapatite-based bone graft substitutes," *Journal of Orthopaedic Reseach. official publication of the Orthopaedic Research Society ,* vol. 26, no. 10, pp. 1363-1370, 2008.

[55] D. Guo, K. Xu and Y. Han, "The in situ synthesis of biphasic calcium phosphate scaffolds with controllable compositions, structures, and adjustable properties," *Journal of Biomedical Materials Research. Part A,* vol. 88, no. 1, pp. 43-52, 2009.

[56] S. Bose, J. T. Darsell, M. Kintner, H. L. Hosick and A. Bandyopadhyay, "Pore size and pore volume effects on alumina and TCP ceramic scaffolds," *Materials Science and Engineering: C,* vol. 23, no. 4, pp. 479-486, 2003.

[57] Y. Chiang, D. Birnie and W. Kingery, Physical ceramics, New York: John Wiley & Sons, 1997.

[58] E. Charrière, S. Terrazzoni, C. Pittet, P. Mordasini, M. Dutoit, J. Lemaître and P. Zysset, "Mechanical characterization of brushite and hydroxyapatite cements," *Biomaterials,* vol. 22, no. 21, pp. 2937-2945, 2001.

[59] E. Chang, W. J. Chang, B. C. Wang and C. Y. Yang, "Plasma spraying of zirconia-reinforced hydroxyapatite composite coatings on titanium. Part I: Phase, microstructure and bonding strength," *Journal of Materials Science: Materials in Medicine,* vol. 8, pp. 193-200, 1997.

[60] X. Miao, Y. Chen, H. Guo and K. Aik Khor, "Spark plasma sintered hydroxyapatite-yttria stabilized zirconia composites," *Ceramics International ,* vol. 30, pp. 1793-1796, 2004.

[61] S. Bose, A. Banerjee, S. Dasgupta and A. Bandyopadhyay, "Synthesis, processing, mechanical, and biological property characterization of hydroxyapatite whisker-reinforced hydroxyapatite composites," *Journal of the American Ceramic Society,* vol. 92, no. 2, pp. 323-330, 2009.

[62] M. Mazaheri, A. M. Zahedi and S. K. Sadrnezhaad, "Two-step sintering of nanocrystalline ZnO compacts: effect of temperature on densification and grain growth," *Journal of the American Ceramic Society,* vol. 91, no. 1, pp. 56-63, 2008.

[63] A. Thuault, E. Savary, J.C. Hornez, G. Moreau, M. Descamps, S. Marinel and A. Leriche, "Improvement of the hydroxyapatite mechanical properties by direct microwave sintering in single mode cavity," *Journal of the European Ceramic Society,* vol. 34, pp. 1865-1871, 2014.

[64] M. Descamps, L. Boilet, G. Moreau, A. Tricoteaux, J. Lu, A. Leriche, V. Lardot and F. Cambier, "Processing and properties of biphasic calcium phosphates bioceramics obtained by pressureless sintering and hot isostatic pressing," *Journal of the European Ceramic Society,* vol. 33, pp. 1263-1270, 2013.

[65] J. Puértolas, J. Vadillo, S. Sánchez-Salcedo, A. Nieto, E. Gómez-Barrena and M. Vallet-Regí, "Compression behaviour of biphasic calcium phosphate and biphasic calcium phosphate–agarose scaffolds for bone regeneration," *Acta Biomaterialia ,* vol. 7, pp. 841-847, 2011.

[66] International Organization for Standardization , "Implants for surgery - In vitro evaluation for apatite-forming ability of implant materials" ISO 23317:2014, 2014.

[67] N. Sultana, Biodegradable polymer based Scaffolds for bone tissue engineering, Springer, 2013.

[68] B. Frank Miller, Encyclopedia and dictionary of medicine, nursing, and allied health, Saunders, 1997.

[69] G. Daculsi, B. Fellah and T. Miramond, The essential role ofcalcium phosphate bioceramics in bone regeneration. In:BenNissan B, editor.

Advances in calcium phosphate biomaterials, Berlin: Springer-Verlag, 2014, pp. 71-96.

[70] M. D. Ball, S. Downes, C. A. Scotchford, E. N. Antonov, C. N. Bagratashvili, V. K. Popov, W. J. Lo, D. M. Grant and S. M. Howdle, "Osteoblast growth on titanium foils coated with hydroxyapatite by pulsed laser ablation," *Biomaterials ,* vol. 22, pp. 337-347, 2001.

[71] X. Zhu, D. W. Son, J. L. Ong and K. Kim, "Characterization of hydrothermally treated anodic oxides containing Ca and P on titanium," *Journal of Materials Science Materials in Medicine ,* vol. 14, no. 7, pp. 629-634, 2003.

[72] H. S. Cheung, M. T. Story and D. J. McCarty, "Mitogenic effects of hydroxyapatite and calcium pyrophosphate dihydrate crystals on cultured mammalian cells," *Arthritis and Rheumatism,* vol. 27, no. 6, pp. 668-674, 1984.

[73] C. Knabe, R. Gildenhaar, G. Berger, W. Ostapowicwz, R. Fitzer, R. J. Radlanski and U. Gross, "Morphological evaluation of osteoblasts cultured on different calcium phosphate ceramics," *Biomaterials ,* vol. 18, pp. 1339-1347, 1997.

[74] E. B. Nery, R. Z. LeGeros, K. L. Lynch and K. Lee, "Tissue response to biphasic calcium phosphate ceramic with different ratios of HA/beta TCP in periodontal osseous defects," *Journal of Peridontology,* vol. 63, no. 9, pp. 729-735, 1992.

[75] J. G. Dellinger, A. M. Wojtowicz and R. D. Jamison, "Effects of degradation and porosity on the load bearing properties of model hydroxyapatite bone scaffolds," *Journal of Biomedical Materials Research. Part A,* vol. 77, no. 3, pp. 563-571, 2006.

[76] Y. Okanoue, M. Ikeuchi, R. Takemasa, T. Tani, T. Matsumoto, M. Sakamoto and M. Nakasu, "Comparison of in vivo bioactivity and compressive strength of a novel superporous hydroxyapatite with beta-tricalcium phosphates," *Archives of Orthopaedic and Trauma Surgery,* vol. 132, pp. 1603-1610, 2012.

[77] J. R. Jones and L. L. Hench, "Regeneration of trabecular bone using porous ceramics," *Current Opinion in Solid State and Materials Science,* vol. 7, pp. 301-307, 2003.

[78] O. Brown, M. McAfee, S. Clarke and F. Buchanan, "Sintering of biphasic calcium phosphates," *Journal of Materials Science: Materials in Medicine volume ,* vol. 21, pp. 2271-2279, 2010.

[79] L. C. Hwa, S. Rajoo, A. Mohd Noor, A. Norhayati and M. Uday, "Recent advances in 3D printing of porous ceramics: A review," *Current Opinion in Solid State and Materials Science,* vol. 21, pp. 323-347, 2017.

[80] S. Bose, M. Roy and A. Bandyopadhyay, "Recent advances in bone tissue engineering scaffolds," *Trends in Biotechnology,* vol. 30, pp. 546-554, 2012.

[81] O. Gauthier, J. M. Bouler, E. Aguado and P. Pilet, "Macroporous biphasic calcium phosphate ceramics: influence of macropore diameter and macroporosity percentage on bone ingrowth," *Biomaterials,* vol. 19, no. 1-3, pp. 133-139, 1998.

[82] H. SchHephake, E. W. Neukam and D. Klosa, "Influence of pore dimensions on bone ingrowth into porous hydroxylapatite blocks used as bone graft substitutes: A histometric study," *International Journal of Oral and Maxillofacial Surgery,* vol. 20, no. 1, pp. 53-58, 1991.

[83] J. I. Gonzalez Ocampo, D. M. Escobar Sierra and C. P. Ossa Orozco, "Porous bodies of hydroxyapatite produced by a combination of the gel-casting and polymer sponge methods," *Journal of Advanced Research,* vol. 7, pp. 297-304, 2016.

[84] E. Chevalier, D. Chulia, C. Pouget and M. Viana, "Fabrication of porous substrates: A review of processes using pore forming agents in the biomaterial field," *Nournal of Pharmaceutical Sciences,* vol. 97, no. 3, pp. 1135-1154, 2008.

[85] P. Sepulveda, H. A. Bressiani, J. Bressiani, L. Meseguer and B. Konig Jr, "Synthesis and properties of ceramic foams for hard tissue repair," *Key Engineering Materials,* vol. 218, pp. 413-416, 2002.

[86] M. Potoczek, A. Zima, Z. Paszkiewicz and A. Slosarczyk, "Manufacturing of highly porous calcium phosphate bioceramics via gel-casting using agarose," *Ceramics International,* vol. 35, pp. 2249-2254, 2009.

[87] L. Cyster, D. Grant, S. Howdle, F. Rose, D. Irvine, D. Freeman, C. Scotchford and K. Shakesheff, "The influence of dispersant

concentration on the pore morphology of hydroxyapatite ceramics for bone tissue engineering," *Biomaterials,* vol. 26, pp. 697-702, 2005.

[88] S. Tarafder, V. K. Balla, N. M. Davies, A. Bandyopadhyay and S. Bose, "Microwave-sintered 3D printed tricalcium phosphate scaffolds for bone tissue engineering," *Journal of Tissue Engineering and Regenerative Medicine,* vol. 7, no. 8, pp. 631-641, 2013.

[89] P. Miranda, A. Pajares, E. Saiz, A. P. Tomsia and F. Guiberteau, "Mechanical properties of calcium phosphate scaffolds fabricated by robocasting," *Journal of Biomedical Materials Research Part A,* vol. 85, no. 1, pp. 218-227, 2008.

[90] A. Asif, R. Nazir, T. Riaz, N. Ashraf, S. Zahid, R. Shahid, A. Ur-Rehman, A. Anwar Chaudhry and I. Ur Rehman, "Influence of processing parameters and solid concentration on microstructural properties of gel-casted porous hydroxyapatite," *Journal of Porous Materials,* vol. 21, pp. 31-37, 2014.

[91] U. T. Gonzenbach, A. R. Studart, E. Tervoort and L. J. Gauckler, "Macroporous ceramics from particle-stabilized wet foams," *Journal of the American Ceramic Society,* vol. 90, no. 1, pp. 16-22, 2007.

[92] S. Rekha Dash, R. Sarkar and S. Bhattacharyya, "Gel casting of hydroxyapatite with naphthalene as pore former," *Ceramics International,* vol. 41, pp. 3775-3790, 2015.

[93] A. Lemos and J. Ferreira, "Designing of bioceramics with bonelike structures tailored for different orthopaedic applications," *Key Engineering Materials,* Vols. 254-256, pp. 1037-1040, 2004.

[94] M. Potoczek, "Gelcasting of alumina foams using agarose solutions," *Ceramics International,* vol. 34, p. 661–667, 2008.

[95] F. S. Ortega, P. Sepulveda and V. C. Pandolfelli, "Monomer systems for the gelcasting of foams," *Journal of the European Ceramic Society ,* vol. 22, pp. 1395-1401, 2002.

[96] J. Luyten, S. Mullens, J. Cooymans, A. De Wilde, I. Thijs and R. Kemps, "Different methods to synthesize ceramic foams," *Journal of the European Ceramic Society,* vol. 29, p. 829–832, 2009.

[97] P. Sepulveda and J. G. P. Binner, "Processing of cellular ceramics by foaming and in situ polymerisation of organic monomers," *Journal of the European Ceramic Society,* vol. 19, pp. 2059-2066, 1999.

[98] C. Zhang, F. Chen, Z. Huang, M. Jia, G. Chen, Y. Ye, Y. Lin, W. Liu, B. Chen, Q. Shen, L. Zhang and E. J. Lavernia, "Additive manufacturing of functionally graded materials: A review," *Materials Science & Engineering A 764 (2019),* vol. 764, p. 138209, 2019.

[99] A. Zocca, P. Colombo, C. M. Gomes and J. Gunster, "Additive manufacturing of ceramics: issues, potentialities, and opportunities," *Journal of the American Ceramic Society,* vol. 98, no. 7, pp. 1983-2001, 2015.

[100] E. Champion, A. Magnaudeix, P. Pascaud-Mathieu and T. Chartier, "Advanced processing techniques for customized ceramic medical devices," in *Advances in Ceramic Biomaterials; Materials, Devices and Challenges*, Woodhead Publishing, 2017, pp. 433-468.

[101] R. Galante, C. G. Figueiredo-Pina and A. P. Serro, "Additive manufacturing of ceramics for dental applications: A review," *Dental Materials,* vol. 35, pp. 825-846, 2019.

[102] A. Butscher, M. Bohner, S. Hofmann, L. Gauckler and R. Müller, "Structural and material approaches to bone tissue engineering in powder-based three-dimensional printing," *Acta Biomaterialia ,* vol. 7, pp. 907-920, 2011.

[103] G. A. Fielding, A. Bandyopadhyay and S. Bose, "Effects of silica and zinc oxide doping on mechanical and biological properties of 3D printed tricalcium phosphate tissue engineering scaffolds," *Dental Materials,* vol. 28, pp. 113-122, 2012.

[104] B. Leukers, H. Gülkan, S. H. Irsen, S. Milz, C. Tille, M. Schieker and H. Seitz, "Hydroxyapatite scaffolds for bone tissue engineering made by 3D printing," *Journal of Materials Science. Materials in Medicine,* vol. 16, no. 12, pp. 1121-1124, 2005.

[105] P. H. Warnke, H. Seitz, F. Warnke, S. T. Becker, S. Sivananthan, E. Sherry, Q. Liu, J. Wiltfang and T. Douglas, "Ceramic scaffolds produced by computer-assisted 3D printing and sintering: characterization and biocompatibility investigations," *Journal of Biomedical Materials*

research. Part B: Applied Biomaterials, vol. 93, no. 1, pp. 212-217, 2010.

[106] R. Chumnanklang, T. Panyathanmaporn, K. Sitthiseripratip and J. Suwanprateeb, "3D printing of hydroxyapatite: Effect of binder concentration in pre-coated particle on part strength," *Materials Science and Engineering C ,* vol. 27, pp. 914-921, 2007.

[107] G. Lee and J. W. Barlow, "Selective laser sintering of calcium phosphate powders," in *International Solid Freeform Fabrication Symposium*, Texas, 1994.

[108] C. Shuaia, P. Li, J. Liu and S. Peng, "Optimization of TCP/HAP ratio for better properties of calcium phosphate scaffold via selective laser sintering," *Materials Characterization,* vol. 77, pp. 23-31, 2013.

[109] A. Woesz, M. Rumpler, J. Stampfl, F. Varga, N. Fratzl-Zelman, P. Roschger, K. Klaushofer and P. Fratzl, "Towards bone replacement materials from calcium phosphates via rapid prototyping and ceramic gelcasting," *Materials Science and Engineering C ,* vol. 25, pp. 181-186, 2005.

[110] S. Bose, D. Ke, H. Sahasrabudhe and A. Bandyopadhyay, "Additive manufacturing of biomaterials," *Progress in Materials Science ,* vol. 93, pp. 45-111, 2018.

[111] J. Brie, T. Chartier, C. Chaput, C. Delage, B. Pradeau, F. Caire, M. P. Boncoeur and J. J. Moreau, "A new custom made bioceramic implant for the repair of large and complex craniofacial bone defects," *Journal of Cranio-Maxillo-Facial Surgery,* vol. 41, pp. 403-407, 2013.

[112] M. Maroulakos, G. Kamperos, L. Tayebi, D. Halazonetis and Y. Ren, "Applications of 3D printing on craniofacial bone repair: A systematic review," *Journal of Dentistry ,* vol. 80, pp. 1-14, 2019.

[113] J. Cesarano, "A review of robocasting technology," *Materials Research Society Symposium Proceeding,* 1999.

[114] J. A. Lewis, "Direct-write assembly of ceramics from colloidal inks," *Current Opinion in Solid State and Materials Science,* vol. 6, pp. 245-250, 2002.

[115] J. E. Smay, J. Cesarano III and J. A. Lewis, "Colloidal inks for directed assembly of 3-D periodic structures," *Langmuir ,* vol. 18, no. 14, pp. 5429-5437, 2002.

[116] U. K. Roopavath, S. Malferrari, A. Van Haver, F. Verstreken, S. Narayan Rath and D. M. Kalaskar, "Optimization of extrusion based ceramic 3D printing process for complex bony designs," *Materials and Design,* vol. 162, pp. 263-270, 2019.

[117] J. A. Lewis, "Direct ink writing of 3D functional materials," *Advanced Functional Materials,* vol. 16, no. 17, pp. 2193-2204, 2006.

[118] E. Feilden, E. García-Tunón Blanca, F. Giuliani, E. Saiz and L. Vandeperre, "Robocasting of structural ceramic parts with hydrogel inks," *Journal of the European Ceramic Society,* vol. 36, no. 10, pp. 2525-2533, 2016.

Chapter 2 Powder elaboration and characterisation

Abstract

Two different batches of a commercial type of hydroxyapatite (HA) powder were characterised to be used in the production of HA parts. Both batches (named HA-AR1 and HA-AR2) were found to have identical phase compositions as detected by XRD analyses. EDX analyses showed that the powders were calcium deficient-HA (CD-HA) with different Ca/P ratios, the lower associated with the HA-AR2 batch. Laser granulometry analyses showed that both powders were characterised by bimodal particle size distribution but different average particle sizes, corresponding to 2.95 μm for HA-AR1 and 2.48 μm for HA-AR2.

Different methods including magnetic stirring, wet and dry ball milling (WBM and DBM) as well as ultrasonic dispersion (US) were used for the deagglomeration of the powders. Results indicated that WBM was an effective method in the reduction of the particle sizes and the US dispersion was found a powerful and quick method to remove the soft agglomerates.

Calcination of the powders revealed that the CD-HA to HA+β-TCP transformation started at 1000 °C for both powders and by increasing the temperature the proportion of the TCP phases increased as well. It was found that both lower Ca/P ratio and the reduction of the powder particle size stimulate the phase transformation.

XRD analyses revealed the characteristic peaks of CaO and TTCP by calcination at 1300 °C, resulting from HA decomposition to TTCP and TCP. The transformation was found to be more emphasized for the powder with the lower Ca/P ratio.

Abbreviations

BET	Brunauer-Emmett-Teller
CD-HA	Calcium deficient hydroxyapatite
DBM	Dry ball milling
DTA	Differential thermal analysis
EDX	Energy-dispersive X-ray spectroscopy
FESEM	Field emission scanning electron microscopy
HA	Hydroxyapatite
HA-AR1	As-received hydroxyapatite powder, batch n.1
HA-AR2	As-received hydroxyapatite powder, batch n.2
ICDD	International Centre for Diffraction Data –
ISO	International standard organisation
PDF	Powder Diffraction Files
PE	polyethylene
SSA	Specific surface areas
TG	Thermogravimetric
TTCP	Tetracalcium phosphate
US	Ultrasonic
WBM	Wet ball milling
XRD	X-ray diffractometry
α-TCP	α-tricalcium phosphate
β-TCP	β-tricalcium phosphate

2.1 Preliminary characterisation of powders

To be used in advanced applications, ceramics must meet specific requirements regarding their chemical compositions and microstructures, on which the starting powder characterisation has a pronounced effect. The particles sizes and the distribution of the particle's sizes, their shapes, state of agglomeration and chemical and phase composition are the most determining characteristics which must be considered in advance of any ceramic production.

Two different batches of commercial hydroxyapatite (HA) powder produced by Plasma Biotal Ltd., UK, were used in this PhD activity, namely P270S OD and P270S BM 192 Lot 2. Both powders were high-purity medical-grade synthetic HA, referred to as HA-AR1 and HA-AR2 (AR = As-received), respectively. According to the technical datasheets issued by the supplier, the powders were synthesised meeting the requirements of ISO 13779-6 standard [1], calcined at 1300 °C for 4 hours, and then were ground for 192 hours to reduce the final particles sizes. For the sake of clarity, it is necessary to specify that the experimental activities were started by using HA-AR1 powder. When additional powders were needed to complete the work, the company had finished the availability of the first batch, so they provided us with the second batch, which was produced by the same process. As is described in followings, the two batches were characterised by similar, but not identical features, thus affecting a number of properties.

The X-ray diffraction (XRD) pattern of as-received powders is presented in Figure 2-1. Because the XRD patterns of the two powders were identical, just the pattern of one, precisely HA-AR1, is shown. Using the reference pattern number 09-0432 for pure HA, issued by ICDD-PDF (International Centre for Diffraction Data – Powder Diffraction Files), it can be seen that the XRD pattern was in a complete match with the reference pattern implying that both HA-AR1 and HA-AR2 powders were pure HA. Moreover, fairly narrow peaks could be assigned to a high degree of crystallinity of the powders. Apart from well-crystallized HA, no other phases were detected.

The elemental compositions of the powders were determined using Energy-dispersive X-ray spectroscopy (EDX) analyses. Results are presented in

Table 2-1, which are the average of 2 separate measurements. Contrary to XRD patterns, minor differences among two batches can be observed, resulting in a slightly different Ca/P atomic ratio, being 1.59 and 1.55 for HA-AR1 and HA-AR2 respectively. Ca/P ratio lower than the stoichiometric value of 1.67 indicates that both powders were calcium deficient, in agreement with previous literature [2]. Because the crystal structure of calcium-deficient HA (CD-HA) is similar to stoichiometric HA, the two phases present almost the same XRD patterns, making not possible to distinguish them by this technique. Minor amounts of Mg, Si and Al were also identified with similar quantities for the two powder batches.

As detailed in part 1.2, the presence of the trace elements has a significant effect on the biological and physical properties of HA bioceramics. By making specific reference to the trace elements found in these powders, Mg improves densification,

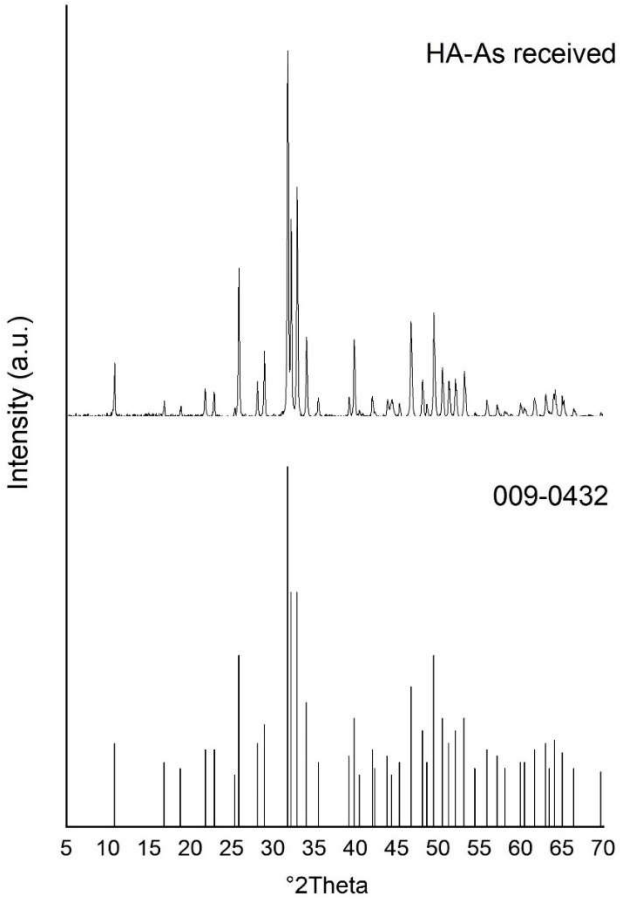

Figure 2-1: XRD patterns of the as-received powders.

Table 2-1: Chemical composition of as-received powders obtained by EDX analyses (at%).

Chemical element	HA-AR1	HA-AR2
Ca	17.07	15.96
P	10.71	10.29
O	69.77	71.41
Si	1.36	1.34
Al	0.46	0.45
Mg	0.62	0.56
Ca/P ratio	1.59	1.55

cellular attachment and proliferation of the new bone [3], Si promotes biological activities and generates finer microstructures [4, 5, 6] and finally Al, when added in the HA and β-Tricalcium phosphate (β-TCP) structures as a dopant, decreases lattice parameters and grain sizes and increases the final density [7].

Figure 2-2 shows the micrograph of the HA-AR1 powder acquired by field emission scanning electron microscopy (FESEM). It can be observed that the particles retain irregular shapes, whose size ranges between about 500 nm and 1 μm. The presence of a certain agglomeration of larger size can be observed as well. A similar morphology and size were observed for HA-AR2 powder.

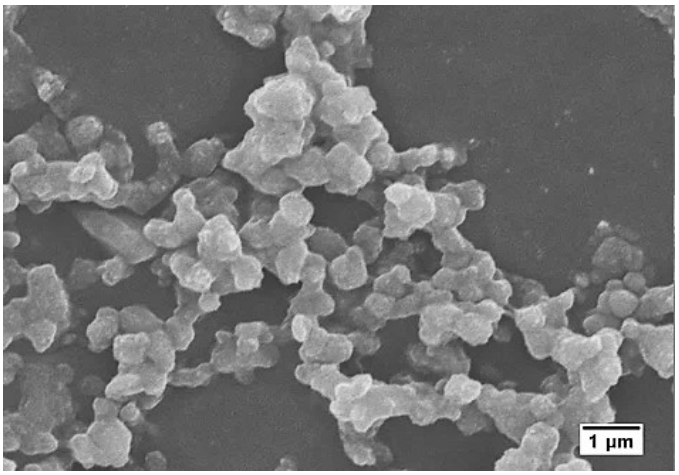

Figure 2-2: FESEM image of the as-received HA-AR1 powder.

The particle size distribution and the related cumulative distribution of both as-received powders, determined by laser granulometry, are depicted in Figure 2-3. The two powders are characterised by similar bimodal particle size distribution. The D_{10}, D_{20}, D_{50}, D_{90} and D_{99} values (i.e., the values corresponding to 10, 20, 50, 90 and 99% of the cumulative distribution curve) of the granulometry tests are collected in Table 2-2. With an average size of 2.95 and 2.48 µm, it seems that HA-AR2 is characterised by lower agglomeration compared to HA-AR1. The specific surface areas (SSA) determined by the Brunauer-Emmett-Teller (BET) method, using the N_2 adsorption isotherm, were 13.7 and 14.8 m^2/g, for HA-AR1 and HA-AR2, respectively, which were consistent with the smaller average particle/agglomerate size of HA-AR2 compared to HA-AR1.

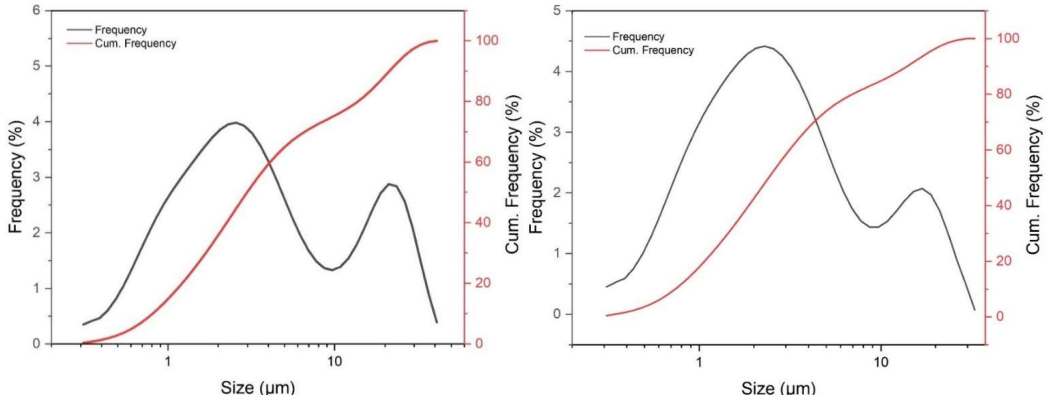

Figure 2-3: Particle size distribution and cumulative frequency of the as-received HA-AR1 (left) and HA-AR2 (right) powders.

Table 2-2: D-values of the as-received powders, HA-AR1 and HA-AR2.

Particle size (µm)	HA-AR1	HA-AR2
D_{10}	0.84	0.69
D_{20}	1.2	1.04
D_{50}	2.95	2.48
D_{90}	21.64	14.23
D_{99}	33.75	27.03

2.2 Determination of calcium to phosphorous atomic ratio

As extensively discussed in the first chapter, the stoichiometry of HA powder and the relative amount of the available calcium to phosphorous atoms in the chemical composition has an utmost influence on the physical and chemical properties and thermodynamic stability of the final sintered material. In the synthesis of HA powder, the control of the stoichiometry is a difficult task and non-stoichiometric compounds can easily take place. CD-HA is not stable in the sintering process and transforms to stoichiometric HA and β-/α- tricalcium phosphate (α-TCP) during heat treatment, which not only affects the microstructure but also the mechanical and biological properties of the final material. Especially, the effects on mechanical properties are very serious. For example, it has been shown that even a very small deviation of the Ca/P ratio of the initial powder, from 1.67 to 1.65 (i.e., 1% relative deviation), leads to significant changes in the mechanical properties of the densified material [8]. Therefore, the precise determination of this ratio is of uttermost importance to predict the final biological and mechanical properties.

As an attractive alternative to chemical analyses, Raynaud et al. [9] suggested a simple and straightforward method based on quantitative XRD for the measurement of the Ca/P ratio in CD-HA with $1.5 < Ca/P < 1.67$. In this method, which is based on a French standard [10], firstly, the powder is subjected to calcination at 1000 °C for 15 hours, which gives rise to complete transformation of CD-HA to stoichiometric HA and β-TCP. Then the Ca/P ratio can be calculated from the relative proportion of the final phases. The integrated intensities of the characteristic diffraction peaks of XRD analyses are used in this quantification. The characteristic peaks corresponding to the plane (2 1 0) at 2θ= 29° for HA and the plane (0 2 10) at 2θ= 31° for β-TCP were used for the quantitative analyses. For compounds containing more than 80 wt% of β-TCP, because of the low intensity of the (2 1 0) peak, despite a small superposition with the (0 2 10) of β-TCP, the most appropriate peak corresponds to the plane (2 1 1) at 2θ= 31.8°.

Two intensity ratios of R_1 for mixtures containing more than 80 wt% β-TCP and R_2 for the remaining mixtures were identified as follow:

$$R_1 = \frac{I_{HA(211)}}{I_{TCP(0\,2\,10)}} \qquad \text{Equation 2-1}$$

$$R_2 = \frac{I_{TCP(0\,2\,10)}}{I_{HA(210)}} \qquad \text{Equation 2-2}$$

Knowing that the integrated intensities are proportional to the volume fraction of each phase and assuming equal density for HA and β-TCP, R_1 and R_2 can be written as follow:

$$R_1 \approx \frac{A_1 \times wt\%\ HA}{B_1 - wt\%\ HA} \quad \text{Equation 2-3}$$

$$R_2 \approx \frac{A_2 \times wt\%\ TCP}{B_2 - wt\%\ TCP} \quad \text{Equation 2-4}$$

in which the A_1, A_2, B_1 and B_2 are fitting parameters represented in Table 2-3. These equations showed good correlations with experimental data [9].

Table 2-3: Fitting parameters for Equations 2-3 and 2-4.

Equation	$A_i \mp \Delta A_i^*$	$B_i \mp \Delta B_i^*$	Correlation coefficient
R_1 (Equation 2-3)	0.93 ± 0.03	95.8 ± 1.2	0.9998
R_2 (Equation 2-4)	5.45 ± 0.18	92.7 ± 0.5	0.9995

* ±Δ is the standard deviation

Using this method, the Ca/P ratios of the HA-AR1 and HA-AR2 were calculated to be equal to 1.625 and 1.60, respectively. It means that both powders were CD-HA, in agreement with EDX analysis, with the following chemical formulas, and were subjected to phase transformation during calcination/sintering processes.

$Ca_{9.75}(HPO_4)_{0.25}(PO_4)_{5.75}(OH)_{1.75}$ Equation 2-5 (HA-AR1)

$Ca_{9.60}(HPO_4)_{0.40}(PO_4)_{5.60}(OH)_{1.60}$ Equation 2-6 (HA-AR2)

When calcination treatments are enough long for complete transformation, the equilibrium reactions will be as follow:

$4Ca_{9.75}(HPO_4)_{0.25}(PO_4)_{5.75}(OH)_{1.75} \rightarrow 3Ca_{10}(PO_4)_6(OH)_2 + 3Ca_3(PO_4)_2 + H_2O$ Equation 2-7 (HA-AR1)

$5Ca_{9.60}(HPO_4)_{0.40}(PO_4)_{5.60}(OH)_{1.60} \rightarrow 3Ca_{10}(PO_4)_6(OH)_2 + 6Ca_3(PO_4)_2 + 2H_2O$ Equation 2-8 (HA-AR2)

From the above equations, it can be seen that there is a quite big difference between the final (nominal) compositions of the two powders after calcination. While HA-AR1 transforms to HA and β-TCP phases with a same molar quantity, the β-TCP phase in the final composition of HA-AR2 is two times of the HA phase. Moreover, the water vapour released during the decomposition of the latter is two times of the former whose entrapment in the sintered microstructure can deteriorate the mechanical properties as well. Therefore, it can be concluded that eventhough the difference between the Ca/P ratios of the two powders is small (1.625 vs 1.60), this small difference can leads to big microstructural and physical variations between the samples obtained from each powder.

2.3 Ball milling and dispersion

The strong influence of the green microstructure on the sintering behaviour and the final microstructure has led to the preferred use of colloidal base methods in the production of ceramic bodies. The colloidal processing, compared to the compaction of dry or semidry powder, is more complicated involving added steps, more expensive and time-consuming. However, because it allows achieving higher

homogeneity and decreases the number of structural defects in both green and sintered materials, it is considered as a prosperous method in the production of green parts. More reliable final parts, especially in the case of complex shapes, are currently fabricated with this method [11].

To get complete advantage of colloidal processing technique, the control of the dispersion of the ceramic particles in the liquid is one of the keys. Well dispersed particles in the slurry are fundamental to obtain finely homogenous green bodies and limit any kind of agglomeration. On the other hand, the size of the dispersed particles is also important. Due to rapid sedimentation rate, particles larger than a few micrometres cannot be effectively processed through the colloidal method. It has been claimed that the particle size should be kept under 1 μm to obtain a stable suspension [11].

However, fine ceramic particles have a high tendency of interacting and forming agglomerates in the colloidal suspension, due to the high surface area. In a suspension of colloidal particles, the particles undergo Brownian motion. Van der Waals forces between particles lead to attractive forces which finally stick particles together. During the sintering process, the agglomerated regions shrink more quickly than the surrounding zones (lower packing density) and this differential densification can lead to serious issues such as large pores and crack-like voids in the final material. Therefore, the control of the interparticle forces between ceramic particles is imperative. Well dispersed, weakly flocculated and high solid loading suspensions can be only achieved by controlling the interparticle forces.

Dispersants are a family of organic polymers which dissociate once added to an aqueous medium to produce negatively charged polymers. Interaction of these charged species with ceramic particles in the solvent leads to a repulsive force between particles, that separates them from each other [11].

Ultrasonic (US) dispersion of slurry and milling are additional techniques which are used to break the agglomeration. While soft agglomerates can be broken down using US dispersion, hard agglomerates, in which the particles are chemically bound together by strong solid bridges, are only broken down by mechanical methods like ball milling. This technique not only reduces the particle sizes but also reduces the particle size distribution range which is beneficial in the reduction of the segregation of the particles.

A fine particle size shows a key role in producing homogenous green microstructure and in the achievement of higher densities during the sintering process. Besides, as previously mentioned, the reduced particle size is also beneficial in obtaining a stable suspension without sedimentation. Therefore a deep investigation of the dispersion behaviour, under different conditions, has been carried out in the case of HA-AR1 powders. Results achieved were later transferred to the second powder batch.

The effect of dispersant and stirring in water suspension, using a magnetic stirrer, on the dispersion behaviour of HA-AR1 powder is presented in Figure 2-4. For this purpose, a 60 wt% HA-AR1 powder suspension in water was produced and 0.64 wt% anionic polyelectrolyte type dispersant was added for suspension

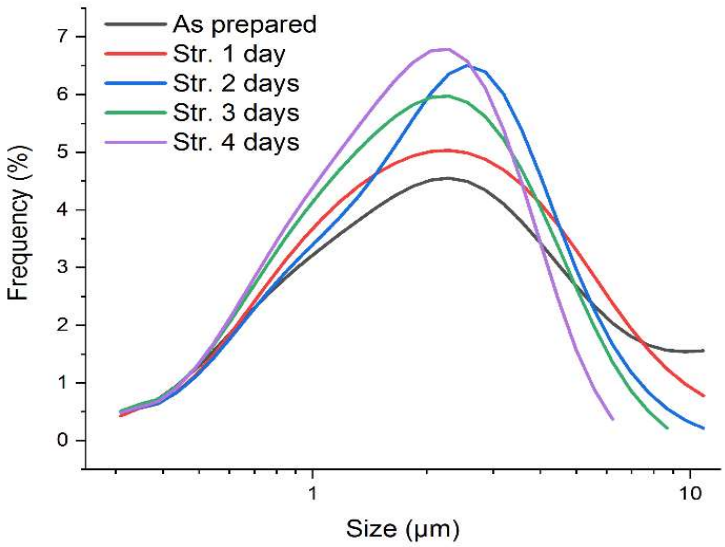

Figure 2-4: Particle size distribution of the slurry prepared from HA-AR1, in the presence of a dispersant as a function of the stirring time (magnetic stirring).

stabilization. By comparing the particle size distribution of the as-prepared ceramic suspension (black curve in Figure 2-4), with the as-received powder (Figure 2-3), we can see that the coarse agglomeration of the powder breaks down and the as-received powder with bimodal distribution turns to mono-dispersed powder suggesting that the coarse agglomeration of the as-received powder were soft agglomerates. By increasing the stirring time this phenomenon became more effective. According to the data shown in Table 2-4, corresponding to the curves in Figure 2-4, magnetic stirring for 4 days reduced the mean particle size to 1.68 µm, achieving a narrower range of distribution.

Table 2-4: D-values of the slurry prepared from HA-AR1, in the presence of a dispersant as a function of the stirring time.

Particle size (µm)	As prepared	1 day	2 days	3 days	4 days
D_{10}	0.71	0.71	0.73	0.66	0.66
D_{20}	1.02	1.00	1.04	0.93	0.92
D_{50}	2.24	2.02	1.98	1.78	1.68
D_{90}	11.37	6.11	4.65	4.12	3.48
D_{99}	25.30	15.51	7.01	6.60	4.98

The effects of ball milling process on the particle size distribution of the as-received powders in two different conditions of dry ball milling (DBM) and wet ball milling (WBM) were studied. The milling processes conducted using zirconia balls with a diameter of 2 mm in polyethylene (PE) containers. The containers were partially filled by powder, grinding balls and in the case of wet milling, distilled water as the conveying medium. The milling parameters including balls size, rotation speed and the occupied fraction of the container were optimised to reduce the milling time and the used energy.

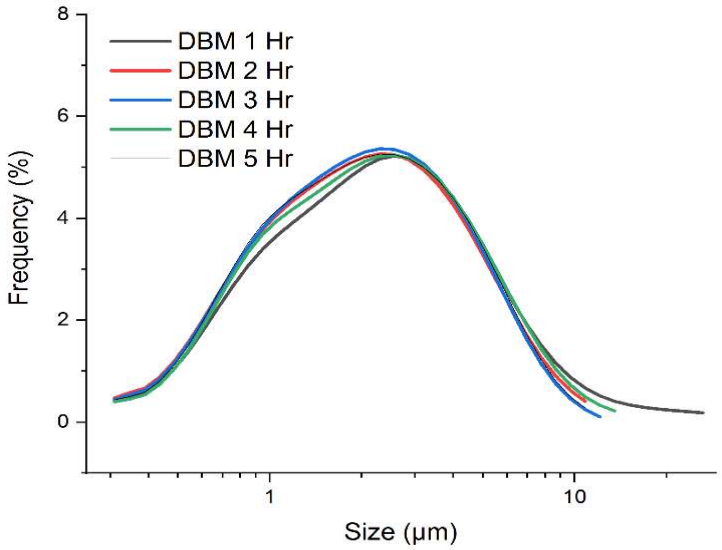

Figure 2-5: Particle size distribution of the DBM HA-AR1 as a function of milling time.

Table 2-5: D-values of the dry ball milled HA-AR1 at different dry-milling times.

	1 Hr	2 Hr	3 hr	4 Hr	5 Hr
D_{10}	0.73	0.63	0.68	0.72	0.64
D_{20}	1.03	0.91	0.95	1.00	0.93
D_{50}	2.09	1.96	1.91	1.99	1.96
D_{90}	6.24	5.01	4.89	5.57	4.89
D_{99}	31.05	11.55	8.22	10.16	8.63

Figure 2-5 shows the particle size distribution of the as-received powder (HA-AR1) after DBM. The corresponding D-values are presented in Table 2-5. Also, in this case, we can observe a clear effect of DBM in breaking large agglomerates. The most dominant reduction of the particles size took place during the first hour of ball milling (again, compare the black curve of Figure 2-5 with the distributions in Figure 2-3). By increasing the milling time, the effectiveness of the milling process was reduced, and it was found that after 3 hours it was not further efficient. Therefore 3 hours was selected as the optimum time of the DBM procedure.

The results of the WBM procedure are presented in Figure 2-6 and Table 2-6. It can be seen that the WBM was much more effective than DBM in the reduction of the particles/agglomerate sizes, even though it took more time. The covering of the ceramic particle with liquid serves to reduce the degree of agglomeration and leads to finer particle size in wet condition. WBM not only reduced the mean particles sizes to less than 1 µm but also significantly narrowed the size distribution.

The mean particle size achieved from the WBM procedure versus time is depicted in Figure 2-7 and shows that the rate of grinding decreased with increasing the milling time. As particles became fairly fine, it became more difficult to obtain further reduction.

The grinding rate follows the particle size according to the following equation [11]:

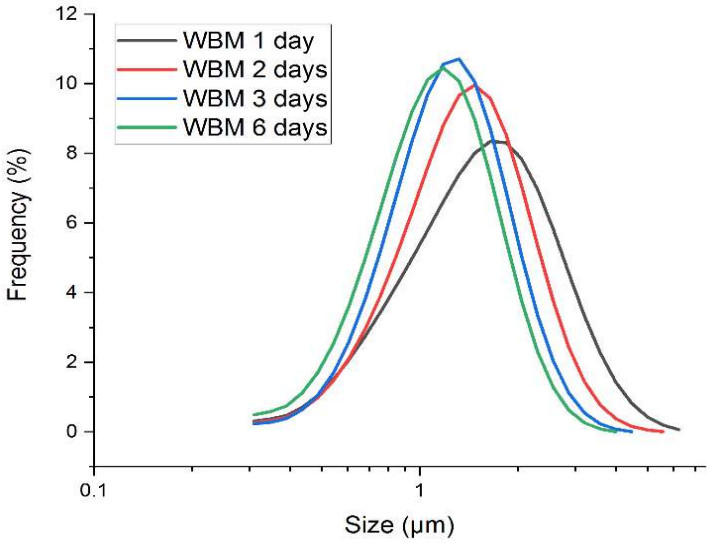

Figure 2-6: Particle size distribution of the wet ball milled HA-AR1 as a function of milling time.

Table 2-6: D-values of the wet ball milled HA-AR1 at different dry milling times.

Particle size (µm)	1 day	2 days	3 days	6 days
D_{10}	0.70	0.71	0.67	0.60
D_{20}	0.91	0.87	0.80	0.73
D_{50}	1.47	1.30	1.16	1.06
D_{90}	2.76	2.26	1.94	1.78
D_{99}	4.02	2.97	2.53	2.35

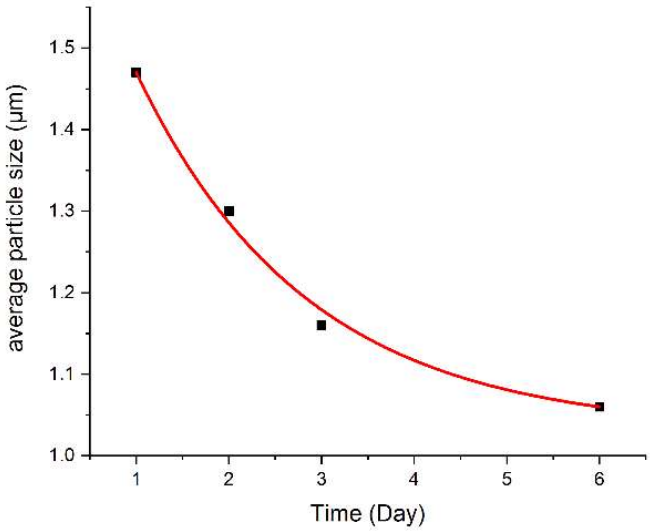

Figure 2-7: Mean particle size of wet ball milled HA-AR1 as a function of WBM duration.

$$Rate\ of\ grinding \approx AR_m^{1/2}\rho x/a \qquad \text{Equation 2-9}$$

in which A, R, ρ, x and a are constant specific for milling media and powder, container radius, ball density, particle size and ball radius, respectively. According to this equation, although the grinding rate decreases with decreasing the particle size, there is not any limit. However, in practice, with decreasing the particle size, their tendency to agglomerate increases and after reaching a particular size, a physical equilibrium is established between the agglomeration and comminution processes which make the further milling not effective. This practical limitation occurred after 6 days in our work when the mean agglomeration size reached 1 µm (see Figure 2-2).

The effect of US agitation on dispersions of the as-received powders as well as DBM and WBM powders were investigated. Figure 2-8 shows the particle size distribution after US dispersion of the as-received powder (referred to as US), as well as of the dry and the wet ball-milled powders (referred to as DBM+US and WBM+US, respectively). The corresponding D-values are presented in Table 2-7. US was performed using Vibra-cell VC 750 US processor (Sonic and materials, Inc. Newtown, US) to reach the maximum dispersion of the suspension. The dispersion condition of the slurries was regularly checked by granulometry test at 5

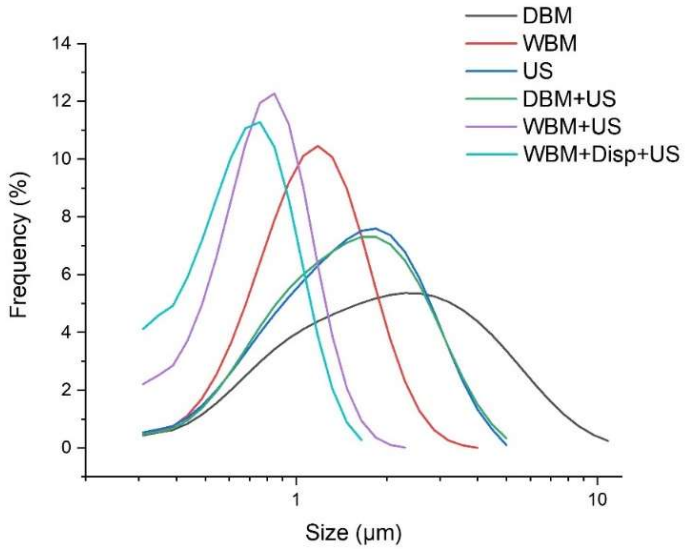

Figure 2-8: Particle size distribution of HA-AR1 prepared from different routes.

Table 2-7: Particles sizes data of HA-AR1 prepared from different routes.

Particle size (µm)	US	DBM + US	WBM + US	WBM +Disp + US
D_{10}	0.62	0.64	0.43	0.36
D_{20}	0.83	0.83	0.52	0.44
D_{50}	1.42	1.40	0.73	0.63
D_{90}	2.73	2.79	1.13	1.00
D_{99}	3.80	3.86	1.44	1.33

minutes time intervals to obtain the minimum time needed by each slurry for the maximum dispersion. At a fixed intensity, the optimum time depended on the solid loading of the slurries. Higher solid loadings required more time. The maximum dispersion time for the tested slurries was about 15 minutes.

Firstly, from Figure 2-8, the effect of the different dispersion methods on the as-received powder is observable. As already discussed, WBM was more effective than DBM, despite the significantly longer time required for its accomplishment. The US carried out for about 15 minutes, provided an intermediate particle size distribution. The better distribution of US particles compared to DBM ones underlines the importance of the US dispersion in a liquid medium.

Secondly, still from Figure 2-8, it can be seen that the application of the US on the as-received powder and the already DBM powder had a comparable effect. This result further evidences the poor effectiveness of the milling process, when carried out in a dry medium. On the other side, US dispersion appears not to be able to break the hard agglomerates, which consist of chemically bound particles [11]. Therefore, it may be concluded that magnetic stirring, DBM and US dispersion (and their combination) are only effective toeliminate the larger soft agglomerates. However, US dispersion can be considered as an advisable alternative to DBM, as it requiresvery shorter times. Moreover, ball-milling can induce some pollution of the powder from the milling media, especially in dry conditions, while US can be considered as a 'cleaner' dispersion method [12].

An effective displacement of the particle size distribution to lower values was achieved under WBM conditions. In fact, thee results showed that WBM was highly effective in crashing the hard agglomerates. Moreover, in this case, the US was effective in further reducing the particle size distribution. The combined process WBM+US was even more effective in the presence of a dispersant: in this case, the mean particle size was about 600 nm, with a very narrow particle size distribution.

2.4 Calcination and thermal behaviour

The calcination of the as-received powders was carried out under static air at temperatures ranging from 800 °C to 1300 °C with 100 °C intervals. The heating and cooling rates were 10 °C/min and holding time at calcination temperatures was 1 hour. As stated in section 2.2, because the as-received powders were calcium deficient, it was expected to observe phase transformation during high-temperature calcinations. Figures 2-9 and 2-10 show the XRD patterns of HA-AR1 and HA-AR2 calcined powders, respectively. Both powders followed a fairly similar trend of phase transformations. Characteristic peaks related to any phase other than HA firstly observed by calcination at 1000 °C. Up to this temperature, none of the powders showed phase transformations, which were ascertained by further calcinations at 950 °C, still showing only characteristic peaks of HA phase. Therefore, 1000 °C was considered as the starting temperature of CD-HA to HA + β-TCP phase transformation for both powders. ICDD-PDF reference patterns numbers 09-0432, 09-0169 and 09-348 were used for the identification of HA, β-

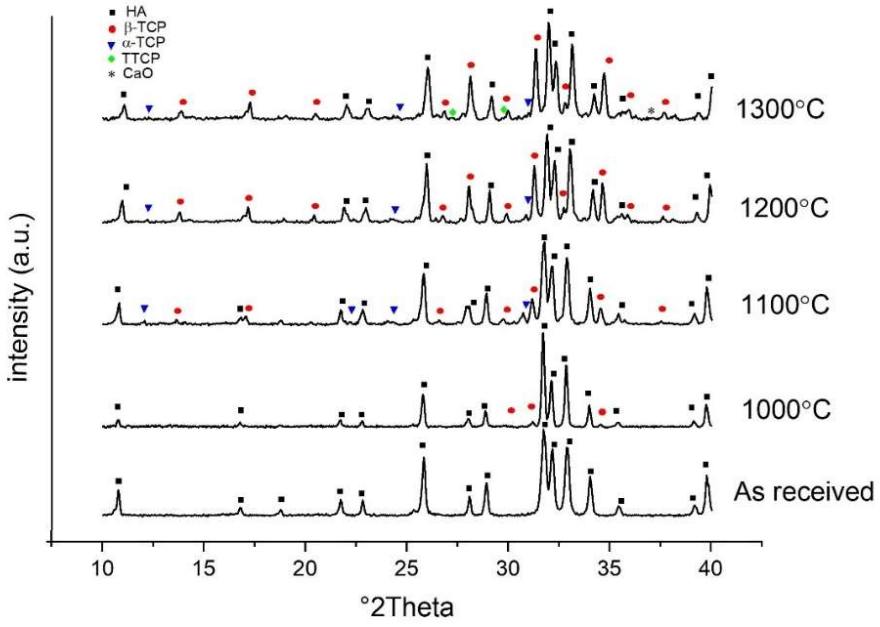

Figure 2-9: X-Ray diffraction patterns of as-received and calcined HA-AR1 powder.

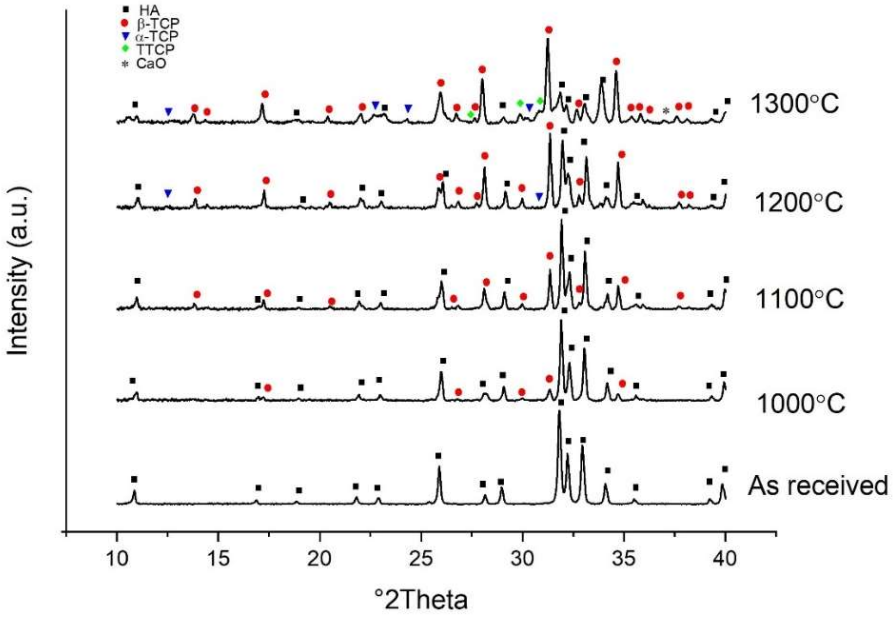

Figure 2-10: X-Ray diffraction patterns of as-received and calcined HA-AR2 powder.

TCP and α-TCP phases, respectively. The formation of α-TCP phase started earlier for HA-AR1 than HA-AR2. In fact, the earliest observations of the characteristic peaks of α-TCP for HA-AR1 and HA-AR2 were in the XRD patterns corresponding to calcinations at 1100 °C and 1200 °C, respectively. It must be considered that the β- to α-TCP phase transformation is reversible and the lack of characteristic peaks of α-TCP can be the result of complete reverse transformation during the cooling cycle. In other words, the presence of both α- and β-TCP can be the indication that

the allotropic transformation of TCP was not completely reversed during the cooling stage.

The XRD results showed that the peak's intensity of TCP phases had a direct relationship with calcination temperature. By increasing the temperature, the peaks correspond to TCP phases intensified while the peaks of HA phase decreased. In addition, due to the lower Ca/P ratio of HA-AR2 compared to HA-AR1 (see Table 2-1), the characteristic peaks of β-TCP phase were higher for HA-AR2 compared to HA-AR1. So, as discussed in 2.2, the final materials were composed of more β-TCP phase for HA-AR2 than HA-AR1. The phase fractions of the calcined powders were calculated thanks to the method developed by Raynaud et. al. [9] (section 2.2), and the results are presented in Table 2-8. We can observe that, at the same calcination temperature, the amount of the β-TCP phase for HA-AR2 was always more than two times that of HA-AR1.

Table 2-8: Amount of the β-TCP phase in the final composition of calcinated powders.

Calcination temperature (°C)	HA-AR1 (%)	HA-AR2 (%)	HA-AR2 Wet BM (%)
1000	3.79	11.6	16.84
1100	12.04	27.69	31.63
1200	22.49	42.05	42.06
1300	33.25	53	62.61

To study the potential effect of the ball milling process on the phase transformation, the same calcination processes were carried out on HA-AR2 powders after WBM (data in Table 2-8). The results are plotted in Figure 2-11. We can observe a key role of WBM in enhancing phase transformation. In fact,

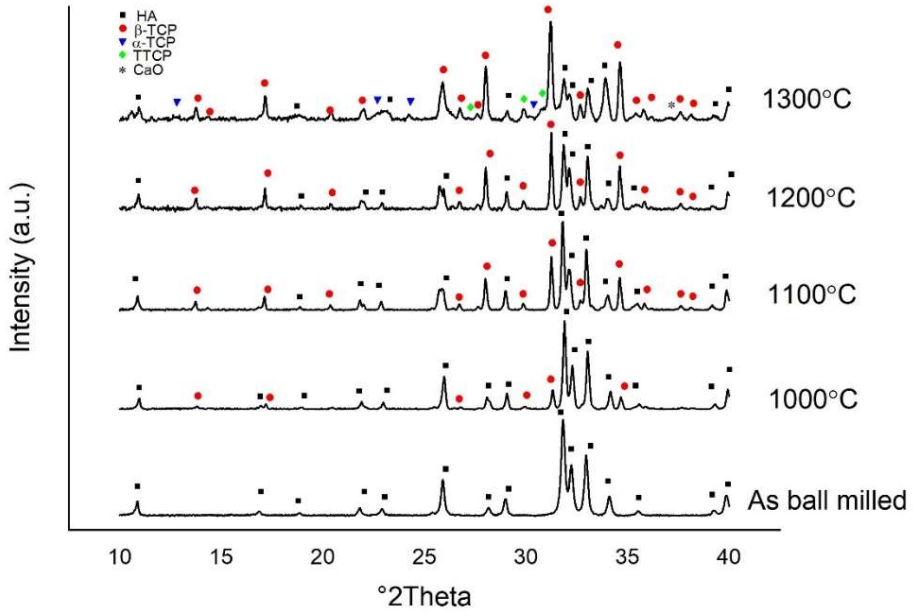

Figure 2-11: X-Ray diffraction patterns of the wet ball milled HA-AR2 calcined at different temperatures.

compared to the as-received powder (Figure 2-10), the characteristics peaks of TCP phases show higher intensity for the ball-milled powder. The enhanced transformation can be attributed to the higher SSA of the ball-milled powder which was 30.13 m2/g, compared to 14.82 m2/g for the as-received powder. The higher surface area provides more possibility to the phase transformation to occur. However, the starting temperature for the transformation was not affected by the ball milling process. Therefore, despite the transformation rate, the startingtemperature of the phase transformation of CD-HA to HA and β-TCP seems to be only a function of temperature, while particle size seemed not to affect it.
Figure 2-12 represents the schematic plot of the data shown in Table 2-8. The data corresponding to each type of powder (namely, as-received HA-AR1, as-received HA-AR2 and wet ball-milled HA-AR2) are well fitted by a linear mathematical equation. The slope of these linear fittings can be a representative of the reactivity level of each powder. The steeper the line, the more reactive the powder. It can be seen that the HA-AR2 with a lower Ca/P ratio is 38% more reactive than the HA-AR1. Moreover, the reduction of the particle size (from as-received to wet ball milled HA-AR2) led to an almost further 10% increase (from 0.138 to 0.151) in the reactivity of the HA-AR2. Therefore, it can be concluded that both the reduction of the Ca/P ratio and the powder particle sizes lead to an increase in the thermal reactivity of the powders.

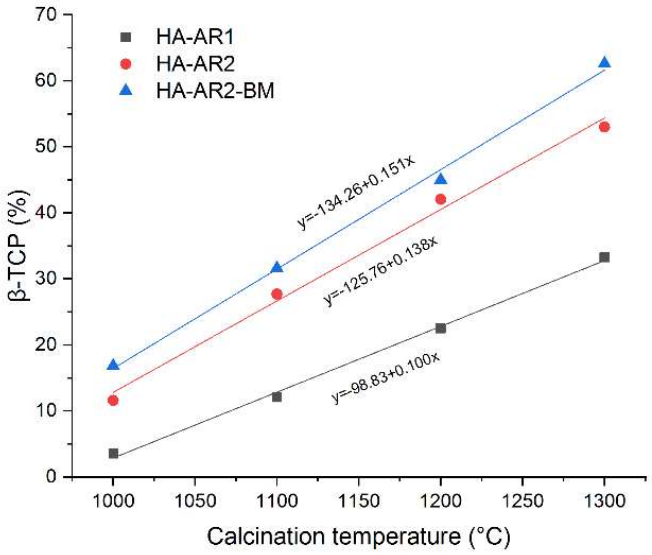

Figure 2-12: β-TCP phase amount (%) in the final composition of three different calcined powders.

Considering the XRD patterns of the powders calcined at 1300 °C, two small peaks at 27 and 37 °2theta can be detected for all types of the calcinated powders. According to the ICDD reference pattern numbers 11-232 and 37-1497, these peaks belong to tetracalcium phosphate (TTCP) and CaO phases, respectively. Decomposition of HA to TTCP and TCP at temperatures higher than 1300 °C was

already reported in the literature [13,14,15,16]. In fact, by heating the HA phase to temperatures higher than 1300 °C, TTCP phase forms according to Equation 2-10 and during the cooling stage, the reversible formation of HA from TTCP gives rise to the formation of CaO according to Equation 2-11.

$$HA \xrightarrow{1300℃} TTCP + \alpha - TCP \quad \text{Equation 2-10}$$

$$TTCP \xrightarrow{1300℃} HA + CaO \quad \text{Equation 2-11}$$

Therefore, it can be expected that the composition of the powders calcined at 1300 °C was a combination of HA, β- and α-TCP (untransformed), TTCP and CaO. However, because the position of the characteristic peaks of TTCP phase is very close to the one of the characteristic peaks of HA and also the ion substitution affected the positions of the peaks, it was not possible to clarify from XRD patterns the final proportion of these phases in the composition of the final material. Nevertheless, the peaks at 27.162 and 10.880 °2theta which correspond to TTCP and HA phases, respectively, grant the presence of both phases. XRD patterns of HA-AR2 powder reveal that calcination at 1300 °C gave rise to a substantial increase in the β-TCP phase amount in the final material along with a significant decrease of HA. Because α-TCP, which transforms to β-TCP during cooling, is a by-product of HA transformation to TTCP, the significant increase of the β-TCP phase after calcination at 1300 °C is another indication of the occurrence of the stated transformation. On the contrary, the intensity of the corresponding peaks in HA-AR1 powder didn't significantly increase at the same calcination temperature. Therefore, it may be assumed that the HA to TTCP phase transformation was more significant for HA-AR2 powder than HA-AR1 one.

The calcination of HA powders also revealed changes in the position of the characteristic peaks of HA and TCP phases. Figures 2-13 and 2-14 show the most important characteristic peaks of the XRD patterns (from 24 to 35 °2theta)of HA-AR1 and HA-AR2, respectively, calcined at different temperatures. Vertical dashed lines show the primary position of each peak. The shift in peaks positions occurred from 1000 °C and 1200 °C for HA-AR2 and HA-AR1, respectively. In both cases, the shifts were towards higher 2θ angles and with increasing the calcination temperature, the shifts increased. The peaks displacements at different calcination temperatures are noted in the graphs. Using quartz as an internal standard verified no systematic errors in the measurements. As stated in section 1.2, these shifts may be attributed to ion substitutions in the crystal structure which affect the lattice parameters. For example, because the ionic radius of Mg^{2+} is smaller than Ca^{2+} (6.5 to 9.9 nm, respectively), the incorporation of Mg^{2+} in the crystal structure of HA to fill the empty calcium positions, leads to a contraction of the crystal lattice and shifts the XRD characteristic peaks to higher 2θ values [17,18]. As observed by EDX analyses, both HA-AR1 and HA-AR2 was calcium deficient and contained some impurities such as Al, Si and Mg. Therefore, it may be expected that these ions diffuse in the crystal lattice and result in a change of crystalline lattice parameters.

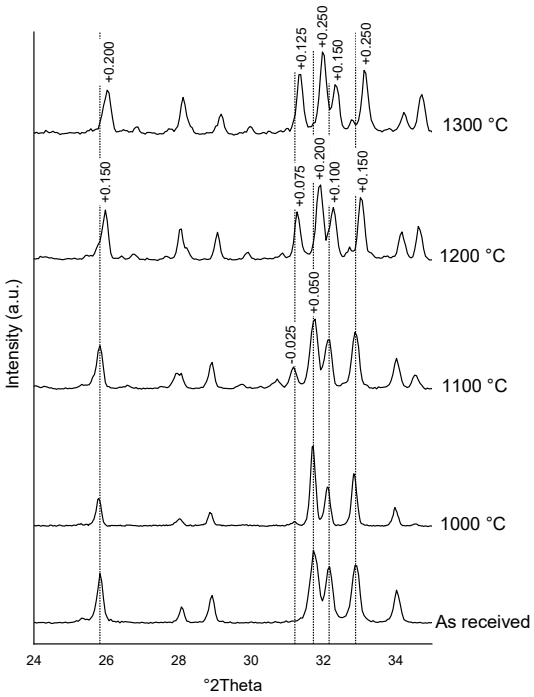

Figure 2-13: Shifts in peaks position of HA-AR1 powder with increasing calcination temperature. Vertical dashed lines correspond to the position of the primary peaks in the as-received powder.

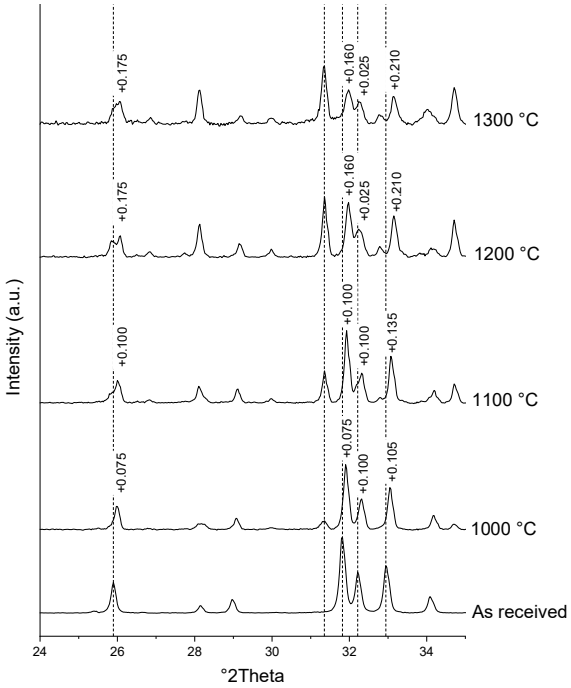

Figure 2-14: Shifts in peaks position of HA-AR2 powder with increasing calcination temperature. Vertical dashed lines correspond to the position of the primary peaks in the as-received powder.

Thermogravimetric-differential thermal analysis (TG-DTA) curves of HA-AR1 powder are plotted in Figure 2-15, which were carried out up to 1400 °C, by the heating rate of 10 °C/min under static air. A slight endothermic peak on the

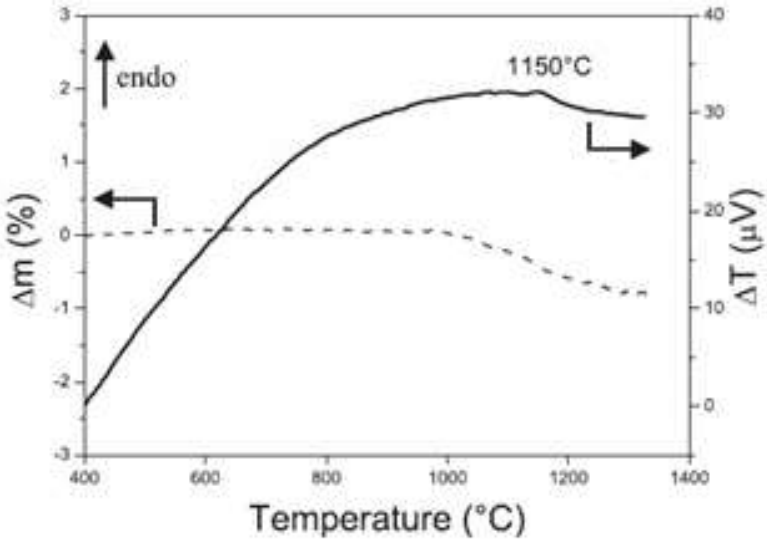

Figure 2-15: DTA-TG curve of HA-AR1 powder indicating endothermic phase transformation at 1150 °C and reduction of the powder mass as a result of dihydroxylation.

DTA curve can be detected at around 1150 °C. This thermal signal can be assigned to CD-HA to HA + β-TCP phase transformation, in agreement with XRD results. In addition, the TG curve shows a mass loss of close to 1% which starts from about 1000 °C. This mass reduction can be attributed to dehydroxylation of HA powders at high temperatures, still confirming the previous results.

2.5 Conclusion

The physical, chemical and thermal properties of the starting powder have a pronounced effect on the final ceramic parts. Two different batches of a commercial HA powder (named HA-AR 1 and HA-AR2) were submitted to XRD, EDX, laser granulometry and FESEM analyses. The results showed that both batches were CD-HA with Ca/P ratio less than 1.67. Also, they were characterised by different average particle sizes, precisely 2.95 μm for HA-AR1 and 2.48 μm for HA-AR2. In addition, HA-AR2 was characterised by lower Ca/P ratio, as confirmed by EDX and a quantitative XRD analyses.

Powders were dispersed by ball milling, under dry and wet conditions. Results showed that WBM was very effective in reducing the particle sizes and breaking the hard agglomerates. The best results were achieved by combining WBM with a short-time US dispersion process, in the presence of a dispersant. In this way, an average particle size of about 600 nm, with a narrow particle size distribution, was obtained

Calcination of the powders for 1 hour at different temperatures indicated that the CD-HA to HA + β-TCP transformation started at 1000 °C for both powders, and the β-TCP amount increased by increasing the calcination temperature, in particular for the powder characterised by the lower Ca/P ratio and lower particle size. XRD analyses showed that calcination at 1300 °C for 1 hour led to the

formation of the TTCP and CaO phases, which were the results of HA to TTCP and TCP phase transformation. The final composition after heat treatment at 1300 °C was found to be a combination of HA, α- and β-TCP, TTCP and CaO phases.

References

[1] International Organization for Standardization, “Implants for surgery - Hydroxyapatite. Part 6: Powders,” *ISO 13779-6,* 2015.

[2] H. Yang, S. Yang, X. Chi, J. Evans, I. Thompson, R. Cook and P. Robinson, “Sintering behaviour of calcium phosphate filaments for use as hard tissue scaffolds,” *Journal of the European Ceramic Society ,* vol. 28, pp. 159-167, 2008.

[3] W. Xue, K. Dahlquist, A. Banerjee, A. Bandyopadhyay and S. Bose, “Synthesis and characterization of tricalcium phosphate with Zn and Mg based dopants,” *Journal of Materials Science Materials in Medicine,* vol. 19, no. 7, pp. 1669-1677, 2008.

[4] C. Bergmann, M. Lindner, W. Zhang, K. K. A. Kirsten, R. Telle and H. Fischer, “3D printing of bone substitute implants using calcium phosphate and bioactive glasses,” *Journal of the European Ceramic Society,* vol. 30, pp. 2563-2567, 2010.

[5] S. Bose, G. Fielding, S. Tarafder and A. Bandyopadhyay, “Understanding of dopant-induced osteogenesis and angiogenesis in calcium phosphate ceramics,” *Trends in Biotechnology,* vol. 31, no. 10, pp. 594-605, 2013 .

[6] K. A. Hing, P. A. Revell, N. Smith and T. Buckland, “Effect of silicon level on rate, quality and progression of bone healing within silicate-substituted porous hydroxyapatite scaffolds,” *Biomaterials ,* vol. 27, pp. 5014-5026, 2006.

[7] A. Tahmasebifar and Z. Evis, “Structural and mechanical characteristics of hydroxyapatite and tri-calcium phosphates doped with Al^{3+} and F^{-} ions,” *Journal of Ceramic Processing Research,* vol. 14, no. 4, pp. 549-556, 2013.

[8] S. Jalota, S. B. Bhaduri and A. C. Tas, “In vitro testing of calcium phosphate (HA, TCP, and biphasic HA-TCP) whiskers,” *Journal of Biomedical Materials research. Part A,* vol. 78, no. 3, pp. 481-490, 2006.

[9] S. Raynaud, E. Champion, D. Bernache-Assollant and J. Laval, “Determination of calcium/phosphorus atomic ratio of calcium phosphate

apatites using x-ray diffractometry," *Journal of the American Ceramic Society,* vol. 84, no. 2, pp. 359-366, 2004.

[10] Norme Francaise, "Détermination quantitative du rapport Ca/P de phosphates de calcium," *NF S 94-066,* 1998.

[11] M. N. Rahaman, Ceramic processing, second edition, CRC Press, 2017.

[12] P. Palmero, B. Bonelli, G. Fantozzi, G. Spina, G. Bonnefont, L. Montanaro and J. Chevalier, "Surface and mechanical properties of transparent polycrystalline YAG fabricated by SPS," *Materials Research Bulletin,* vol. 48, no. 7, pp. 2589-2597, 2013.

[13] Y. Liu and Z. Shen, "Dehydroxylation of hydroxyapatite in dense bulk ceramics sintered by spark plasma sintering," *Journal of the European Ceramic Society,* vol. 32, pp. 2691-2696, 2012.

[14] C.-J. Liao, F.-H. Lin, K.-S. Chen and J.-S. Sun, "Thermal decomposition and reconstitution of hydroxyapatite in air atmosphere," *Biomaterials,* vol. 20, pp. 1807-1813, 1999.

[15] C. Moseke and U. Gbureck, "Tetracalcium phosphate: Synthesis, properties and biomedical applications," *Acta Biomaterialia ,* vol. 6, pp. 3815-3823, 2010.

[16] T. Wanga and A. Dorner-Reisel, "Thermo-analytical investigations of the decomposition of oxyhydroxyapatite," *Materials Letters,* vol. 58, pp. 3025-3028, 2004.

[17] I. Fadeev, L. Shvorneva, S. Barinov and V. Orlovskii, "ynthesis and structure of magnesium-substituted hydroxyapatite," *Inorganic Materials,* vol. 39, no. 9, pp. 347-350, 2003.

[18] H. S. Ryu, K. S. Hong, J.-K. Lee, D. J. Kim, J. H. Lee, B.-S. Chang, D.-h. Lee, C.-K. Lee and S.-S. Chung, "Magnesia-doped HA/β-TCP ceramics and evaluation of their biocompatibility," *Biomaterials,* vol. 25, pp. 393-401, 2004.

Chapter 3 Gelcasting Method: Elaboration and Characterisation of Dense Parts

Abstract

Gelcasting is a ceramic fabrication technique with several advantages such as simplicity, feasibility to produce homogenous microstructures and complex parts, and superior mechanical performance. This technique was employed for the production of dense hydroxyapatite (HA) bioceramics. Two different batches of commercially available HA powders with different Ca/P ratios were used. The dispersion process of HA powders was carried out through dry and wet ball-milling processes, providing powders with different particle size distributions. Agar, a natural food-grade non toxic biopolymer, was used as the gelling agent and an anionic polyelectrolyte was exploited as the dispersant to stabilise the ceramic suspension and increase the solid loading. The compositions of the slurries were optimised through rheological analyses. The sintering behaviour of the powders was studied using dilatometry tests and the different stages of the sintering processes along with the related microstructural developments were identified. The effect of the heating rate and the initial particle size on the sinterability and the grain growth were investigated and on the basis of these results, the sintering process was optimised. Having a reverse relationship between sinterability and the mean particle size of the starting powder, criteria were established based on the mean particle size of the starting powder for obtaining dense microstructures by sintering at 1300 °C for 1 and 3 hours . Phasic and microstructural evolutions during the sintering stage were identified with regards to powder type, particle's size and the heating rate. An abnormal grain refinement was observed for the sintering of the powder with the lower Ca/P ratio. This grain refinement was found to be resulting from the HA to tetracalcium phosphate (TTCP) phase transformation at 1300 °C leading to a bimodal grain size distribution of the final material. Well densified microstructures were led to

superior mechanical properties of the samples derived from the finest powder as were characterised by compression tests.

Abbreviations

ASTM	American society for testing and materials
CaP	Calcium phosphate
CD-HA	Calcium deficient hydroxyapatite
DBM	Dry ball milling
EDX	Energy-dispersive X-ray spectroscopy
FESEM	Field emission scanning electron microscopy
HA	Hydroxyapatite
HA-AR1	As-received hydroxyapatite powder, batch n.1
HA-AR2	As-received hydroxyapatite powder, batch n.2
ICDD	International Centre for Diffraction Data –
PAA	Polyacrylic acid
PMAA	Polymethacrylic acid
PMMA	Poly(methyl methacrylate)
TD	Theoretical density
TTCP	Tetracalcium phosphate
US	Ultrasonic
WBM	Wet ball milling
XRD	X-ray diffractometry
α-TCP	α-tricalcium phosphate
β-TCP	β-tricalcium phosphate

3.1 Introduction

Gelcasting is a superior forming technique which has several advantages over other ceramic forming methods. Homogenous microstructure, high mechanical performance, good control on the sintering process and the possibility of production of complex shapes, which is important especially in biomedical applications, are some of the strong points of this technique. Gelacasting was originally developed for the production of dense parts [1]; however, the high strength in the green state, resulting from in situ polymerisations, also makes it suitable for the production of porous parts. Porous samples with porosity as high as 90% have been fabricated through this technique [2, 3, 4, 5, 6, 7, 8, 9] and the produced parts have enough strength in the green state to be further machined to achieve more complexity. Hydroxyapatite (HA) is one of the materials whose production of dense and porous parts through gelcasting technique has been widely reported in the literature [1, 2, 3, 4, 5, 6, 7, 8, 9, 10] [11].

Based on the colloidal processing systems, control of the interparticle forces and achievement of a stable suspension are of utmost importance in the gelcasting technique. An effective dispersant, able to neutralize the ceramic's interparticle forces, not only stabilises the colloid but also helps to achieve higher solid loadings and to reduce the viscosity of the slurry [12].

Sintering, as the final step in many ceramic processing techniques, controls the final physico-mechanical properties of the materials. Being conducted in high-temperature regimes, many phase transformations would take place during sintering such as in the case of the calcium phosphates (CaP) which are key factors in determining the final characteristics of the materials[13]. Therefore, identification and controlling the sintering behaviour of the material are critical in tailoring the final properties of the calcium phosphate parts.

In the following sections, at first, the criteria in the selection of the gelling agent and the dispersant used in the production of dense and porous parts are presented. Afterwards, the sintering behaviour of HA powders considering the particle size distribution will be studied and different parameters effective in the sintering condition will be discussed. In the end, the production procedure and the physical and mechanical properties of dense samples will be presented.

3.2 Selection of the gelling agent

A high purity agar (Agar-agar, Sigma-Aldrich, A7049, ash > 2%), a polysaccharide constituted by chains of glycosyl units [12] was chosen as the gelling agent. This material is a natural food-grade biopolymer which is obtained from red algae and belongs to polysaccharides [14]. According to European regulation n° 1272/2008 [15], agar is classified as non-hazardous substance and can be an environmentally friendly replacement for the early gelling system of acrylamides which had certain toxicity issues.

One of the first reports on the utilization of agar as a binder was reported by Maini in forming biopolymer sheets [16]. Since then, this system has been used in gelcasting of a wide variety of ceramics such as alumina [17, 18, 19], TiO_2 [20], Si_3N_4 [21], ferroelectric ceramics [16] and also HA [8, 9].

The advantages of polysaccharide-based biopolymers as gelling agents are not limited only to their non-toxicity. Because low amounts of these biopolymers are needed for the gel formation (<1 wt% of the ceramic solids content), the debinding thermal cycle is accompanied with very limited residual voids. The obtained gels are relatively strong and offer an environmentally friendly approach by polymerisation in water-based suspensions [16].

Gelation of agar is accomplished through a thermo-reversible heating/cooling cycle. First, the biopolymer is dissolved in hot water and then gels over the cooling cycle. Figure 3-1 shows the change in the viscosity of agar-water mixtures with different agar contents during heating and cooling cycles. Upon heating, with the starting of agar dissolution in water, the viscosity increases and then at higher temperatures becomes stable. During the cooling cycle, the viscosity increases slowly until a certain temperature, at which the increase becomes more significant due to gelation [16].

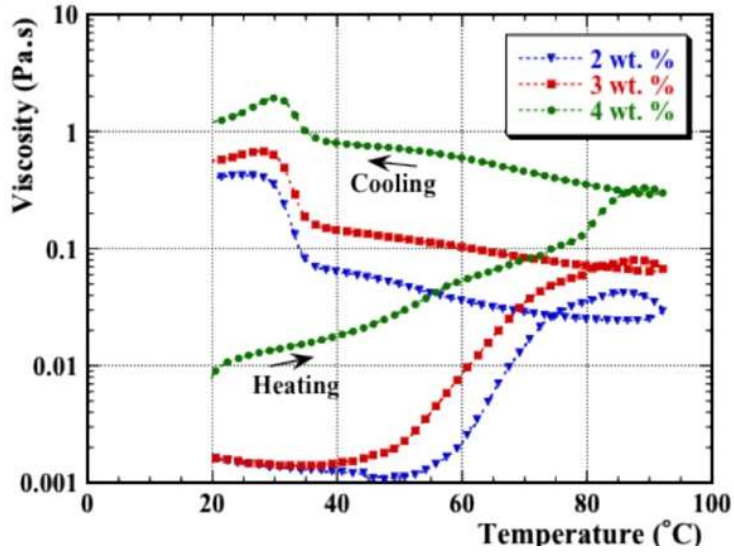

Figure 3-1: Change in the viscosity of agar solution in water with different concentrations during heating and cooling cycles. Reprinted from [16] with the permission of John Wiley and Sons under the license no 4739041029621.

Figure 3-2 represents the viscoelastic response of a 4% agar solution defined by relative values of elastic modulus (G') and viscous modulus (G"). In temperatures that the G' is less than G" the material is referred to be a liquidus, but when G' is greater than G'', the material behaves more like an elastic solid. Therefore, the cross-over point which is around 30 °C shows the temperature at which the sol to gel transition occurs.

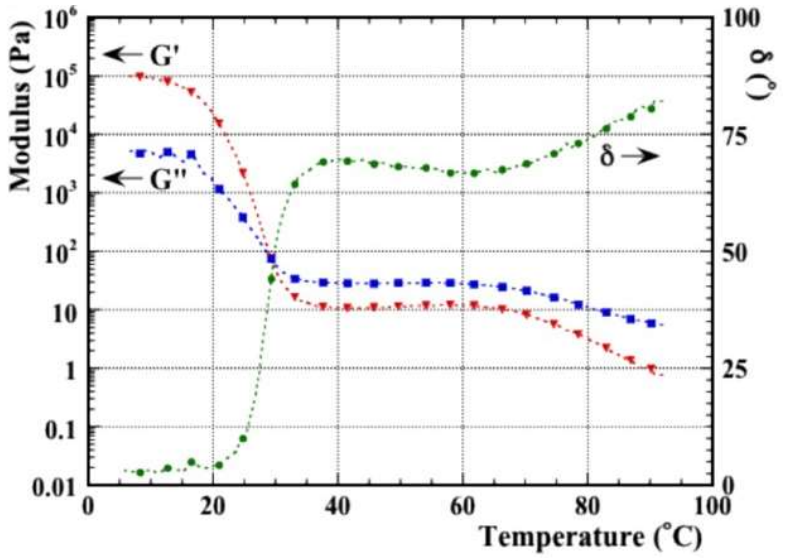

Figure 3-2: Viscoelastic behaviour of a 4% solution of agar in water as a function of the temperature. Reprinted from [16] with the permission of John Wiley and Sons under the license no 4739041029621.

The temperatures at which the dissolution and gelation of agar at different concentrations take place are illustrated in Figure 3-3. It is evident that the dissolution of agar, starting at a relatively low temperature (around 60 °C), completes at around 90 °C. On the other hand, during the cooling stage, the gelation starts around 38 °C, and completes below 29 °C. The gelation onset and completion temperatures are seen to increase very slightly with agar concentration [16].

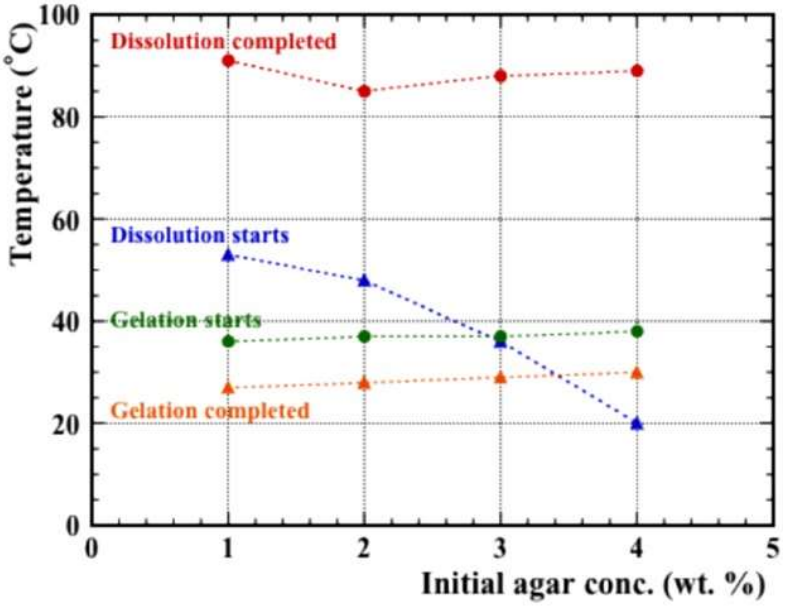

Figure 3-3: The starting and completion points of agar dissolution and gelation with different concentrations. Reprinted from [16] with the permission of John Wiley and Sons under the license no 4739041029621.

Besides the positive sides of the using of the polysaccharides as the gelling agent, there are also some disadvantages. Due to the low agar solubility in water, a large amount of water is used for the production of the gelling medium which is subsequently added to the ceramic suspension. Therefore, the final solid loading of the slurry is shifted towards lower values. Moreover, removing of this additional water during drying step induces further difficulties and can be a source of drying flaws. Obtaining a high green density and afterwards, sintered density can also be particularly challenging [16].

3.3 Rheological studies

Because gelcasting is originated from colloidal processing, in order to obtain high strength complex parts, the control of the rheology of the slurry and the ceramic's interparticle forces are critical. The rheological behaviour of suspensions critically affects the generation of flaws in green bodies. In view of an optimised microstructure for the gelcasting process, an ideal slurry is the one with low viscosity consisting of high solid loading of individually stable separated solid particles. High solid loadings are essential not only for obtaining high-density green bodies but also, with decreasing the portion of water in the slurry, reduces the shrinkage associated with the drying stage and the risk of drying flaws [11]. Fine ceramic particles suspended in a slurry tend to stick together and induce flocculation which decreases the stability and homogeneity of the slurry and increases the viscosity, hindering high solid loadings.

Among several ways to overcome the attractive forces between ceramic particles, the most common method is electrosteric stabilisation. It is a combination of electrostatic and steric stabilisations and is commonly achieved in aqueous mediums through the use of polyelectrolytes [12]. Polyelectrolytes are polymers that have at least one type of ionisable group (e.g., carboxylic acid group) and the dissociation of these polymers in water produces electrostatic charges.

The sodium or ammonium salts of polymers such as polymethacrylic acid (PMAA) and polyacrylic acid (PAA), which have a functional carboxylic acid -COOH group are two examples of commonly used polymers for electrosteric stabilisation of advanced ceramics. Dissociation of these polymers in water produces negatively charged species. These negatively charged species are adsorbed to the ceramic particle surface (Figure 3-4), which neutralises positive charges of ceramic particles and allow them to be dispersed in water, and consequently reduces the viscosity [12, 22].

Literature showed that the most efficient dispersant for HA powder is an anionic polyelectrolyte [23]. Duramax D-3021 (Rohm and Haas, France), a 40 wt.% solution of an ammonium salt of a polycarboxylate polyelectrolyte NH_4^+ PAA, with a low molecular weight of approximately 2500 Da, was used as an anionic dispersant to produce electrosteric stabilisation in this study. As a further advantage, it is sodium-free and leaves no measurable residue after firing [24].

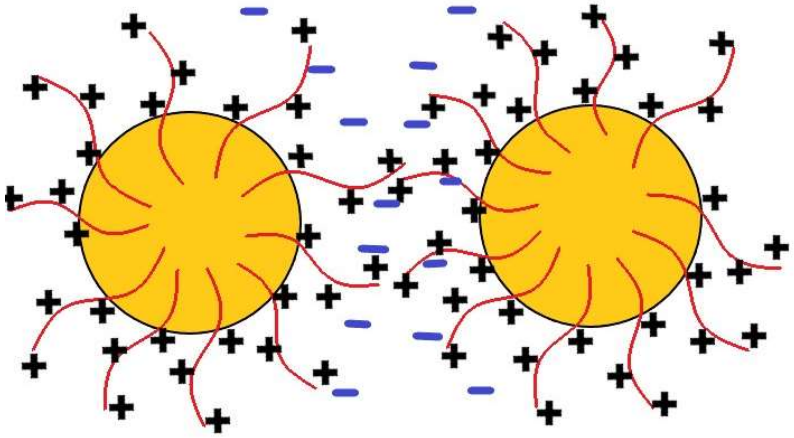

Figure 3-4: Schematic illustration of the electrosteric repulsion forces generated by the adsorption of ionic polymer molecules onto the ceramic surfaces.

Studies on the effect of dispersant concentration on the viscosity and stability of the colloidal suspensions have shown that there is an optimum concentration at which the dispersant is most effective [22]. Any concentrations lower or higher than the optimum amount lead to viscosity increase and reduce the capability to achieve higher solid loadings. It has been claimed that at lower amounts, the electric layer is not enough, and it is not possible to achieve an effective repulsion between particles. On the other hand, when the dispersant amount is higher than the optimum value, too high electrolyte concentration compresses the electric double layer and makes the repulsion less effective, therefore the viscosity increases. Besides, at higher amounts of dispersant, the presence of free ionic PAA in the liquid medium may cause inter-locking of PAA polymer chain, and cause viscosity increase by bridging the solid particles [22]. The right amount of dispersant leads to uniform microstructure both in green and sintered states [25].

The study of the viscosity of HA slurries with different solid loadings has shown that, in low solid loadings, the HA slurries show Newtonian behaviour. With increasing the solid loading, the slurry transferred to shear thinning behaviour. The transition of Newtonian to shear thinning behaviour can be attributed to an increasing difficulty for particles to orientate in the direction of the shear stress. Therefore, the powder concentration, and then the viscosity, increase. However, it was also observed that, after a specific value of solid loading, the rheological behaviour changes from shear-thinning to shear thickening, which means that it is not suitable anymore for casting [23].

The viscosity evolution of the slurries made from the as-received powder HA-AR1 was studied using a rotational viscometer (Brookfield HBDV-II, Brookfield, Massachusetts, USA). The viscosities of slurries with two different solid loadings of 54 and 70 wt% at different shear rates were measured and the effect of various amounts of dispersant on the viscosities was analysed. The results are presented in Figure 3-5 as a log-log plot of viscosity versus shear rate. It can be seen that regardless of the solid loading and dispersant concentration, with increasing the shear rates the viscosities of the slurries decrease. The exponential decrease in

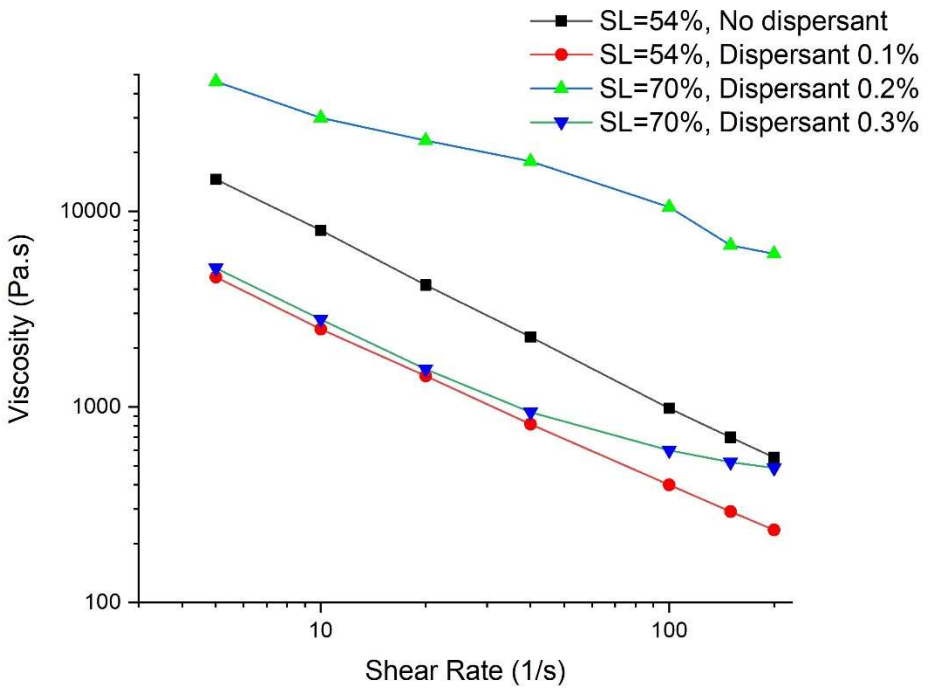

Figure 3-5: Viscosity of slurries made of HA-AR1 powder at different combinations of solid loading and dispersant as a function of shear rate.

viscosity as shear rate increases demonstrates the shear thinning behaviour.A direct relationship between viscosity and the solid loading can be observed by comparing the 54 wt% slurries with the 70 wt% slurry. Increasing the solid loading leads to the viscosity increase. Even though the higher solid loaded slurry contained 0.2% dispersant, it showed higher viscosities at all range of shear rates. However, with increasing the dispersant to 0.3%, its viscosity dropped and it showed almost similar viscosity to the 54 wt% slurry with 0.1% of dispersant.

It should be noted that increasing the dispersant concentration led to lower viscosities out of working range of our viscometer making it impossible to measure the viscosity of the slurries with a higher amount of dispersant. Therefore, higher solid loaded slurries from both dry ball-milled (DBM) and wet ball-milled (WBM) powders with suitable rheology for mixing and casting were obtained with higher amounts of dispersant. The characterisation of the samples made from those slurries, as presented in the following sections, proved their suitability for gelcasting process.

In the viewpoint of the final mechanical properties, it must be considered that a higher solid loading does not definitely lead to a higher mechanical strength. In practice, a lower solid loading is associated with improved rheological behaviour and lower viscosity of the slurry which reduces the possibility of formation defects such as flock or air bubbles. In fact, the degassing process for the elimination of air bubbles is easier when the viscosity is low. Therefore, these types of defects would be lower in the pieces produced from low viscosity slurries. The findings of Padilla et al. [11] supported this hypothesis since they found the highest mechanical

strength for the samples produced from slurries with solid loadings lower than the highest solid loading suitable for casting. Therefore, it seems that, to obtain samples with the highest mechanical properties a compromise between the rheology and solid loading should be considered.

3.4 Elaboration of green samples

In the previous chapter, the characterisation of two HA powder batches (named HA-AR1 and HA-AR2) was carried out. Both powders revealed as calcium-deficient hydroxyapatite (CD-HA); HA-AR1 was characterised by a Ca/P ratio of 1.59 and an average particle size of 2.95 μm, while these parameters were 1.55 and 2.48 μm for HA-AR2, respectively. It was also shown that by ball milling of the powders under dry and wet conditions, the particle size distributions of the powders were reduced and less agglomerated powders were achieved. WBM appeared more efficient in the reduction of the ceramics particles sizes and it led to mean particle sizes of less than 1 μm.

Powders obtained from DBM and WBM processes of both HA-AR1 and HA-AR2 with the mean particle sizes between 1.5 and 2.0 μm, and 0.6 and 1.2 μm, respectively, were used for the production of green dense bodies with different solid loadings. Different ranges of mean particles sizes were selected in order to study the effect of the particle size distribution on different processing parameters as well as micro and macrostructural characteristics of the produced samples. The ceramic slurries were produced by mixing the HA powders with demineralized water and dispersant and stirred for 24 hours under magnetic stirring for complete dispersion. The castings were carried out under vacuum conditions, to eliminate the trapped bubbles and before it the particle size distributions of the initial powders were measured using laser granulometry .

Considering possible applications in load-bearing conditions, the aim in the production of the dense samples was to achieve high mechanical properties. To this aim, different stages of the production process, such as reduction of particle sizes through ball milling, slurry's rheology, drying, debinding, and sintering were conducted in the most effective way.

The successive steps of the gelcasting procedure used in the production of the dense samples are shown in Figure 3-6. The procedure started with two different preparations in parallel: the first was a suspension made of a mixture of powder, dispersant and demineralized water, and the second was a solution of agar as the gelling agent in demineralised water. The former was heated to 60 °C, while the latter was first heated to 90 °C and kept at this temperature for 10 minutes to ensure complete dissolution of agar and then cooled to 60 °C. The two preparations were mixed to one suspension at 60 °C, and the mixed slurry cast into Poly(methyl methacrylate) (PMMA) cylindrical moulds. The internal diameter and height of the moulds were 14 mm and 30 mm respectively. To avoid air entrapment the casting was carried out under vacuum of about 10^{-2} Pa by means of a rotary pump. Gelation was obtained by cooling the casts to 15 °C inside a water bath and keeping the

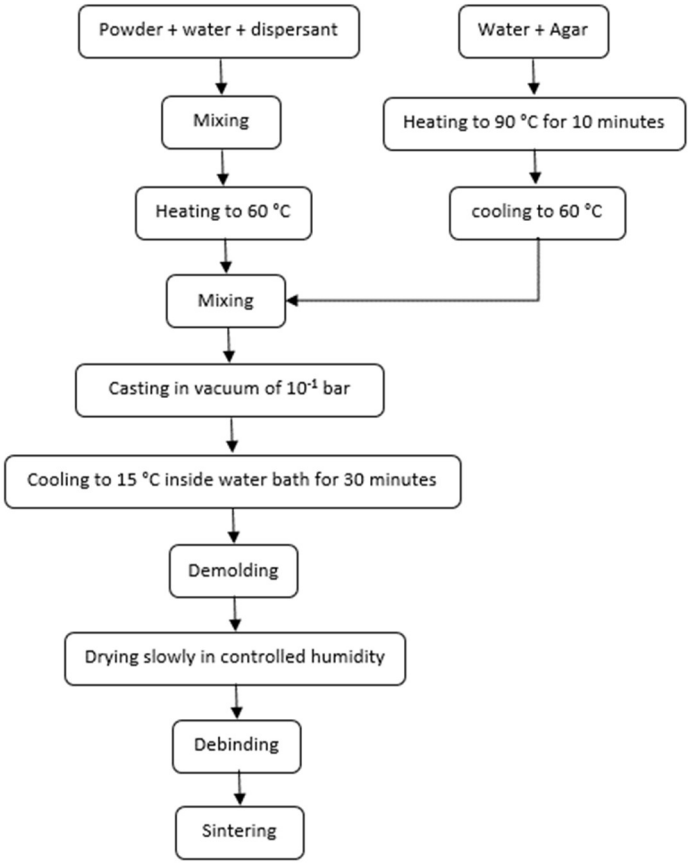

Figure 3-6: The flowchart of the gelcasting procedure used in the production of dense HA.

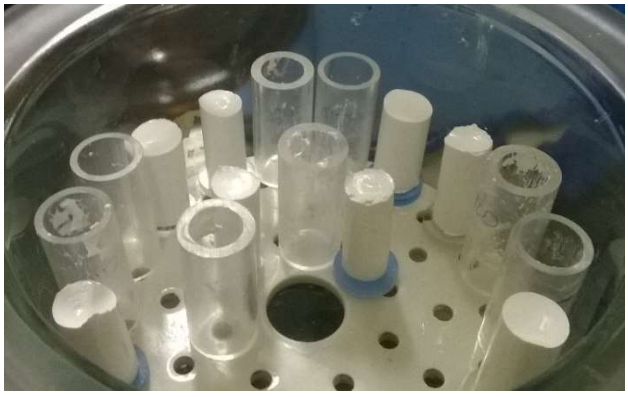

Figure 3-7: Wet HA gelcast dense samples after demoulding.

samples there for 30 minutes. After gelation, the casts were well polymerised and easily demoulded, providing well-shaped pieces (Figure 3-7). Neither contraction or cracking was observed, and the samples showed enough strength to be carefully handled.

Drying is an important and complex stage in the ceramic production which needs to be accomplished with caution. The interaction of three independent processes of evaporation, shrinkage and fluid flow in the pores leads to the drying

of parts [12]. To obtain a dried part with minimum residual stresses these processes should be controlled during the whole process. During drying, the solid-liquid interface (specific energy = γ_{sl}) is replaced by the solid-vapour interface (specific energy = γ_{sv}). Because $\gamma_{sv} > \gamma_{sl}$, the energy of the system rises. To prevent exposure of the solid, liquid stretches from interior to exterior, therefore the liquid goes into tension. The tension in the liquid is balanced by compressive stresses on the solid network that causes shrinkage. The pressure gradient increases with decreasing the initial ceramic particles sizes. The higher the drying rates, the faster is the surface contraction. Therefore, the strain rate varies more intensely through the article inducing higher drying stresses [12]. For a flat plate made from a ceramic with particle size in the range of 0.5-1 μm, when the evaporation rate is high, the tension can be as high as 0.5 MPa. Therefore, it is of utmost importance that during drying, the evaporation and the fluid flow in the pores are conducted regularly throughout the body. To satisfy these conditions, we implemented the drying in several steps. Firstly, the as demoulded wet parts were put in closed dessicators with fixed relative humidity value >90% overnight. Afterwards, the relative humidity of the chambers was reduced to 80, 60 and 35% and the green samples were kept under each humidity conditions for 2 days. Finally, the samples were dried for 24 hours at room temperature and a further 24 hours at 80 °C in an oven. The final parts were cylindrical samples with regular shapes free of flaws and cracks (Figure 3-8).

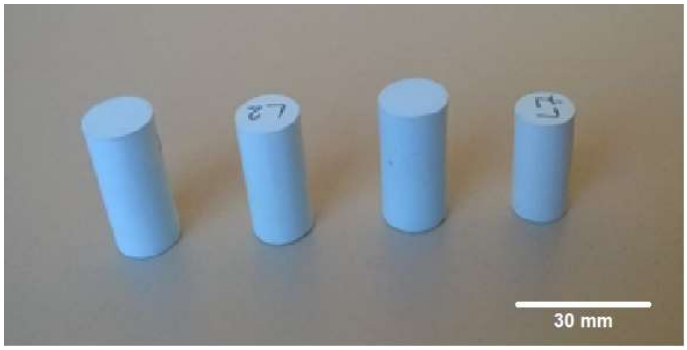

Figure 3-8: HA gelcast dense samples in the green state.

Table 3-1 collects the processing data including solid loadings, mean particle sizes and green densities of the dried samples produced from DBM powders. Each batch consisted of at least 6 samples produced from a specific slurry. In all cases, the amount of agar was 0.5 wt% related to water. The green densities were calculated by weight and geometrical measurements. In gel-casting, it is important to increase the solid loading of the slurries as much as possible, because it directly transforms into the green density of the cast parts. On the other hand, high viscosity jeopardizes homogeneity and casting. It is, therefore, important to maintain slurry fluidity at the optimum solid loading [26].
Figures 3-9 and 3-10 illustrate the green densities versus the solid loadings and the mean particle sizes, respectively. Solid loading and mean particle size are not independent parameters: in fact, very fine particles, characterised by high specific

Table 3-1: Processing data of the dense samples produced from DBM powder.

Batch designation	Powder batch	Solid loading (%)	Mean particle size (µm)	Green density (g/cm^3)
D1-A	HA-AR1	63	1.63	1.66 ± 0.01
D1-B		64	1.64	1.67 ± 0.00
D1-C		65	1.68	1.69 ± 0.00
D1-D		75	1.79	1.78 ± 0.01
D1-E		71	1.79	1.71 ± 0.01
D1-F		70	1.7	1.70 ± 0.01
D1-G		66	1.71	1.66 ± 0.01
D1-H		67	1.65	1.66 ± 0.01
D1-I		68	1.75	1.70 ± 0.00
D1-J		69	1.67	1.67 ± 0.01
D1-K		60	1.61	1.63 ± 0.00
D2-A	HA-AR2	60	1.69	1.66 ± 0.01
D2-B		63	1.62	1.65 ± 0.01

surface area limit the achievement of high solid loadings. From these figures, it may be seen that the green density increased with increasing each of these two parameters. Landi et al. [27] also reported an increase of the green density of HA samples with increasing of the primary powder's particle size . However, a little discrepancy from the linear trend is observable in both graphs. The observed inconsistencies partly resulting from the inherent error in the manual measurement of the geometries. Another explanation is the combined effect of solid loading and particle size. For example, samples D1-D and D1-E, characterised by a similar mean particle size but different solid loadings, showed different green densities. The higher solid loading of the sample D1-D (75%), led to closer particles in the green state, and therefore to a higher green density. Finally, we can observe that the features of the starting powder batch did not influence the green density: for

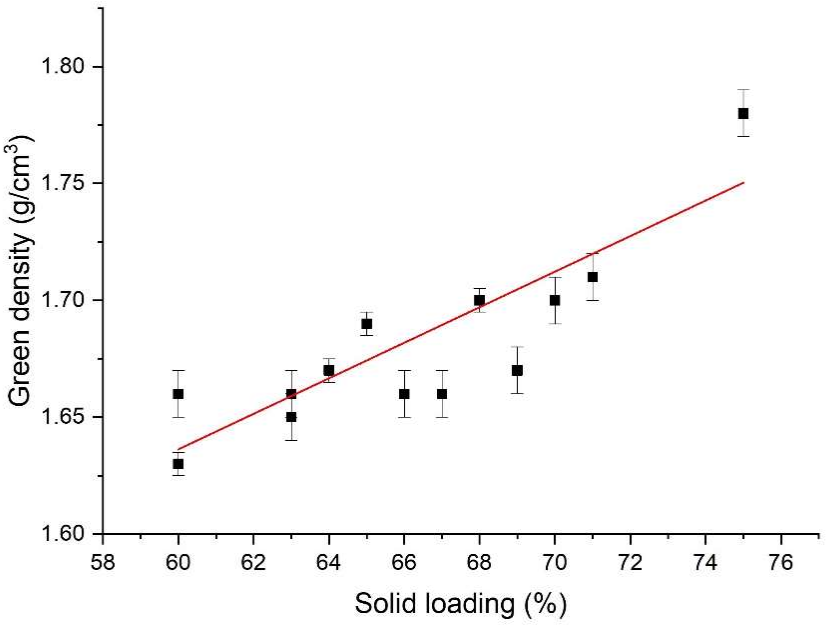

Figure 3-9: Green density versus solid loading for green samples produced from DBM powder.

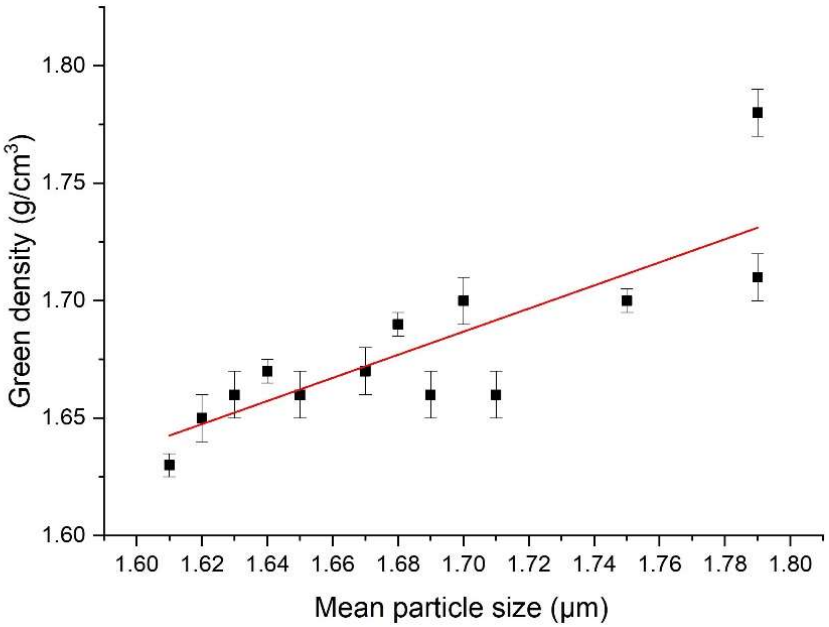

Figure 3-10: Green density versus mean particle size for green samples produced from DBM powder.

example, comparing D1-A and D2-B, the same solid loading and mean particle size allowed to produce green samples with almost the same relative density. However, the specific features of the two powder batches will affect sinterability and microstructural development, as discussed later.

The processing data of the dense samples produced from WBM powder are similarly presented in Table 3-2. Compared to DBM samples, the samples produced from WBM powders needed a higher amount of gelling agent to produce self-standing green samples. For a lower amount of agar, the samples didn't keep their cylindrical shapes after demoulding and in many cases, they bent to one side. The needed agar amount correlated to the initial powder particle sizes: with decreasing the particle sizes, more agar was required because of a higher surface of powder particles. The agar used for the production of these samples was in the range of 0.8 to 1.1% related to water.

Table 3-2: Processing data of the dense samples produced from WBM powder.

Batch designation	Powder batch	Solid loading (%)	Mean particle size (µm)	Green density (g/cm^3)
W1-A	HA-AR1	60	0.74	1.63 ± 0.01
W1-B		60	0.81	1.68 ± 0.00
W1-C		60	0.70	1.59 ± 0.01
W1-D		60	0.83	1.69 ± 0.01
W1-E		60	0.89	1.69 ± 0.00
W2-A	HA-AR2	60	0.74	1.65 ± 0.02
W2-B		63	1.08	1.70 ± 0.01
W2-C		63	0.71	1.64 ±0.01
W2-D		63	0.99	1.80 ±0.00
W2-E		63	1.18	1.80 ± 0.01
W2-F		60	1.22	1.86 ± 0.00

The relationship between green densities and mean particle sizes of the samples produced from WBM powders are plotted in Figure 3-11. Like DBM samples, there was a direct link between the green density and mean particle size; by increasing the mean particle size the green density increased. The correlation between green density and particles size has been already demonstrated in the literature [22, 23]. In fact, to achieve higher green densities, it is recommended to use a powder characterised by a bimodal size distribution, so that the smaller particles fill the voids between the larger ones [28]. Therefore, since particles with larger mean particle size are normally accompanied by a wider particle size distribution, the particles with different sizes fill the interparticle spaces more efficiently therefore their green densities are higher, explaining both Figures 3-10 and 3-11.

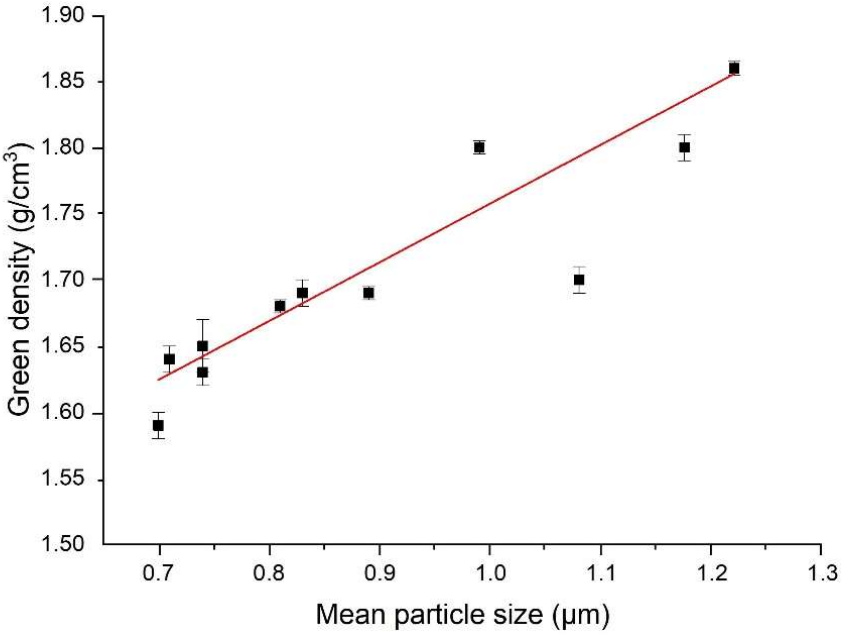

Figure 3-11: Green density versus mean particle size for the green samples produced from WBM powders.

However, if data from DBM and WBM powders are simultaneously plotted (Figure 3-12) it can be seen that, despite the higher solid loading and the larger particle size of the DBM samples compared to the WBM ones, their green densities were comparable. From the data collected in Tables 3-1 and 3-2, the average green densities were 1.68 (±0.04) g/cm3 for DBM samples and 1.71 (±0.08) g/cm3 for WBM ones (the numbers in brackets are standard deviations). It seems that when DBM and WBM are compared, the finer particles in WBM play a major role in producing more compact structures, probably due to better particles packing. The small interparticle spaces are effectively filled by the very fine WBM particles, thus promoting the green density.

This hypothesis was confirmed by the observation of the green microstructures of the samples obtained from DBM and WBM powders (after debinding) presented in Figure 3-13. The difference of the particle size distributions among the two

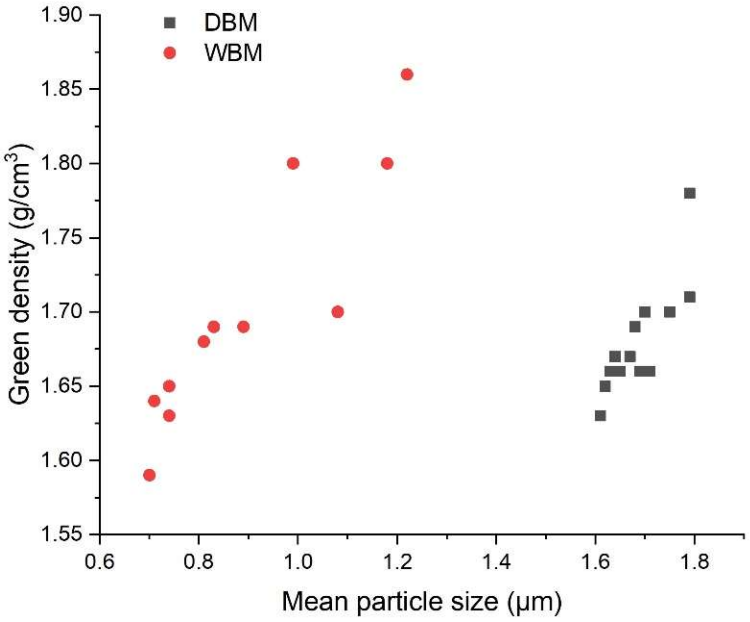

Figure 3-12: Green density versus mean particle size for the green samples produced from WBM and DBM powders.

images is noticeable. A great range of particle sizes can be recognized in the DBM microstructure. While the space between large agglomerates can be filled by smaller particles, some large pores can be easily observed. On the other hand, it can be seen that the microstructure obtained from WBM powder shows higher homogeneity and the particles are more closely packed compared to the DBM sample.

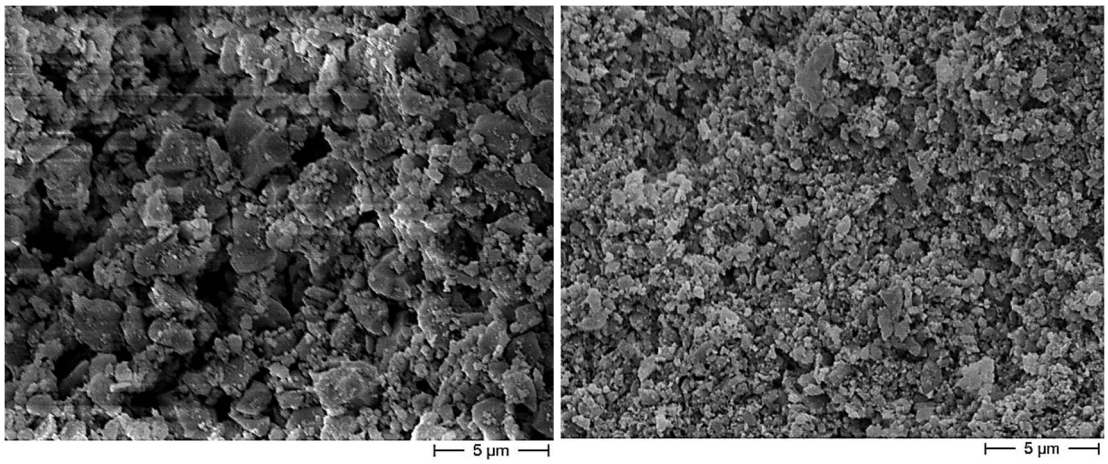

Figure 3-13: Microstructure of the green samples produced from dry (left) and wet (right) ball-milled powders.

3.4.1 Binder burnout

Debinding or binder burnout is a thermal process to remove the binder and other organic additives from the green parts. This thermal treatment is carried out at temperatures significantly lower than sintering temperature and the organic additives must be removed completely without affecting the green structure or creation of new microstructural defects. Even though just a few percent of organic additives are used in gelcasting, debinding should be performed using very low heating rates to minimize the potential residual stresses [12] and/or formation of microcracks. Because the organic additives consist of different components with different volatilities, their decomposition accomplishes in a quite long-range of temperatures. Dispersant with low molecular weight is removed in a lower temperature range than the gelling agent with high molecular weight.

Thermogravimetry analysis of the agar used in gelcasting is presented in Figure 3-14. It is clear that the complete removal of this component was done in 3 different steps. The first step involves the removal of the water absorbed on agar particles that is done under 100 °C. After that, the material is stable up to 230 °C, at which rapid decomposition of almost 50% of the component is achieved. The decomposition of the remaining matter becomes slower afterwards up to 600 °C, at which almost all of the organic matter is already decomposed. Having this information, the binder removal process for all of the green samples were done by heating at 600 °C for 1 hour using a slow heating rate of 1 °C/min. The residual mass was burned out during the subsequent sintering cycle, as described later on.

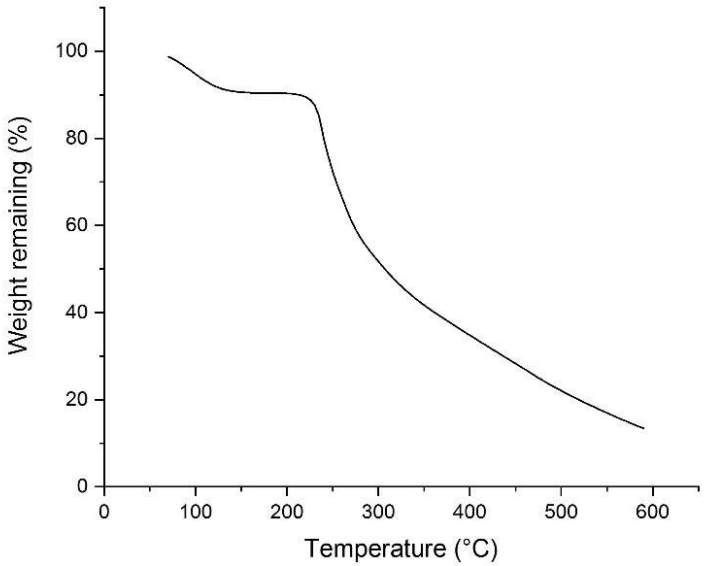

Figure 3-14: Thermogravimetry curve of agar.

Figure 3-15 shows the microstructure of a green body obtained from WBM powder, before and after debinding process. In both cases the microstructures are

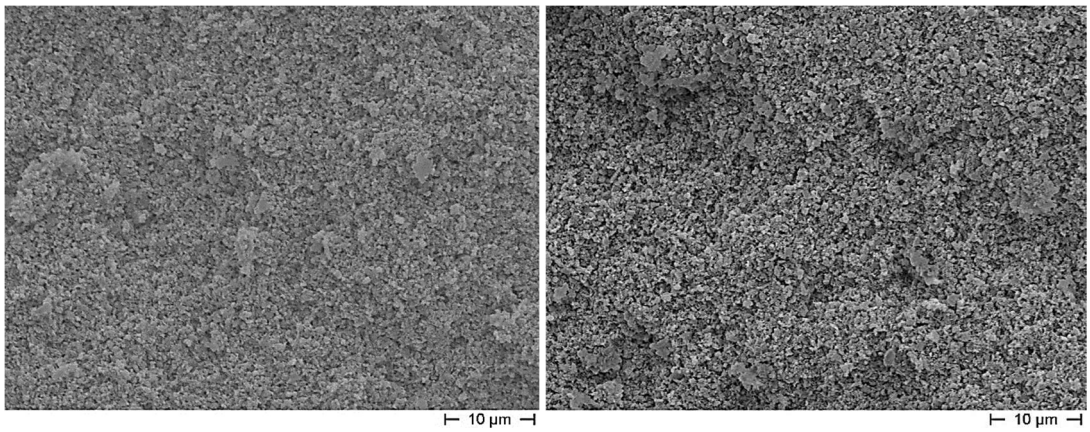

Figure 3-15: Microstructure of the green dense samples before (left) and after (right) debinding.

homogeneous and compact; in addition, no defects or microcracks due to the agar decomposition can be observed after debinding.

The X-ray diffraction pattern of the sample after debinding is presented in Figure 3-16, showing all the characteristics peaks of the HA phase, and meaning that no phase evolution occurred during debinding, as expected.

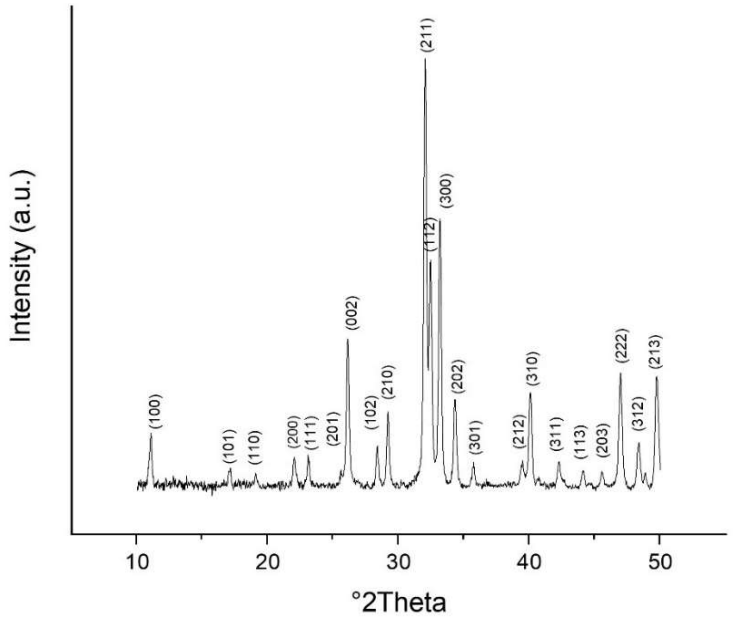

Figure 3-16: X-ray diffraction pattern of the HA sample after debinding.

3.5 Optimisation of the sintering process

Sintering, as the final stage of the ceramic manufacturing, is an irreversible process that strongly bonds ceramic particles together and eliminates the pores between them. The materials after sintering is a solid body with highly improved

mechanical properties. The driving force of the sintering process is the reduction of surface energy that leads to the consolidation of the green part through the coalescence of the ceramic particles and can be accompanied by grain growth [29]. Higher temperatures usually lead to a higher degree of densification, but increased grain growth and possible phase transformation also should be taken into account.

Suitable sintering process normally depends on the final desired properties. As discussed in the first chapter, dehydroxylation and several phase transformations may take place during the sintering of HA which can play a significant role in the final physical and chemical characteristics of the material. The type and proportion of the phases present in the final material, the level of porosity and the mechanical properties are parameters which must be considered in designing the sintering cycle of HA bioceramics.

The sintering behaviour of ceramics is normally characterised by a dilatometry test which measures the linear shrinkage of the material under specific heat treatment as a function of time and temperature. The concurrent density can be calculated by simple mathematics. It is also possible to detect any phase transformation during dilatometry tests from the associated volume changes.

In this work the dilatometry measurements (Netzsch 402E, Netzsch, Selb, Germany) of HA materials were conducted under different heating cycles. Firstly, the test was carried out on a green sample made from DBM powder by sintering at 1300 °C for 3 hours with the heating rate of 1 °C/min. The linear changes related to shrinkage behaviour and possible phase transformations were identified. Afterwards, the effects of different heating rates on the shrinkage behaviour of the material were identified by conducting the same heat treatment but with different heating rates of 5 and 10 °C/min. Similar tests were implemented on the samples made from WBM powders to identify the influence of the initial powder's particle size on the sintering behaviour. The samples used in the dilatometry tests were produced by gelcasting route andBefore the tests, the organic matter (agar and dispersant) of the samples was eliminated by thermal debinding at 600 °C.

Figure 3-17 shows the dilatometry curve (black line) of the sample made from DBM HA-AR1, sintered at 1300 °C for 3 hours with the heating rate of 1 °C/min. The red curve is the corresponding first derivative, showing the instantaneous shrinkage rate. From the beginning of the test to 645 °C, the sample only showed a constant CTE (Coefficient of linear thermal expansion) proved by the positive values of the first derivative curve (is not clear enough in Figure 3-17). The second region belongs to the first sintering stage corresponding to the joining of the ceramic particles and the formation of necks between powder particles. This stage starts from 645 °C, indicated by the negative derivative values, and occurs by the surface diffusion mechanism. End of the second sintering stage occurs at about 1000 °C.

The main consolidation of the material occured during the second sintering stage, which started from about 1000 °C, with activation of the grain boundary and volume diffusion mechanisms. During this stage, the ceramic particles merge into each other by the elimination of the free interparticle spaces, and the density rises. With increasing the temperature, the matter diffusion rate increases, and as shown

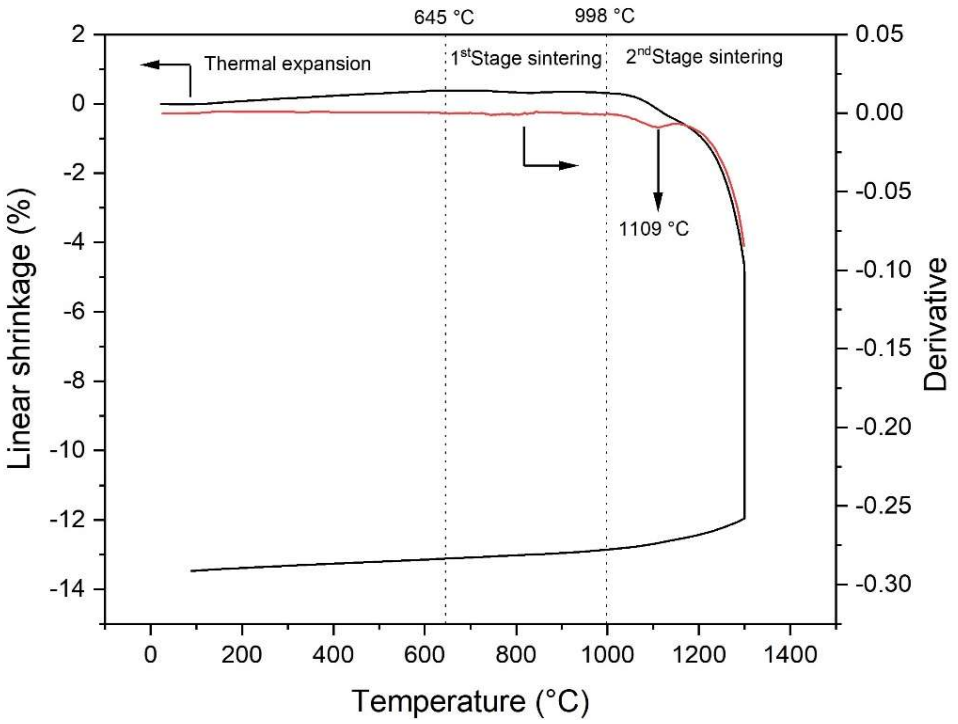

Figure 3-17: Linear shrinkage (black line) and the corresponding derivative curve (red line) of the DBM sample as a function of temperature (heating rate: 1 °C/min).

by the derivative curve, the shrinkage rate of the material increases as well. At around 1109 °C, an inflexion point in the derivative curve indicated by shrinkage discontinuity was observed. This point can be ascribed to the starting of the β-tricalcium phosphate (β-TCP) to α-tricalcium phosphate (α-TCP) allotropic transformation [30]. Due to an almost high difference between the crystallographic densities of the two phases (3.067 and 2.863 g/cm3 for β- and α-TCP, respectively [31]), the lattice volume expansion during β- to α-TCP phase transition (about 7%) prevents the densification and decreases the sinterability of the ceramic.

By increasing the temperature and the enhancement of atomic diffusion, the densification mechanisms become more prominent and lead to the recovery of the volume expansion due to the phase transition. The increase of the shrinkage rate continued up to the maximum sintering temperature (1300 °C), which corresponds to the beginning of the isothermal stage. However, up to this temperature, a second inflexion point in the derivative, ascribable to the maximum shrinkage rate [32], was not present. Therefore, at 1300 °C, the highest (but not maximum) densification rate was achieved, and the second sintering stage was persistent up to this temperature. The total linear shrinkage of about 13.5% was registered by the dilatometer at the end of the whole thermal treatment.

To study the effect of the initial ceramic particle size on the sintering behaviour, the same dilatometry test was conducted on the HA sample obtained from WBM powder. The mean particle size was 0.74 µm compared to the mean particle size of 1.72 µm for the DBM sample. The sintering behaviour of the two samples is

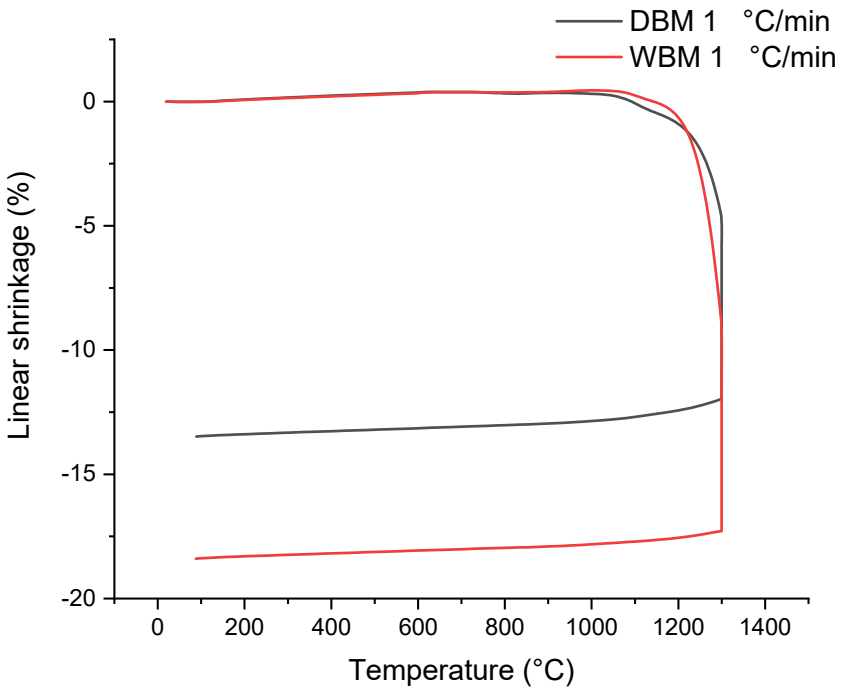

Figure 3-18: Linear shrinkage of WBM (red line) and DBM (black line) samples as a function of temperature.

compared in Figure 3-18. The WBM sample achieved about 40% more densification than the DBM sample and was characterised by a total linear shrinkage of about 18.5%. The higher densification can be reasonably imputed to the higher surface area of the smaller particles (although this datum is not available here) that enhanced the atomic diffusion during the sintering process. This was however expected considering particles packing evidenced by field emission scanning microscopy (FESEM) observations on green samples (Figure 3-13).

The data obtained from the derivative curve of the WBM sample were similar to those obtained by the derivative curve of the DBM sample. The first stage sintering of WBM sample started at the same temperature as the DBM sample (645 °C). However, the onset temperature of the second sintering stage, which is responsible for the main densification, reduced to 978 °C, 20 °C less than DBM powder. On the other hand, the inflexion point due to the phase transformation of β- to α-TCP was 1114 °C, 5 °C higher than the DBM sample.

The effect of heating rate on the densification behaviour was studied on samples obtained from both DBM and WBM powders. The gelcast samples were subjected to dilatometry tests by sintering at 1300 °C for 3 hours under different heating rates of 1, 5 and 10 °C/min. The results are illustrated in Figures 3-19 and 3-20 for the samples obtained from the DBM and WBM powders, respectively. It can be seen that the heating rate had a significant effect on the densification of the samples obtained from DBM powder. The final densification increased from 13.5% for 1 °C/min test to 15.4% for 5°C/min and to 16.4% for 10 °C/min tests. Even if these differences in linear shrinkages can be appreciated in the second sintering stage (i.e., from ~ 1000 °C to 1300 °C), the different densification behaviours can be

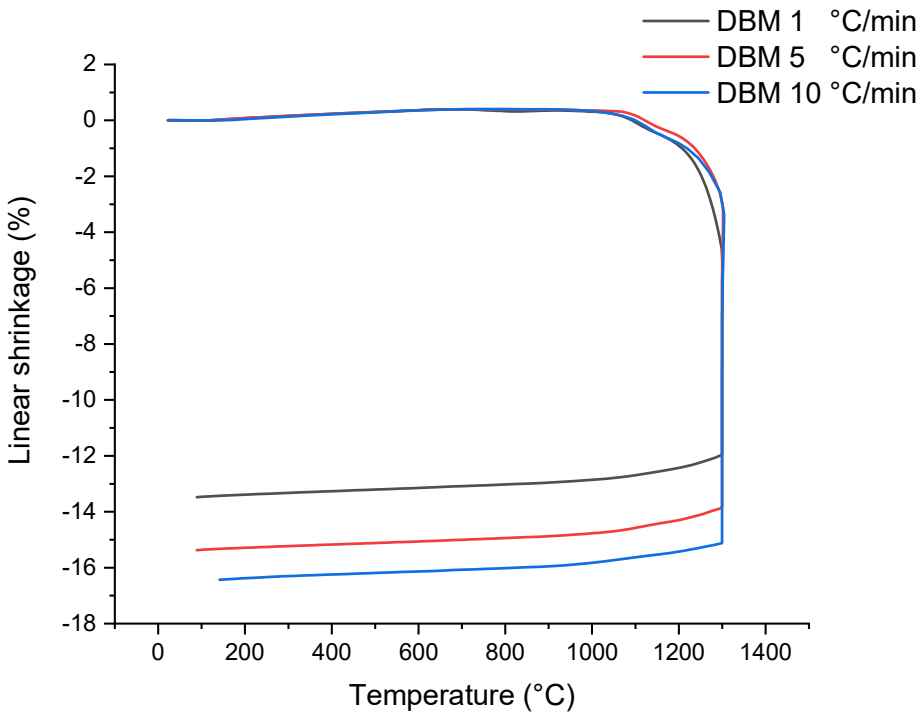

Figure 3-19: Effect of the heating rate on the sintering behaviour of the gelcast DBM samples.

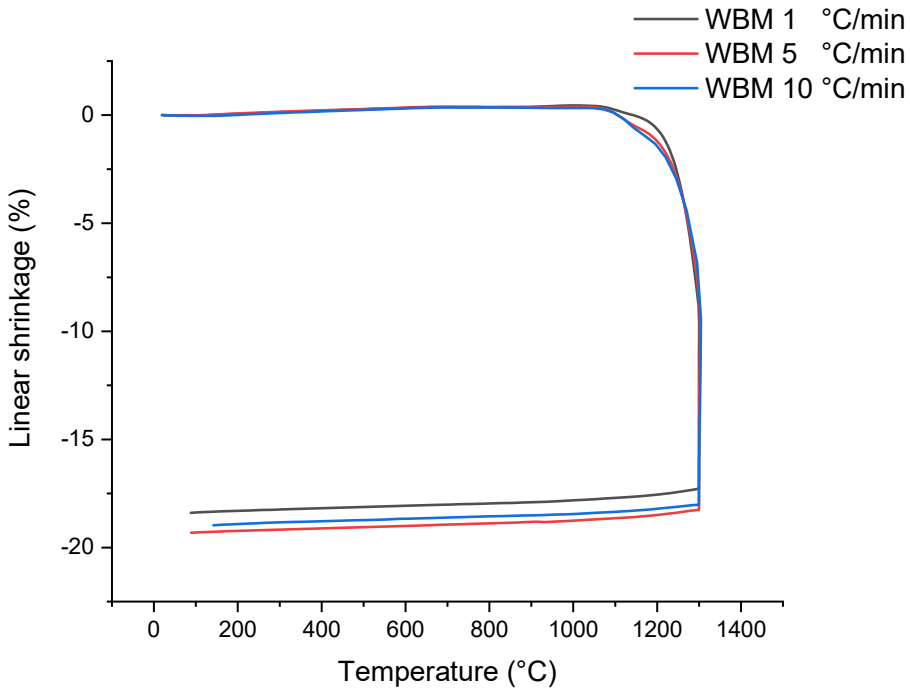

Figure 3-20: Effect of the heating rate on the sintering behaviour of the gelcast WBM samples.

ascribed to the particle attachment occurring in the first sintering stage [33]. As discussed in detail in section 1.4, surface diffusion governs the first stage of the sintering process, in which the ceramic particles stick together and form necks. The

attachment of the primary particles decreases the total surface area of the powder compact and therefore reduces the successive densification stages, due to volume or grain boundary diffusion, occurring at higher temperatures. At lower sintering rates, because there is more time for surface-diffusion sintering to occur, more particle attachments take place. Similar results were reported by Yasuda et al. [25], who investigated the sintering behaviour of HA nanopowders at different heating rates (100 and 200 °C/h).

As illustrated in Figure 3-20, for WBM samples the final linear shrinkages were 18.4%, 19.3% and 19.0% for heating rates of 1, 5 and 10 °C/min, respectively. It seems that the densification of these samples is less affected by the heating rate compared to DBM specimens. However, the positive effect of the higher heating rates on the sintering densification is recognizable as well.

Densification and shrinkage data of the dilatometry tests are presented in Table 3-3. Assuming the final materials as a biphasic calcium phosphate composed of HA and β-TCP phases, the theoretical densities (TD) are calculated by a low of mixture from the theoretical densities of 3.156 and 3.067 g/cm^3 for HA and β-TCP, respectively [31]. Considering the minimum relative density of 95 %TD as the criteria of a dense structure [12], all of the WBM samples achieved almost complete densification during the tests and can be considered as dense bodies. On the other hand, for DBM samples, despite a significant increase in the shrinkage by increasing the heating rate, the final densities were still poor.

Considering solely the isothermal sintering at 1300 °C, the isothermal shrinkage was increased by increasing the heating rates for both types of the samples. For the DBM samples, the isothermal shrinkages were 7.4, 11.2 and 12.5% corresponding to the heating rates of 1, 5 and 10 °C/min, respectively. These figures were 7.7, 9.3 and 11.2% for the WBM samples, respectively. It can be seen that DBM samples experienced relatively higher densification than WBM ones during the isothermal state, suggesting that the WBM samples already achieved most of their densification before the isothermal stage and therefore, the densification continued with lower degrees.

The difference in the densification behaviour of the DBM and WBM samples was more emphasized during the heating stage. Unlike isothermal sintering, during the heating stage, the WBM samples showed substantially more densification than

Table 3-3: Densities and shrinkage data obtained from dilatometry tests.

	DBM samples			WBM samples		
Heating rate (°C/min)	1	5	10	1	5	10
Relative green density (%)	48	48	48	53	53	53
Relative final density (%)	73.5	78.6	81.6	97.0	98.8	98.5
Heating shrinkage (%)	4.6	3.0	3.0	9.6	9.0	6.8
Isothermal shrinkage (%)	7.4	11.2	12.5	7.7	9.3	11.2
Total shrinkage (%)	13.5	15.4	16.4	18.4	19.3	19.0

the DBM ones. The highest difference was observed for the heating rate of 5 °C/min where the shrinkage of the WBM sample was 3 times that of the DBM one. For other heating rates, this difference was more than two times as well.

Table 3-4 collects the temperatures characteristics of the sintering behaviours and the phase transformations acquired from the dilatometry tests. It appears that both surface diffusion and main densification were controlled by the heating rate: they occurred at higher temperatures by increasing the heating rate. Comparing the samples sintered at the same heating rates, it can be seen that, in general, these changes started earlier for the samples produced from WBM powder. In fact, the higher surface area of the WBM powder enhances atomic diffusion and makes it more reactive, compared to the samples produced from DBM powder. On the other hand, it seems that the starting temperatures of the β- to α-TCP phase transformation was not dependent on the powder particle size. Data showed that except a little difference in the case of 1 °C/min heating rate, the phase transformations started exactly at the same temperature for samples heated at 5 and 10 °C/min. In general, it can be seen that, depending on the heating rate, this phase transformation occured in the temperature range of 1109-1145 °C.

Table 3-4: Temperature characteristics of sintering behaviour and phase transformation obtained from dilatometry tests.

	DBM samples			**WBM samples**		
Heating rate (°C/min)	1	5	10	1	5	10
Starting temperature of the first sintering stage (°C)	645	783	795	645	708	770
Starting temperature of the second sintering stage (°C)	998	1058	1071	978	1032	1045
β- to α-TCP transformation temperature (°C)	1109	1132	1145	1114	1132	1145

Figure 3-21 shows the FESEM observations of the final microstructure of the DBM and WBM dilatometry samples. The diffused open pores are recognizable for all DBM samples. Because at the end of the second sintering stage, the sample microstructure should be composed of closed isolated pores, which are then eliminated during the last, third sintering stage, it can be concluded that the second stage was not finished for the DBM samples, and the third was not started yet in these materials. This is in agreement with densification data, as the third sintering stage normally occurs from the relative density of ~ 90 %TD, until the achievement of full densification [33, 34]. Even though the porosity decreased by increasing the heating rate, there was a significant fraction of remaining pores even for the highest heating rate. On the other hand, the closed and isolated pores in the microstructure of the WBM samples indicated that the second sintering stage was finished, and they were in the third one.

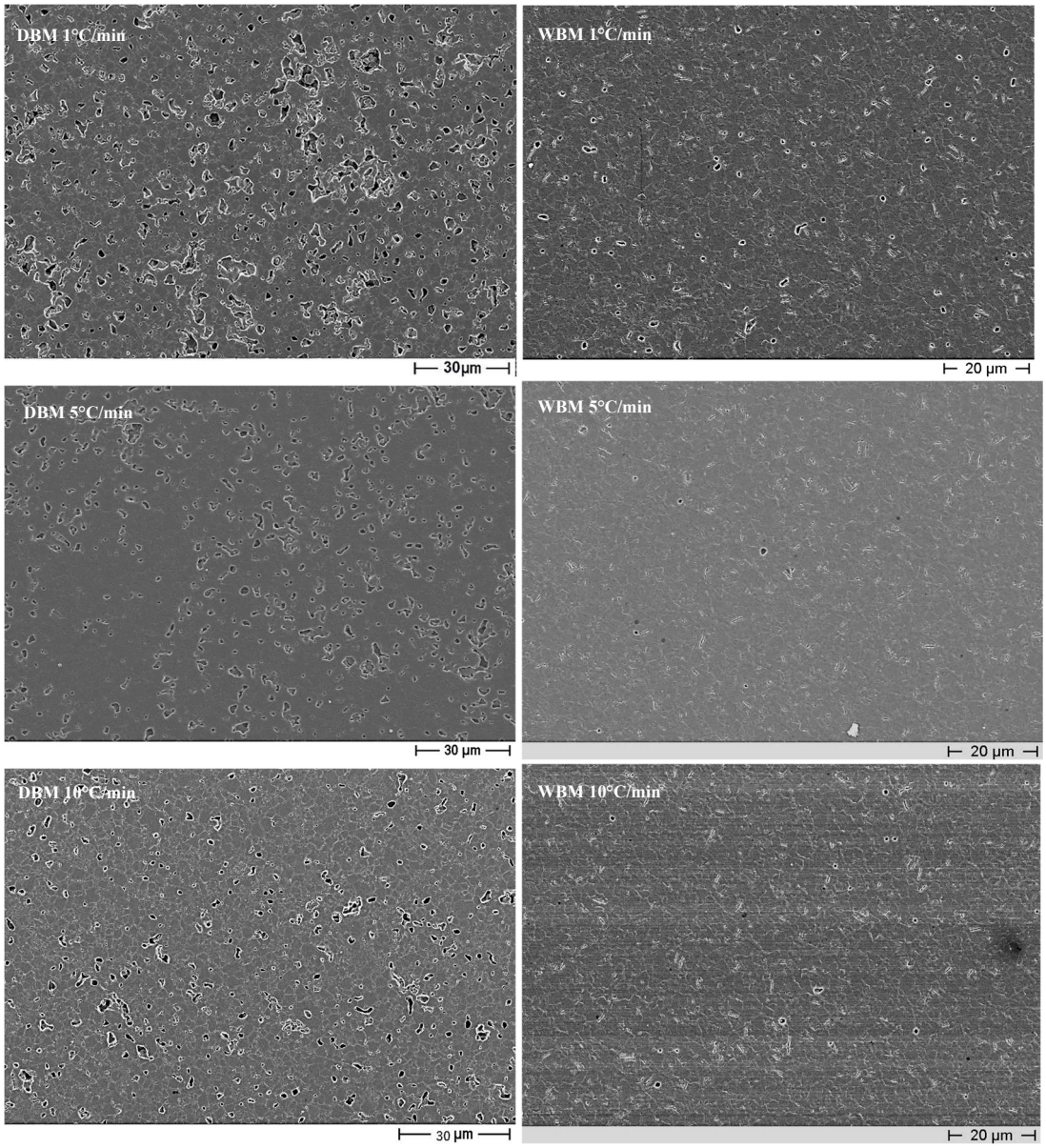

Figure 3-21: FESEM microstructures of the DBM and WBM samples submitted to dilatometry tests at 1300 °C/3h with different heating rates.

To better understand the densification state of the samples under each sintering conditions, the relative densities along with the sintering temperatures are plotted as a function of time in Figure 3-22. The densities were calculated from the real-time sample size data recorded by the device every minute of the tests and were determined regardless of the phase evaluation during the tests considering the TD of HA equal to 3.156 g/cm^3.

First, we can observe again that all DBM samples achieved moderate final densities, always lower than 85 %TD, meaning that the third sintering stage did not occur in these materials. On the opposite, final densities > 90 %TD were achieved for all WBM samples, these values being reached either in the heating (for 5 and 10 °C/min samples) or isothermal (for 1 °C/min) steps.

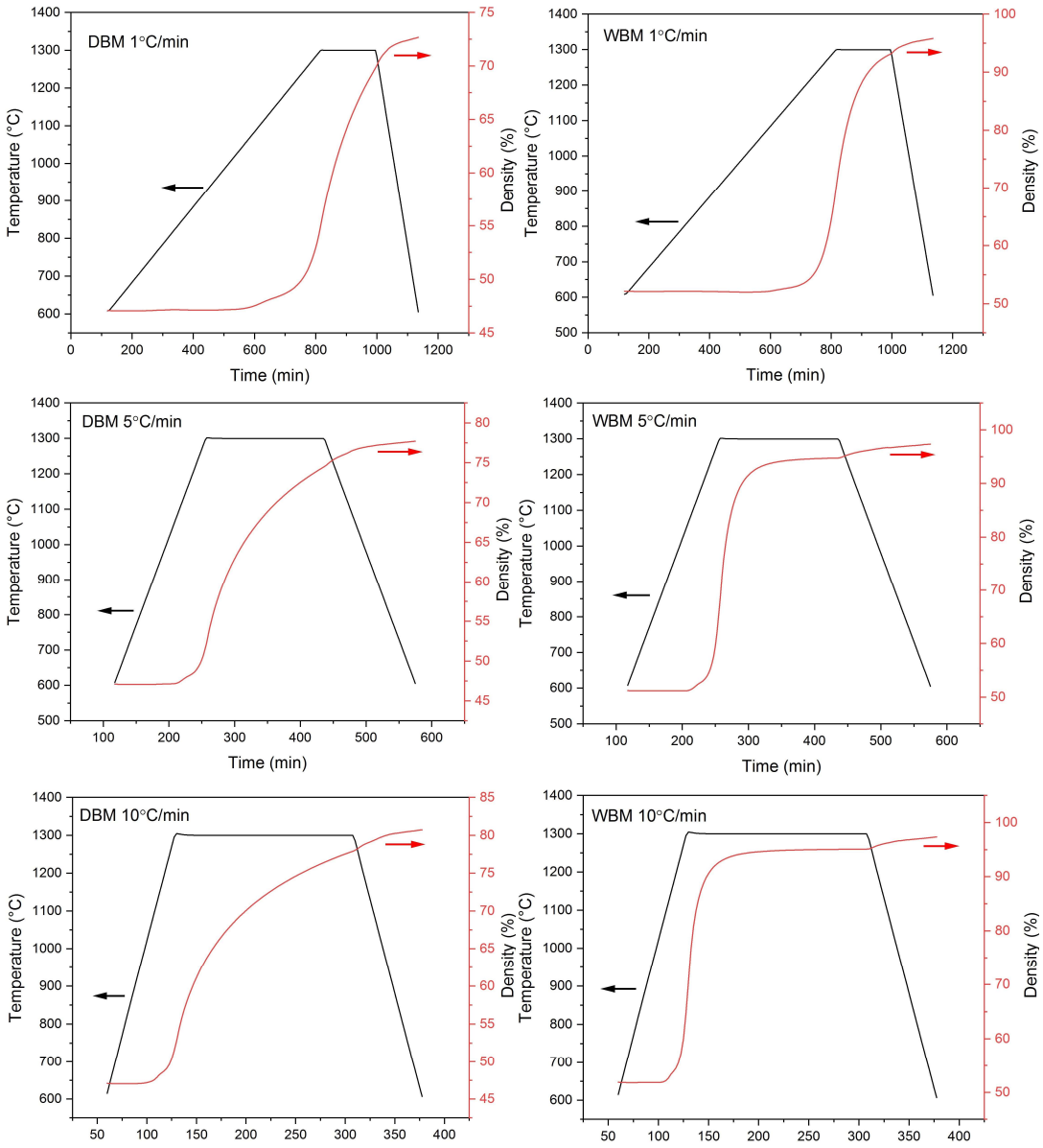

Figure 3-22: Temperature profile and densification curves as a function of time for DBM and WBM samples, heated at 1, 5 and 10 °C/min.

Second, as mentioned before, we can suppose that the highest sintering rate was achieved at the highest temperature (1300 °C), which corresponds to the beginning of the isothermal stage. Therefore, during isotherm, the densification rate decreases, as shown by the reduction of the slopes of the density curves. In a particular way, the densification curves correspond to WBM samples almost reached a plateau during the isothermal sintering stage, indicating almost complete densification of these samples.

As already mentioned, the second sintering stage, which provides a major contribution to the total sintering, continues until around 90 %TD [12, 33]. This criterion was used to calculate the densification rate of the second sintering stage during isothermal sintering at 1300 °C. While the reduction of the densification rate

during isothermal stage didn't follow a linear trend, to have a comprehensible comparison between tests, the slope of a line traversing two points was considered. In particular, lines starting at the beginning of the isotherm stage and finishing at the end of the densification were used for this calculation. Because the DBM samples didn't reach 90 %TD, the calculations for these samples were made on the density at the end of the isothermal stage. The results are presented in Table 3-5. It can be seen that, for both powder types, the densification rate increases significantly by increasing the heating rate. This effect is more pronounced for WBM samples where the densification rate obtained from the heating rate of 10 °C/min is almost 6 times the sample heated by 1 °C/min. Furthermore, at the same heating rates, the densification rates of the WBM samples were significantly higher than those of DBM samples. Conclusively, it can be seen that using WBM procedure to reduce the particle sizes in combination with higher heating rates, the sinterability of the as-received powder was improved near to 15 times, which can be very constructive in the designing of materials with high density and therefore high mechanical strength.

Table 3-5: Densification rate ($g.cm^3min^{-1}$) during isothermal sintering of DBM and WBM samples submitted to dilatometry test.

Sintering rate (°C/min)	1	5	10
DBM samples	2.56×10^{-3}	3.92×10^{-3}	4.45×10^{-3}
WBM samples	5.64×10^{-3}	20.61×10^{-3}	31.61×10^{-3}

The required time to reach full densification for each sintering test can be derived from the graphs of Figure 3-22. For WBM samples, this time can be easily taken from the corresponding graphs. However, for DBM samples, because their densification didn't finish in the test time, mathematical extrapolations were used. Cubic equations well fitted to the curves of Figure 3-22. Calculated times were presented in Table 3-6. It can be seen that to obtain almost full densification (i.e. 95 %TD) for DBM sample at 1300 °C heated at 1°C/min, which had the lowest sinterability, sintering must be conducted for more than 6 hours. In the case of DBM samples heated by 5 and 10 °C/min, the required time was more than 4 hours. On the other hand, for WBM samples, with heating rate of 1 °C/min full densification occured at 180 min, while for the samples heated at 5 and 10 °C/min this condition was achieved at 64 and 47 min respectively, suggesting that the sintering for 3 hours was deleterious, leading to oversintering.

Table 3-6: Required time for complete densification, min.

Sintering rate (°C/min)	1	5	10
DBM samples	384	272	244
WBM samples	180	64	47

The FESEM images of the final microstructures of different dilatometry tests are presented in Figure 3-23. Considering the mean particle size of 1.72 and 0.74 µm of the DBM and WBM powders, respectively, a significant grain coarsening in the microstructure of the WBM samples can be observed. This grain coarsening is the result of the third sintering stage, which corresponds to the grain boundary migration and elimination of smaller grains. Moreover, the samples oversintered at 1300 °C (heating rates of 5 and 10 °C/min) showed higher grain coarsening compared to sample heated at 1 °C/min.

The effect of heating rate can be recognized on DBM samples as well. It can be seen that the high heating rate of 10 °C/min led to more homogeneous grain size distribution compared to the heating rate of 1 °C/min, with a lower average grain

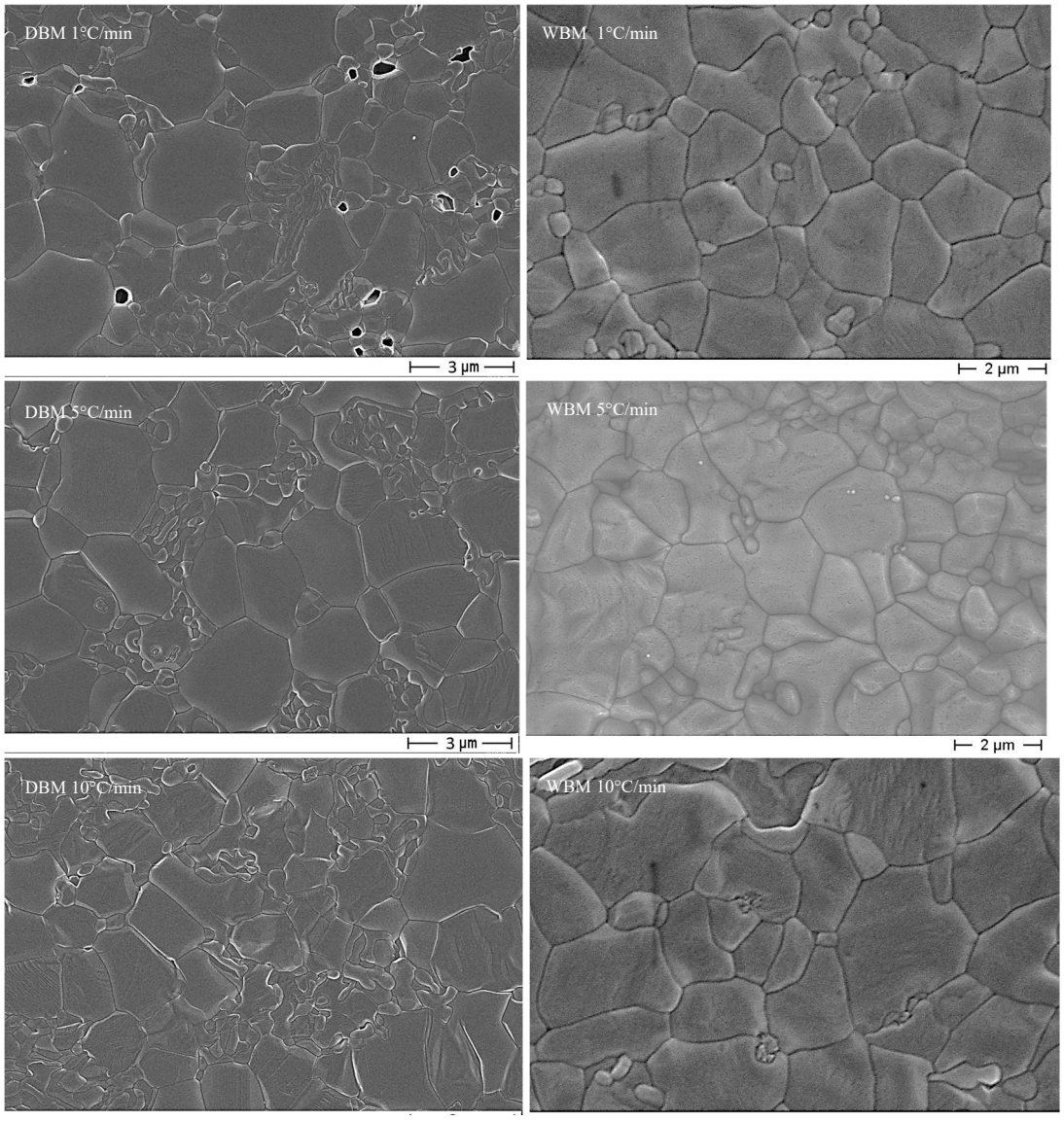

Figure 3-23: FESEM microstructures of DBM and WBM samples, submitted to dilatometry tests at 1300 °C/3h, at different heating rates.

size. A deeper investigation of the microstructural evolution as a function of starting particle size and the heating rate is presented in part 3.6.

3.5.1 Microstructure development in the sintering process

As discussed in the previous part, the dilatometry curves allow evidencing the temperatures related to the physical-microstructural-compositional changes of samples. These temperatures vary according to the initial powder's particle size and heating rate. To analyse the characteristics of the materials in these points, dilatometry tests were stopped to that temperatures, and the densification behaviour, microstructure and phase composition of the samples in each of these points were evaluated. For this study, we selected WBM gelcast samples, heated at 5 °C/min. The following temperatures were selected as representatives of specific features of the material:

- 1000 °C, as the temperature just before the onset sintering temperature
- 1132 °C, as the starting temperature of the TCP phase transformation
- 1200 °C as the temperature of the maximum rate of the TCP phase transformation
- 1250 °C as the temperature between the maximum phase transformation rate and isothermal sintering
- 1300 °C as the starting temperature of the isothermal sintering condition
- 1300 °C with 1 and 3 hours isothermal sintering as intermediate and the final sintering conditions.

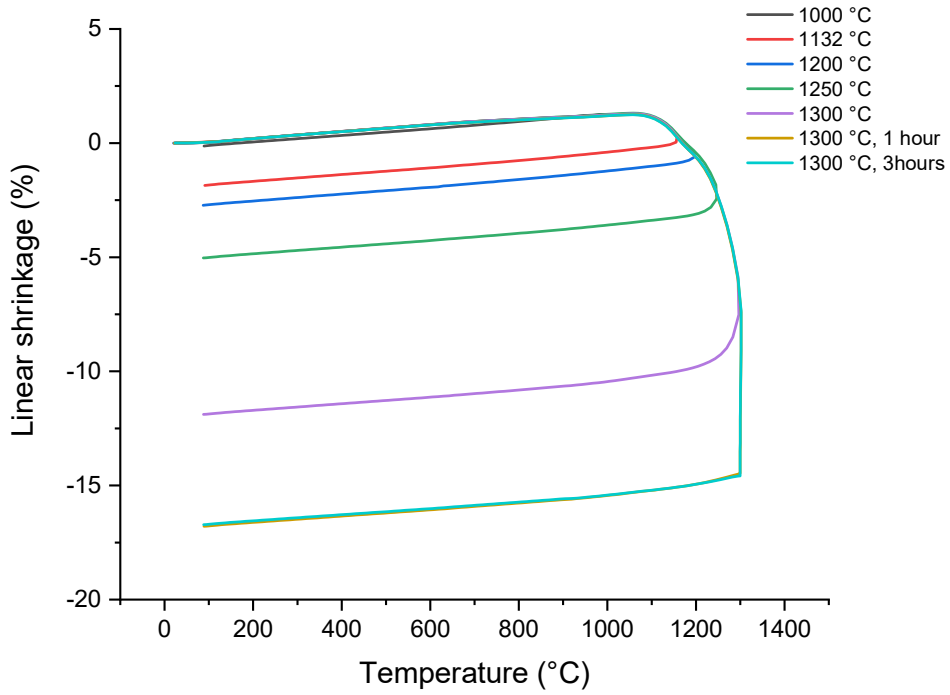

Figure 3-24: Dilatometry curves up to different temperatures for gelcast WBM samples.

Figure 3-24 displays the shrinkages as a function of temperature, obtained from the dilatometry tests, and Table 3-7 collects the corresponding densifications and phase compositions data. The superpositions of the dilatometry curves till selected temperatures prove the reproducibility of the data acquired. The amount of the β-TCP phase was calculated from X-ray diffraction analyses carried out on the fired samples (Figure 3-25), using the method described in section 2.2. The theoretical densities were calculated accounting the weight percentages of the β-TCP phase in the final materials.

Table 3-7: Linear shrinkage, density and the β-TCP phase amount of WBM samples submitted to dilatometry tests.

Thermal treatment	Final linear shrinkage (%)	Density (gr/cm^3)	Relative density (%)	β-TCP percentage (%)	TD (g/cm^3)
Green state	-	1.89	59.9	-	3.156
1000 °C	0.1	1.90	60.3	9.71	3.148
1132 °C	1.9	2.00	63.8	29.40	3.133
1200 °C	2.7	2.05	65.6	34.39	3.129
1250 °C	5.0	2.21	70.6	38.13	3.126
1300 °C	11.9	2.76	88.5	42.80	3.122
1300 °C – 1 hour	16.8	3.02	96.9	47.36	3.118
1300 °C - 3 hours	16.8	3.02	96.8	46.36	3.119

The X-ray diffractometry (XRD) patterns of the samples (Figure 3-25) showed that the phase compositions significantly changed during the sintering process. The phase transformations will be discussed in the following sections. However, it can be seen that the β-TCP phase fraction increased during the sintering process, both during the heating stage and the isothermal treatment at 1300 °C.

The FESEM micrographs of the fired samples are presented in Figure 3-26. It can be seen that at 1000 °C (Figure A), a few degrees Celsius less than the onset sintering temperature, the material showed a quite homogeneous compact structure, even if some particles agglomerates seem to be present due to necks formation, entrapping a certain porosity. The density of this material was closed to the green density.Using XRD data, the calculated β-TCP phase was ~10%, showing that the CD-HA to HA + TCP phase transformation already started at this temperature.

Dilatometry data corresponding to 1132 °C, i.e. the starting temperature of the β- to α-TCP phase transformation, exhibits very limited densification of about 2% with the relative density of 60.3 %TD. A significant amount of CD-HA to HA + TCP phase transformation, close to 30%, took place up to this temperature and reduced the TD of the final material to 3.133 g/cm^3. Compared to 1000 °C, the total volume of porosity was slightly reduced, and the particles agglomerates grew to bigger sizes. Nonetheless, the continuous network of porosity is still recognizable (Figure B).

The first evidence of densification appeared at 1200 °C as shown in Figure C. The adjacent particles attached each other providing irregularly shaped units,

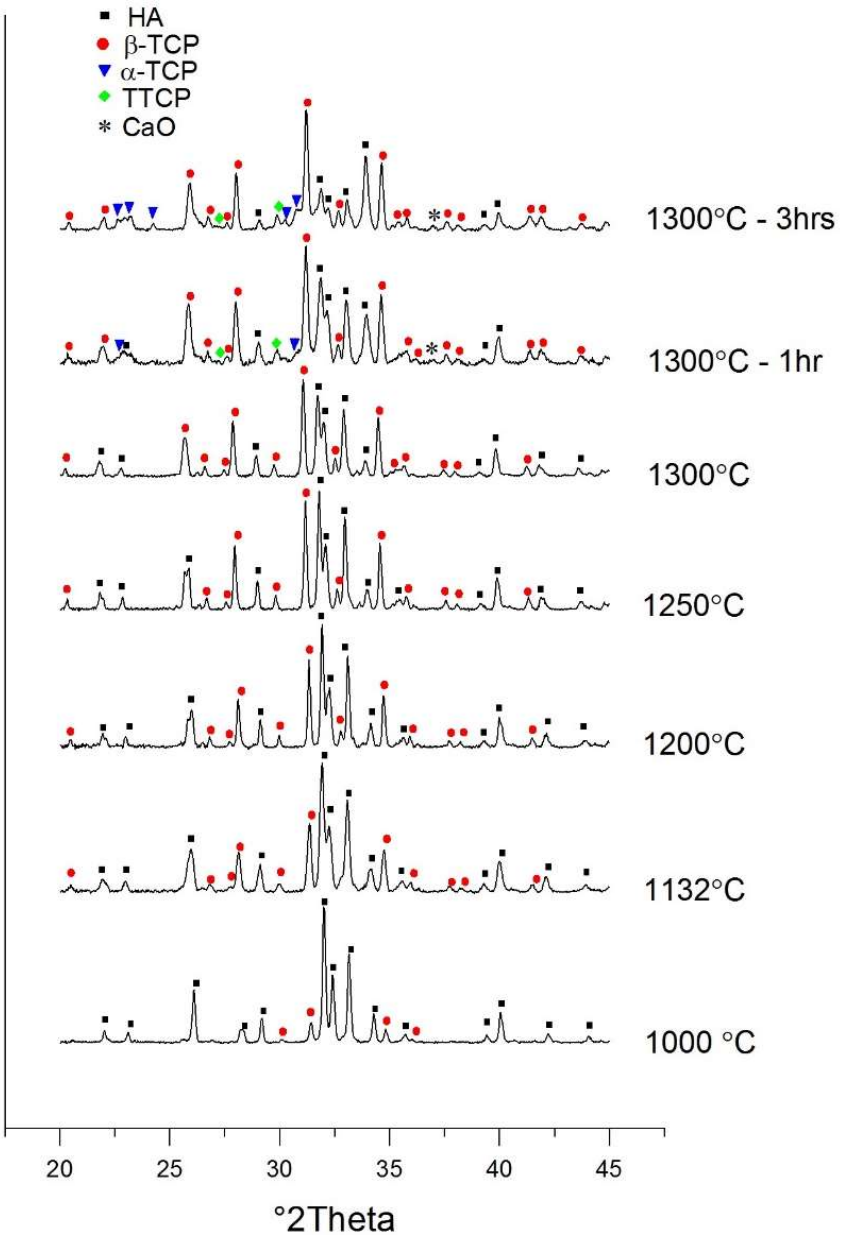

Figure 3-25: X-ray diffraction patterns of the samples after dilatometry tests.

surrounded by a continuous network of connected pores, typical to the materials sintered at the intermediate sintering stage. The XRD data showed a 5% increase of β-TCP fraction compared to the previous temperature. With 2.7% shrinkage, the final density was 65.6 %TD.

Image D shows that when the temperature reached 1250 °C, almost all of the ceramic particles participated in the densification process. The joining of the ceramic particles led to a continuous network of solid material. The pores shrank but remained as a continuous phase. However, no evidence of grain growth is visible, which is characteristic of the intermediate stage of sintering. The total shrinkage at this temperature was 5% and the density reached 76 %TD. The β-TCP phase contributed to more than 38% to the total phase composition.

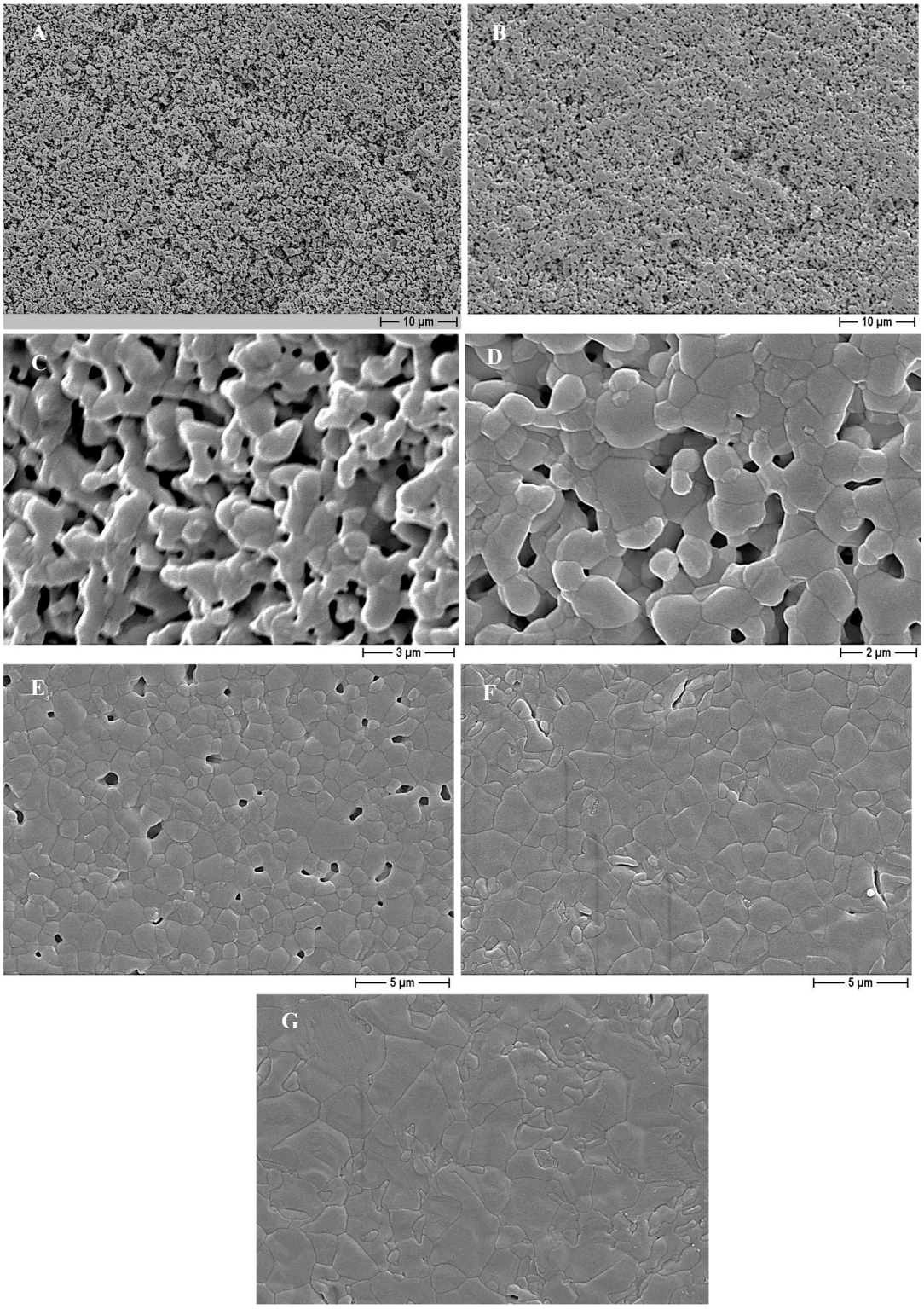

Figure 3-26: Microstructural evolution during sintering of WBM samples up to (A) 1000 °C, (B) 1132 °C, (C) 1200°C, (D) 1250 °C, (E) 1300°C, (F) 1300 °C for 1 hour, (G) 1300 °C for 3 hours.

The main feature of the 1300 °C-fired microstructure was the presence of isolated closed pores, as depicted in Figure E. The location of the pores, besides the achievement of 88.5 %TD indicated that the second sintering stage was almost

finished at this temperature. The linear shrinkage showed a quick increase to about 12%, and the amount of β-TCP reached 42.8%.

Isothermal sintering at 1300 °C for 1 and 3 hours led to the microstructures depicted in images F and G, respectively. It is clear that the grain boundary migration occurring during third sintering stage resulted in the elimination of the majority of the closed pores. By comparing total shrinkages and fired densities of the samples sintered for 1 and 3 hours, it can be stated that 1 h was sufficient to reach full densification. The dilatometry curve of the 3 hours sintering entirely over-wrote on the curve related to 1 hour sintering. For both tests, the final shrinkage was 16.8% and the fired density was around 97 %TD, allowing to classify these samples as dense materials. Microstructural observations allow stating that the prolonged sintering at 1300 °C led to uncontrolled grains coarsening, which is deleterious for mechanical properties.

The final amount of β-TCP was near to 47%, showing that at complete sintering, almost half of the HA phase was transformed to β-TCP, characterised by different biological and mechanical properties than HA [13, 30]. Because the sintering occurs at a temperature higher than the transformation temperature of CD-HA to HA + β-TCP, these phase transformations are inevitable. Therefore, it is reasonable to expect that the properties of the final material will be intermediate of those of the constituent phases.

3.6 Elaboration of dense samples

3.6.1 Effect of sintering heating rate on microstructural development

Sintering behaviour and final microstructure of HA ceramics are affected by starting particles size and sintering cycle parameters, these features having already been discussed and optimised in the previous paragraphs. However, there are also other phenomena such as several phase developments like dehydroxylation of the starting material and phase transformations such as CD-HA to HA and β-TCP and β- to α-TCP which influence the final microstructure. Therefore, a comprehensive study of the sintering behaviour and the microstructural evolution of HA samples, as a function of sintering rate and time, are reported in this section and the in next one respectively.

The effect of different heating rates on the microstructural evolution of HA bioceramic was evaluated by sintering of identical samples at the same sintering temperature of 1300 °C for 3 hours but with different heating rates of 1, 5 and 10 °C/min. The samples were produced from WBM HA-AR1 powder, characterised by a mean particle size of 0.74 μm. Three samples were used for each sintering cycle and the sintering cycles were same as the previous dilatometry tests but carried out in an conventional electrical resistance chamber furnace.

As already observed by the dilatometry tests, increasing the heating rates led to higher sinterability of the materials, either for DBM and WBM samples. The

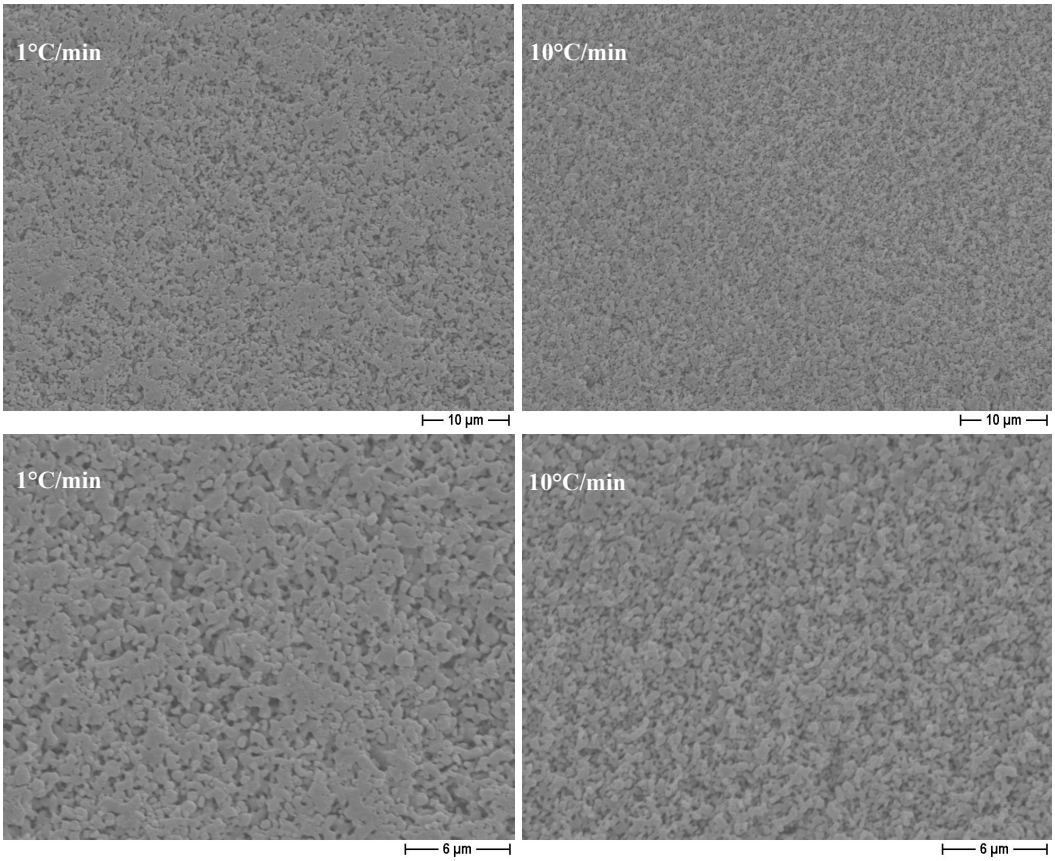

Figure 3-27: Effect of the heating rates on the microstructure of the HA samples heated to 1000 °C: 1 °C/min (left images) and 10 °C/min(right images).

improved sinterability was attributed to less important particles sticking during the first sintering stage, thus inducing less reduction of the material's specific surface area. Figure 3-27 shows the microstructure of HA samples after heating to 1000 °C (the temperature just before the onset of the second sintering stage) heated at 1 and 10 °C/min at two different magnifications. While the sample heated at the higher heating rate was entirely characterised by isolated particles, the sample heated at the lower rate was composed of joined particles forming big clusters, and entrapping large pores. Reduced particles joining leaves higher specific surface area, which favours atomic diffusion in volume and through grain boundaries during the second sintering stage, the main contributor to the densification. The formation of particle clusters, due to particles joinings, was also reported as one of the main reasons for the inhomogeneous final microstructure of sintered HA bioceramics [33, 35].

Table 3-8 collects the main density data of the samples sintered at 1300 °C for 3h, at different heating rates. The samples dimensions were measured by a digital calliper, and the densities were calculated based on the Archimedes' method using the following formula:

$$Density\ (Archimedes) = \frac{wt(air)}{wt(air)-wt(water)} \times \rho(water)$$ Equation 3-1

where *wt(air)* and *wt(water)* are weights of the sample in the air as immersed in water, respectively, and *ρ(water)* is the water density at the test temperature. The relative densities were calculated considering the relative amounts of HA and β-TCP phase in the final materials. The results showed a good agreement with the results obtained from the dilatometry tests on WBM samples. The β-TCP phase amount in the final ceramics was almost the same, except for the material sintered at the highest heating rate, which showed a slightly higher β-TCP than the other ones. Linear shrinkages in any dimension of samples were calculated according to the following formula:

$$d = \frac{l_{green}-l_{sintered}}{l_{gren}}$$ Equation 3-2

where l_{green} and $l_{sintered}$ are a particular dimension of a sample in green and sintered states, respectively. The reported shrinkage is the average of two shrinkages of the height and the diameter of the samples.

Table 3-8: Effect of the heating rates on the physical and compositional properties of WBM samples.

Heating rate (°C/min)	Green density (g/cm³)	Final density (g/cm³)	Shrinkage (%)	β-TCP (%)	Relative density (%)
1	1.70 ± 0.01	3.00 ± 0.00	17.98 ± 0.46	25.6	95.7 ± 0.1
5	1.70 ± 0.01	3.05 ± 0.00	18.15 ± 0.52	25.8	97.3 ± 0.0
10	1.70 ± 0.01	3.04 ± 0.00	18.11 ± 0.43	27.0	97.0 ± 0.0

The FESEM images of the sintered microstructures are shown in Figure 3-28. It can be seen that all three final microstructures were highly dense and characterised by similar microstructural features. However, to highlight the effect of the different heating rates on the grain size distribution, image analysis was carried out using ImageJ image processing software and the mean diameter of at least 800 grains was measured for each sample. The results in terms of histograms, showing both number and volume distributions of the grain size, are illustrated in Figure 3-29. The volumetric distributions were calculated assuming that the grains hold spherical shapes and using the sphere volume formula $V = {}^{4}/_{3}\pi r^{3}$, where V and r are volume and radius of sphere, respectively. D-values (D_{10}, D_{50} and D_{90}) derived from the cumulative distributions (not shown) are also listed in Table 3-9. It can be seen that regardless of the heating rates, the grain sizes were distributed in a similar range for all of the samples. However, the increased number of bigger grains with increasing the heating rate is noticeable. It can be seen that, while the grains sizes measurements show an almost monomodal distribution for the sample sintered at 1 °C/min, this distribution is not mono modal for the other two samples. The modal distribution of the grain size for the samples sintered at 5 and 10 °C/min demonstrates the abnormal grain growth for these samples. Because the second

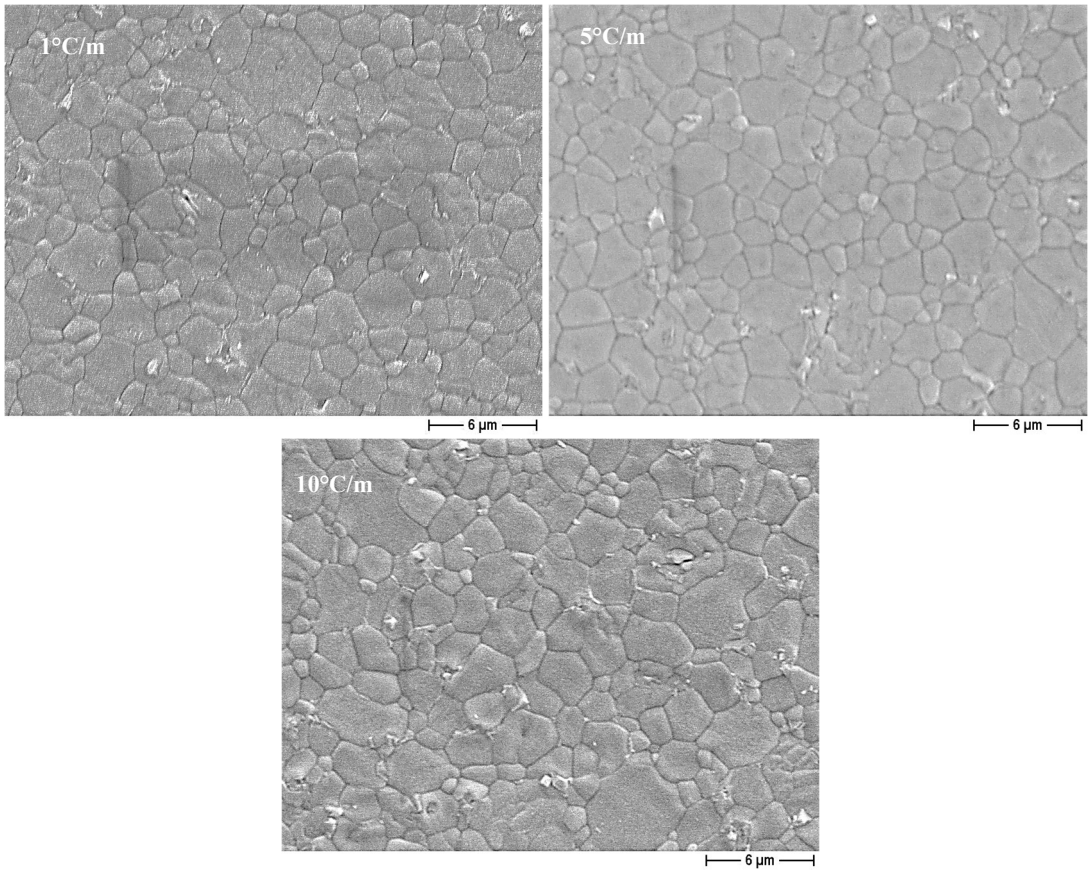

Figure 3-28: Microstructure of WBM samples sintered at different heating rates.

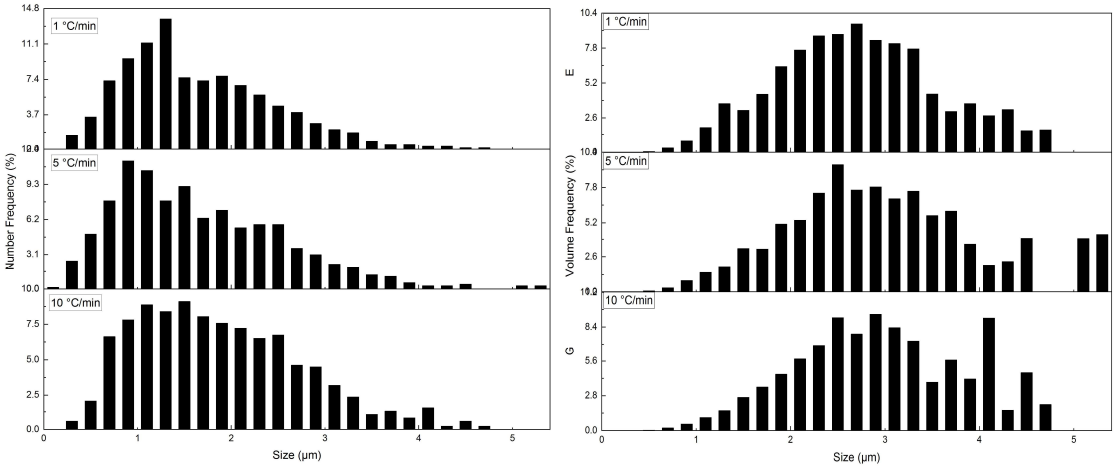

Figure 3-29: Number and volume distribution of the grains in the final microstructure of WBM samples sintered at different heating rates.

sintering stage finished earlier at higher heating rates, the grain growth can be attributed to the grain boundary diffusion (i.e. the sintering mechanism active in the third sintering stage), which relatively had more time to occur. Considering that the

initial ceramic powders (WBM HA-AR1) also showed monomodal distribution, it can be assumed that despite the other samples, during sintering at the heating rate of 1 °C/min all of the particles experienced regular coarsening.

Table 3-9: D_{10}, D_{50} and D_{90} values, from number and volume distributions of the grains in the final microstructure of WBM samples sintered at different heating rates.

Heating rate (°C/min)	Number distribution (µm)			Volume distribution (µm)		
	D_{10}	D_{50}	D_{90}	D_{10}	D_{50}	D_{90}
1	0.63	1.42	2.69	1.52	2.59	3.79
5	0.54	1.42	2.85	1.65	2.82	4.47
10	0.72	1.66	3.01	1.72	2.85	4.13

3.6.2 Effect of sintering time on microstructural development

The effect of different sintering times on the microstructural evolution of HA bioceramics was evaluated by sintering identical WBM samples produced from both HA-AR1 and HA-AR2 powder batches, characterised by similar but not identical particle size. Sintering were carried out at 1300 °C, for 0 (no isotherm), 1, 2 and 3 hours. The heating rate in all of the tests were 5 °C/min. Three samples were tested for each sintering time and the mean particle sizes of the initial powders were 0.83 and 0.63 µm for the samples produced from HA-AR1 and HA-AR2, respectively.

The results obtained after sintering are presented in Tables 3-10 and 3-11 for HA-AR1 and HA-AR2 samples, respectively. In general, an increase in the final density by increasing the isothermal time is noticeable. The linear shrinkages of HA-AR2 samples were always higher compared to HA-AR1 ones, as expected on the basis of the lower mean particle size. The relative density of HA-AR2 sample sintered at 1300 °C with no isothermal stage was more than 90 %TD. Under the same condition, HA-AR1 sample achieved a relative density of 86.5 %TD, underlying the higher reactivity of the sample made from the finer particles. The corresponding microstructures are depicted in Figure 3-30. The images show that

Table 3-10: Effect of the different sintering times on the physical and compositional features of WBM samples produced from HA-AR1 powder.

Isothermal time (h)	Green density (g/cm^3)	Final density (g/cm^3)	Shrinkage (%)	β-TCP (%)	Relative density (%)
No isotherm	1.69 ± 0.01	2.71 ± 0.01	15.35 ± 0.22	31.15	86.5 ± 0.8
1	1.69 ± 0.01	2.95 ± 0.02	17.67 ± 0.38	30.70	94.2 ± 0.6
2	1.69 ± 0.01	3.03 ± 0.00	18.46 ± 0.50	32.97	96.8 ± 0.0
3	1.69 ± 0.01	3.04 ± 0.02	18.52 ± 0.32	33.75	97.1 ± 0.6

Table 3-11: Effect of the different sintering times on the physical and compositional features of WBM samples produced from HA-AR2 powder.

Isothermal time (h)	Green density (g/cm^3)	Final density (g/cm^3)	Shrinkage (%)	β-TCP (%)	Relative density (%)
No isotherm	1.60 ± 0.01	2.83 ± 0.02	17.26 ± 0.39	40.88	90.6 ±
1	1.60 ± 0.01	2.98 ± 0.02	18.53 ± 0.15	48.94	95.6 ± 0.8
2	1.60 ± 0.01	3.04 ± 0.01	19.24 ± 0.08	55.25	97.7 ± 0.3
3	1.60 ± 0.01	3.01 ± 0.01	18.95 ± 0.29	58.74	96.8 ± 0.5

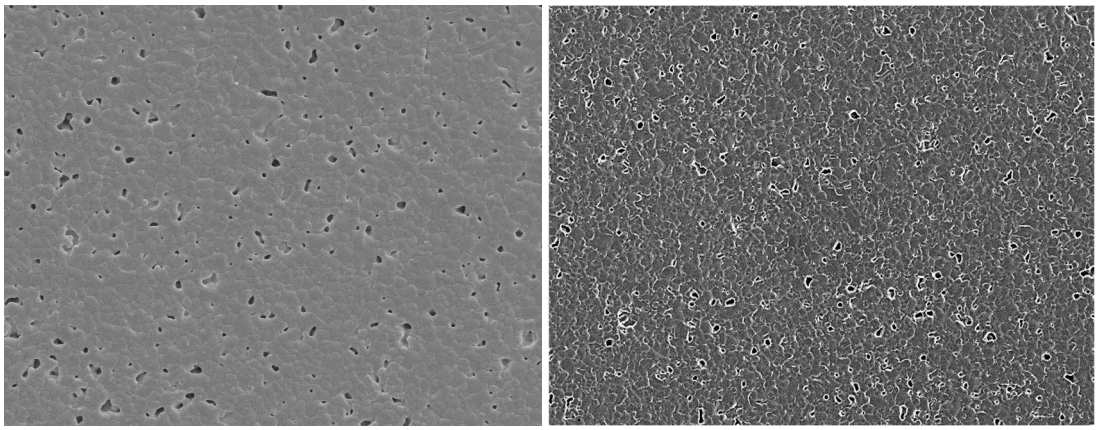

Figure 3-30: FESEM microstructure of the samples obtained from HA-AR1 (left) and HA-AR2 (right) sintered at 1300 °C, without the isothermal stage.

pores were less in number and smaller sizes for the HA-AR2 sample, indicating the completion of the second sintering stage for this powder, independently of the isotherm time at 1300 °C.

While the density of the HA-AR1 samples progressively increased by increasing the sintering time, for the HA-AR2 samples, the density increased up to 2 hours, and then slightly decreased for a longer sintering time. This density reduction can be attributed to the microstructural changes resulting from over sintering. Ben Ayed et al. [36] observed the formation of intra-granular porosities induced from over-sintering. In addition, dehydroxylation of HA phase and water vapour production during decomposition of CD-HA to HA and β-TCP may also contribute to the density reduction [37].

FESEM images of the sintered microstructures are presented in Figures 3-31 and 3-32 for the HA-AR1 and HA-AR2 samples, respectively. HA-AR1 samples exhibited homogenous microstructure composed of relatively equiaxed grains. The grains sizes continuously increased with increasing the sintering time so that the 3-hours sintered sample was characterised by the biggest grains. On the other hand, the sintered microstructures of the HA-AR2 samples seemed unbalanced and unsteady. The microstructure after 1-hour sintering showed inhomogeneously distributed grains, with a large size distribution. Coarser grains with a complex morphology are attributed to the lower Ca/P ratio of ceramics made from HA-AR2 powders (see 2.1) [38]. It can be seen that by increasing the sintering time, a significant microstructural change occurred, giving rise to a bimodal grain size distribution characterised by some large grains surrounded by plenty of smaller grains, as we can see in the sample sintered at 1300°C for 3h.

The number and volume distributions of grain sizes are presented in Figures 3-33 and 3-34, and the corresponding D-values are collected in Tables 3-12 and 3-13 for HA-AR1 and HA-AR2 samples, respectively. In both cases, sintering to 1300 °C without the isothermal stage, resulted in the normal distribution of the grain

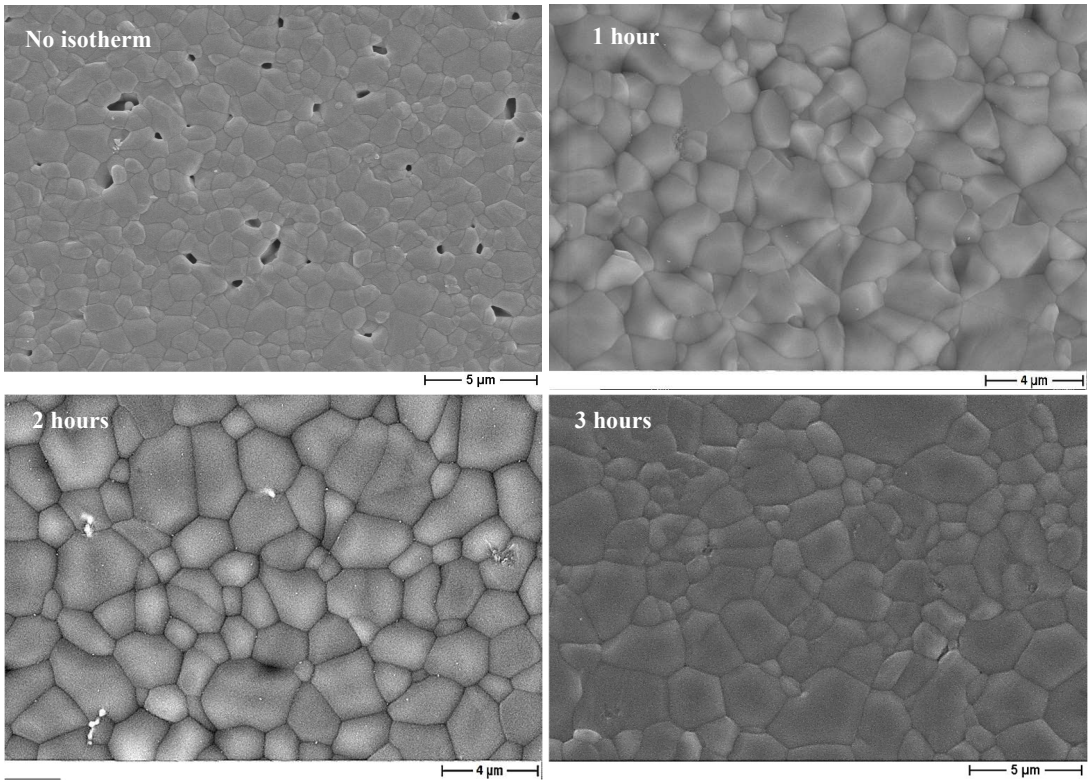

Figure 3-31: Microstructures of HA-AR1samples sintered at 1300 °C for different times.

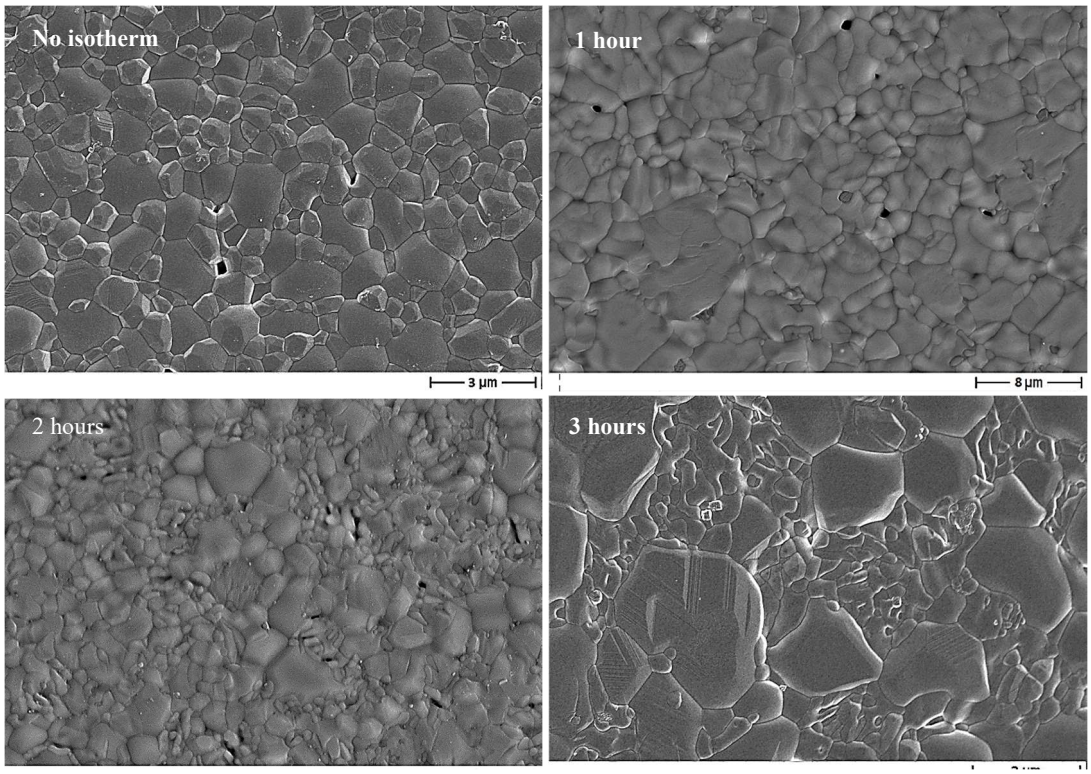

Figure 3-32: Microstructure of HA-AR2 samples sintered at 1300 °C for different times.

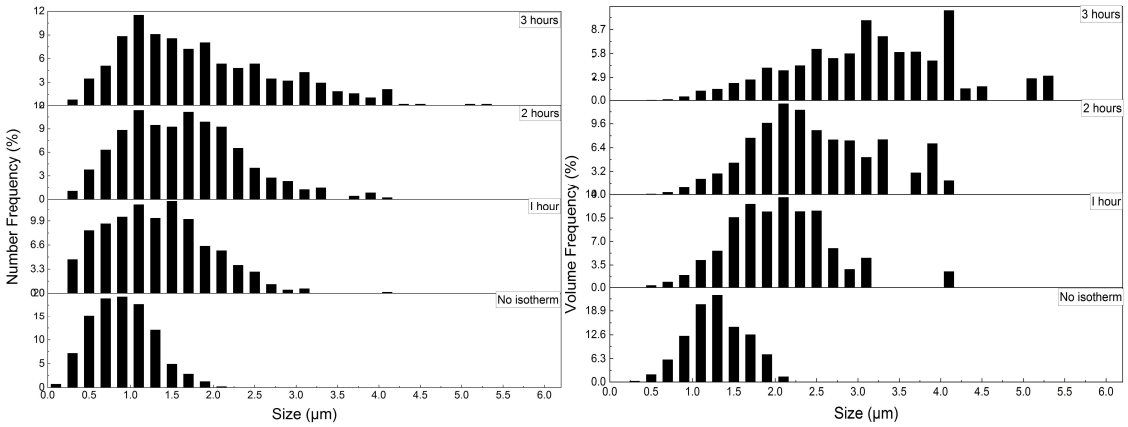

Figure 3-33: Number and volume distribution of the grain size in HA-AR1 sintered microstructures.

Table 3-12: D_{10}, D_{50} and D_{90} values, from number and volume distributions of the grain sizes in HA-AR1 sintered microstructures.

Isothermal time (h)	Number distribution (µm)			Volume distribution (µm)		
	D_{10}	D_{50}	D_{90}	D_{10}	D_{50}	D_{90}
No isotherm	0.33	0.78	1.29	0.74	1.18	1.66
1	0.44	1.18	2.06	1.20	1.92	2.71
2	0.66	1.47	2.47	1.43	2.30	3.54
3	0.67	1.59	3.20	1.78	3.18	5.07

sizes, similar to initial powder's particles sizes. The volumetric mean grain sizes are 1.18 and 0.91 µm, comparable to mean particle sizes of 0.83 and 0.63 µm of the starting WBM powders from HA-AR1 and HA-AR2 batches, respectively, meaning a moderate and regular grain growth during sintering, and no uneven particle coarsening due to the last sintering stages. However, when isothermal steps were performed, the grain growth was no more homogenous, with the appearance of larger size distribution grains. Below 90 %TD, the second sintering stage prevails, and boundary dragging by the open pores prevents the grain growth. In

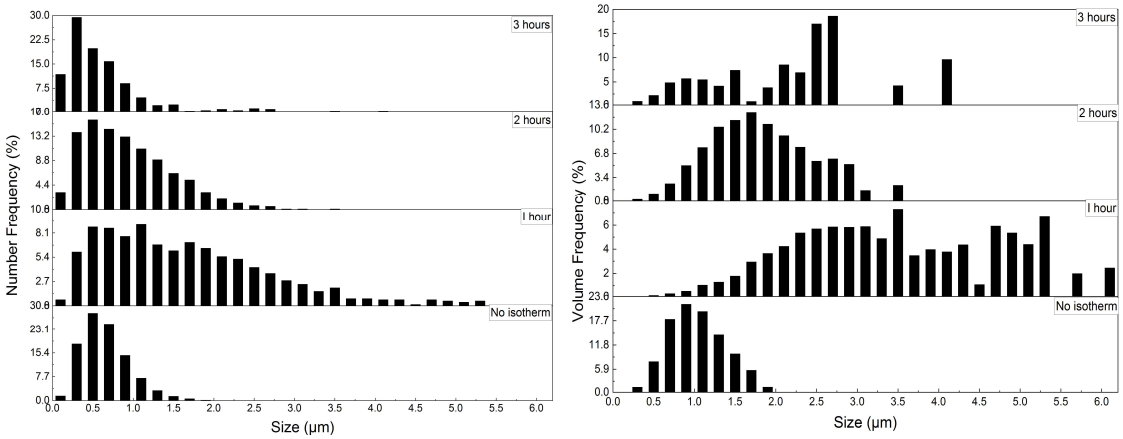

Figure 3-34: Number and volume distribution of the grain size in HA-AR2 sintered microstructures.

Table 3-13: D_{10}, D_{50} and D_{90} values, from number and volume distributions of the grain sizes in HA-AR2 sintered microstructures.

Isothermal time (h)	Number distribution (µm)			Volume distribution (µm)		
	D_{10}	D_{50}	D_{90}	D_{10}	D_{50}	D_{90}
No isotherm	0.22	0.51	0.95	0.51	0.91	1.43
1	0.36	1.37	3.02	1.81	3.32	5.19
2	0.20	0.74	1.61	0.93	1.69	2.66
3	0.09	0.37	1.09	0.79	2.21	3.80

contrast, the collapse of open pores in the last stage leads to an abrupt grain growth above 90 %TD [33].

For the HA-AR1 samples, grain sizes were increased by isothermal sintering time. The longer the isothermal sintering, the larger the final grains. The narrow, monomodal distribution shifted towards a larger distribution. The evolution of the D-values, obtained from the number distribution curve of the grain sizes, is presented in Figure 3-35. It can be seen that with increasing the sintering time, the bigger grains (i.e., the curve corresponding to D_{90} values) grew faster than the smaller grains (D_{10} and D_{50} trends). The bigger the grains, the higher the growth rate. This difference in the growth rate explains the increasing difference in the size between small and large grains by increasing the sintering time.

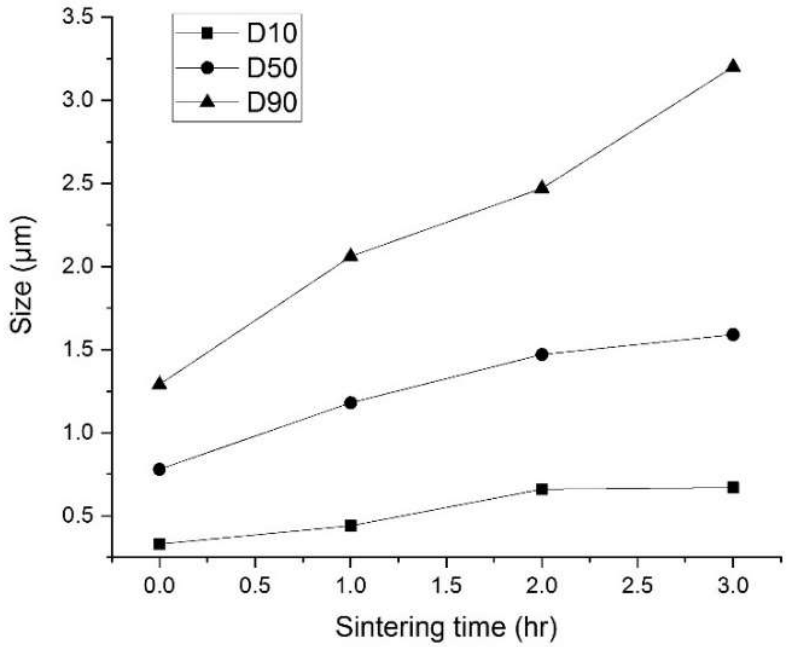

Figure 3-35: Evolution of D-values, obtained from the number grain size distribution, for HA-AR1 samples.

In the case of HA-AR2 samples, as already shown in the microstructural images, the grain size evolution followed a different path (Figure 3-36). In these samples, after 1-hour sintering, grain growth occurred by a very high rate. The

microstructure was characterised by a large range of grains sizes, and the mean grain size values were, at the same sintering time, almost two times those of the HA-AR1 samples. As already mentioned, the Ca/P ratio of HA-AR2 was lower than HA-AR1 which led to a higher grain coarsening, as explained in 1.4 [35]. However, after this period, for each additional sintering hour, the average grain size almost halved, moving from 1.37 µm to 0.74 µm after 2 hours sintering, and from 0.74 µm to 0.37 µm after 3 hours sintering. From Figure 3-36, we can observe that, again, the larger grains experienced more severe size changes. Because the grain growth is inevitable during sintering, the reduction of the grain sizes suggested that other microstructural evolutions occurred in HA-AR2 sample, which caused large grains to evolve into smaller ones.

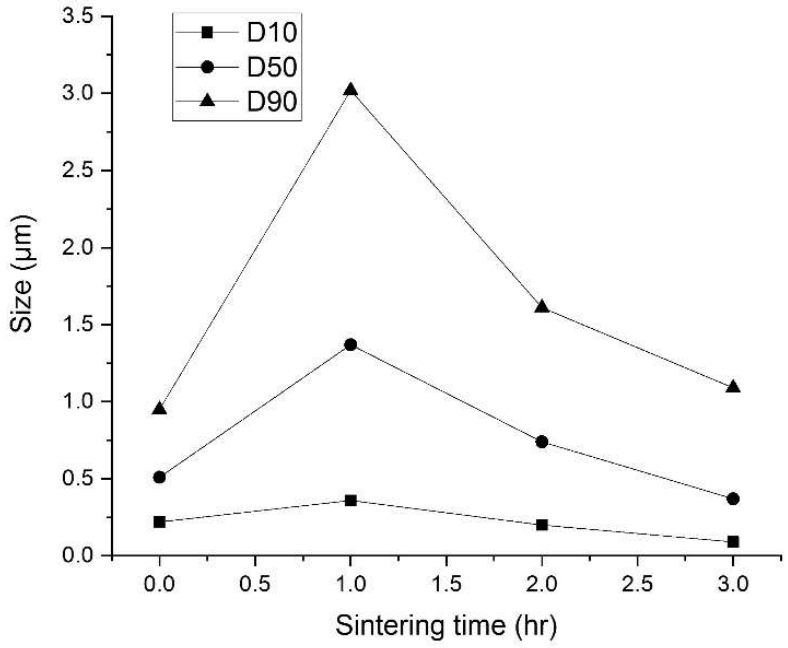

Figure 3-36: Evolution of D-values, obtained from the number grain size distribution, for HA-AR2 samples.

XRD analyses showed that, unlike the HA-AR1 samples, for the HA-AR2 samples the contribution of the β-TCP phase in the final material increased with sintering time (see data collected inTables 3-10 and 3-11). The β-TCP phase fraction rose from 40% at the beginning of the isothermal stage to around 60% after 3 hours sintering. This increase in the β-TCP phase fraction can be attributed to two different phase transformations occurring at high temperatures: CD-HA to HA and β-TCP and, HA to tetracalcium phosphate (TTCP) and α-TCP. As already discussed in 2.3 for the calcination of HA-AR2, the former starts from 1000 °C and the latter from 1300 °C. Upon cooling, the allotropic transformation of α- to β-TCP takes place. Therefore, in the final material, the β-TCP phase fraction was the sum of β-TCP from CD-HA transformation and β-TCP resulting from the allotropic transformation of α-to β-TCP.

To better understand the material's phase and microstructural evolutions during sintering, Energy-dispersive X-ray spectroscopy (EDX) analyses were carried out on the 3-hours sintered sample of HA-AR2, targeting big and small grains (Figure 3-37). The results were presented in

Table 3-14. The difference between the Ca/P ratios is noticeable. The Ca/P ratio close to 1.5 suggested that the big grains composed of TCP, while the Ca/P ratio of 2 suggested that the small grains were TTCP. Because TTCP originates from HA transformation at 1300 °C, it is reasonable to assume that the reduction of the grain size occurred because of the nucleation and growth of the new TTCP crystals from HA, according to the following equation:

$$HA(Ca_{10}(PO_4)_6(OH)_2 \xrightarrow{>13\ ^{\circ}C} TTCP(Ca_4(PO_4)_2O) + \alpha - TCP(Ca_3(PO_4)_2) + H_2O \qquad \text{Equation 3-3}$$

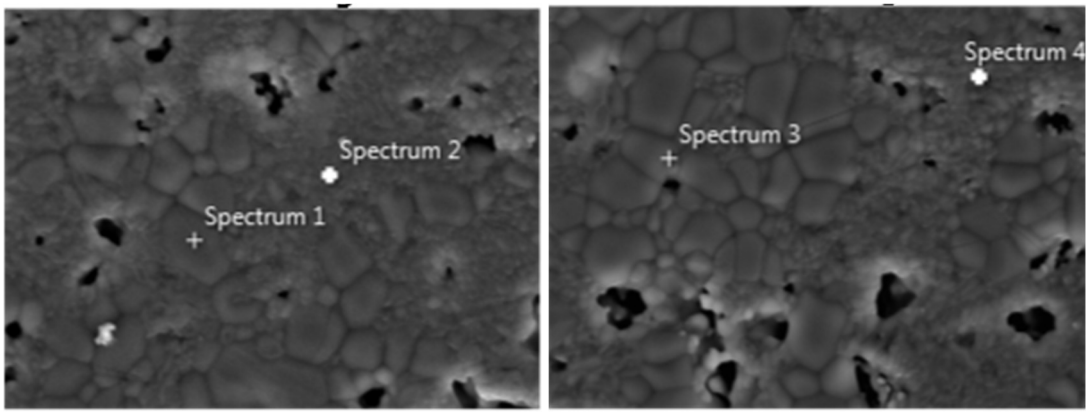

Figure 3-37: EDX spots on the small and coarse grains. Spectra 1 and 3 correspond to large grains, spectra 2 and 4 correspond to small grains.

Table 3-14: Results of EDX analyses carried out on big and small grains of HA-AR2 sample sintered at 1300 °C for 3 hours. The values are expressed as at%.

	Big grains	Small grains
Ca	23.73	25.41
P	15.60	12.39
O	59.09	57.99
Si	0.38	3.27
Mg	0.81	0.42
Al	-	0.52
Ca/P ratio	1.52	2.05

The decomposition of HA to TTCP has already been reported in several previous works [39,40,41,42,43,44,45,46] especially in the papers dealing with the plasma-sprayed HA coatings on titanium substrates where the high cooling rate of the molten HA particles deposited on the cold metal preserves the TTCP in the material and prevents its decomposition during the cooling stage. TTCP is considered as an undesired phase in these processes [42,43] and it is claimed to be catalysed by titanium [44]. Wang and Chaki [45] reported the decomposition of HA to TCP and TTCP by increasing the sintering temperature to more than 1150 °C. Zhou et al. [46] found TTCP as a product of HA decomposition thermally treated

to 1450 °C. It seems that the stated phase transformation also took part in the reduction of the final densities of the samples made from HA-AR2 due to the formation of water molecules which trapped between grains and led to intergranular voids .

The TTCP phase transforms to HA and CaO during the cooling process according to the following reaction:

$$TTCP(Ca_4(PO_4)_2O + H_2O \rightarrow HA(Ca_{10}(PO_4)_6(OH)_2) + CaO \qquad \text{Equation 3-4}$$

Therefore, it can be said that at the sintering temperature, the material was composed of HA, TTCP and α-TCP. But after cooling, the TTCP phase converted to HA and CaO, and α-TCP to β-TCP. However, it must be considered that all of these phase transformations are thermodynamic reactions and in practice, they are affected by experimental conditions and therefore could be incomplete. Furthermore, the transformation of TTCP to HA and CaO needs moisture to occur, whose presence in dense structure could be very low and not sufficient to allow a complete reaction. Therefore, it is reasonable to observe also TTCP and α-TCP phases in the final material [47].

XRD patterns of the sintered samples are presented in Figures 3-38 and 3-39 for the HA-AR1 and HA-AR2 samples, respectively. Characteristic peaks of TTCP and CaO phases as traces were identified by ICDD file numbers 25-1137 and 37-1497 for indexing of TTCP and CaO phases, respectively. Because of the close similarity of the structure of TTCP to the structure and lattice parameters of HA [42], its X-ray intensities are very similar to HA.

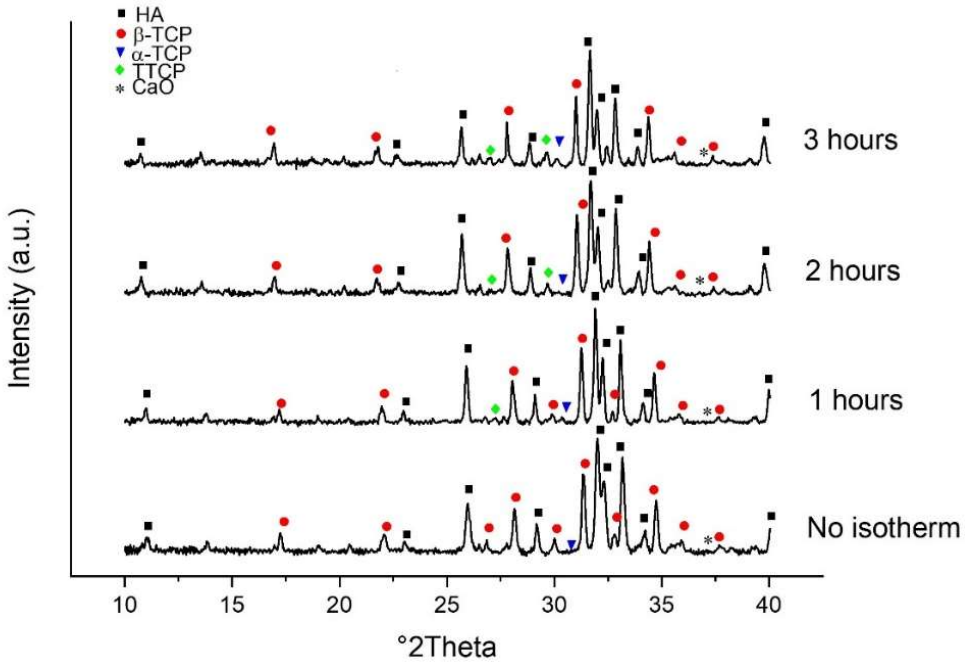

Figure 3-38: X-Ray diffraction patterns of HA-AR1 sintered samples.

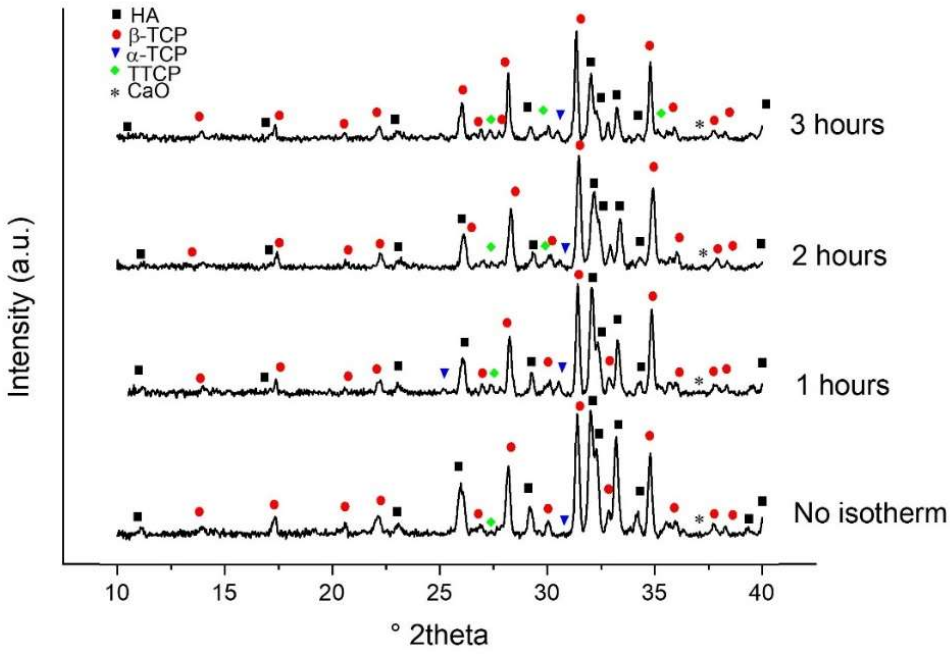

Figure 3-39: X-Ray diffraction patterns of HA-AR2 sintered samples.

The phase identification showed that except the samples sintered without the isothermal stage, all other samples were composed of CaO and four different phases belong to CaP family including HA, β-TCP, α-TCP and TTCP. Sintering without isothermal treatment showed that while the HA-AR1 sample contained CaO in its composition, the HA-AR2 sample held TTCP. The transformation of TTCP to HA without the formation of CaO at temperatures below 500 °C was also reported in the literature [48]. The intensities of the characteristic peaks of TTCP phase increased with increasing the sintering time for both types of powders, pointing an increase of TTCP phase in the final material. However, while β-TCP to HA ratio was almost constant for the HA-AR1 samples, this ratio increased with increasing the isothermal sintering time for the HA-AR2 samples (Tables 3-10 and 3-11) as a result of the excessive phase transformation of HA to TTCP + TCP. Detection of TTCP in the final microstructure, as demonstrated by EDX analyses performed on the small grains, showed that the reverse phase transformation of TTCP to HA was not completed for at least some part of the samples. The presence of the characteristic peak of CaO in the XRD patterns may prove the occurrence of this transformation. However, it must be considered that CaO can also be a by-product of CD-HA to HA+β-TCP phase transformation [49,50]. As stated in chapter 1, CaO can cause microstructural decohesion and strength decrease due to the volume changes arriving from CaO transformation to $Ca(OH)_2$ and then $CaCO_3$ [51].

3.6.3 Sintering of the dense samples

3.6.3.1 Samples obtained from DBM powders

Sintering of the gelcast samples produced from DBM powder was conducted at 1300 °C for 3 hours, using heating rate of 10 °C/min, in an atmospheric furnace. Such sintering conditions were selected on the basis of the results discussed in the previous sections. For this study, both HA-AR1 and HA-AR2 batches were used. For the sake of clarity, it is here recalled that the as-received powders were characterised by a similar particles size, being HA-AR2 slightly finer (D_{50} of about 2.5 µm, see 2.1) than HA-AR1 (D_{50} of about 2.95 µm). After DBM, the powders achieved similar particle size, in the range 1.6-1.8 and 1.6-1.7 µm for HA-AR1 and HA-AR2, as given in Table 3-15. Cylindrical samples, with the diameters in the range of 12 to 15 mm and the heights in the range of 22 to 29 mm, kept their regular shapes after sintering without any distortion. As already mentioned, dimensions were measured by digital calliper, while density was calculated by the Archimedes' method. The TD of each sample, that was used to determine the relative density, was calculated considering the relative amounts of HA and β-TCP phases in the final material. β-TCP phase fractions were calculated using the XRD data of each sample based on the method described in section 2.2. All this information are collected in Table 3-15.

Table 3-15: Physical and densification data of DBM samples produced from HA-AR1 and HA-AR2 powders.

Batch designation	Powder batch	Mean particle size (µm)	green density (g/cm^3)	Linear shrinkage (%)	Relative density (%)
D1-A	HA-AR1	1.63	1.66 ± 0.01	13.63 ± 0.65	82.6 ± 0.1
D1-B		1.64	1.67 ± 0.00	13.47 ± 1.08	82.2 ± 0.0
D1-C		1.68	1.69 ± 0.00	13.10 ± 0.84	84.2 ± 0.1
D1-D		1.79	1.78 ± 0.01	11.35 ± 0.91	80.0 ± 0.8
D1-E		1.79	1.71 ± 0.01	11.12 ± 0.12	76.5 ± 0.5
D1-F		1.70	1.70 ± 0.01	11.70 ± 0.38	77.8 ± 0.6
D1-G		1.71	1.66 ± 0.01	11.53 ± 0.63	76.4 ± 0.6
D1-H		1.65	1.66 ± 0.01	12.80 ± 0.48	78.7 ± 0.5
D1-I		1.75	1.70 ± 0.00	11.75 ± 0.38	77.8 ± 0.6
D1-J		1.67	1.67 ± 0.01	12.07 ± 0.63	76.8 ± 0.8
D1-K		1.61	1.63 ± 0.00	12.55 ± 0.45	77.1 ± 0.7
D2-A	HA-AR2	1.69	1.66 ± 0.01	17.09 ± 0.20	91.0 ± 0.2
D2-B		1.62	1.65 ± 0.01	16.19 ± 0.29	90.0 ± 0.4

The final relative densities of the fired HA-AR1 samples were in the range of 76.5 and 84.1 %TD, with an average value of around 79 %TD. On the other hand, the final densities of the HA-AR2 samples were around 90 %TD suggesting better sinterability of the DBM samples obtained from the latter powder. However, as it is shown in the next section, the sintering of the WBM samples of both batches led to almost identical final densities which were higher than the final densities of the DBM samples. Considering the relative density of more than 95 %TD as a criterion for the dense bodies, it may be concluded that it was not feasible to produce highly dense materials by DBM with both powder types.

Considering linear shrinkage, it is reasonable to find a reverse relationship between the sintering shrinkage and the mean particle size of the initial ceramic powder. This relationship is depicted in Figure 3-40 for HA-AR1 samples made from DBM powder. It can be seen that, in general, with decreasing the mean particle size the final shrinkage increases. However, it must be considered that the sintering shrinkage is also influenced by the green density. When the green density is high, the low interparticle distances favour the densification. Nevertheless, As we observed in 3.4.1, considering DBM samples, the green density was higher for the samples made from powders with higher mean particle size. Therefore, the combined effect of starting particle size and green density can be the reason for the variation of the experimental points from the linear trend. However, a high green density is beneficial to obtain sintered parts with minimum distortion and residual stresses.

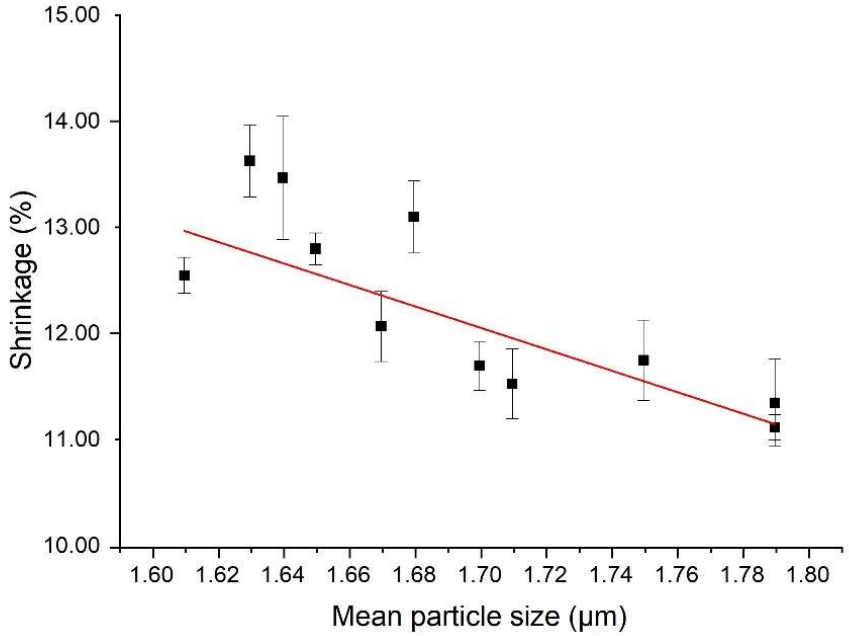

Figure 3-40: Shrinkage of the DBM samples as a function of mean particle size.

Figure 3-41 collects the FESEM images of the sintered microstructures, obtained from HA-AR1 and HA-AR2 powders. As expected from their final densities, we can observe that HA-AR2 samples contained closed and isolated pores, indicating the completion of the second sintering stage. On the other hand, HA-AR1 samples were characterised by a higher amount of open porosities. The higher magnifications images show that both materials were characterised by a bimodal grain size distribution, which was more significant for HA-AR2. As discussed earlier, bimodal grain size distribution can be imputed to HA to TTCP and TCP transformation taking part at the sintering stage.

3.6.3.2 Samples obtained from WBM powders

Sintering of the WBM green samples obtained again from both powder batches, HA-AR1 and HA-AR2, was carried out at 1300 °C using the heating rate of 5 °C/min. According to the previous results obtained from dilatometry tests, samples were sintered at 1300 °C for 1 and 3 hours, to investigate the effect of isothermal sintering time on the microstructural evolution. Like DBM samples, all the samples maintained their regular cylindrical shapes after sintering; the dimensions of the samples were measured using a digital calliper and the densities were calculated by the Archimedes' method.

Data related to the sintering of the WBM samples are presented in Table 3-16. All of the densities were higher than 90 %TD (with a single exception), demonstrating again the high sinterability and the completion of the second sintering stage of these samples. It can be seen that almost all of the samples whose mean particle sizes were less than 1 µm, achieved almost full densification (>95 %TD). In general, 3-hours sintering led to higher densities compared to 1-hour sintering, but in two cases (samples W2-A and W2-C) the trend reversed, and the 1-hour sintered densities were slightly higher than 3-hours sintering.

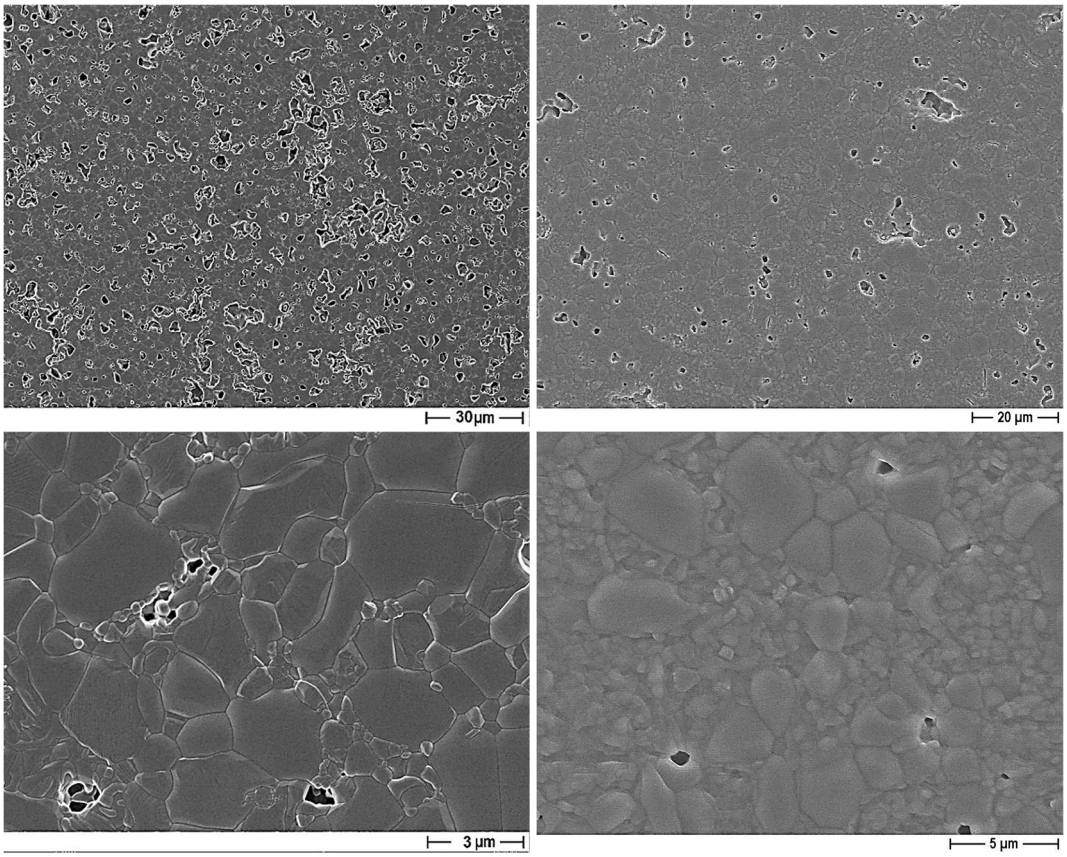

Figure 3-41: Microstructure of sintered materials made from DBM HA-AR1 (left) and HA-AR2 (right) powders, at lower (top) and higher (bottom) magnifications.

Table 3-16: Physical and densification data of WBM samples produced from HA-AR1 and HA-AR2 powders.

Batch designation	Powder batch	Mean particle size (µm)	Green density (gr/cm^3)	Linear shrinkage (%)		Relative density (%)	
				1 hour	3 hours	1 hour	3 hours
W1-A	HA-AR1	0.74	1.63 ± 0.01	-	18.40 ± 0.10	-	94.4 ± 0.3
W1-B		0.81	1.68 ± 0.00	-	18.09 ± 0.08	-	95.6 ± 0.5
W1-C		0.70	1.59 ± 0.01	-	18.06 ± 0.07	-	96.2 ± 0.0
W1-D		0.83	1.69 ± 0.01	17.45 ± 0.43	18.23 ± 0.56	91.7 ± 0.4	95.9 ± 0.5
W1-E		0.89	1.69 ± 0.00	17.88 ± 0.30	18.08 ± 0.14	94.6 ± 0.3	95.7 ± 0.3
W2-A	HA-AR2	0.74	1.65 ± 0.02	19.17 ± 0.19	19.03 ± 0.18	97.9 ± 0.1	97.2 ± 0.3
W2-B		1.08	1.70 ± 0.01	13.68 ± 0.11	14.25 ± 0.19	89.2 ± 0.1	93.2 ± 0.5
W2-C		0.71	1.64 ±0.01	17.71 ± 0.25	17.37 ± 0.13	97.6 ± 0.1	97.0 ± 0.2
W2-D		0.99	1.80 ±0.00	15.00 ± 0.23	15.58 ± 0.10	94.3 ± 0.6	96.8 ± 0.2
W2-E		1.18	1.80 ± 0.01	12.13 ± 0.21	13.73 ± 0.10	86.4 ± 0.9	90.0 ± 0.2
W2-F		1.22	1.86 ± 0.00	-	12.67 ± 0.27	-	91.2 ± 0.2

Comparing HA-AR1 and HA-AR2 samples, it appears that, while the sintering shrinkages of HA-AR1 samples were almost similar, around 18%, (a low difference can be attributed to errors in measurement of the dimension), this parameter varied in a wide range from 12.7 to 19.0% for HA-AR2 samples. Considering the shrinkage data of the DBM samples, collected in Table 3-15, it can be seen that the samples obtained from DBM HA-AR2 powders had higher shrinkage than the HA-AR2 samples obtained from the WBM powders (except W2-A and W2-C samples), even if the DBM samples were characterised by larger starting particle size. Therefore, we can state a key role played by the green densities, as we observed that the higher the green densities, the lower the shrinkages. It can be postulated that in high green densities, the interparticle spaces are low and therefore, the samples shrink less to reach the maximum densification. However, the effect of the initial particle sizes should not be underestimated. For instance, comparing D2-B and W2-A samples with similar green densities, it is clear that the final shrinkage of fully densified WBM sample with the mean particle size of 0.74 µm was almost 3% more than the sample made from DBM powder, with the mean particle size of 1.62 µm.

The linear shrinkage of the WBM samples sintered for 1 and 3 hours as a function of mean particle sizes is plotted in Figure 3-42. While the increase of the linear shrinkage with decreasing the mean particle size was the general trend for both sintering times, it can be seen that with decreasing the mean particle size, the distance between the two curves decreases. Specifically, samples W2-A and W2-C produced by very fine particles (0.7 – 0.8 µm) showed lower densification after 3 h, compared to 1 hour sintering. Therefore, it can be concluded that prolonged sintering, for more than 1 hour, was detrimental for these samples and oversintering resulted in the density decrease, as already evidenced by dilatometry studies.

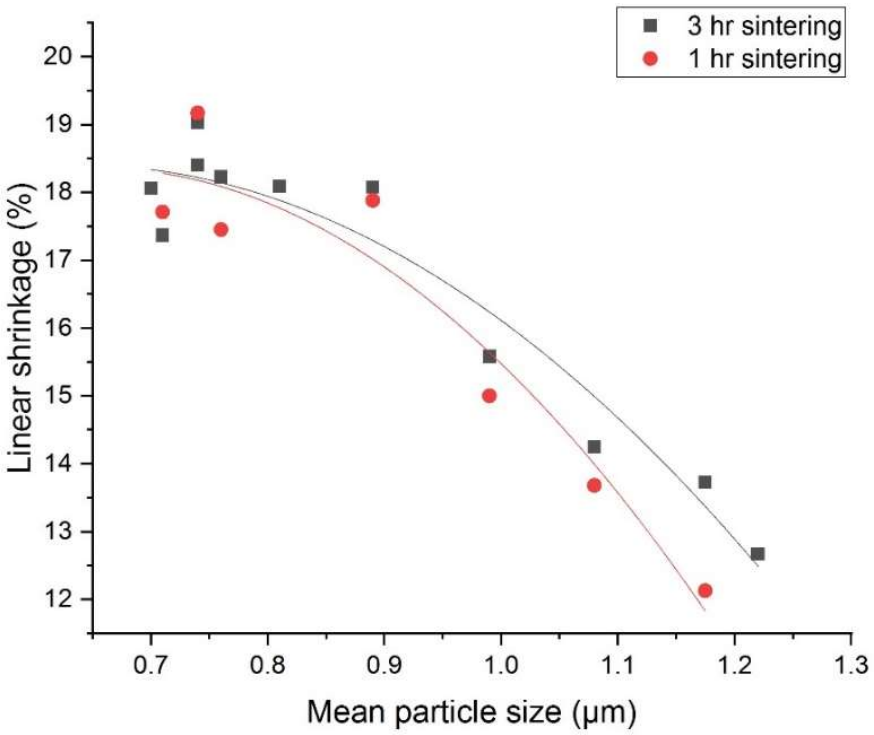

Figure 3-42: Linear shrinkage versus mean particle size of the samples produced from WBM powder after sintering for 1 and 3 hours at 1300 °C.

Figure 3-43 shows the final relative densities after 1 and 3 hours sintering. The general trends were similar to the sintering shrinkage: a reduction of the mean particle sizes led to a higher density and the difference between the two curves diminished with the mean particle size reduction. However, it is possible to distinguish a value in which the density of 1 hour sintered samples overcome the 3-hours sintered ones. This value is located at the intersection point between the fitting curves and it corresponds to the mean particle size of 0.78 µm. For the samples made from powders characterised by mean particle size lower than this value, a decrease in the density occured by prolonging the isothermal time for more than 1 h. It seems that the physical changes due to oversintering were responsible for this phenomenon. Water vapour and other volatile components created from phase transformation during the sintering process and the volume expansion due to certain phase transformation are some of these compositional-microstructural changes, responsible for density decrease. It has been stated that the dehydroxylation process of HA occurs gradually but in two steps, first at about 900 °C and then at 1300 °C [27]. While water vapours produced at 900 °C can be easily eliminated from the material through open porosities, the dehydroxylation by-products generated at 1300 °C remain inside the close-porosity structure. In fact, after reaching the maximum density, grain growth became important and induced an intra-granular porosity, which was responsible for density decrease [52].

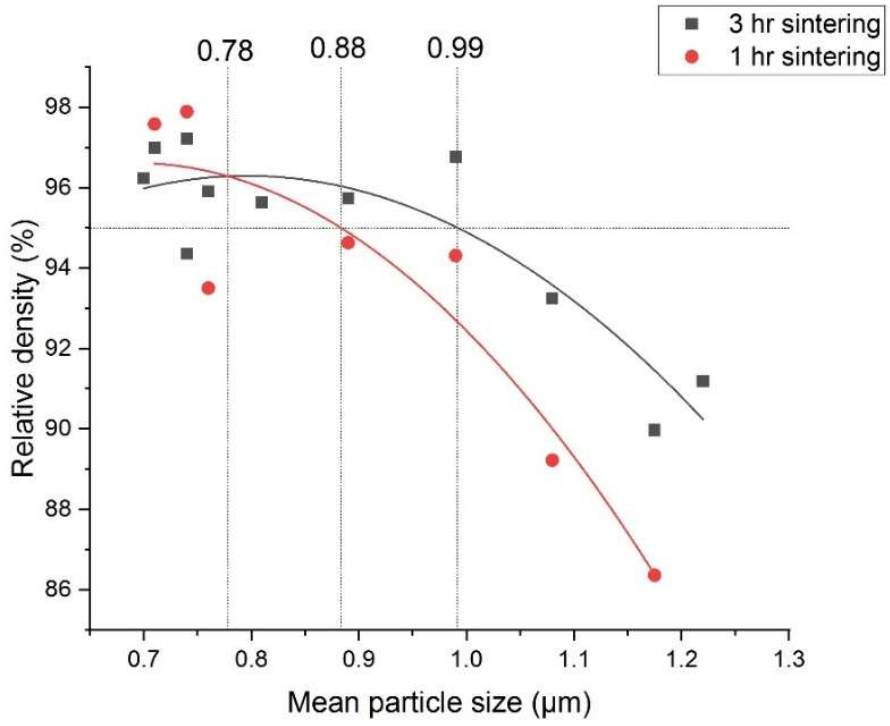

Figure 3-43: Relative density versus mean particle size of the samples produced from WBM powder after sintering for 1 and 3 hours at 1300 °C.

Considering the relative density of 95 %TD as a criterion of a dense body, it is possible to determine the maximum mean particle sizes able to give rise to dense bodies, after 1 and 3 hours sintering. The horizontal line, corresponding to the relative density of 95 %TD, intercepts the curves related to the 1 and 3 hours sintering at mean particle sizes of 0.88 and 0.99 µm, respectively. It may be said that these values are the maximum limits to achieve dense parts by sintering for 1 and 3 hours and each part produced from powders with mean particle size lower than these values will produce fully dense materials. In other words, in order to obtain dense bodies by sintering for 1 or 3 hours at 1300 °C, it is only necessary to reduce the mean particle size of the initial HA powder to less than 0.88 and 0.99 µm, respectively.

3.6.3.3 Phase development as a function of the starting particle size

In the previous sections, an unexpected formation of very fine grains in the samples obtained from HA-AR2 powder was observed and attributed to the phase transformation of HA to TTCP and α-TCP. These transformations mainly occurred during isothermal treatments at 1300 °C for more than 1 hour. The longer the sintering time, the higher was the transformation degree which took place. The generated α-TCP phase converted to β-TCP phase during the cooling step and increased the overall β-TCP fraction in the final material.

On the other hand, the study of the grain size distribution of the final microstructures indicated the high reduction of the larger grains due to the HA to

TTCP phase transformation. The decreased number of large grains and their replacement with smaller ones suggested that these bigger grains were more affected by the phase transformation. It seems that after reaching a specific size, the grains were more susceptible to the phase transformation, and the reduction of the grain size was a consequence of the nucleation of the new TTCP phase. The analysis of the final microstructures of the samples obtained from powders with different initial particle sizes and their XRD composition showed that there was a direct relationship between the final β-TCP amount and the initial particle size distribution. Figure 3-44 shows the amount of β-TCP in the HA-AR2 samples sintered for 3 hours at 1300 °C as a function of the initial powders' mean particle size. It can be seen that with increasing the mean particle size, the participation of β-TCP in the final composition increased. There was a good linear correlation between the mean particle size and the final amount of the β-TCP. The β-TCP phase in the final materials results from two different phase transformations: (1) transformation of CD-HA to HA and β-TCP which happens at temperatures higher than 1000 °C, and (2) allotropic transformation of α-TCP to β-TCP, in which the α-TCP was the by-product of phase transformation of HA to TTCP at 1300 °C. Considering that the first reaction started at lower temperatures and that it was independent of the initial powder's particle size (Section 3.5), it can be concluded that it was the second reaction which was dependent on the initial particle sizes, and this reaction occurred more easily with increasing the initial powder particle size.

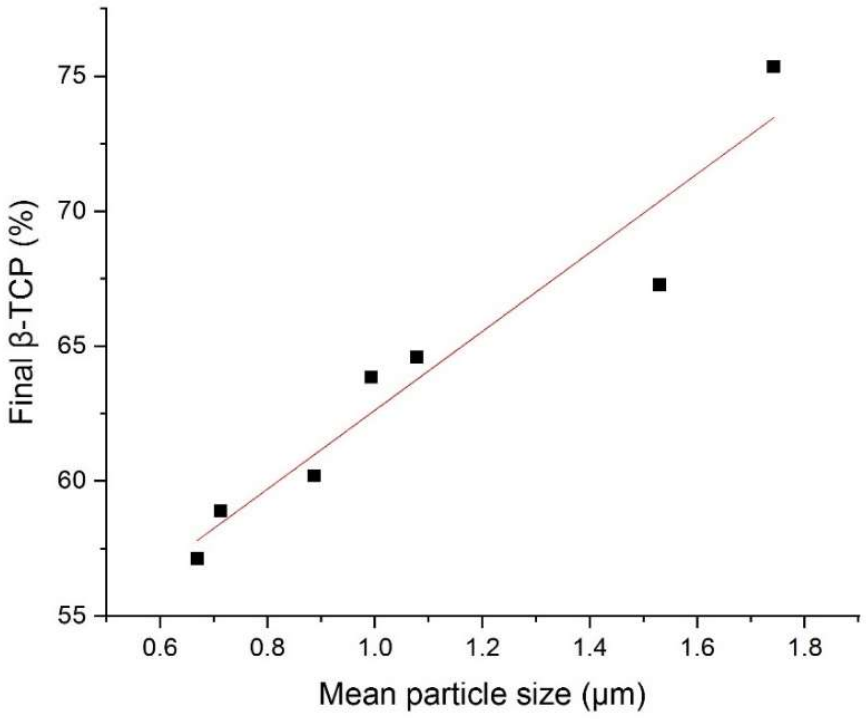

Figure 3-44: Relationship between the final β-TCP phase amount in the final sintered HA-AR2 samples and the starting powder's particle size.

3.7 Mechanical properties

To study the mechanical properties of the produced materials, uniaxial compressive strength tests were carried out on the dense cylindrical DBM and WBM HA gelcast samples (obtained from both HA-AR1 and HA-AR2 powder batches) produced and sintered according to the previous sections. The tests were performed in accordance to ASTM C773-88(2016) [53] under displacement control mode using an MTM Zwick/Roell Z050 (ZwickRoell AG, Ulm, Germany) machine with the displacement rate of 0.1 mm/min. Depending on the drying and sintering shrinkages the diameter of the DBM and WBM samples varied in the range of 10.71-12.84 mm and 8.98-10.52 mm respectively, and the height to the diameter ratio was between 1.9 and 2.1, according to ASTM C773-88(2016) regulations. Rubber pads were used in order to reach a uniform distribution of the load over the sample surfaces.

Some typical stress-strain curves obtained from the compression tests of the DBM and WBM dense samples are presented in Figure 3-45. For both types of materials, two different regimes of deformation can be identified before fracture: an initial region I, which shows a quasi-linear stress-strain relationship, followed by a steeper linear region II, where stress increases very rapidly until the onset of fracture. We can observe that region I extends up to 0.2-0.3% strain for the DBM samples, while higher values (about 0.5%) characterise the WBM curves. The transition between the two regions is almost negligible. This type of compression

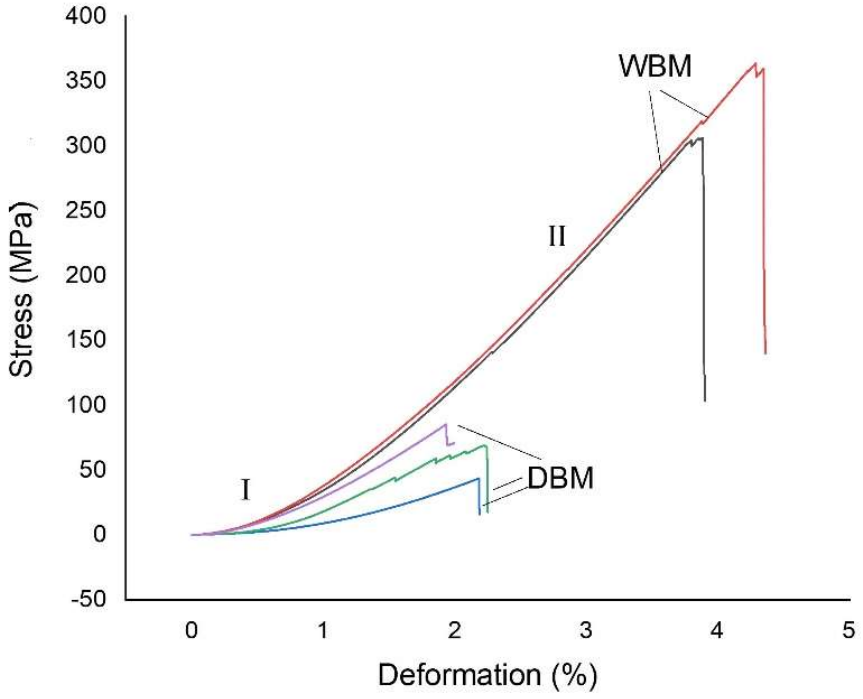

Figure 3-45: Typical stress-strain curve achieved from compression tests of HA dense samples.

behaviour is characteristic of CaP bioceramics and it has been already reported in the literature [54,55]. It has been mentioned that while region II is the typical mechanical behaviour of a ceramic, region I is due to the closure of the non-interconnected porosities since samples were not fully densified and contained porosity. It can be seen that the final fractures did not happen in a single point of stress-strain curves but different steps. In fact, the final collapse of the samples occurred after the creation of lateral cracks which reduced the applied load after the onset of the fracture.

Results obtained from the compression tests of some of the produced dense samples are collected in Table 3-17. The results are the average of at least 5 samples. The stress and deformation values corresponding to the first peak of the curves were used to determine the fracture strength (σ) and strain (ε), respectively, and the elastic modulus (E) was calculated from the slope of the compression stress-strain curves in region II. The corresponding values of the green and sintered densities, as well as the β-TCP phase amount of the final materials, are collected in Table 3-17, too. It can be seen that the different types of powders (HA-AR1 and HA-AR2), milled under different conditions (DBM and WBM) yielded different properties, which gave rise to an almost wide range of mechanical values. The maximum fracture strength near to 300 MPa along with a high E modulus of 10.0 GPa belonged to the samples obtained from WBM samples prepared from HA-AR1 powder, characterised by a final density of around 95 %TD. On the other hand, DBM samples prepared from HA-AR1 powders, with a final density of only 76 %TD, showed the lowest values of fracture strength and E modulus (41 MPa and 3.5 GPa, respectively).

Table 3-17: Mechanical properties of HA samples obtained from compression tests along with corresponding green and final densities as well as β-TCP phase percentage.

Batch	Powder batch	Green density (g/cm^3)	Final density (g/cm^3)	Final relative density (%)	β-TCP fraction (%)	Fracture strength (MPa)	Fracture strain (%)	E modulus (GPa)
D1-G	DBM HA-AR1	1.66±0.01	2.39±0.02	76.4±0.6	37	41±14	1.8±0.2	3.5±0.7
D1-I		1.70±0.00	2.43±0.02	77.8±0.6	30	79±28	2.7±0.4	4.0±1.4
D2-B	DBM HA-AR2	1.65±0.01	2.83±0.01	90.0±0.4	70	48±15	1.7±0.4	4.2±1.3
W1-B	WBM HA-AR1	1.68±0.00	3.00±0.01	95.6±0.5	25	295±45	3.9±0.3	10.0±0.2
W2-D	WBM HA-AR2	1.80±0.00	3.00±0.01	96.8±0.2	65	102±36	2.8±0.9	6.0±1.5

As discussed in detail in chapter 1, various processing parameters such as green density, initial powder's particle size, sintering conditions and the Ca/P atomic ratio of the initial powder affect the final mechanical properties of HA bioceramics [51]. It is possible to distinguish such effects in the mechanical properties presented in Table 3-17. For instance, by comparing D1-G and D1-I samples, both produced

from DBM HA-AR1 batch, it can be observed that while their elastic modulus was similar, the fracture strength of the former was almost half of the latter. This difference can be attributed to the lower final density of D1-G compared to D1-I. In addition, the effect of the initial solid loadings should not be neglected. As stated in Table 3-1, D1-G made from lower solid loading slurry than D1-I, and as it was discussed in 3.4 the former suffered higher internal stresses during drying which was more likely to lead to drying microcracks than the latter.

Dehydroxylation and the HA to β-TCP phase transformation have been shown to deteriorate the strength and mechanical properties of HA bioceramics in different independent studies [37,43,45,54,55,56,56,57]. It has been claimed that the degradation of mechanical properties in HA is due to weakening of the grain boundary as a result of segregation of decomposition product at grain boundary regions [45]. This effect can be observed in our work by comparing the results of the DBM samples prepared from HA-AR2 and HA-AR1 powders. For example, while the final density of D2-B (obtained from HA-AR2), was as high as 90 %TD, this sample achieved a poor compressive strength (48 MPa), which was similar or lower to the strengths of D1-G and D1-I samples (both prepared from HA-AR1 powders), even though these two samples had low final densities (76 and 78 %TD, respectively). This poor mechanical performance can be imputed to the high amount of β-TCP phase in D2-B, with lower mechanical properties compared to HA. Such hypothesis was confirmed by comparing the properties of WBM samples, and specifically, W1-B (prepared from HA-AR1) and W2-D (prepared from HA-AR2): despite the latter was characterised by a slightly higher fired density, it showed a significant lower compressive strength compared to W1-B, due to its significantly higher β-TCP phase amount.

In comparison with the compressive strength and elastic modulus of the cortical bone which are in the range of 130-180 MPa and 12-18 GPa, respectively, with porosity between 5 and 13% [60], it seems that only W1-B samples achieved acceptable results. However, it must be considered that in order to use an implant in load-bearing applications, the resistance of the implant material to crack propagation which is quantified by the fracture toughness should also be investigated. In this work, the fracture toughness has not been investigated and will be the object of further investigations. However, previous literature data report a low fracture toughness for HA ceramics less than 1 $MPa.m^{1/2}$, significantly lower of that of human bone with the fracture toughness of 2-12 $MPa.m^{1/2}$ [52,59].

The mechanical properties of CaP bioceramics reported in the literature vary in a wide range of values. Bending strength, compressive strength, and tensile strength of dense HA ceramics are in the ranges of 38–250 MPa, 120–900 MPa, and 38–300 MPa, respectively [51,52]. These wide ranges are due to the several parameters influencing the mechanical properties of CaPs. Preparation route, initial particle size distribution, sintering cycle, grain size, porosity, crystallinity, chemistry and phase decomposition are such parameters. In general, it can be said that the amorphous phase, microporosity, and grain size decrease the mechanical properties of CaPs. Conversely, High crystallinity, low porosity, and small grain size result in

higher mechanical properties [52,60]. on the other hand, the lack of standardization across laboratories makes also the comparison between different works difficult. For instance, considering compressive strength as the most studied mechanical property, different samples sizes have been used in different works, and according to the following equation strength has a reverse relationship with the samples size:

$$\left(\frac{\sigma_1}{\sigma_2}\right) = \left(\frac{V_2}{V_1}\right)^{\frac{1}{m}} \qquad \text{Equation 3-2}$$

where σ_i and V_i are failure strengths and volumes for sample i, respectively, and m is the material's Weibull modulus. For example, Jarcho et al. [57] reported compressive strength as high as 917 MPa for HA pressed cylindrical samples of 2 mm height and 4.6 mm diameter, on the other hand, Prokopiev and Sevostianov [61] reported compressive strength of 5-14 MPa for samples with 38 mm diameter and 40mm in length. While several processing parameters also can play a role in this enormous difference, it is difficult to say that the sample size was not effective in this matter.

Most of the available data in the literature regarding the compressive strength of HA belongs to the samples made by cold pressing. While plenty of works are dealing with the gelcasting of the porous HA [1, 2, 3, 4, 5, 6, 7, 8, 9, 10] [11], few articles related to the gelcasting of the dense HA can be found in the literature [11,26,37,62] in none of which the compressive strength was characterised. In Figure 3-46 the compressive strengths of WBM samples made from HA-AR1 and HA-AR2 are compared with the literature values of pressed HA materials [61,63,64,65,66]. The compressive strengths are plotted as a function of the samples

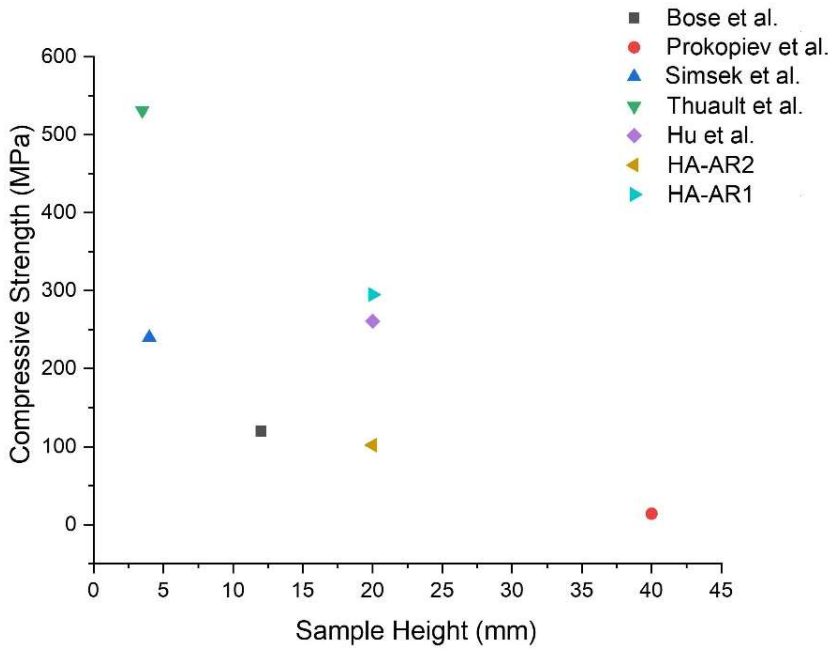

Figure 3-46: Compressive strength of the WBM samples in comparison with the strength of the pressed HA in the literature.

height before tests reported in the corresponding papers. The results reported by Jarcho et al. [57] is voluntarily excluded from this comparison because of unusual samples' height. It can be seen a logarithmic decrease of the strength by increasing the sample size. Despite the fact that literature data belong to HA pressed samples, which normally show better mechanical properties than the samples made by casting methods, it can be seen that the strengths of our samples are comparable with the pressed ones. In addition, the strength of HA-AR1 sample is superior to the pressed samples with the same height and is located in the upper range of the graph.

3.8 Conclusion

Gelcasting was chosen for the production of dense and porous HA parts due to several advantages over other ceramic processing methods [1]. Two different batches of commercially available CD-HA powders with different Ca/P ratios were used for the production. The particle size distributions of the as-received powders were refined through dry and wet ball milling (DBM and WBM) methods and a variety of particle size distribution was achieved. High purity agar as a non-toxic environmentally friendly [15] material was utilized as the gelling agent. An optimum amount of an anionic polyelectrolyte (Duramax D-3021) which is recommended for HA slurries, was used as the dispersant resulting to a high solid loaded slurries with suitable rheological properties for casting.

The sintering behaviour of the powders was studied using dilatometry tests and different sintering stages and phase transformation were identified on the dilatometry curves. Sinterability was improved 15 times by tailoring the particle size and the sintering process. Highest sinterability for the DBM and WBM samples were found by heating rates of 10 and 5 °C/min, respectively.

FESEM observations showed unusual grain refinement during sintering of the samples made from the powder with the lower Ca/P ratio leading to bimodal grain size distribution. EDX analyses showed that the compositions of the fine and coarse grains were near to TCP and TTCP phases, respectively, suggesting HA to TTCP + TCP phase transformation during sintering of this powder.

By investigating the effect of the starting powder particle size on the sinterability, it was found that by decreasing the initial particle size to less than 0.88 and 0.99 µm it was possible to obtain dense bodies (more than 95 %TD) through sintering at 1300 °C for 1 and 3 hours, respectively.

The mechanical properties of the samples were influenced by initial particle size, green density and Ca/P ratio of the powders. Very high compressive strength around 300 MPa was achieved from WBM samples characterised by the highest Ca/P ratio, and a high final density of 95 %TD.

References

[1] O. O. Omatete, M. A. Janney and S. D. Nunn, "Gelcasting: From laboratory development towards industrial production," *Journal of the European Ceramic Society,* vol. 17, pp. 407-413, 1997.

[2] P. Sepulveda, H. A. Bressiani, J. Bressiani, L. Meseguer and B. Konig Jr, "Synthesis and properties of ceramic foams for hard tissue repair," *Key Engineering Materials,* vol. 218, pp. 413-416, 2002.

[3] F. Mendonça, L. Louro, J. de Campos and M. Prado da Silva, "Porous biphasic and triphasic bioceramics scaffolds produced by gelcasting," *Key Engineering Materials,* vol. 361, pp. 27-30, 2008.

[4] A. Asif, R. Nazir, T. Riaz, N. Ashraf, S. Zahid, R. Shahid, A. Ur-Rehman, A. Anwar Chaudhry and I. Ur Rehman, "Influence of processing parameters and solid concentration on microstructural properties of gel-casted porous hydroxyapatite," *Journal of Porous Materials,* vol. 21, pp. 31-37, 2014.

[5] A. Lemos and J. Ferreira, "Designing of bioceramics with bonelike structures tailored for different orthopaedic applications," *Key Engineering Materials,* Vols. 254-256, pp. 1037-1040, 2004.

[6] M. Sakamoto, M. Nakasu, T. Matsumoto and H. Okihana, "Development of superporous hydroxyapatites and their examination with a culture of primary rat osteoblasts," *Journal of Biomedical Materials research. Part A,* vol. 82, no. 1, pp. 238-242, 2007.

[7] S. Rekha Dash, R. Sarkar and S. Bhattacharyya, "Gel casting of hydroxyapatite with naphthalene as pore former," *Ceramics International,* vol. 41, pp. 3775-3790, 2015.

[8] M. Potoczek, "Hydroxyapatite foams produced by gelcasting using agarose," *Materials Letters,* vol. 62, pp. 1055-1057, 2008.

[9] M. Potoczek, A. Zima, Z. Paszkiewicz and A. Slosarczyk, "Manufacturing of highly porous calcium phosphate bioceramics via gel-casting using agarose," *Ceramics International,* vol. 35, pp. 2249-2254, 2009.

[10] B. Chen, D. Jiang, J. Zhang, M. Dong and Q. Lin, "Gel-casting of β-TCP using epoxy resin as a gelling agent," *Journal of the European Ceramic Society ,* vol. 28, pp. 2889-2894, 2008.

[11] S. Padilla, M. Vallet-Regı, M. Ginebra and F. Gil, "Processing and mechanical properties of hydroxyapatite pieces obtained by the gelcasting method," *Journal of the European Ceramic Society,* vol. 25, p. 375–383, 2005.

[12] M. N. Rahaman, Ceramic processing, second edition, CRC Press, 2017.

[13] L. L. Hench, An introduction to bioceramics, second edition, Imperial College Press, 2013.

[14] J. A. Delcour and K. Poutanen, Fibre-rich and whole grain foods, Woodhead Publishing Limited, 2013.

[15] The European parliament and the council of the European Union, "Classification, labelling and packaging of substances and mixtures", Regulation (EC) No 1272/2008, 2008.

[16] K. P. Plucknett and C. D. Munro, "Biopolymer-based gel casting of ferroelectric ceramics," *Advanced Engineering Materials,* vol. 16, no. 6, pp. 684-698, 2014.

[17] J. Luyten, S. Mullens, J. Cooymans, A. De Wilde, I. Thijs and R. Kemps, "Different methods to synthesize ceramic foams," *Journal of the European Ceramic Society,* vol. 29, p. 829–832, 2009.

[18] M. Potoczek, "Gelcasting of alumina foams using agarose solutions," *Ceramics International,* vol. 34, p. 661–667, 2008.

[19] S. Olhero, G. TarõÁ, M. Coimbra and J. Ferreira, "Synergy of polysaccharide mixtures in gelcasting of alumina," *Journal of the European Ceramic Society,* vol. 20, pp. 423-429, 2000.

[20] W. J. Tseng and P. T. Lin, "Effect of solids concentration on TiO2/Ni composite foams prepared by aqueous gelcasting of particle-stabilized emulsions," *Journal of the European Ceramic Society,* vol. 37, p. 5265–5272, 2017.

[21] J. M. Wu, Y. X. Ma, Y. Chen, L. J. Cheng, A. N. Chen, R. Z. Liu, C. H. Li, Y. S. Shi and J. P. Lin, "Preparation of Si_3N_4 ceramics by aqueous

gelcasting using non-toxic agar powder as gelling agent without cooling crosslink process," *Ceramics International,* vol. 45, p. 20961–20966, 2019.

[22] S. Padilla, R. Garcia-Carrodeguas and M. Vallet-Regi, "Hydroxyapatite suspensions as precursors of pieces obtained by gelcasting method," *Journal of the European Ceramic Society,* vol. 24, pp. 2223-2232, 2004.

[23] F. Lelièvre, D. Bernache-Assollant and T. Chartier, "Influence of powder characteristics on the rheological behaviour of hydroxyapatite slurries," *Journal of Materials Science: Materials in Medicine volume,* vol. 7, p. pages489–494, 1996.

[24] S. Mei, J. Yang, J. M. F. Ferreira and R. Martins, "Optimisation of parameters for aqueous tape-casting of cordierite-based glass ceramics by Taguchi method," *Materials Science and Engineering A ,* vol. 334, pp. 11-18, 2002.

[25] H. Yasuda, S. Mahara, Y. Umakoshi, S. Imazato and S. Ebisu, "Microstructure and mechanical property of synthesized hydroxyapatite prepared by colloidal process," *Biomaterials ,* vol. 21, pp. 2045-2049, 2000.

[26] B. Chen, Z. Zhang, J. Zhang, M. Dong and D. Jiang, "Aqueous gel-casting of hydroxyapatite," *Materials Science and Engineering A,* Vols. 435-436, pp. 198-203, 2006.

[27] E. Landi, A. Tampieri, G. Celotti and S. Sprio, "Densification behaviour and mechanisms of synthetic hydroxyapatites," *Journal of the European Ceramic Society ,* vol. 20, pp. 2377-2387, 2000.

[28] L. C. Hwa, S. Rajoo, A. Mohd Noor, A. Norhayati and M. Uday, "Recent advances in 3D printing of porous ceramics: A review," *Current Opinion in Solid State and Materials Science,* vol. 21, pp. 323-347, 2017.

[29] Z. Zak Fang, Sintering of advanced materials, fundamental and processing, Woodhead Publishing, 2010.

[30] T. Kokubo, Bioceramics and their clinical applications, Woodhead Publishing in Materials, 2008.

[31] J. Elliot, "Structure and chemistry of the apatites and other calcium orthophosphates," in *Studies in inorganic chemistry*, Elsevier, 1994.

[32] P. Palmero, M. Lombardi, L. Montanaro, M. Azar, J. Chevalier, V. Garnier and G. Fantozzi, "Effect of heating rate on phase and microstructural evolution during pressureless sintering of a nanostructured transition alumina," *International Journal of Applied Ceramic Technology,* vol. 6, no. 3, pp. 420-430, 2009.

[33] E. Champion, "Sintering of calcium phosphate bioceramics," *Acta Biomaterialia,* vol. 9, p. 5855–5875, 2013.

[34] G. Okuma, D. Kadowaki, T. Hondo, S. Tanka and F. Wakai, "Interface topology for distinguishing stages of sintering," *Scientific Reports,* vol. 7, no. 11106 , 2017.

[35] N. Y. Mostafa, "Characterization, thermal stability and sintering of hydroxyapatite powders prepared by different routes," *Materials Chemistry and Physics,* vol. 94, pp. 333-341, 2005.

[36] F. Ben Ayed, J. Bouaziz and K. Bouzouita, "Pressureless sintering of fluorapatite under oxygen atmosphere," *Journal of the European Ceramic Society,* vol. 20, pp. 1069-1076, 2000.

[37] S. Laasri, M. Taha, A. Laghzizil, E. Hlil and J. Chevalier, "The affect of densification and dehydroxylation on the mechanical properties of stoichiometric hydroxyapatite bioceramics," *Materials Research Bulletin,* vol. 45, pp. 1433-1437, 2010.

[38] S. Raynaud, E. Champion and D. Bernache-Assollant, "Calcium phosphate apatites with variable Ca/P atomic ratio II. Calcination and sintering," *Biomaterials ,* vol. 23, pp. 1073-1080, 2002.

[39] C.J. Liao, F.H. Lin, K.S. Chen and J.S. Sun, "Thermal decomposition and reconstitution of hydroxyapatite in air atmosphere," *Biomaterials,* vol. 20, pp. 1807-1813, 1999.

[40] Y. Liu and Z. Shen, "Dehydroxylation of hydroxyapatite in dense bulk ceramics sintered by spark plasma sintering," *Journal of the European Ceramic Society,* vol. 32, pp. 2691-2696, 2012.

[41] T. Wanga and A. Dorner-Reisel, "Thermo-analytical investigations of the decomposition of oxyhydroxyapatite," *Materials Letters,* vol. 58, pp. 3025-3028, 2004.

[42] C. Moseke and U. Gbureck, "Tetracalcium phosphate: Synthesis, properties and biomedical applications," *Acta Biomaterialia ,* vol. 6, pp. 3815-3823, 2010.

[43] H. Guo, K. Aik Khor, Y. Chiang Boey and X. Miao, "Laminated and functionally graded hydroxyapatite/yttria stabilized tetragonal zirconia composites fabricated by spark plasma sintering," *Biomaterials ,* vol. 24, p. 6678675, 2003.

[44] W. Jie, L. Xiaoguang, Z. Xingdong and J. Xiaoyang, "Thermal decomposition of hydroxyapatite structure induced by titanium and its dioxide," *Journal of Materials Science Letters,* vol. 13, pp. 159-161, 1994.

[45] P. E. Wang and T. K. Chaki, "Sintering behaviour and mechanical properties of hydroxyapatite and dicalcium phosphate," *Journal of Materials Science: Materials in Medicine,* vol. 4, pp. 150-158, 1993.

[46] J. Zhou, X. Zhang, J. Chen, S. Zeng and K. De Groot, "High temperature charcateistics of synthetic hydroxyapatite," *Jouran of Materials Science: Materials in Medicine,* vol. 4, pp. 83-85, 1993.

[47] K. deGroot, C. P. A. T. Klein, J. G. C. Wolke and J. M. A. de Blieck-Hogervorst, "Chemistry of calcium phosphate bioceramics," in *CRC handbook of bioactive ceramics*, Boca Raton, CRC Press, 1990, pp. 3-16.

[48] F. H. Lin, L. Chun-Jen, C. Ko-Shao and S. Jui-Sheng, "Thermal reconstruction behavior of the quenched hydroxyapatite powder during reheating in air," *Materials Science and Engineering C,* vol. 13, pp. 97-104, 2000.

[49] M. Zilm, S. D. Thomson and M. Wei, "A comparative study of the sintering behavior of pure and manganese-substituted hydroxyapatite," *Materials,* vol. 8, pp. 6419-6436, 2015.

[50] A. Tahmasebifar and Z. Evis, "Structural and mechanical characteristics of hydroxyapatite and tri-calcium phosphates doped with Al3+ and F- ions," *Journal of Ceramic Processing Research,* vol. 14, no. 4, pp. 549-556, 2013.

[51] W. Suchanek and M. Yoshimura, “Processing and properties of hydroxyapatite-based biomaterials for use as hard tissue replacement implants,” *Journal of Materials Research,* vol. 13, no. 1, pp. 94-117, 1998.

[52] S. V. Dorozhkin, “Calcium orthophosphate bioceramics,” *Ceramics International,* vol. 41, pp. 13913-13966, 2015.

[53] American society for testing and materials, "Standard test method for compressive (crushing) strength of fired whiteware materials" ASTM C773-88, 2016.

[54] S. Raynaud, E. Champion, J. P. Lafon and D. Bernache-Assollant, “Calcium phosphate apatites with variable Ca/P atomic ratio III. Mechanical properties and degradation in solution of hot pressed ceramics.,” *Biomaterials,* vol. 23, no. 4, pp. 1081-1089, 2002.

[55] P. Miranda, A. Pajares, E. Saiz, A. P. Tomsia and F. Guiberteau, “Mechanical properties of calcium phosphate scaffolds fabricated by robocasting,” *Journal of Biomedical Materials Research Part A,* vol. 85, no. 1, pp. 218-227, 2008.

[56] A. Karimzadeh, M. R. Ayatollahi, A. Bushroa and M. Herliansyahd, “Effect of sintering temperature on mechanical and tribological properties of hydroxyapatite measured by nanoindentation and nanoscratch experiments,” *Ceramics International,* vol. 40, pp. 9159-9164, 2014.

[57] M. Jarcho, C. H. Bolen, M. B. Thomas, J. Bobick, J. F. Kay and R. H. Doremus, “Hydroxylapatite synthesis and characterization in dense polycrystalline form,” *Journal of Materials Science,* vol. 11, pp. 2027-2035, 1976.

[58] A. J. Wagoner Johnson and B. A. Herschler, “A review of the mechanical behavior of CaP and CaP/polymer composites for applications in bone replacement and repair,” *Acta Biomaterialia,* vol. 7, pp. 16-30, 2011.

[59] T. C. Yong, R. Singh, A. K. Liang, Y. W. Hong, I. Sopyan and T. W. Dung, “Sintering behaviour of hydroxyapatite ceramics prepared by different routs,” *Advances in Bioceramics & Porous Ceramics II,* vol. 30, no. 6, pp. 127-138, 2009.

[60] H. Liu, Nanocomposites for Musculoskeletal Tissue Regeneration, Kidlington, UK: Woodhead Publishing, 2016.

[61] O. Prokopiev and I. Sevostianov, "Dependence of the mechanical properties of sintered hydroxyapatite on the sintering temperature," *Materials Science and Engineering A,* vol. 431, pp. 218-227, 2006.

[62] B. Chen, T. Zhang, J. Zhang, Q. Lin and D. Jiang, "Microstructure and mechanical properties of hydroxyapatite obtained by gel-casting process," *Ceramics International,* vol. 34, pp. 359-364, 2008.

[63] A. Thuault, E. Savary, J.-C. Hornez, G. Moreau, M. Descamps, S. Marinel and A. Leriche, "Improvement of the hydroxyapatite mechanical properties by direct microwave sintering in single mode cavity," *Journal of the European Ceramic Society,* vol. 34, pp. 1865-1871, 2014.

[64] S. Bose, A. Banerjee, S. Dasgupta and A. Bandyopadhyay, "Synthesis, processing, mechanical, and biological property characterization of hydroxyapatite whisker-reinforced hydroxyapatite composites," *Journal of the American Ceramic Society,* vol. 92, no. 2, pp. 323-330, 2009.

[65] X. Hu, W. Zhang and D. Hou, "Synthesis, microstructure and mechanical properties of tricalcium phosphate–hydroxyapatite (TCP/HA) composite ceramic," *Ceramics International,* 2019.

[66] D. Şimşek, R. Çiftçioğlu, M. Güden, M. Çiftçioğlu and S. Harsa, "Mechanical properties of hydroxyapatite composites reinforced with hydroxyapatite whiskers," *Key Engineering Materials,* Vols. 264-268, pp. 1985-1988, 2004.

Chapter 4 Gelcasting Method: Elaboration and Characterisation of Porous Parts

Abstract

Highly porous structures with interconnected spherical pores were produced by gelcasting of foamed suspensions, produced from both dry and wet ball-milled hydroxyapatite (HA) powders with different particle size distributions. Two different HA powder batches were used, differing mainly on the the Ca/P ratio. The effect of different constituents of the ceramic slurry (solid loading, agar content, foaming agent content) on the porosity and pore sizes of the porous samples were investigated. By controlling these parameters, highly porous ceramics, with porosity in the range of 63 to 87% and pore sizes from 4 to 650 μm, were produced. The mechanical properties of the samples were chaarcterised between 2 and 15 MPa by performing uniaxial compression tests. While the strengths of the samples reduced reasonably by increasing the pore volume fraction, the obtained strength was in a good correlation with the previous results.

Functionally graded scaffolds, mimicking the natural bone structure, were developed using the optimised gelcasting techniques for dense and porous samples. The produced multifunctional bilayer parts took advantages of both high mechanical strength provided by the central dense part and superior biological performance fulfilled by the porous outer layer all together.

Abbreviations

ACP	Amorphous calcium phosphate
CaP	Calcium phosphate
DBM	Dry ball milling
FESEM	Field emission scanning electron microscopy
FGM	Functionally graded material
HA	Hydroxyapatite
HA-AR1	As-received hydroxyapatite powder, batch n.1
HA-AR2	As-received hydroxyapatite powder, batch n.2
PMMA	Poly(methyl methacrylate)
SDS	Sodium dodecyl sulphate
SLS	Sodium lauryl sulphate
TCP	Tricalcium phosphate
WBM	Wet ball milling

4.1 Production of porous ceramics

Gelcasting technique combined with direct foaming of ceramic slurries is a simple and powerful method to develop porous ceramic structures. The structures produced by this method consist of interconnected spherical pores, with fully densified struts. Compared to porous bodies at the same porosity level developed by other methods, this technique leads to higher mechanical properties [1]. The aeration is produced under rigorous mechanical stirring of ceramic slurries. Addition of foaming agents such as surfactants reduces the surface tension between air and liquid and results in the formation of bubbles. In situ polymerisation of the gelling agent dissolved in the liquid phase, makes it possible to retain the bubbles during solidification of the ceramic body. The bubbles are finally converted to pores in the porous part during the sintering process.

The procedure used for the fabrication of gelcast hydroxyapatite (HA) porous samples, presented in Figure 4-1, was similar to the procedure used for the production of the dense samples (see chapter 3, Figure 3-6). The only difference was the addition of an appropriate amount of surfactant to the final suspension and its mechanical stirring before casting in order to generate foam. The mechanical stirring of the slurry was carried out using a stirrer with rectangular blades at the speed of 2000 rpm. The blades had 1.4 mm thickness and twisted for deriving a downward airflow direction during rotation. The stirring started at low speed to dissolve the surfactant in the slurry and then the speed increased to 2000 rpm to generate foam. The maximum foam volume, in which the foam formation rate was equal to foam collapsing [2] was reached after 1 minute. In comparison to foaming times reported in the literature which ranged from 4 to 30 minutes [3, 4, 5], our foaming time was significantly shorter. This had a positive effect on the process: in fact, because the foaming process was carried out at 60 °C (over agar polymerisation temperature), a fast foaming process was very important to reduce the risk of loosing water by evaporation. The produced foam was cast in PMMA moulds and after completion of the gelling reaction, which occurred during 30 minutes at 15°C, samples were demoulded. Like the dense samples, the drying step was carried out under controlled humidity conditions and the debinding of the organic matters was completed at 600 °C for 2 hours. The highly porous structure allowed an easier release of by-products as compared to dense pieces.

Sodium dodecyl sulphate (SDS) (L4390, Sigma Aldrich), also known as sodium lauryl sulphate (SLS), a synthetic organic compound with formula $CH_3(CH_2)11SO_4Na$, is an anionic surfactant [6] that was used for foam generationin this work. It consists of a 12-carbon tail attached to a sulphate group. Its hydrocarbon tail, combined with a polar headgroup, provides the compound amphiphilic properties and so makes it useful as a surfactant [6].

As in the case of the gelcast dense bodies, also for porous bodies, agar was used as the gelling agent. It has shown that both solid loading and agar concentration affect the slurry at the foaming temperature (60 °C): higher solid loading and higher agar concentration increase the viscosity of the slurry [7]. The viscosity of the slurry

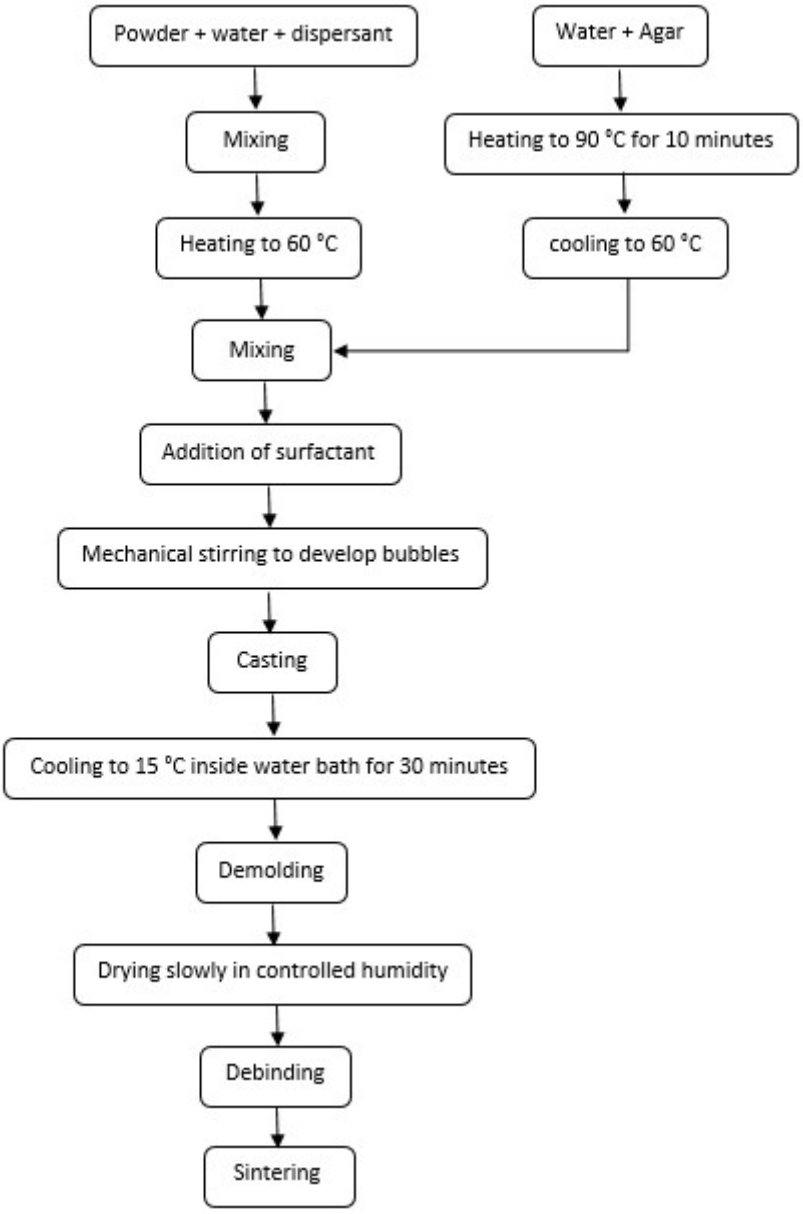

Figure 4-1: Flowchart of the gelcasting procedure used in the production of porous HA.

should be low enough not to limit the castability of low-density foam. On the other hand, the amount of agar in the slurry must be enough to create a strong gel to withstand body weight. Preliminary tests showed that the porous bodies produced at agar content less than 1.1% were not stable and failed during drying. This minimum value was very close to the minimum agar content (1%) determined in a previous literature work [8]. It should be specified that the agar percentage is always referred to the water amount.

Different amounts of HA powder, agar and surfactant (i.e. SDS) were tested for the production of porous ceramics. The starting HA powder derived from two batches, named HA-AR1 and HA-AR2, which differ on starting particle size and Ca/P ratio, being respectively 1.59 and 1.55 for the first and the second batch. In addition, the powders from both batches were submitted to ball milling, performed

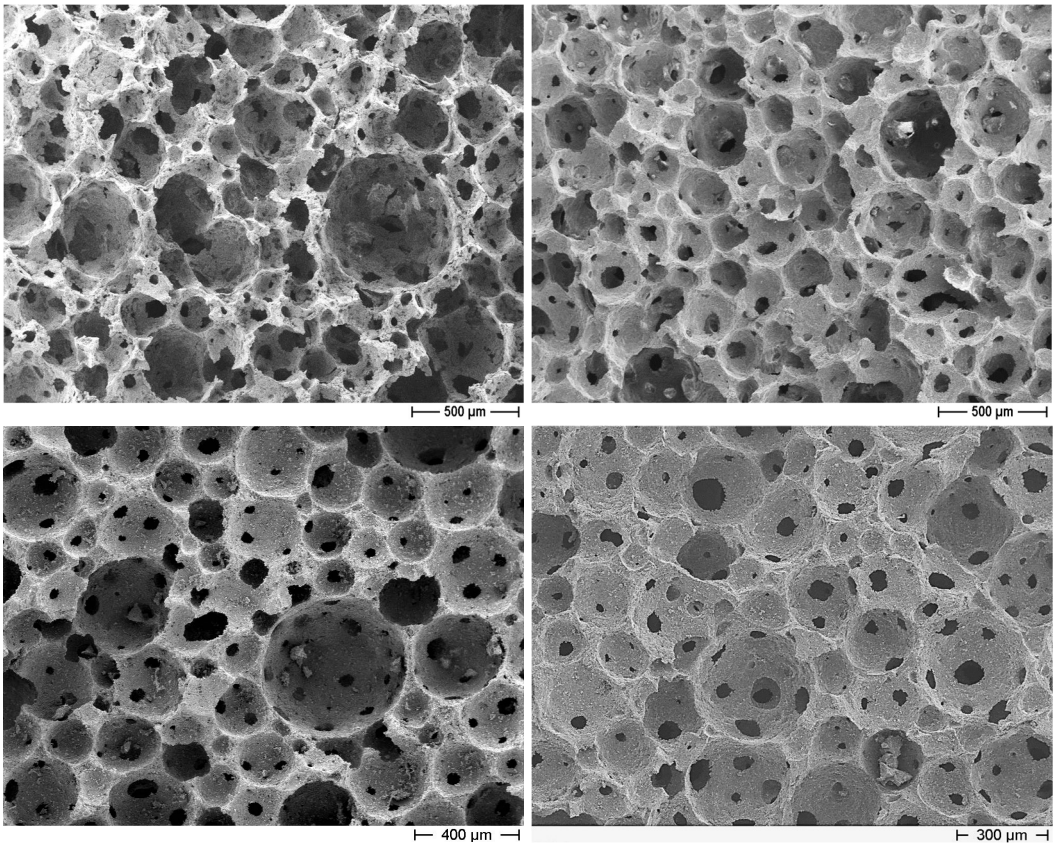

Figure 4-2: Cross-section FESEM micrographs of some representative porous HA parts produced from different slurry compositions.

either under dry (DBM) and wet (WBM) conditions. Considering both HA-AR1 and HA-AR2 batches, DBM powders were characterised by mean particle size in the range 1.6 - 1.9 µm, while the mean particle sizes of the WBM powders were in the range 0.65 - 1 µm, similar to the data reported in Chapter 3. Highly porous samples with hierarchical pore structure were obtained from all of the combinations. SDS was very effective in foam creation and even 0.1% SDS resulted in highly porous final bodies.

Some representative field emission scanning electron microscopy (FESEM) micrographs of the sintered porous samples are presented in Figure 4-2. All of the porous structures were composed of evenly distributed spherical cells entirely interconnected by approximately circular windows. Porous ceramics with different porosity levels between 63 and 87% was tailored by changing the initial slurry's composition with regard to solid loading, agar and SDS amount. The porosities were calculated from dimension and weight measurements of at least 5 samples of the same production. Figure 4-3 displays the mean pores and windows sizes of the HA porous ceramics (as observed by FESEM), at different porosity levels, obtained from different compositions of the slurry made from both DBM and WBM powders. The vertical bar lines indicate the minimum and the maximum pores and windows sizes measured for each sample. It can be seen that each sample was

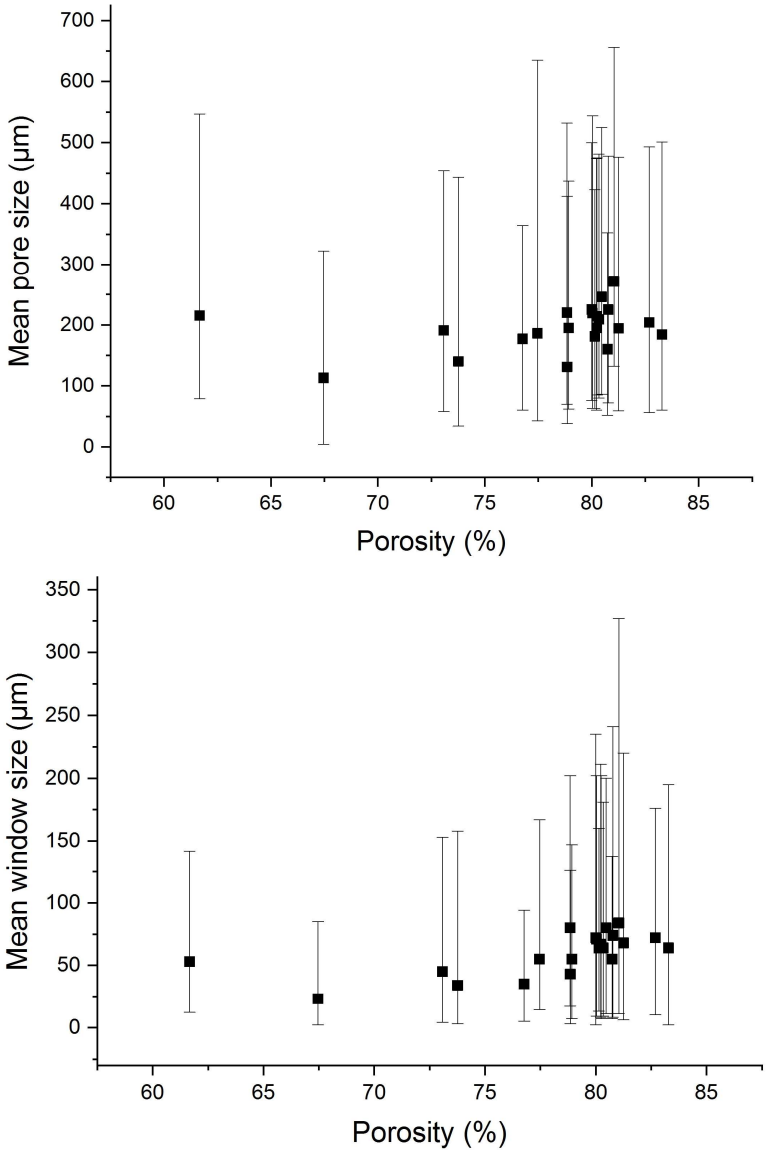

Figure 4-3: Cell and window size data retrieved from FESEM images of the porous ceramics at various porosities obtained from different initial compositions.

characterised by a quite wide range of pore and windows sizes, and independently from the final porosity percentage, the pores and windows sizes could be tailored. Therefore, it seems that this fabrication method is an effective tool for the production of HA porous parts with different microstructural architectures, useful for different types of final applications. Therefore, in the next sections, the effect of the slurry features, prepared by both HA-AR1 and HA-AR2 powders, and either milling methods, on the final micro/macro-structures will be discussed.

4.2 HA-AR1 samples: role of the constituents on micro-macrostructural features

The main features of the slurry constituents (namely: powder, agar and SDS amounts in the aqueous medium) as well as of the green and sintered porous bodies produced by DBM and WBM of HA-AR1 powder are collected in Table 4-1. First of all, we can observe that all WBM slurries were characterised by a significantly lower solid loading than DBM ones, due to the lower initial particle size of WBM particles. Attempts to further increase the solid content in WBM slurries led to viscosity increase, and the slurries were difficult to be further processed. Nonetheless, it can be seen that the green densities of the samples produced from both powders were comparable. However, higher sinterability of the WBM powders led to higher shrinkage and therefore the final samples were less porous than the samples obtained from DBM powders.

Considering the samples produced from DBM powder, we can observe that increasing the solid loading at a fixed amount of agar (i.e., comparing samples D1-FA and D1-FC) or increasing agar at a fixed solid loading (i.e., comparing samples D1-FB and D1-FC) resulted in a lower porosity. A similar trend can be observed for the samples produced from the WBM powder. For examples, for samples produced at 41% solid loading, the progressively increasing of agar from 1.2 to 1.5% led to a continuous porosity decrease from 77% to 71%. Comparing the shrinkage values of the porous samples with those of the dense samples made from HA-AR1 (presented in Tables 3-15 and 3-16), it can be seen that the porous samples showed higher shrinkage than the dense ones. This suggests that in the porous samples, the ceramic particles encountered fewer barriers from surrounding particles, making it easier for the structure to shrink.

Table 4-1: Main features of the slurry constituents, of the green and sintered samples produced from DBM and WBM of HA-AR1 powders.

Batch	Powder	Mean particle size (µm)	Solid loading (%)	Agar (% related to water)	SDS (%)	Green density (g/cm^3)	Final density (g/cm^3)	Shrinkage (%)	Porosity (%)
D1-FA	DBM	1.62	55	1.3	1.2	0.43±0.01	0.66±0.02	15.44±0.79	79.0±0.5
D1-FB		1.71	62	1.1	1.2	0.39±0.61	0.58±0.02	13.53±0.61	81.2±0.7
D1-FC		1.66	62	1.3	1.2	0.47±0.16	0.72±0.01	14.80±0.56	76.8±0.2
W1-FA	WBM	0.71	44	1.3	1.2	0.53±0.53	1.02±0.04	21.42±0.53	67.2±1.3
W1-FB		0.65	44	1.2	1.2	0.44±0.28	0.84±0.01	20.95±0.56	73.1±0.4
W1-FC		0.68	41	1.2	2.0	0.43±0.32	0.82±0.03	21.82±0.28	76.8±1.0
W1-FD		0.79	41	1.3	1.2	0.41±0.27	0.76±0.03	20.87±0.33	75.6±0.8
W1-FE		0.78	41	1.4	1.2	0.43±0.30	0.80±0.02	20.90±0.34	74.0±0.5
W1-FF		0.65	41	1.5	1.2	0.46±0.28	0.89±0.01	21.59±0.10	71.5±0.4

Figure 4-4 depicts some representative FESEM images, showing the microstructure of the struts of the sintered porous ceramics prepared from DBM and WBM of HA-AR1 powders. First, in the left image, the high pores interconnectivity is evident thanks to the numerous windows, in almost spherical shape on the pores walls. Then, it can be observed that contrary to DBM samples, in which residual pores between particles can be easily observed (see the arrows in the left image), well-densified struts were recognized in the WBM samples. This difference is imputed to the higher sinterability of WBM powder, which resulted in the elimination of the intergranular pores, as demonstrated by dilatometry measurements and FESEM observations of dense samples. It should be mentioned that, while well-densified struts provide higher mechanical properties to the porous ceramic parts, the presence of micronic or submicronic residual pores enhance cell adhesion and proliferation and facilitate fibrovascular colonization, thus improving the biological performance of the porous scaffold [9,10]. Therefore, since the densification degree can be tailored by controlling the sintering parameters, as described in the previous chapter, it will be possible to design and tailor the porous ceramics architecture towards specific mechanical or biological functions.

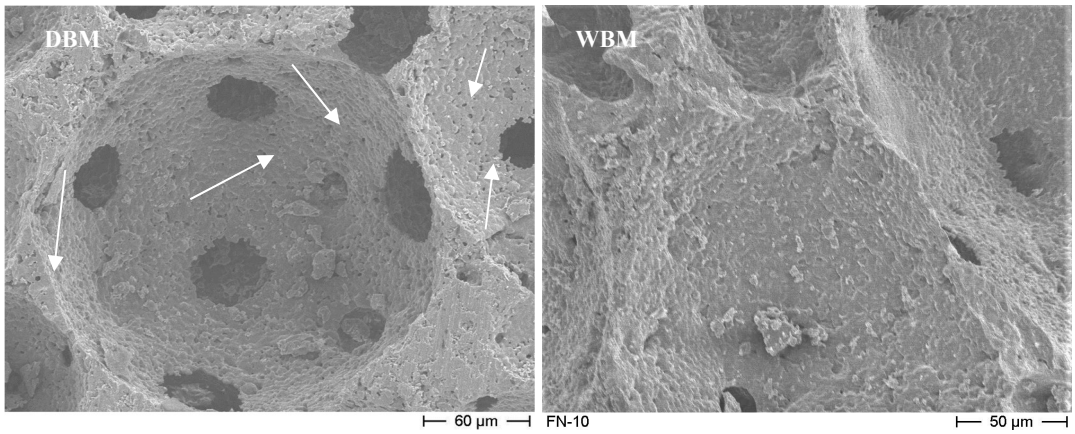

Figure 4-4: FESEM images of the porous ceramics produced from DBM and WBM of HA-AR1 powders.

A deepening of the role of the slurry composition on the microstructural features of the sintered porous ceramics is presented in the followings. First, in order to highlight the role of the agar content on final structural features, Figure 4-5 depicts the microstructure of two DBM samples (namely, D1-FB and D1-FC), characterised by the same solid loading (62%) but different agar concentrations (1.1% and 1.3%, respectively). The corresponding pore size distributions, obtained by image analysis of at least 800 pores for each sample, are depicted in Figure 4-6. While the range of the available pores sizes was comparable, it can be seen that increasing the agar content in D1-FC resulted in a higher fraction of smaller pores.

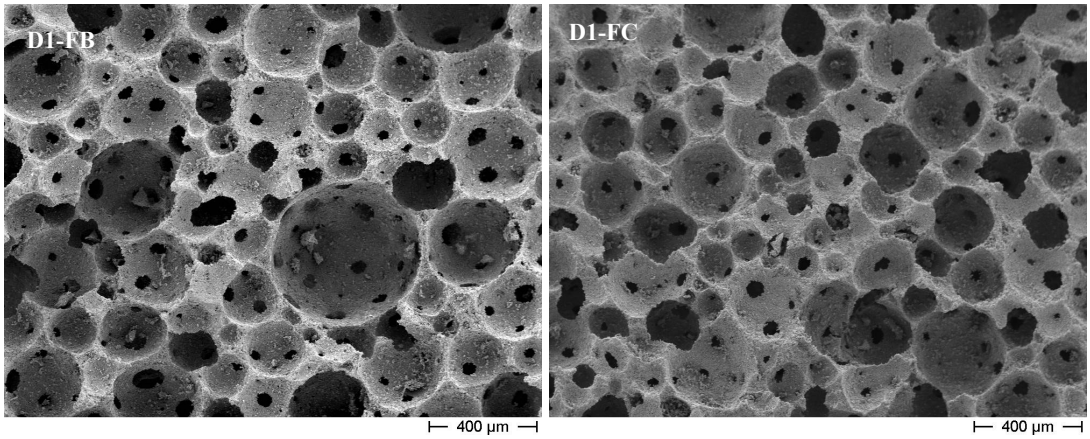

Figure 4-5: Cross-sections FESEM micrographs of two DBM samples, characterised by the same solid loading (62%) and different agar amounts (1.1% for D1-FB, and 1.3% for F1-FC).

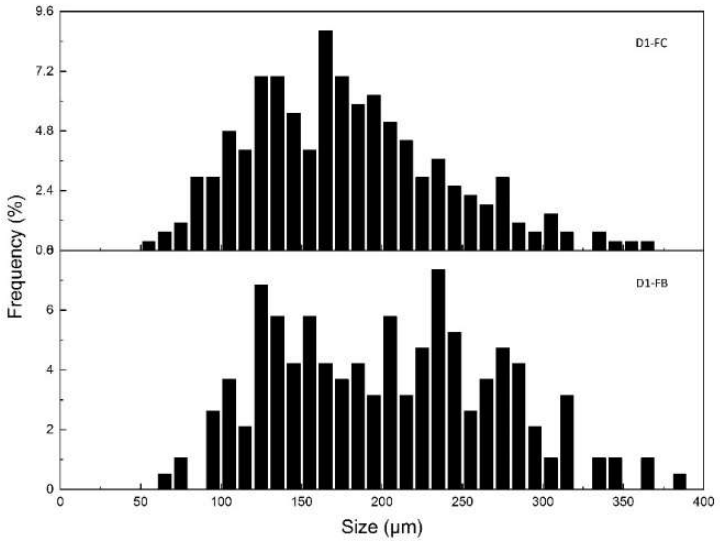

Figure 4-6: Pore size distribution (in number) of the pores for two DBM samples characterised by the same solid loading (62%) and different agar amounts (1.1% for D1-FB, and 1.3% for F1-FC).

Table 4-2 presents the data related to pores and windows sizes of D1-FB and D1-FC samples. D_{10}, D_{50} and D_{90} values were derived from cumulative distributions (not depicted) and allowed comparison between samples. From this table the role of agar concentration in the slurry can be appreciated: by increasing the agar amount, total porosity decreased, and pores and windows sizes decreased as well.

Table 4-2: Data related to slurry composition and micro/macrostructural features of some DBM sintered porous ceramics

	Solid loading (%)	Agar (%)	SDS (%)	Porosity (%)	Mean pore size (µm)	Mean window size (µm)	D_{10} (µm)	D_{50} (µm)	D_{90} (µm)
D1-FB	62	1.1	1.2	81.2±0.7	215	53	115	200	285
D1-FC	62	1.3	1.2	76.8±0.2	177	35	98	165	258

FESEM images of three WBM samples, obtained by 3 different slurry compositions (in terms of powder, agar and SDS contents, as reported in Table 4-3) are depicted in Figure 4-7, while the corresponding pore size distribution, obtained by image analysis, are depicted in Figure 4-8. The different slurry compositions produced porous ceramics characterised by different pores sizes distributions. Data related to slurry composition and microstructural features of the sintered porous ceramics (pores and windows sizes) are collected in Table 4-3. It can be seen that decreasing the agar amount from 1.3% in W1-FA to 1.2% in W1-FB, at the same solid loading and SDS amount led to a 6% increase in the total porosity from 67% to 73%. The porosity increase was accompanied by the increase in the mean pore and window sizes, from 113 µm to 191 µm and from 23 µm to 45 µm, respectively. D10 values show that 10% of the observed pores for the less porous ceramic (W1-FA) were smaller than 19 µm, while this value for W1-FB was 92 µm, proving the presence of very large pores in the latter sample. Decreasing the solid loading from 44% in W1-FB to 41% in W1-FC resulted in a further 3% increase of the porosity. However, this further increase in the porosity was linked to a decrease in the final pore and windows sizes. The decrease in pores and windows sizes can be attributed to the higher SDS amount in the fabrication of the last sample. It is claimed that increasing the surfactant amount leads to higher hydrophilic interfaces on ceramic

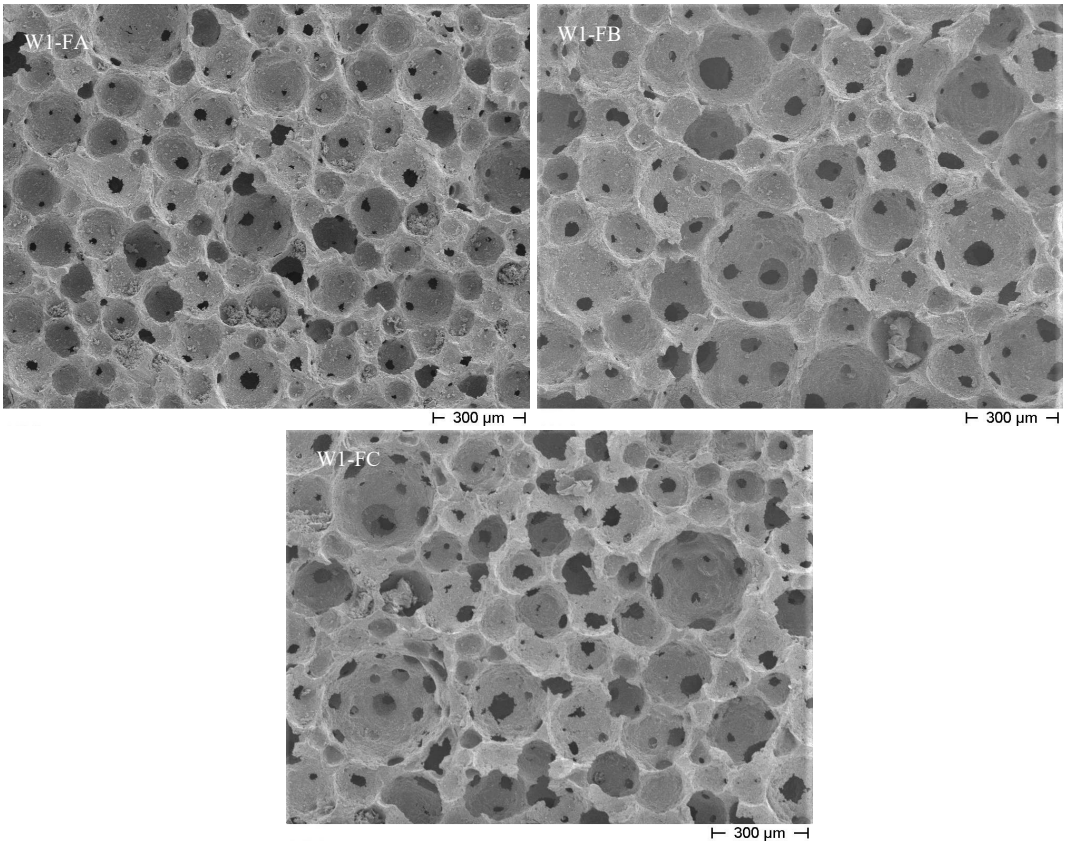

Figure 4-7: Cross-section FESEM micrographs of WBM samples with different solid loadings, SDS and agar amounts.

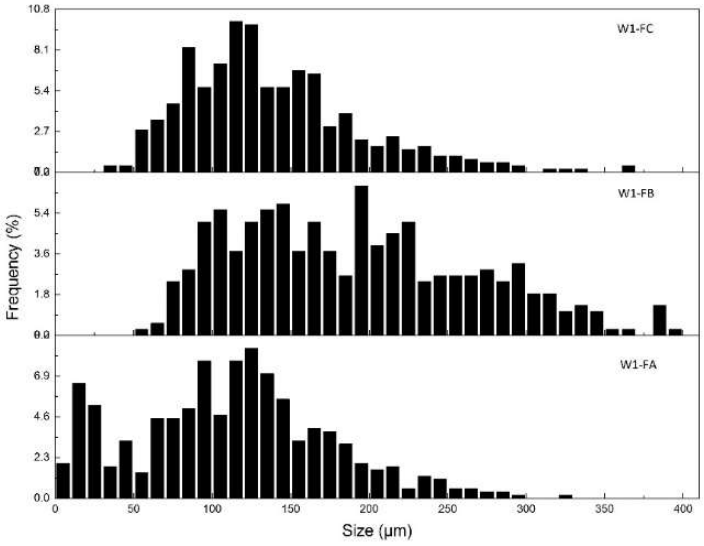

Figure 4-8: Pore size distribution of WBM samples with different solid loadings, SDS and agar amounts.

Table 4-3: Data related to slurry composition and micro/macrostructural features of some WBM sintered porous ceramics.

	Solid loading (%)	Agar (%)	SDS (%)	Porosity (%)	Mean pore size (µm)	Mean window size (µm)	D_{10} (µm)	D_{50} (µm)	D_{90} (µm)
W1-FA	44	1.3	1.2	67.2±1.3	113	23	19	109	186
W1-FB	44	1.2	1.2	73.1±0.4	191	45	92	178	292
W1-FC	41	1.2	2	76.8±1.0	140	34	70	122	212

particles. In other words, the number of hydrophilic members connected to the ceramic particles increases, which favour attracting water molecules. The higher the hydrophilic members, the higher the attracted water molecules. Therefore, the opportunities of contacting a bubble with other ones decreases and as a result bubbles can't merge to produce bigger ones [5]. Therefore, SDS molecules play a role in increasing the stability of the interfacial film and prevent the coalescence between bubbles, responsible for the formation of larger pores.

4.3 HA-AR2 samples: role of the constituents on micro-macrostructural features

Further study on the foaming behaviour of HA suspensions was conducted on the DBM and WBM of HA-AR2 powders. The processing parameters and the results obtained from some of these samples are listed in Table 4-4. It must be mentioned that the produced porous ceramics were not limited to those reported in this table and several supplementary samples were also prepared and investigated to fully understand the foaming behaviour of the suspensions. Table 4-4 shows that, contrary to the samples made from HA-AR1, in general, foaming of DBM slurries resulted in lower green densities compared to samples produced from WBM powders. For example, samples D2-FA (from DBM batch) and W2-FG (from

Table 4-4: Main features of the slurry constituents, of the green and sintered samples produced from DBM and WBM of HA-AR2 powders

sample	Powder	Mean particle size (µm)	Solid loading (%)	Agar (% related to water)	SDS (%)	Green density (g/cm^3)	Final density (g/cm^3)	Shrinkage (%)	Porosity (%)
D2-FA	DBM	1.66	45	1.3	1.0	0.29±0.01	0.46±0.00	16.19±0.19	85.3±0.1
D2-FB		1.69	50	1.3	1.0	0.29±0.00	0.41±0.00	12.38±0.11	86.7±0.0
D2-FC		1.42	60	1.3	1.0	0.35±0.06	0.53±0.03	14.80±0.34	83.0±0.9
W2-FA	WBM	0.80	50	1.3	0.6	0.40±0.02	0.60±0.03	13.65±0.38	80.7±0.8
W2-FB		0.75	41	1.3	0.1	0.44±0.02	0.63±0.03	12.78±0.47	81.3±1.0
W2-FC		0.71	41	1.3	0.1	0.44±0.01	0.66±0.01	14.40±0.22	78.6±0.3
W2-FD		0.64	41	1.45	0.5	0.46±0.01	0.75±0.01	17.22±0.03	75.8±0.3
W2-FE		0.66	41	1.2	0.5	0.42±0.01	0.68±0.02	16.96±0.44	78.1±0.6
W2-FF		0.57	41	1.3	0.5	0.45±0.00	0.74±0.01	17.73±0.48	76.3±0.2
W2-FG		1.06	45	1.3	1.0	0.40±0.00	0.61±0.01	15.36±0.42	80.3±0.2

WBM batch) were prepared within the same slurry parameters (i.e., solid loading, agar and SDS amounts), but the starting powders were characterised by different particle sizes. It can be seen that the DBM green density (0.29 g/cm^3) was significantly lower than WBM one (0.40 g/cm^3). This difference resulted in almost 5% more porosity in the final DBM porous ceramics and was imputed to both lower green density and lower sinterability of the less fine particles, as discussed in the previous chapter.

By comparing Table 4-4 with Table 4-1, it can be observed that while the mean particle sizes of the powders are comparable, the linear shrinkages of the samples made from HA-AR2 were, in general, lower than the ones made from HA-AR1, especially in the case of WBM samples. In fact, for HA-AR1 samples, the linear shrinkage of WBM green structures was always significantly higher compared to DBM ones. On the opposite, when HA-AR2 powders are used, DBM and WBM samples showed comparable shrinkages, the former between 12.38% and 16.19%, the latter between 12.78% and 17.73%.

By focusing on HA-AR2 batch, further observations can be made by comparing the linear shrinkage of porous and dense samples made by both DBM and WBM powders (Tables 3-15 and 3-16). We can observe that the shrinkage of both DBM and WBM porous samples was always lower than the dense ones. This behaviour was in contrast with the behaviour observed for HA-AR1 powders, where the shrinkages of the porous samples were always higher than the dense ones. Further investigations will be necessary to deepen these different behaviours.

In the following sections, the effect of the constituents of the ceramic slurries on the foaming behaviour of HA-AR2 will be presented and at the end of this chapter, the mechanical properties of the obtained samples will be studied.

4.3.1 Effect of surfactant concentration on porosity

Figure 4-9 illustrates the effect of different SDS amounts on the green and sintered porosity of HA porous ceramics. The samples were produced from slurries at 45% solid loading and 1.3% agar. The SDS amount ranged from 0.125 to 3 wt%. As shown in this figure, it is not possible to determine a clear relationship between the surfactant concentration and the green and sintered porosities and these values were fluctuating with changing the surfactant concentration. This observation is in agreement with the study of Park et al. [2], who investigated the effect of SDS concentration on the final pores sizes and accordingly the final porosity levels of cordierite gelcast porous ceramics. The authors produced porous parts at different SDS amounts and observed that the final pore sizes didn't change significantly by changing the surfactant concentration in the slurry but by the foaming time. According to the authors, the type of surfactant is the more important factor in controlling cells sizes, while the concentration plays a minor role. However, the dependence of the foam volume to the surfactant concentration has been already reported for HA and alumina bioceramics [4, 11, 12]. Notwithstanding, in the reported works other chemical compounds were used as a surfactant.

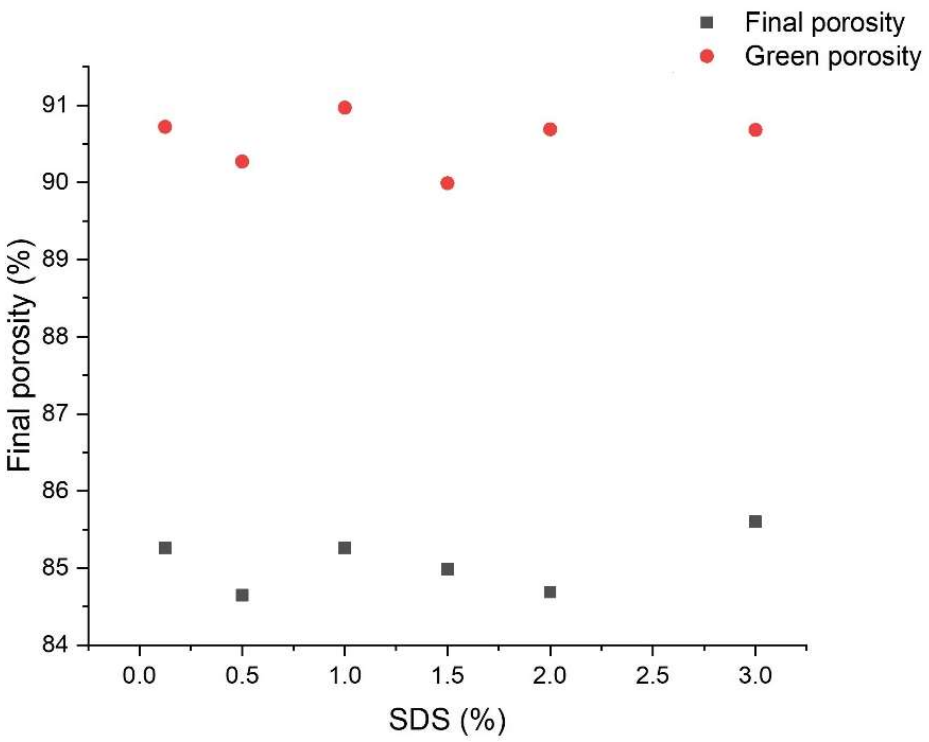

Figure 4-9: Effect of the SDS content on the green and final porosity of HA porous ceramics.

The effect of SDS concentration on the pore size distribution and mean pore sizes are presented in Figures 4-10 and 4-11, respectively. The porous ceramics were produced from a slurry of WBM HA-AR2 powder at 50% solid loading and 1.3% agar. All the produced porous ceramics were composed of a large range of pore

sizes. It can be seen that by changing SDS concentration, the size distribution of the pores and the average pore sizes changed as well. However, it was not possible to find a specific correlation between SDS quantity and the pores sizes which was again in agreement with the work done by Park et al. [2].

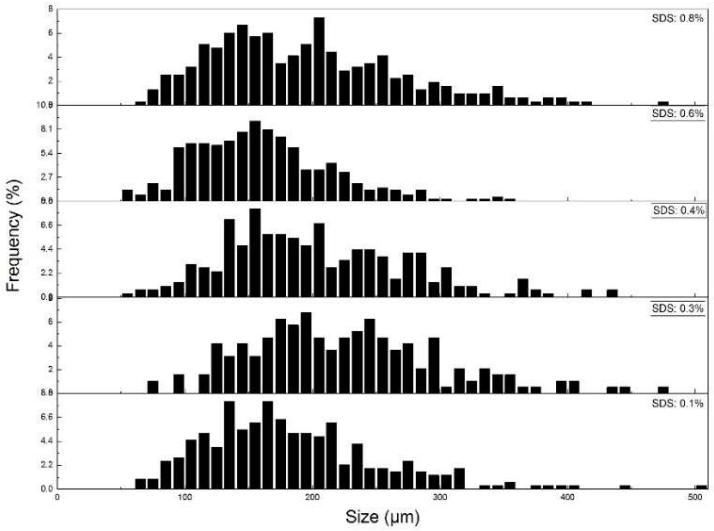

Figure 4-10: Pore size distribution of the porous ceramics produced at different SDS concentrations.

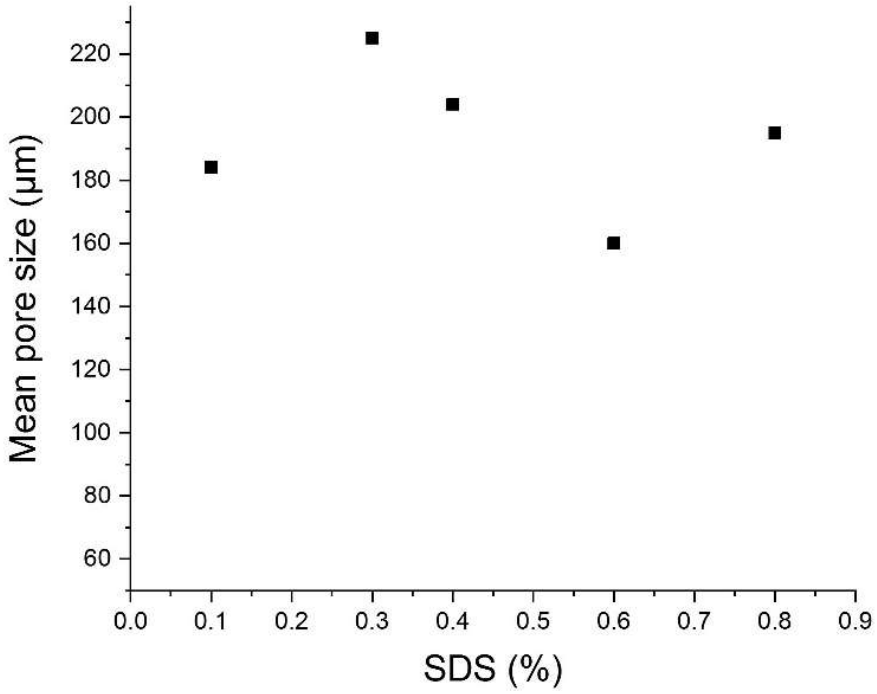

Figure 4-11: Mean pore size as a function of SDS concentration.

4.3.2 Effect of the agar concentration on porosity

The influence of agar concentration on the foaming capability of HA suspensions is illustrated in Figure 4-12. The samples were made from WBM HA-AR2 at the solid loading of 41 wt% and 0.1wt% SDS. Contrary to SDS concentration, in this case, we can observe a clear relationship between agar amount and final porosity. The final porosity decreased proportionally to the increase of agar amount. In fact, at higher agar amount, the slurry showed a viscosity increase, [7] which hinders the mobility of the particles and makes bubble formation and growth more difficult, resulting in a lower porosity.

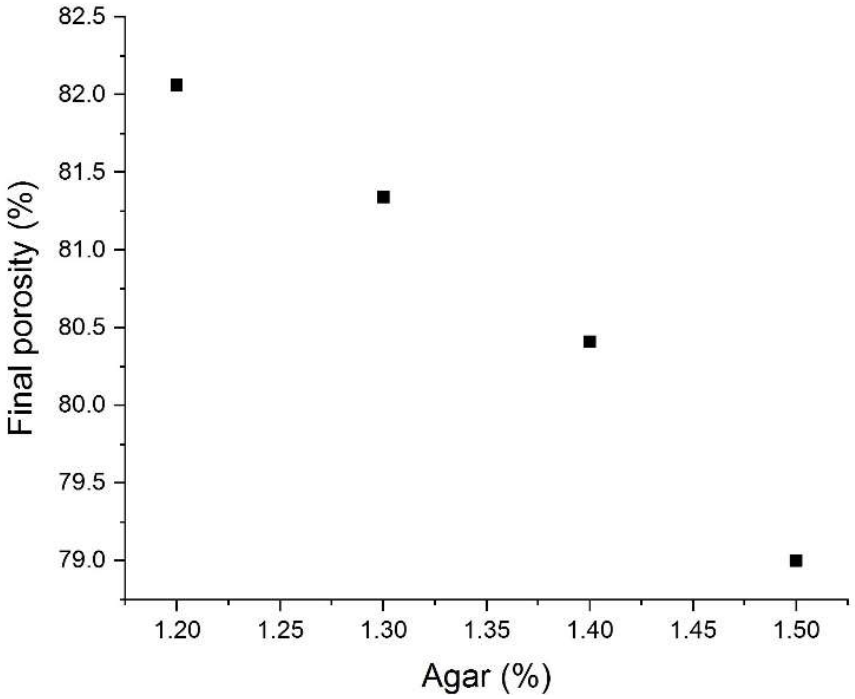

Figure 4-12: Effect of agar concentration on the final porosity. Results observed at 0.1% SDS in the slurry.

The same study was repeated at higher SDS concentration (1wt%), while solid loading was still at 41wt%. Results are presented in Figure 4-13. In contrast to previous results, in this case, the final porosity didn't decrease with increasing the agar amount but fluctuated in a range of 1%. It seems that the SDS amount is the prominent factor in controlling the final porosity and, at higher concentrations, there are enough SDS molecules to effectively decrease the gas/liquid surface tension even at high viscosities. Therefore, foams reach high porosity independent from the agar amount.

Pores size distribution as a function of agar concentration for samples produced at 41 wt% solid loading and 1% SDS content are presented in Figure 4-14. It can be seen that with increasing the agar amount, the fraction of pores with smaller sizes increases. The higher viscosity of the slurry, resulting from the higher amount of

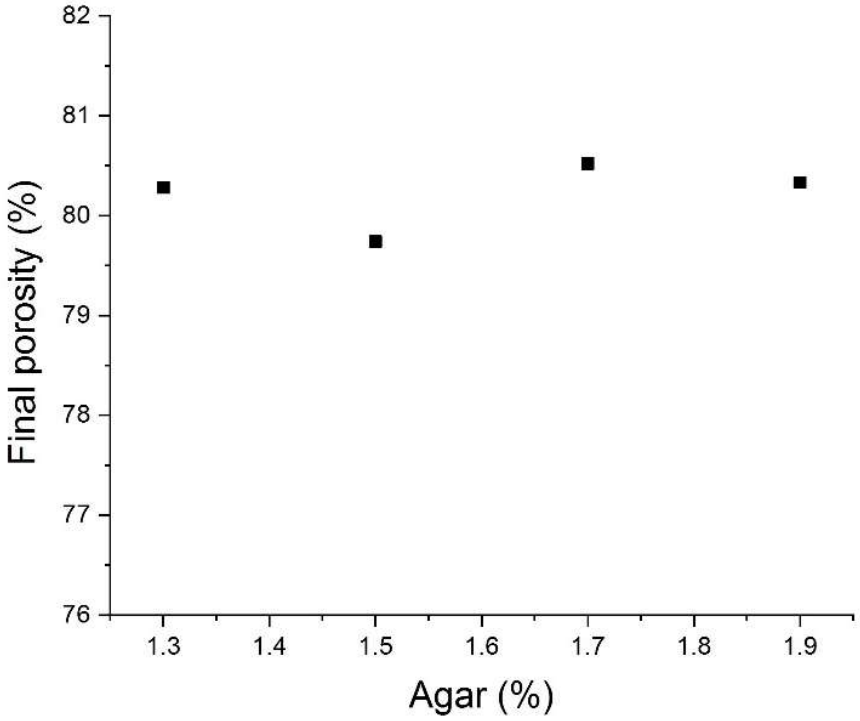

Figure 4-13: Final porosity as a function of agar concentration of the slurry. Results observed at 1% SDS in the slurry.

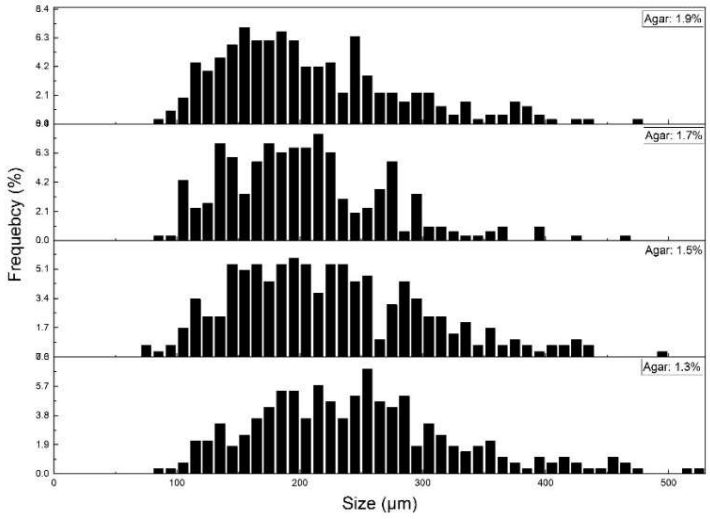

Figure 4-14: Pore size distribution as a function of agar concentration.

agar, limits the mobility of the bubbles. As a result, the interaction of the bubbles is decreased and the possibility of the coalescence of the bubbles to produce bigger ones is lessened [5]. Another related fact is that under the mechanical stirring condition, the bubbles are stretched by a high degree of shear force and forms rod-shaped bubbles. The low surface energy between the air in the bubble and the HA slurry allows bubbles to be further stretched and split into many small ones [5].

Therefore, the number of bubbles with smaller sizes increases in the final porous ceramic part.

The mean pore sizes of the produced porous ceramic parts versus agar content are depicted in Figure 4-15. It can be seen that with increasing the agar amount the mean pore sizes were decreased. However, this decrease became less pronounced by increasing the agar content. To better understand the effect of agar amount on the pore sizes, the viscosity of the slurries has also to be considered during the foam production processes, which can be the object of further studies.

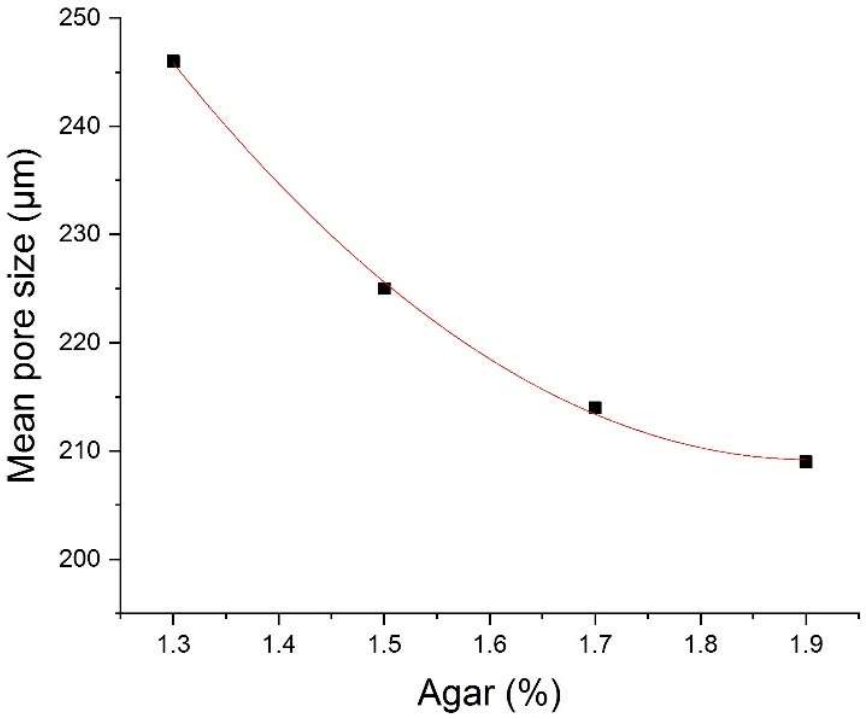

Figure 4-15: Mean pore size as a function of the agar content.

4.3.3 Effect of solid loading on porosity

The effect of different solid loadings on the foaming characteristics was studied as well. Slurries were prepared at a fixed amount of agar (1.3% related to water), and variable solid loadings. Two different SDS concentrations of 0.1 and 0.5% were investigated.

Figure 4-16 shows the porosity of the developed porous ceramics. It can be seen that the final porosities were higher for the samples produced with 0.1% SDS and

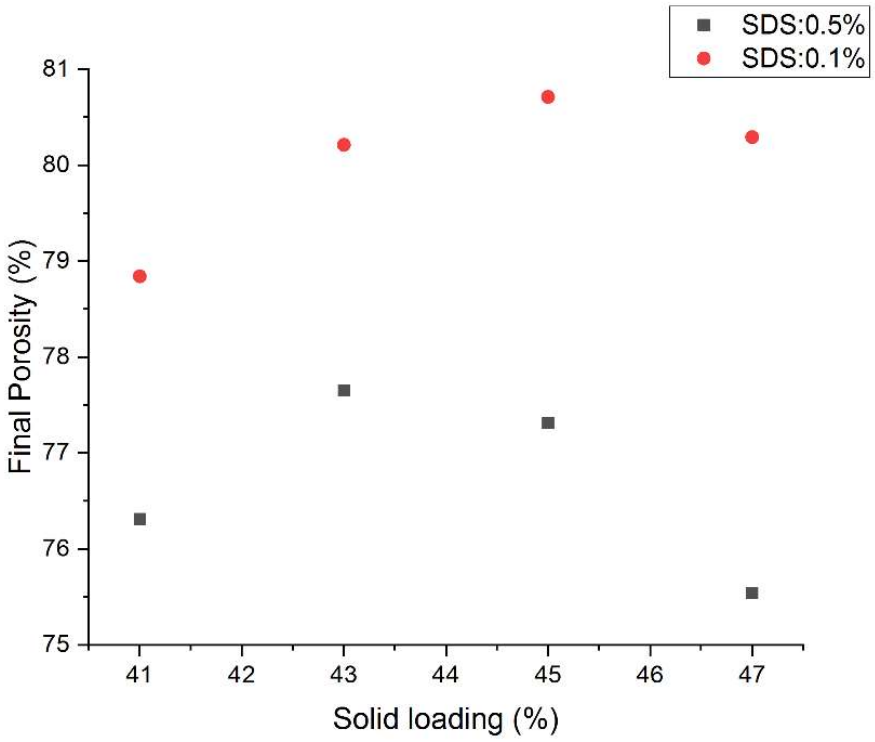

Figure 4-16: Effect of slurry's solid loading on the final porosity of HA porous ceramics.

both trends showed a maximum at a certain solid loading, which corresponded to 43% and 45% for the samples produced at 0.5% and 0.1% SDS, respectively.

Pores size distributions for the samples produced at 0.1% SDS are presented in Figure 4-17. It can be seen that by increasing the solid loading, the number of the bigger pores increased in the porous structure, and the sizes were distributed in a

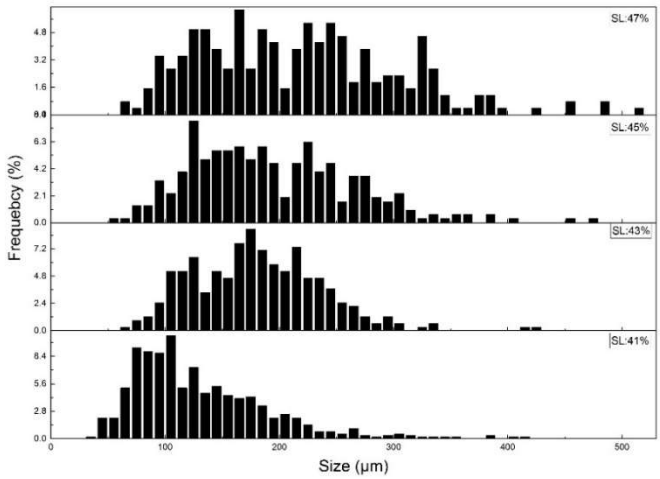

Figure 4-17: Pores size distributions of the sample produced at 0.1% SDS, at different solid loadings.

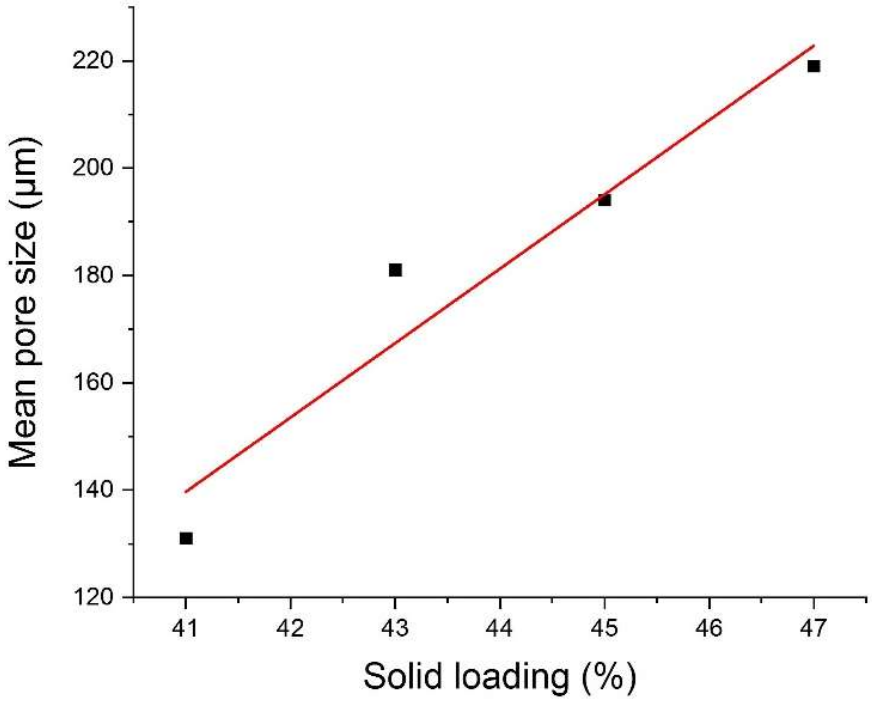

Figure 4-18: Mean pore size as a function of solid loading.

larger range. The mean pores sizes of the produced porous parts as a function of solid loading is depicted in Figure 4-18. By increasing the solid loading, the mean pore size increased showing an almost linear relationship with the slurry's solid loading. As the solid particles' content increases in the slurry, a stronger liquid film around bubbles is produced. Therefore, the split of a stretched bubble to form smaller pores becomes more difficult and, as a result, bigger pores survived in the final material [5].

4.4 Mechanical properties of porous ceramics

The mechanical properties of HA porous samples were studied by means of uniaxial compressive strength. Testing machine and testing conditions were the same as those used for the dense samples.

Figure 4-19 shows a typical stress-strain curve recorded during compressive tests of the HA porous samples. The highly porous samples exhibited the classic behaviour of the porous ceramic. Deformation starts with an initial linear elastic phase followed by a stress plateau due to a progressive damage accumulation owing to the brittle crushing of the solid walls between pores. According to the Ashby model for low relative density open-cell porous parts [13], the initial elastic step can be attributed to cells walls bending or face stretching. Just after the linear phase, there is an increase in the stress resulting from the densification of the damaged material. The observable load reduction in the plateau stage can be attributed to the

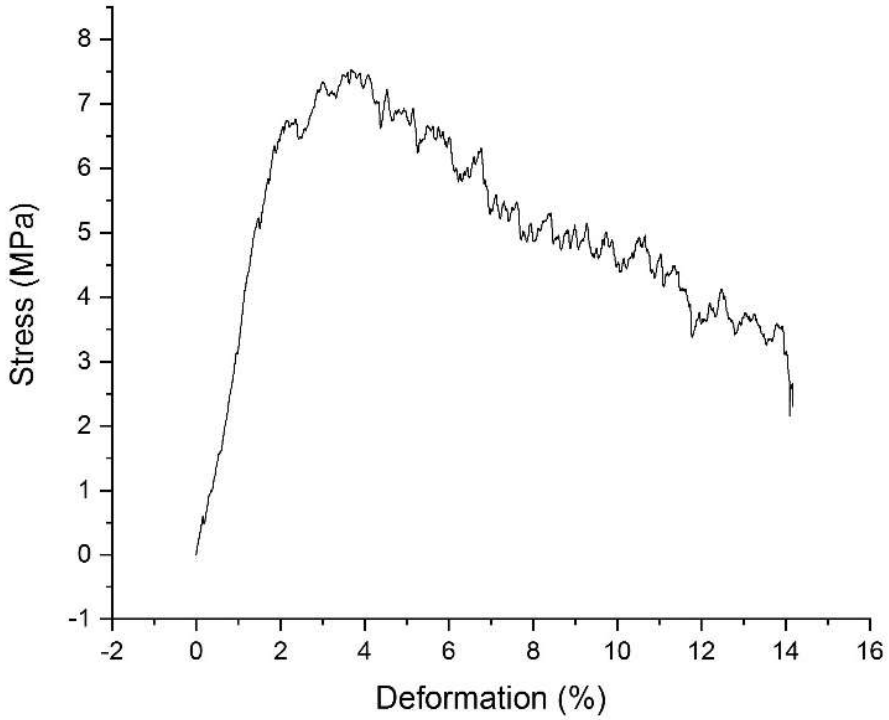

Figure 4-19: Typical stress-strain curve achieved from compression tests of HA porous ceramic samples.

propagation of small cracks in the ceramic, either by wall bending or buckling that leads to sample fragmentation [14].

In contrast to the solid material for which the mechanical properties are controlled by isolated pores, for highly porous material the mechanical behaviour is controlled by the distribution of the solid phase. Because of the short distance between adjacent pores, the maximum size of the cracks is controlled by the thickness of the solid walls between pores. After initiation, the cracks soon reach the walls of the pores, resulting in the solid wall break. Then, another solid wall breaks, as noted in the stress-strain curve [14]. Therefore, a macro-crack with global brittle fracture cannot be developed.

The compressive strengths of the porous materials were calculated by the maximum stress reached during the compression tests. All the tested samples had a compressive strength of more than 2 MPa except one sample which showed the lowest strength of 1.85 MPa, associated with the maximum porosity of 83.7%. The maximum achieved strength was about 15 MPa, associated with the porous sample produced from WBM HA-AR1 powder, characterised by the final porosity of 67.5%.

The compressive strengths of the porous ceramics as a function of the final porosity are presented in Figure 4-20. The strengths logically decreased by increasing the pore volume fractions. The decrease in the mechanical properties with increasing porosity is related to the decrease in the quantity of the material submitted to loading [15]. While, in general, the scatter of the results can be

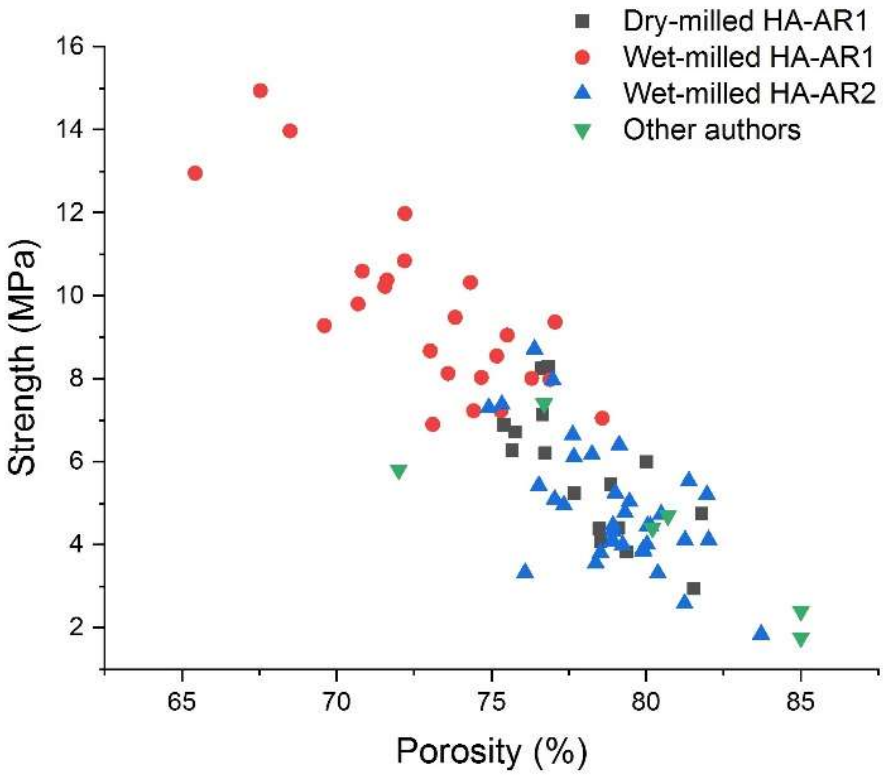

Figure 4-20: Compressive strength of the HA porous samples as a function of final porosity.

confined between two almost closed parallel lines, it can be seen that there is relatively larger scatter of the results with decreasing the porosity. Such a relatively higher scatter can be attributed to brittle fracture which is more likely for the materials with a higher proportion of solid.

The compressive strength results of HA porous parts reported by other authors [16, 17, 18, 19, 20] are also included in Figure 4-20 (green triangles). These results have been selected from scientific papers dealing with porous ceramics produced by direct foaming method and with porosity in the range of current study. It can be seen that there is a good correlation between the results obtained here and the reported literature data.

By comparing the strength of the porous HA samples obtained by the direct foaming method with other routes, it appears that the porous ceramics produced by direct foaming have better mechanical strength than samples produced by other techniques. For example, the compressive strength of HA porous samples produced by the polymeric sponge method was in the range of 2-10 MPa for porosity range 36-60% [16], while we achieved almost the same strength in the porosity range of 70 to 85% and for a lower porosity, the strength even increased to 16 MPa. These results reveal that the direct foaming method has relatively excellent capability in the production of high strength cellular structures.

4.5 Production of bi-layer ceramics

While the design and production of biodegradable scaffolds with desirable biological properties such as osteoconductivity and osteoinductivity are the main challenges in the tissue engineering, an ideal bone graft must also provide sufficient mechanical properties that match the host bone tissue. Despite the fact that highly porous calcium phosphate (CaP) scaffolds with suitable architecture can be designed and fabricated to provide such biological properties, these porous structures lack enough mechanical strength. On the other hand, due to low surface area, dense HA ceramics show a low resorption rate under physiological conditions, which can result in poor fixation between the scaffold and the newly generated bone [21].

Functionally graded materials (FGM) are characterised by gradual transitions in either compositions/constituents or microstructures (e.g., grain size, texture, porosity, etc.), along with at least one direction, leading to functional changes associated with at least one property [22]. In other words, FGMs are multifunctional structures which are designed to provide two or more functions at the same time.

Many natural tissues are examples of FGM structures. Simple observation of natural bone reveals that it consists of a graded structure in which the pore size and distribution vary across its transverse section. Dense and solid cortical bone in the outer layer and spongy porous cancellous bone in the inner layer compose the whole structure in which each layer has specific functions to perform [23].

The described morphological variations in bone structure can be inspiring for the design of artificial bone grafts. In fact, the ability to produce multifunctional materials with tailored properties has escalated the interest to FGM in recent years. To better mimic the natural bone, the scaffold needs to be designed as a multilayer structure, consisting of different layers of porous and dense structures, to fulfil the biological and mechanical requirements of the target tissue. A key in achieving the expected properties is to provide continuity at the interfaces of the layers [24].

CaP coating on titanium substrate is one of the earlier studied FGMs in the biomedical application [24, 25]. This structure exploits the excellent bioactivity of HA, with the high strength and toughness of Ti substrate. The coating layer can be designed to consists of two different CaPs with different properties. For example, the upper layer was made from CaP phases, such as tricalcium phosphate (TCP) or amorphous calcium phosphate (ACP), with better bone formation properties, while the layer underneath is a dense HA layer with lower resorption rate and stronger bonding to the implant's surface [27]. However, disadvantages such as poor interfacial bonding between ceramic and metal [28] and thermally induced microcracks in the surface of the material due to heterogeneous characteristic along the thickness direction of FGM [25] limit the applicability of these structures. Other works focused on HA/zirconia/alumina FGM bio-composites [29, 30], but crack propagation at the interface (due to the large difference of fracture toughness and undesirable reaction between HA and zirconia) and formation of intermediate layers are some major drawbacks of this system [29].

Porosity-graded structures based on CaP bioceramics have been developed as well. They are designed to meet both biological and mechanical requirements. The outer porous layer is designed to provide access for cells, blood vessels, and enhance bone formation, while the inner ceramic should improve mechanical strength. These kinds of materials have been produced in two or more layers, and mechanical and biological properties were shown to be improved compared to single-layer materials [30, 31, 32]. Depending on the final application, the configuration of dense and porous layer might be reverse, i.e. structures with dense core material and external porous layer, or the opposite configuration. Another use for such a scaffold is in the field of bioresorbable bone substitution, where graded implant porosity can grant guided degradation progress and cell ingrowth [27].

Functionally graded porous HA ceramics can be produced using alternative routes, e.g. sintering of laminated structures of HA tapes filled with polymer spheres [34] or combining biodegradable polyesters such as polylactide, polylactide-*co*-glycolide and polyglycolide, with carbonated nanocrystalline HA [34].

Wang et al. [33] prepared functionally graded calcium phosphate in which the porosity of three layers increased from 0% to30% and finally to 60%. Authors found that at similar overall porosity the mechanical properties of the three-layer FGM was higher than the homogenous porous CP.

Lee et al. [30] produced cylindrical bilayer HA samples using sequential freeze-casting. The porosity of the inner and outer layer was controlled by changing the initial HA solid loading of the slurries. In fact, by increasing the solid loading from 10% to 50 vol%, the porosity decreased from 78% to 10%. Although there were tight adhesions of the two layers in the green state, different sintering shrinkage led to delamination of layers characterised by a large difference in porosity amount.

Chamari et al. [34] combined sacrificial template process and freeze-drying to produce porous core and dense shell respectively and obtained two-layer HA scaffolds.

In current work, we exploited the already optimised gelcasting techniques for the production of the dense and porous samples in order to produce bi-layer HA samples from WBM powder. The bilayer samples were fabricated by positioning cylindrical green dense samples at the centre of larger moulds and filling the residual vacant space with HA foams. After casting of the porous layer, the whole structures were demoulded, dried and sintered under the same conditions already described and optimised for the production of the porous or dense samples.

A representative digital photograph of a bi-layer sample, fabricated by this technology, is presented in Figure 4-21. As previously described, this architecture was designed and developed to provide the necessary biological functions through the outer porous layer, and at the same time assures sufficient mechanical properties through the core dense part.

Figure 4-21: Bi-layer sample produced from WBM powder.

To obtain continuous and well-attached interface between the two layers both layers must undergo similar shrinkage during the sintering stage. This aspect has a key importance, especially when multi-layer samples are produced from WBM powder, where different milling times result in different particle size distributions, and therefore different linear shrinkages during sintering. To this aim, both layers must be produced from the same batch of the powders, under controlled and optimised processing parameters. The interface of a representative bi-layer sample is shown in Figure 4-22. We can observe that the manufacturing of both layers from powder with similar sinterability gave rise to a defect-free homogenous interface where the two layers were uniformly attached without distinctive separation.

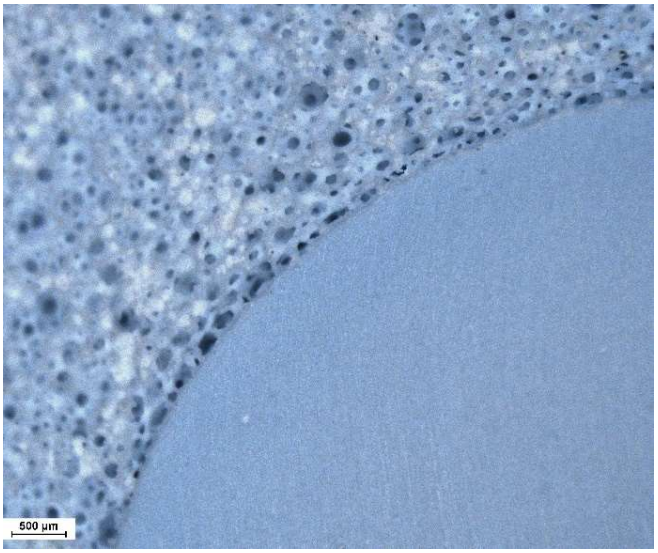

Figure 4-22: The interface of dense and porous layers indicating uniform and homogeneous attachment of the two layers.

The produced bilayer structures prove the feasibility of exploiting several advantages of the gelcasting method in the production of multilayer multifunctional scaffolds. In this design, the outer porous part enhances interlocking with the surrounding bone and the inner dense part acts as a load-bearing region. By tailoring the ratio between the two parts and their structural position, the functional diversity of the graded porous HA scaffolds can be expanded [35]. Furthermore, this graded structure could be added by further functionalities. An example will be provided in the last chapter, in which a third polymeric porous layer will be added, and functionalized with antibacterial agents. Therefore, such an innovative structure has potential for use in the biomedical field, but can also be viewed as a model system towards the design and fabrication of further innovative architectures with targeted multi-functionalities.

4.6 Conclusion

Highly porous ceramics characterised by hierarchical interconnected pore structure with the porosity range of 63-87% were obtained from DBM and WBM HA powders using the gelcasting of foam technique. The slurry compositions were tailored to obtain a large range of pore sizes even for the sample with the lowest porosity. The pores and windows sizes ranged from 4 to 656 μm and 2 to 327 μm, respectively. It was observed that changing the SDS concentration, as the foaming agent, didn't have any particular effect on the final porosity and pore sizes. On the other hand, it was found that at low SDS concentrations, increasing the agar amount led to a decrease in the final porosity. The effect of the solid loading on the porosity also was found to be dependent on the SDS concentration.

The typical stress-strain curves of the porous ceramics were achieved from the compression tests of the porous parts. The strength increased reasonably by decreasing the porosity percentage. The minimum and maximum compressive strengths were 2 and 15 MPa corresponding to the samples with the minimum and the maximum porosity, respectively.

Functionally graded structures were also produced utilizing already optimised gelacasting techniques for dense and porous samples. The bilayer samples were designed to have improved mechanical strength of the dense samples along with the higher biological performance of the porous samples presenting the multifunctional properties.

References

[1] X. Mao, S. Shimai and S. Wang, "Gelcasting of alumina foams consolidated by epoxy resin," *Journal of the European Ceramic Society ,* vol. 28, pp. 217-222, 2008.

[2] J. K. Park, J. S. Lee and S. I. Lee, "Preparation of porous cordierite using gelcasting method and its feasibility as a filter," *Journal of Porous Materials,* vol. 9, pp. 203-210, 2002.

[3] S. Padilla, M. Vallet-Regı, M. Ginebra and F. Gil, "Processing and mechanical properties of hydroxyapatite pieces obtained by the gelcasting method," *Journal of the European Ceramic Society,* vol. 25, p. 375–383, 2005.

[4] P. Sepulveda and J. Binner, "Processing of cellular ceramics by foaming and in situ polymerisation of organic monomers," *Journal of the European Ceramic Society,* vol. 19, pp. 2059-2066, 1999.

[5] H. Kim, S. Lee, Y. Hanc and J. Park, "Control of pore size in ceramic foams: Influence of surfactant concentration," *Materials Chemistry and Physics,* vol. 113, pp. 441-444, 2009.

[6] C. Gloxhuber and K. Kunster, Anionic Surfactants: Biochemistry, toxicology, dermatology (2nd ed.), New York: Dekker, 1992.

[7] M. Potoczek, "Hydroxyapatite foams produced by gelcasting using agarose," *Materials Letters,* vol. 62, pp. 1055-1057, 2008.

[8] M. Potoczek, "Gelcasting of alumina foams using agarose solutions," *Ceramics International,* vol. 34, p. 661–667, 2008.

[9] P. Sepulveda, H. A. Bressiani, J. Bressiani, L. Meseguer and B. Konig Jr, "Synthesis and properties of ceramic foams for hard tissue repair," *Key Engineering Materials,* vol. 218, pp. 413-416, 2002.

[10] I. V. Antoniac, Handbook of Bioceramics and Biocomposites, Springer, 2016.

[11] M. Potoczek, A. Zima, Z. Paszkiewicz and A. Slosarczyk, "Manufacturing of highly porous calcium phosphate bioceramics via gel-

casting using agarose," *Ceramics International,* vol. 35, pp. 2249-2254, 2009.

[12] L. J. Gibson and M. F. Ashby, Cellular solids: structure and properties, Cambridge University Press, 1999.

[13] S. Meille, M. Lombardi, J. Chevalier and L. Montanaro, "Mechanical properties of porous ceramics in compression: On the transition between elastic, brittle, and cellular behavior," *Journal of the European Ceramic Society ,* vol. 32, pp. 3959-3967, 2012.

[14] J. Le Huec, T. Schaeverbeke, D. Clement, J. Faber and A. Le Rebeller, "Influence of porosity on the mechanical resistance of hydroxyapatite ceramics under compressive stress," *Biomaterials,* vol. 16, no. 2, pp. 113-118, 1995.

[15] M. Sakamoto, M. Nakasu, T. Matsumoto and H. Okihana, "Development of superporous hydroxyapatites and their examination with a culture of primary rat osteoblasts," *Journal of Biomedical Materials research. Part A,* vol. 82, no. 1, pp. 238-242, 2007.

[16] S. Tarafder, V. K. Balla, N. M. Davies, A. Bandyopadhyay and S. Bose, "Microwave-sintered 3D printed tricalcium phosphate scaffolds for bone tissue engineering," *Journal of Tissue Engineering and Regenerative Medicine,* vol. 7, no. 8, pp. 631-641, 2013.

[17] S. Bose, M. Roy and A. Bandyopadhyay, "Recent advances in bone tissue engineering scaffolds," *Trends in Biotechnology,* vol. 30, pp. 546-554, 2012.

[18] L. Cyster, D. Grant, S. Howdle, F. Rose, D. Irvine, D. Freeman, C. Scotchford and K. Shakesheff, "The influence of dispersant concentration on the pore morphology of hydroxyapatite ceramics for bone tissue engineering," *Biomaterials,* vol. 26, pp. 697-702, 2005.

[19] P. Sepulveda, J. Binner, S. Rogero, O. Higa and J. Bressiani, "Production of porous hydroxyapatite by the gel-casting of foams and cytotoxic evaluation," *Journal of biomedical Materials Research,* vol. 50, no. 1, pp. 27-34, 2000.

[20] I. Sopyan and J. Kaur, "Preparation and characterization of porous hydroxyapatite through polymeric sponge method," *Ceramics International ,* vol. 35, pp. 3161-3168, 2009.

[21] R. Z. LeGeros, "Properties of osteoconductive biomaterials: Calcium phosphates," *Clinical Orthopaedics and Related Research,* vol. 395, pp. 81-98, 2002.

[22] C. Zhang, F. Chen, Z. Huang, M. Jia, G. Chen, Y. Ye, Y. Lin, W. Liu, B. Chen, Q. Shen, L. Zhang and E. J. Lavernia, "Additive manufacturing of functionally graded materials: A review," *Materials Science & Engineering A 764 (2019),* vol. 764, p. 138209, 2019.

[23] K. Leong, C. Chua, N. Sudarmadji and W. Yeong, "Engineering functionally graded tissue engineering scaffolds," *Journal of Mechanical Behaviour of Biomedical Materials I,* pp. 140-152, 2008.

[24] Y. Miyamoto, A. Kaysser, B. Rabin, A. Kawasaki and R. G. Ford, Functinally graded materials, design, preocessing and applications, Springer, 1999.

[25] C. Chu, J. Zhu, Z. Yin and P. Lin, "Optimal design and fabrication of hydroxyapatite–Ti asymmetrical functionally graded biomaterial," *Materials Science and Engineering A,* vol. 348, pp. 244-250, 2003.

[26] M. N. Rahaman, Ceramic processing, second edition, CRC Press, 2017.

[27] C. Han, Y. Li, Q. Wang, D. Cai, Q. Wei, L. Yang, S. Wen, J. Liu and Y. Shi, "Titanium/hydroxyapatite (Ti/HA) gradient materials with quasi-continuous ratios fabricated by SLM: Material interface and fracture toughness," *Materials and Design,* vol. 141, pp. 256-266, 2018.

[28] H. Guo, K. Aik Khor, Y. Chiang Boey and X. Miao, "Laminated and functionally graded hydroxyapatite/yttria stabilized tetragonal zirconia composites fabricated by spark plasma sintering," *Biomaterials ,* vol. 24, p. 6678675, 2003.

[29] R. Gandhi, J. Roderick Davey and N. N. Mahomed, "Hydroxyapatite coated femoral stems in primary total hip arthroplasty: a meta-analysis," *The Journal of Arthroplasty,* vol. 24, no. 1, pp. 38-42, 2009.

[30] H. Lee, T. S. Jang, J. Song, H. E. Kim and H. D. Jung, "The production of porous hydroxyapatite scaffolds with graded porosity by sequential freeze-casting," *Materials,* vol. 10, no. 4, p. 367, 2017.

[31] Q. Fu, M. N. Rahaman, F. Dogan and B. S. Ba, "Freeze-cast hydroxyapatite scaffolds for bone tissue engineering applications," *Biomedical Materials,* vol. 3, 2008.

[32] Q. Wang, Q. Wang and C. Wang, "Preparation and evaluation of a biomimetic scaffold with porosity gradients in vitro," *Anais da Academia Brasileira de Ciências,* vol. 84, no. 1, pp. 9-16, 2012.

[33] W. Pompe, H. Worch, M. Epple, W. Friess, M. Gelinsky, P. Greil, U. Hempele, D. Scharnweber and K. Schulte, "Functionally graded materials for biomedical applications," *Materials Science and Engineering A,* vol. 362, pp. 40-60, 2003.

[34] S. Chamary, D. Hautcoeur, J. C. Hornez, A. Leriche and F. Cambier, "Bio-inspired hydroxyapatite dual core-shell structure for bone substitutes," *Journal of the European Ceramic Society,* vol. 37, pp. 5321-5327, 2017.

[35] H. D. Jung, T. S. Jang, L. Wang, H. E. Kim, Y. H. Koh and J. Song, "Novel strategy for mechanically tunable and bioactive metal implants," *Biomaterials,* vol. 37, pp. 49-61, 2015.

Chapter 5 Robocasting: Elaboration of Dense, Porous and Multi-layer structures

Abstract

The robocasting technique was used for the production of dense, porous and functionally graded multilayer parts from as-received and wet ball milled HA. The parts were printed and sintered in different three-dimensional (3-D) geometries; cubic porous part, cylindrical dense part and cylindrical multilayer part (built as an inner dense part, surrounded by concentric rings). Different ink formulations were needed for successful production of each part. The physical qualities of the samples such as filaments and pores sizes, density and porosity were determinded before and after sintering. The samples were characterised by fully dense struts comparable to gelcast samples. FESEM microstructural observations revealed that the successive layers were well squeezed together, and no borderline were observed between them. Optimisation of the paste formulation led to the production of multilayer structures with pore sizes more than 1.3 mm which is not achievable with other methods. The mechanical properties were found comparable with the results already reported in the literature for robocast calcium phosphate materials. Cracks initiation and propagation during compression tests were monitored utilizing an environmental SEM, equipped with an in-situ compression test device.

Abbreviations

BCP	Biphasic calcium phosphate
BM	Ball-milled
CAD	Computer-aided design
CaP	Calcium phosphate
CFU	Colony Forming Units
CT-scan	Computed tomography scan
DCPD	Dicalcium phosphate dihydrate
EDX	Energy-dispersive X-ray spectroscopy
FESEM	Field emission scanning electron microscopy
FGM	Functionally graded material
HA	Hydroxyapatite
HA-AR1	As-received hydroxyapatite powder, batch n.1
HA-AR2	As-received hydroxyapatite powder, batch n.2
HCA	Hydroxycarbonate apatite
ISO	International standard organisation
OCP	Octacalcium phosphate
PCL	polycaprolactone
SBF	Simulated body fluid
TEM	Transmission electron microscopy
TTCP	Tetracalcium phosphate
WBM	Wet ball milling
XRD	X-ray diffractometry
β-TCP	β-tricalcium phosphate

5.1 Introduction

Among the wide variety of additive manufacturing technologies, direct-writing techniques are particularly suitable for the fabrication of ceramic parts. The direct-writing techniques are fabrication methods in which a pattern-generating device, e.g. an ink deposition nozzle, is controlled by a computer to create materials with controlled architecture and composition [1].

Robocasting is a continuous (filamentary) direct-writing technique (Figure 5-1) that relies on the deposition of ceramic inks to create structures layer-by-layer. The inks are typically colloidal suspensions in a liquid formulated with the desired rheological (or flow) behaviour. Apparent viscosity, yield stress under shear and compression, and viscoelastic properties (i.e. the shear loss and elastic moduli) are important rheological parameters that are tailored for the specific application of interest. The greatest challenge for designing inks are three dimensional (3-D) periodic structures because they should contain self-supporting (or spanning) features [1]. In fact, the main application of the robocasting technique is for the production of complex 3-D scaffolds with tailored porosities. There is good control over the porosity fraction and pores size and interconnection with this method that is rarely possible with conventional methods such as polymer infiltration and foaming techniques.

Figure 5-1: Schematic view of ink-based continuous filament deposition. Reprinted from [1] with the permission of Elsevier under the license no 4771311338686.

In view of the materials that can be processed, robocasting is a very flexible technique which has been employed for a wide variety of ceramic materials. Once a ceramic ink with suitable rheology is produced, it is possible to print the desired structure. Successful production of parts with complex geometries and pore structures from ceramic materials such as alumina [187, 188, 189, 190], silicon carbide [188, 191], bioglasses [7, 8] and electroceramics [9] has been already

reported in the literature. The simplicity and relatively low cost of the robocasting technology make it possible for the research and academic centres worldwide to make researches based on this fabrication technique.

Several research studies related to the robocasting of calcium phosphate bioceramics have been accomplished, due to their important application in tissue engineering which demands complex shapes with tailored microstructures. Production of dense and porous structures of hydroxyapatite (HA) and β-tricalcium phosphate (β-TCP) with a different combination of mechanical and biological properties have been described in several scientific papers. Studies range from the production of simple geometries to customized complex structures designed based on the individual patients data [10, 11, 12, 13, 14, 15, 16]. For instance, Mishna et al [10] produced periodic scaffolds from concentrated HA ink. The scaffolds consisted of a 3-D tetragonal mesh with different final porosities and pores sizes, achieved by changing the filament size and the spacing between them. Miranda et al. [11, 17] used a similar formulation in the production of periodic porous scaffolds of HA and β-TCP and analysed the compressive strength of the scaffolds. They found that the fracture strength of the HA scaffolds was more than two folds the strength of the β-TCP scaffolds. Such a significant difference was attributed to the microcrack formation during sintering of β-TCP material. Moreover, they found that the compressive strength of the HA scaffolds almost doubled after immersion in the simulated body fluid (SBF) for 20 days thanks to bone-like apatite growth on the surface of the HA rods. Such an improvement, which allow achieving the strength values similar to the cortical bone, was not achieved for the β-TCP scaffolds, due to the non-active nature of the β-TCP ceramic in contact with body fluid. While the same increase can be expected for HA scaffolds, independently of the fabrication method, the apatite growth may reduce the pore interconnectivity in scaffolds produced by conventional methods due to the limited pore and windows size achievable. On the opposite, controlled immersion in SBF seems a simple way for improving the mechanical performance of structures from apatite-forming materials fabricated by robocasting [11], without affecting the interconnectivity of the structure, and therefore their biological performance.

Some works focus on the improvement of the mechanical properties thanks to the production of hybrid polymer/ceramic structures, exploiting various polymer infiltration methods [12, 14, 18]. Martinez-Vazquez et al. [12] produced β-TCP scaffolds by robocasting technique, characterised by 36% macroporosity, and used polymer infiltration to produce hybrid impregnated ceramic/polymer structures. They proved that infiltration with polycaprolactone (PCL) or polylactic acid (PLA), two biodegradable polymers, increases the compressive strength of the ceramic scaffolds more than three and six-folds, respectively.

In a recently published report, Paredes et al. [14] fabricated periodic 3-D HA scaffolds by robocasting constructed from hollow rods. To this aim, the authors changed the regular nozzle with a log-pile structure of hollow rods, a coaxial needle, to extrude HA tubes with the outer and inner diameter of 1.28 and 0.54 mm, respectively. The scaffold was composed of 42% macroporosity between rods and

additional 11% macroporosity due to inner channels. The HA/PCL hybrid scaffolds were obtained by filling the internal channels with PCL. It was shown that infiltration of the hollow rods with PCL polymer increased the compressive strength of almost two folds. However, the strength of the scaffold produced from dense ceramic filaments was much higher than the impregnated scaffold.

Some attempts have been made to increase the biological performance of the robocast scaffolds with the addition of microporosities in the range of 1-10 μm through the freeze-drying method. For example, in two independent works, Rolecek et al. [15] and Vazquez et al. [19] obtained multi-scale porous HA scaffolds by controlled freezing of ceramic suspensions in several steps, followed by sublimation of the produced ice crystals. While the introduction of the microporosity is promising to improve the cell proliferation, the increase in biological properties is achieved at the cost of the reduction in the compressive strength.

In an innovative work, Ceserano et al. [16] produced a customized HA scaffold bone implant with controlled macro, micro and submicron porosity sizes by robocasting technique, to be implanted in the damaged part of mandible in a real human patient. The implant geometry was taken from a computed tomography scan (CT scan) of the patient's head. Microporosity in the order of 3–8 μm was created with the use of porogenic fugitive spheres. By controlling the volume fraction of fugitive spheres, it was possible to produce open and interconnected microporosity. Interconnected porosity in this size is suitable as reservoirs for growth factors or other drugs to provide localized delivery and induction of bone ingrowth and vascularization. Porosity less than 1 μm, which promotes vascularization and bone ingrowth, was controlled via sintering temperature. HA scaffolds with the same strength and modulus of natural bone were produced, by tailoring the rod size and spacing, microporosity amount and size, and sintering temperature.

In the following sections, the production of porous and dense parts, as well as functionally graded multi-layer structures (FGM) composed of dense and porous sections, produced from HA powder using the robocasting method will be presented. Different parameters influencing the fabrication procedure as well as physical, microstructural and mechanical properties will be discussed.

5.2 Ink formulation for robocasting applications

The preparation of a suitable ink or slurry with high reproducibility is the most important and challenging factor in the fabrication of the ceramic parts with the robocasting method. A suitable ink for robocasting must have the correct flow characteristics for extrusion. This means that the ink must be highly shear-thinning to allow extrusion through the fine orifice of the nozzle, and also must have high elastic modulus, G', and high yield stress, τ_0, to retain its shape upon deposition. Furthermore, an appropriate ink must have a high volume fraction of ceramic powder, to be homogenous, and free of air bubbles. Aqueous inks are preferred due to their simplicity, lower cost, low toxicity and slower drying, while low

concentrations of organic matters are desired to allow fast burnout and high densities [7, 20].

The initial ink formulation for robocasting was based on very fast drying of the filaments as soon as they were extruded. The quite simultaneous drying provided enough strength to support the printed structure [20]. However, this approach had limitations such as sensitivity to solid loading and difficulty in controlling the drying procedure.

The next generation of the robocasting ink was developed based on colloidal gels. There are formulations in which the gelation of the ink is achieved by changing the pH of the slurry. For example, Marchi et al. [4] developed an alumina ink in which the coagulation was achieved by in situ gelation of $AlCl_3$ with increasing the pH of the slurry.

In 2002, Smay et al. [21] developed a colloidal gel formulation which has been used since then for the production of robocasting ink of different ceramic materials [2, 10, 12, 14, 15, 17, 18, 22, 23]. This formulation is based on the addition of ammonium polyacrylate-based substance (such as Darvan C and Darvan 821, used as dispersing agents) and polyethyleneimine (PEI, used as gelling agent) to the water slurry of ceramics. PEI is a highly branched, cationic polyelectrolyte with a 1:2:1 ratio of primary, secondary, and tertiary amines (NHx). The ionized PEI interacts with the ammonium polyacrylate-based dispersant adsorbed on the particles' surfaces and creates a network that provides viscoelastic behaviour to the ink. The minimum ink elasticity required to assemble a given periodic structure can be estimated by setting criteria for the maximum acceptable deflection of the ceramic filaments upon spanning between two previously deposited rods. Either higher density or bigger span distances and rod diameter need stronger inks to be formulated [24].

The effect of the addition of PEI on the elastic modulus of a HA ink is presented in Figure 5-2. It can be seen that by addition of PEI, the elastic modulus increases, which reflects the strengthening of the gelled HA particle network. The low amount of organic matter results in an easy and fast debinding procedure and leaves fewer voids in the final structure. In this formulation, hydroxypropyl methylcellulose is also added to the suspension to increase the overall viscosity.

Another formulation for robocasting ink uses Pluronic® F-127 solution, a synthetic copolymer of ethylene oxide and propylene oxide, as the gelling agent. Pluronic solutions exhibit a reverse thermal behaviour: they are fluid at low temperatures (close to 0 °C) but form a soft gel at room temperature. This water-based ink can be used to print hydrophilic ceramics and its applicability for robocasting of different ceramics has been demonstrated [3,8,13].

It is recommended that to achieve higher green densities, the ceramic powder should be a mixture of small and large particles because the small particles fill the voids between the larger ones [25]. For example, it was shown that if the amount of fine particles reaches 30%, a bi-modal mixture of powders with a size ratio of 1:7 can increase the powder density by 30% [26]. The optimal composition corresponding to the highest achievable density is illustrated in Figure 5-3.

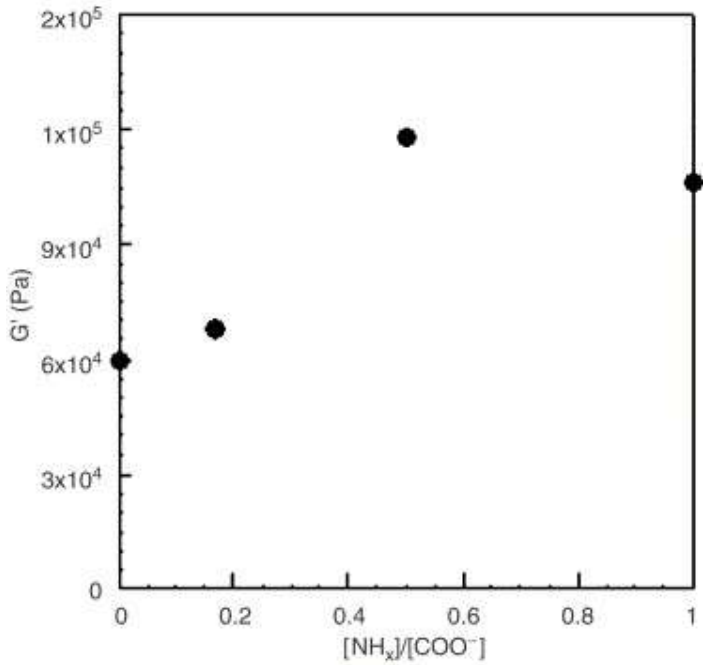

Figure 5-2: The elastic modulus (G′) of concentrated HA suspensions as a function of PEI addition expressed as a ratio of $[NH_x]/[COO^-]$. Reprinted from [10] with the permission of Elsevier under the license no 4771560904048.

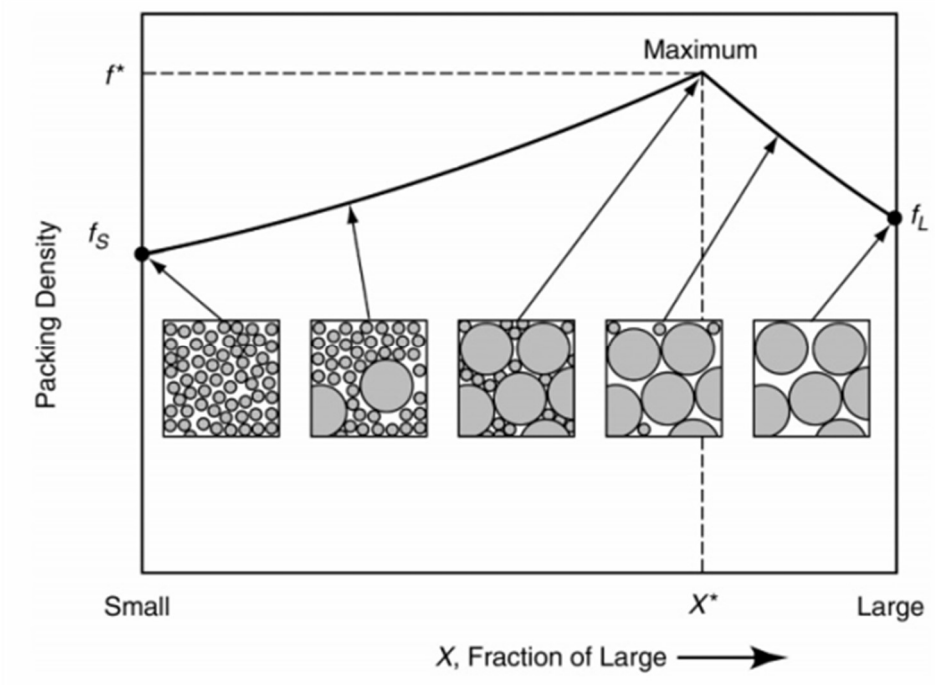

Figure 5-3: Bimodal powder packing (variation of the packing density with particle size, volumetric porosity and powder particulate size for 3-D printing process). Reprinted from [26] with the permission of John Wiley and Sons under the license no 4771580460502.

5.3 Production of robocasting parts

5.3.1 Design of CAD models

The first step in the production by robocasting or any other 3-D printing methods is the design of the desired structure model. This is normally done by using any computer-aided design (CAD) software [27]. The CAD output, that is in the form of electronic files, then converted to an STL file which is only the surface geometry of the three-dimensional object. Once completed, the STL file needs to be sliced in a virtual environment into many two-dimensional (2-D) layers and produces a G-code file containing instructions specifically tailored for the type of 3-D printer being used. These conversions were done by Cura software which is an open-source 3-D printer slicing application. A 3-D printing client software loads this G-code file and uses it to instruct the 3-D printer during the printing process to achieve computer-controlled layer-by-layer extrusion of the ink. Each layer is processed sequentially one on top of the other to form a three-dimensional part [28].

3-D periodic scaffolds designed for the robocasting production are illustrated in Figure 5-4. Three types of scaffolds were designed for fabrication: porous, dense and FGM.

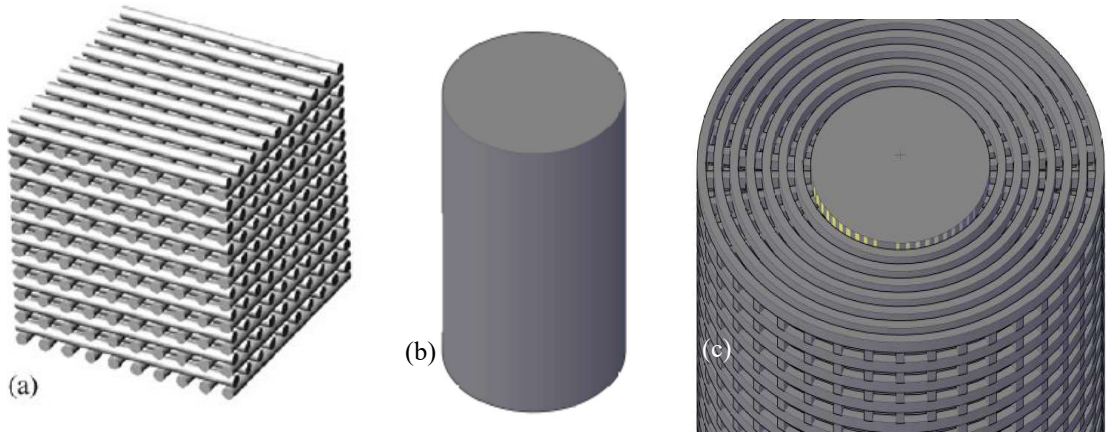

Figure 5-4: Schematic illustration of the 3-D periodic articles designs for robocasting production; porous (a), dense (b) and multi-layer (c) models.

The porous part was a tetragonal network of struts, consisted of a linear array of parallel rods aligned with the x- or y-axis such that their orientation was orthogonal to the previous layer. The part consisted of 24 layers, each one included 12 parallel struts. Because only nozzles with a diameter of 400 µm were available, the thickness of the strut was designed to be 400 µm. The separation between parallel rods (D_{rod}) in each layer was in the same size as the struts, 400 µm, so the centre-to-centre rod spacing (L) of the adjacent struts was 800 µm. The spacing in the z-axis, between parallel layers, h, was defined as 300 µm to provide enough

squeeze between parallel layers which needed to maintain sufficient integrity of the whole part. Having all of the stated dimensions, the designed porous structure size was 9.6 × 9.6 × 7.3 mm^3.

The dense part was a cylinder with a diameter of 10 mm and a height of 15 mm. The raster pattern to fill in the part was chosen to minimise the amount of space between the filaments during printing. The rod spacing between the filaments needs to be sufficiently small to cause the filaments to completely squeeze together during printing, but not so small as to cause overfill of the area being printed. This was empirically found to be d/1.2, where d is the diameter of the nozzle [188].

Another consideration is the surface roughness of the filaments. To have a good interface between adjacent filaments, the extruded filaments have to be reasonably smooth when exiting the nozzle. Macroscopically rough filament's surfaces entrap small pockets of air, leading to defects after sintering [188].

The multi-layer structure, designed to be a simplified model of a functionally graded structure, was a combination of the dense and porous parts. To the best of our knowledge, it was for the first time that the monolithic and porous structures are combined in one integrated part to be printed by robocasting technique at once. Considering that direct ink writing of dense and porous parts requires specific paste formulations with different rheologies and also different printing parameters such as the speeds of the extrusion and the nozzle movement, the aim was to study the feasibility of printing dense and porous structure integrated into one part, in view of the paste formulation and control of printing parameters.

The design of multi-layer structure imitated the structure of the natural bone which is usually a combination of dense cortical bone and porous cancellous bone with gradient porous structure. There are two types of stiffness gradient in bones: radial gradients in long bones, and linear gradients in short and irregular bones [29]. The multi-layer structure design was such to achieve radial-gradient design by designing the porous part around a dense cylindrical core. The porous part was composed of two different layers which were placed successively. One consisted of radial rods and another one comprised concentric rings, in such a way that the diameter of the rings increased by increasing the distance from the core. In this way, the porosity increases linearly from the centre to the periphery.

Because of technical limitations, it was not possible to construct the porous part of the multi-layer samples from 400 μm thickness struts. The programming of the slicing software needed the size of the struts to be doubled. Therefore, in the final design, struts of the porous part were composed of 2 adjacent filaments that were printed side by side without spacing between them forming struts of 800 μm thickness. The overall diameter and height of the multi-layer model were 20 mm and 19.6 mm, respectively. The central dense core diameter was 8.8 mm.

5.3.2 Fabrication processes

The scaffolds were fabricated from as-received (AR) and wet ball-milled (WBM) HA-AR2 powders. The fabrication process started with the preparation of

suitable ceramic inks. Before the preparation of the inks, the HA powders were sieved to particle sizes smaller than 80 µm in order to remove larger hard agglomerates. Colloidal gel inks were prepared by a sequence of addition and mixing steps.

The inks were prepared by first mixing the ammonium polymethacrylate dispersing agent (Darvan C-N, Vanderbilt Minerals, LLC, 15000 $g.mol^{-1}$) with demineralized water. Then the mixture was heated to 44 °C and an appropriate amount of hydroxypropyl methylcellulose (Methocel E4M, Dow Chemical Company, USA) as a viscosifying agent was added to the mixture. The temperature of 44 °C was selected based on the previous experiments as a minimum temperature that is high enough to provide a good dissolution of Methocel in water. After the dissolution of Methocel, the previously sieved powder was added to the mixture in small increments and homogenised properly after each addition. The gelation of the ink was achieved by the addition of polyethylenimine (PEI) as a concentrated liquid. In order to achieve better homogenization of the mixed materials, the obtained inks were passed several times through a triple roll mill and were stored overnight in fridge inside parafilm.

The 3-D printing of the previously designed scaffolds was conducted by a custom-designed robotic deposition device equipped with a screw-type extruder which was assembled on a Stepcraft 840 V2 CNC machine (Stoneycnc, UK). The 3-axis motion was independently controlled by a custom-designed, computer-aided direct-write program.

The printing syringe was partially filled with the ink, with special care to prevent air bubbles being trapped inside it, and then placed on the three-axis motion stage. The deposition was done over a smooth alumina plate at room temperature using nozzle with circular orifice of 400 µm diameter at the volumetric flow rate required to maintain a constant x–y printing speed (Figure 5-5). During the deposition of the spanning elements, the rod first anchors to one of the supports, traverses the gap, and then anchors to the second support. By traversing the gap, a

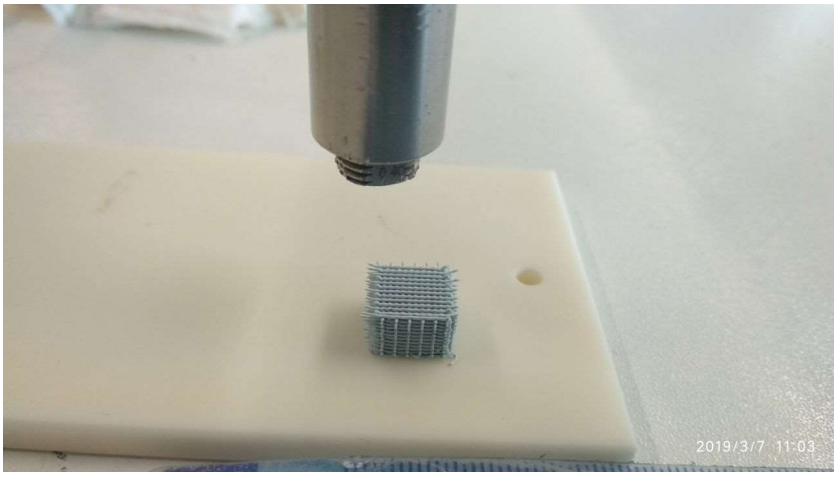

Figure 5-5: The nozzle, the alumina substrate and the successfully printed porous structure.

slight tension is employed on the deposited since the ink bend 90° upon exiting nozzle to lie in the x-y plane and the connecting points are the nozzle and the first support. Elastic deformation would occur instantaneously; however, equilibrium shape is obtained after a short time (approximately a few seconds) because of the viscoelastic nature of the filament rods. By finishing the construction of one layer, the nozzle is translated up a distance, D_z, and another layer is deposited. This process was repeated until the entire scaffold was printed. The humidity inside printing chamber was kept over 55% to control the drying of the thin printed filaments.

One key step was the achievement of a certain degree of adhesion between the alumina substrate and the first printed layer before each print. This adhesion was controlled by primarily levelling of the nozzle tip by which the zero point of the vertical movement of the printing stage (direction Z) was defined. The Z=0 point was the height of the substrate surface where the printing process started. The alumina substrate surface must be smooth, and the adhesion must be not so loose to endanger the scaffold stability, and nor so tight that the removal of the scaffold from the substrate became difficult. For the porous parts, after successful laying down of the first layer, the printing of the successive layers was done almost without difficulty. However, the printing of the multi-layer and dense parts were very sensitive to the Z=0 point. A very small amount of tightness between the first layer and the substrate, induced elastic forces through the viscoelastic ceramic filaments which were released during the printing of the successive layers and damaged the parts. On the other hand, under the loose attachment of the first layer to the substrate, the parts were not stable and printing was not possible from the first point. Therefore, the Z=0 points needed to be defined very accurately before printing these parts. The “zero height” was set by slowly lowering the nozzle until it was just in contact with the substrate. Immediately before printing each part, a dummy line (known as the “lead-in”) was printed to ensure homogenous flow before the part is printed. The required length of the lead-in ranged from 5 mm for large nozzles to 100 mm for the smaller ones.

Another important consideration was the speeds of printing and the ink extrusion. Printing speed was controlled by the motion of the extruder stage and the extrusion speed was controlled by the rotational speed of the extruder screw. These two speeds should be adjusted to be in harmony. Higher printing speeds lead to stretched filaments while the lower speeds result in the buckling of the printed rods.

While faster printing speed is preferable as it reduces the time to build a part, the multi-layer scaffolds, because of very delicate design, were very responsive to the printing speed and they needed to be printed using very low speeds. High printing speeds reduce the accuracy of the tool path when changing direction and cause sharp corners to become rounded. On the other hand, printing the dense and especially porous parts was feasible in a wide range of printing speeds.

Table 5-1 represents the formulations of the inks prepared for the successful production of each type of scaffolds. In this table, the dispersant percentage is

presented in relation to the solid content, while Methocel and PEI amounts are calculated in relation to the water content of the slurry.

Starting with the fabrication of the porous structure from AR, unmilled powders, the first ink formulation by which porous samples were printed successfully, is labelled as A1 in Table 5-1. With the same formulation, the scaffolds produced from the ball-milled (BM) powder was also successful (samples B1). However, because of lower particle size distribution, the final formulation consisted of less solid matter and a higher amount of dispersant needed for dispersion of the solid particles.

Table 5-1: Ink formulations for the fabrication of the robocasting samples.

Scaffold type	Powder type	Ink code	Solid loading (vol%)	Dispersant (%)	Methocel (%)	PEI (%)	Printing speed (mm/min)
Porous	As-received	A1	54.6	1.25	6.5	16	290
		A2	54.6	1.25	6.5	10	290
	Ball- milled	B1	49.2	4	6.5	16	290
		B2	49.2	4	3.5	8	290
		B3	51	4	6.5	8	290
Dense	As-received	A3	54.6	1.25	6.5	14	226
	Ball- milled	B3	51	4	6.5	8	226
Multi-layer	Ball- milled	B3	51	4	6.5	8	129

Further attempts were dedicated for decreasing the organic matter in the formulation, with the aim of achieving higher sintered densification. To this aim, the A2 formulation of the AR powder was found printable in which, compared to A1 formulation, the PEI amount decreased from 16 to 10%, by keeping constant the amount of the other components. The optimisation of the BM powder formulation attained even more success. Formulation designated as B2 was achieved with a similar solid loading of B1 but the percentages of the organic additives almost halved. However, because of difficulties in the drying step (which will be discussed in the next part), we needed to restore the Methocel amount to the previous quantity. The new formulation is designated as B3 in Table 5-1. It has the advantage of higher solid loading (51 vol%) than the previous ones (49 vol%). The printing speed of the porous samples production was fixed to 290 mm/min.

Printing of the dense and multi-layer samples was carried out with more complications. Because of the complexity of the raster pattern which must swept circular pattern, and also the presence of sharp corners, we needed to decrease the printing speed from 290 to 226 mm/min for the dense samples and to 129 mm/min for the multi-layer samples. While the ink B3 was suitable for the production of the dense and multi-layer scaffolds from the WBM powder, for successful printing of the dense samples from AR powder the formulation was modified by increasing the PEI amount to 14%, designated as ink A3. The successful printing of the multi-layer samples was just conducted using the BM powder.

The pictures of some representative samples of different scaffold types after printing are shown in Figure 5-6. It can be seen that the final scaffolds were the accurate and reproducible resemblance of the CAD models. The porous parts are the periodic arrangement of the filaments with precise dimensions and have regular

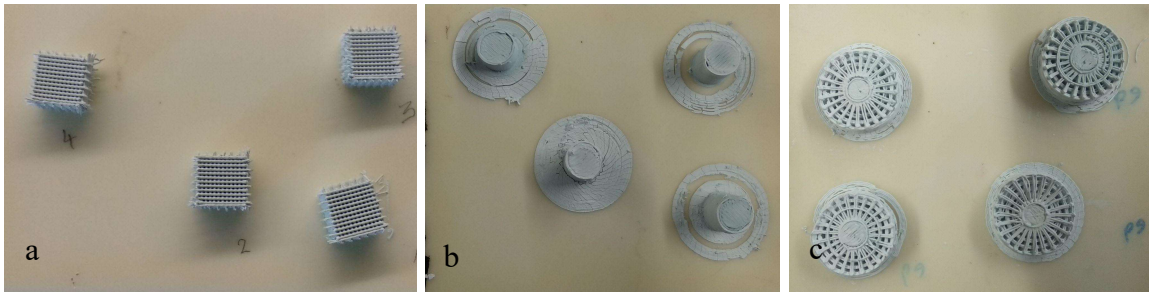

Figure 5-6: The as-printed pictures of the different scaffolds: porous (a), dense (b) and multi-layer (c).

internal characteristics. The dense parts consist of the arrays of filaments laid adjacent to each other which completely squeezed together without considerable free spaces between them.

The drying of the printed parts was done in the room atmosphere for 24 hours by gradually decreasing the humidity inside the printing chamber. After drying, the samples were removed from the alumina substrate with caution to avoid any damage and they were transferred to a furnace to be debound and sintered according to the thermal cycle shown in Figure 5-7.

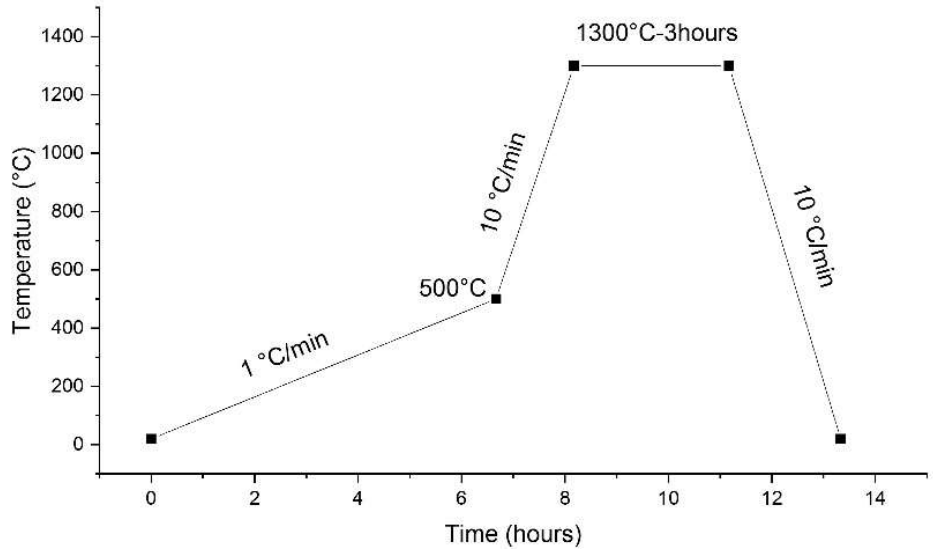

Figure 5-7: Thermal treatment cycle applied to the robocast samples for debinding and sintering.

The debinding was performed by slow heating (1 °C/min) of the samples to 500 °C. TGA analyses of the green samples (Figure 5-8) showed that by heating to 500 °C almost all of the organic matters in the scaffolds would be removed. To minimize any potential residual stresses, the debinding was done using a very slow heating rate of 1°C/min. Sintering of the samples was accomplished at 1300 °C for 3 hours. The heating rate after debinding was increased to 10 °C/min to minimize the joining

of the ceramic particles during the first stage sintering. After sintering, the samples were cooled down to room temperature, still at 10 °C/min.

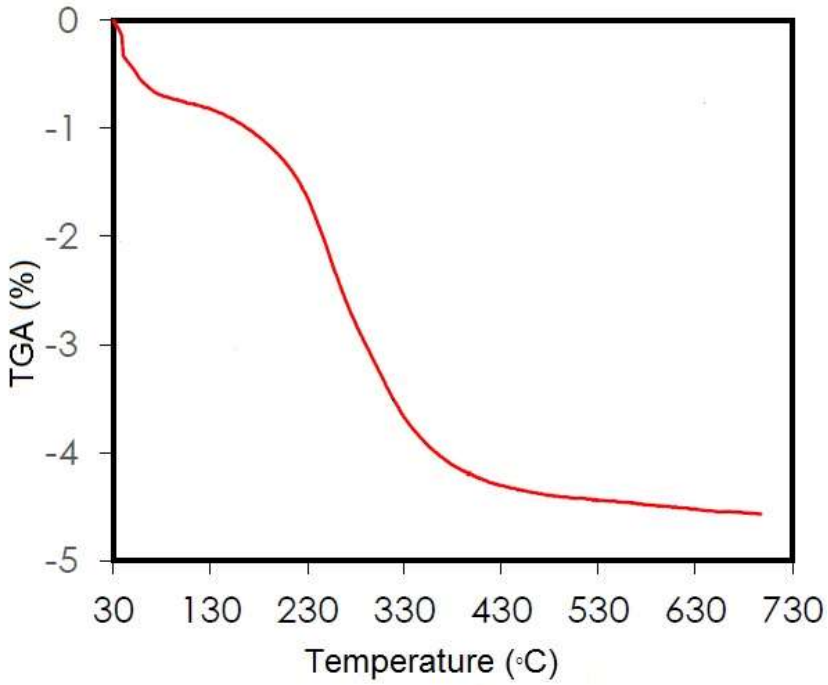

Figure 5-8: TGA analyses of the green samples produced by robocasting of HA ink.

5.4 Results and discussion

5.4.1 Physical characteristics and dimensions

As stated in the previous part, the porous samples were successfully printed from 5 different ink formulations of AR and WDM powders. The 24 layers superimposed regularly and constructed a 3-D tetragonal mesh of interpenetrating ceramic rods. Figure 5-9 shows a representative image of these samples after drying, obtained by a stereoscopic microscope. It can be seen that these samples were three-dimensional scaffolds with interconnected pore channels made by repeated arrays of parallel filaments. Interconnection of adjacent layers produced tetragonal pores which are uniformly distributed in the whole structure. The average dimensions of the dried specimens were 9.21×9.21×7.00 mm^3 and 9.33×9.33×7.09 mm^3 for the samples produced from WBM and AR HA, respectively, which means 4.06 and 2.81% of drying shrinkage, respectively.

Figure 5-10 shows the filament condition of the scaffold produced from ink B2 compared to the scaffolds prepared from the other inks. Numerous drying cracks on the sample prepared from ink B2 compared to the smooth crack-free surface of the samples obtained from other inks can be observed. Considering the inks formulations, it seems that the lower amount of organic matter in the composition of ink B2 is responsible for the inappropriate drying of the corresponding samples. In fact, the increase of the elastic modulus, G′, of the inks by increasing the organic matter, rises the tolerance of the scaffold against the drying induced stresses and

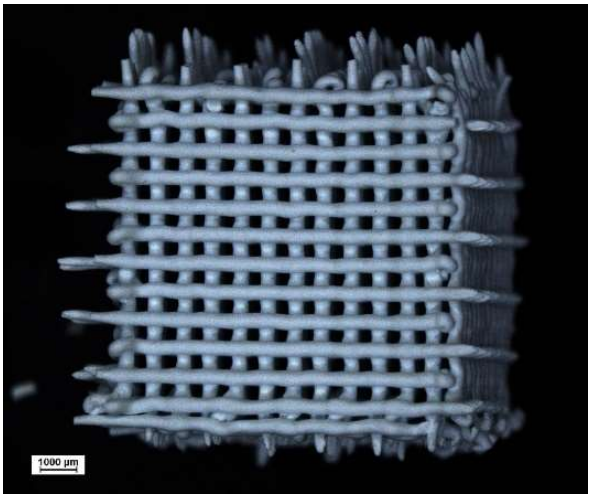

Figure 5-9: Representative picture of porous scaffolds obtained by a stereoscopic microscope.

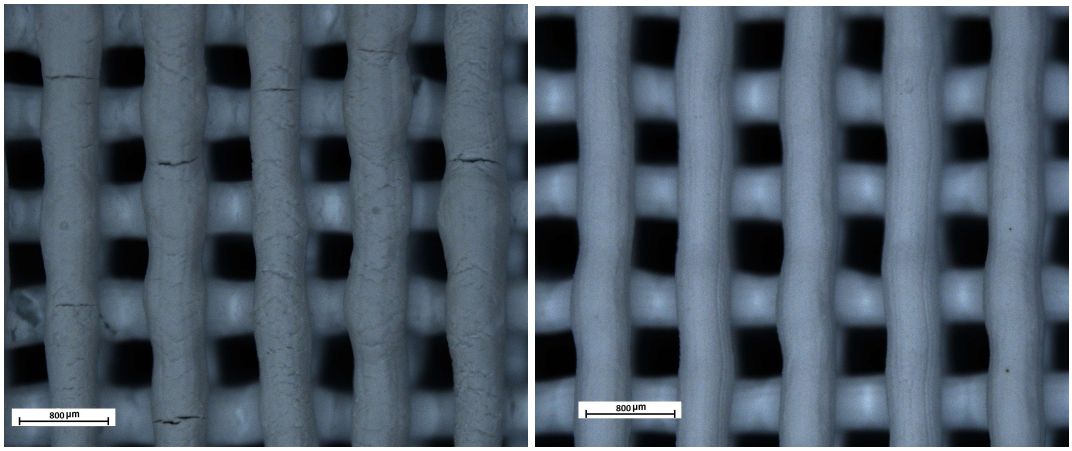

Figure 5-10: Stereomicroscope images of the dried samples prepared from the ink B2 (left) in comparison with a representative image of the samples prepared from other inks (right) indicating the inappropriate drying condition of the samples prepared from ink B2.

increases the filament strength. Another explanation can be the stronger polymeric network as a result of higher organic matter which encapsulates the ceramic particles more intensely and reduces the drying rate of the filaments. Therefore, it seems that at least 6.5% Methocel and 8% PEI is necessary for the ink formulation to avoid drying cracks.

The pictures of a representative sintered 3-D porous sample from different views are presented in Figure 5-11. The debinding and sintering stages didn't deteriorate the highly defined, precise dimensions and regular quadratic channel structure of the final scaffolds. No significant strut bending can be noticed and the debinding and the sintering process did not result in any macro cracks. The physical geometry of the spanning elements resembles that ceramic rods simply supported at its ends. The sintered dimensions of the samples obtained from as-received and

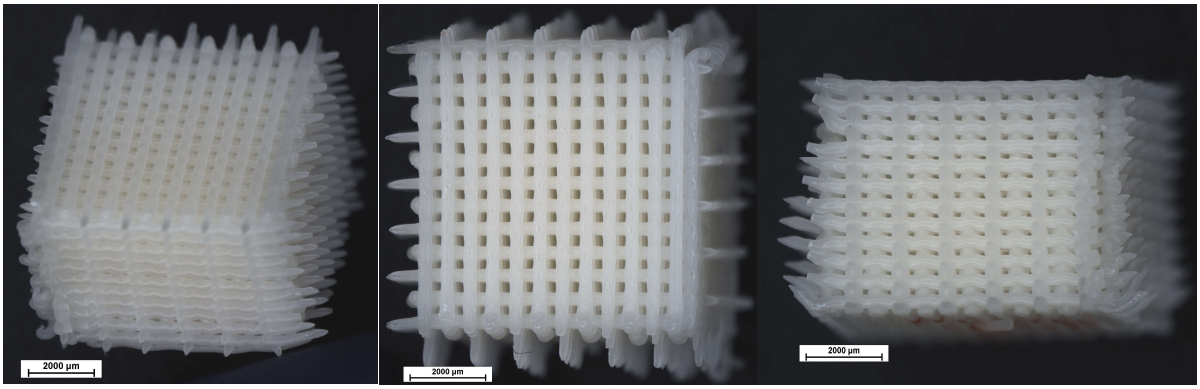

Figure 5-11: Perspective, top and side view of a representative porous 3-D HA scaffold.

WBM powder was 8.15×8.15×6.20 mm^3 and 7.55×7.55×5.75 mm^3, respectively, indicating 12.65% and 18.02% sintering shrinkage, respectively.

In Figure 5-12 the contact area of the interpenetrating struts of subsequent layers of a porous scaffold is depicted. It can be seen that the superimposed ceramic filaments well integrated into each other. The connection area shows a homogeneous microstructure without noticeable borderline between struts.

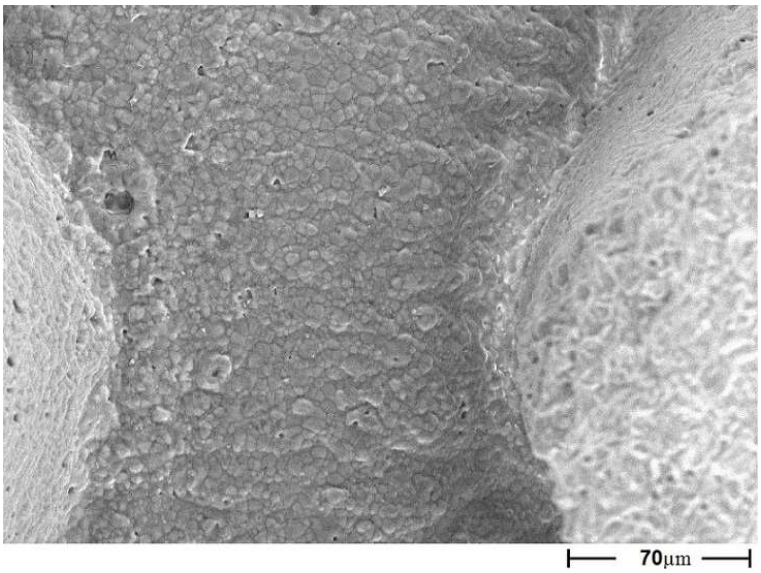

Figure 5-12: SEM image showing the connection of the robocasting rods of adjacent layers.

Table 5-2 lists the physical characteristics of the 3-D porous scaffolds after sintering. The values are the average values of at least 10 samples of each batch of samples. The density and porosity measurements were conducted based on the Archimedes' method according to ISO 10545-3:2018 "Ceramic tiles: Determination of water absorption, apparent porosity, apparent relative density and bulk density" [30]. It can be seen that the samples obtained from BM powder, due

Table 5-2: Physical characteristics of the porous 3-D samples.

Powder type	Strut size (µm)	Pore size (µm)	Apparent density (g/cm^3)	Density of solid part (g/cm^3)	Open porosity (%)
As-received	354±9	312±14	1.95±0.15	2.87±0.01	32.0±5.2
Ball-milled	341±7	275±8	2.06±0.10	2.97±0.01	30.7±3.4

to higher sintering shrinkage, had smaller strut and pore size compared to the samples obtained from the AR powder. Containing pore size in the range of 100-400 µm, which has been reported as the optimum pore size for biological performance, both types of the samples seem to be suitable for tissue engineering purposes. The densities of the struts relative to the theoretical density were 92% and 95% for the AR and WBM samples, respectively, and are comparable to the densities achieved for the samples made by gelcasting technique. Having bigger pore sizes, the samples made from the AR powder were slightly more porous (open porosity of 32.0%) than the samples made from WBM powder (30.7%). However, compared to the designed porosity of 44%, it is clear that the fabrication processes such as drying and sintering resulted in a decrease in the porosity of the samples. The spreading of underlying layers due to the weight of the upper layers may be a reason for the decrease in the final porosity of the printed samples.

The microstructure of a cross-sectional cut of two representative porous samples made from as-received and WBM powders are depicted in Figure 5-13. Both of the samples show residual microporosity within HA rods. Presence of microporosity indicates that the measured porosities were the contributions from macroporosity stemming from the voids space between HA rods and microporosity present within individual rods. It has been shown that the quantity of microporosity has a direct relationship with the amount of the organic binder used in the formulation of the robocasting ink [13]. The higher the organic matter, the higher the microporosity.

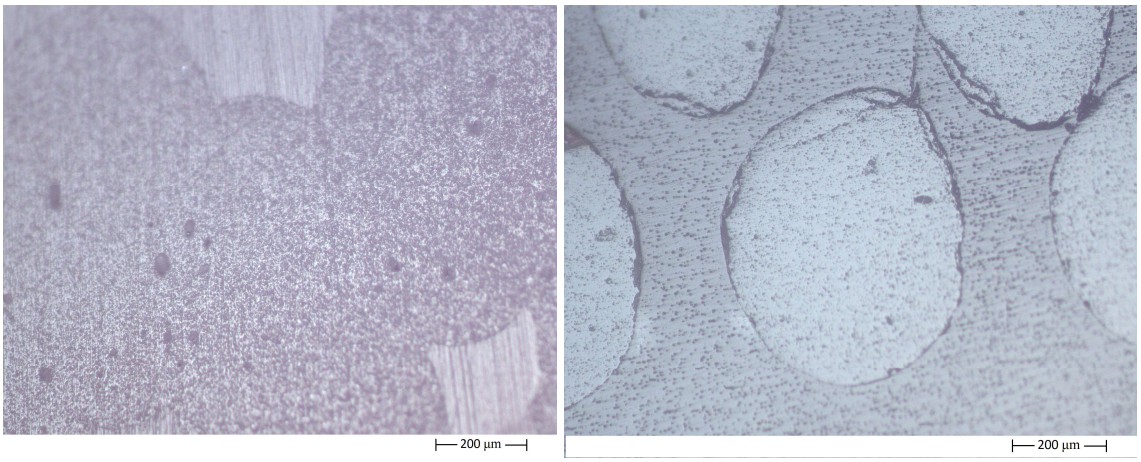

Figure 5-13: Optical microscopy images of the cross-section of porous samples made from AR (left) and WBM (right) powders showing the microporosity within struts remained from binders burn out.

Despite their negative effect on mechanical properties, it should be recalled that microporosities could improve the biological performance of the scaffolds [31,32]. Figure 5-14 depicts an optical image of some representativesof the dense samples after sintering. It is observable that the dense samples were well-constructed cylinders with regular dimensions, in good resemblance with the CAD design. Similar to the porous samples, higher drying shrinkage was observed for the dense samples made from WBM powder. The average heights of the dried samples were 14.13 ± 0.32 and 13.88 ± 0.15 mm for the as-received and WBM samples, respectively. After sintering, these dimensions were 12.09 ± 0.22 and 11.67 ± 0.09 mm, respectively, providing 14.43 ± 0.05 % and 15.90 ± 0.05% sintering shrinkage, respectively. Compared to the porous samples, the sintering shrinkages of the dense samples were higher for the samples made from the AR powders, and lower for the samples made from WBM ones. Because of the patterned geometry of the side-wall of the samples, due to the circular cross-section of the constructive filaments, it was not possible to acquire the exact diameter of the samples. Density and porosity measurements released that the dense samples were not entirely bulk and on average, AR and the WBM fired samples had 7.29 ± 1.87% and 8.73 ± 1.58% open porosities, respectively. While their density of solids was comparable to the porous parts from the same type of powder, the presence of open porosities decreased their apparent densities to 2.63 and 2.69 g/cm^3, respectively. Figure 5-15 highlights the flaws in the structure generated by the printing process. It can be seen that the adjacent filaments are not well squeezed into each other and there are quite big spaces between them. This condition was observed only in the centre of the samples; in fact, in the peripheral areas, no free spaces between deposited filaments could be observed.

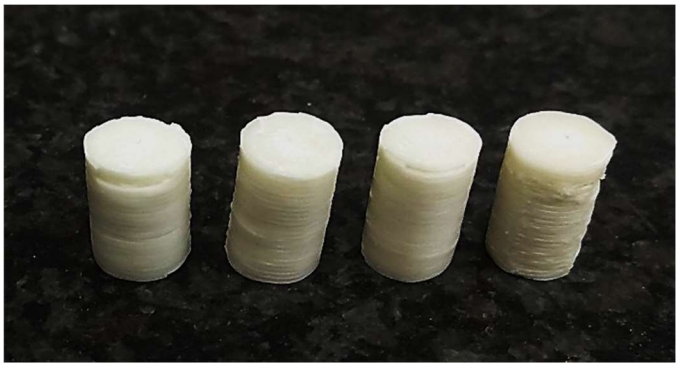

Figure 5-14: Optical image of some representative dense samples.

Images from the top and side view of a representative multi-layer sample, make by stereomicroscope, are presented in Figure 5-16. It can be seen that these samples were a well-suited regular combination of the dense core surrounded by concentric rings which are bonded together by several radial filaments. The interception of the concentric rings and radial filaments resulted in isosceles trapezoids whose sizes increased by increasing the distance from the dense core. In the porous part, we can

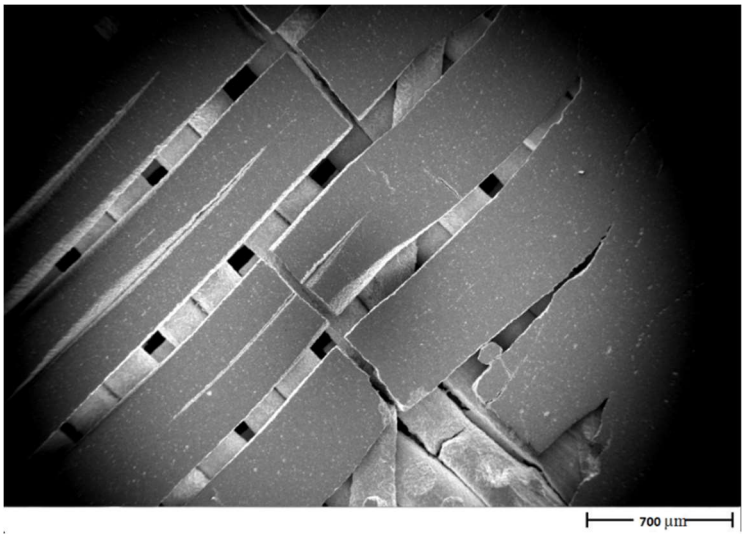

Figure 5-15: SEM image of a robocast dense sample illustrating the filaments condition at the centre of the specimens.

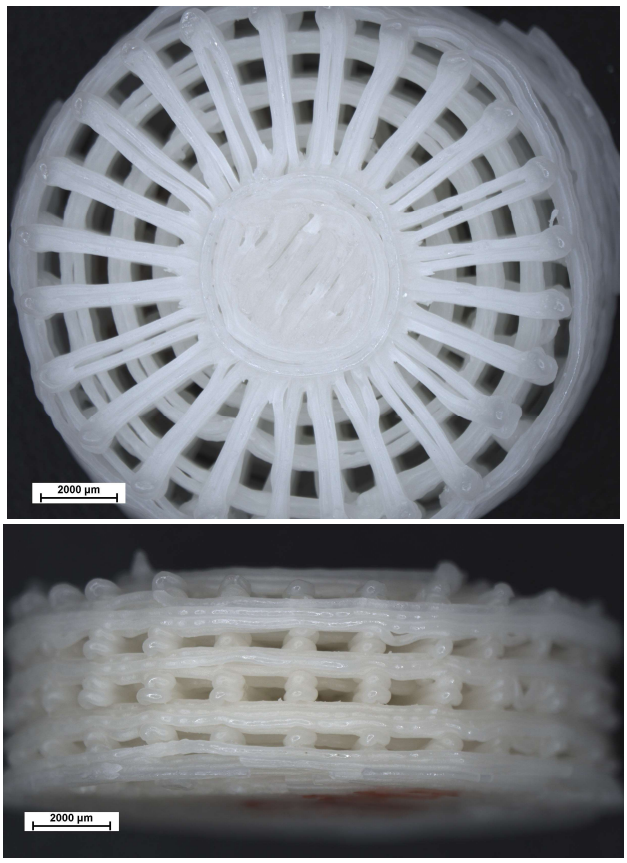

Figure 5-16: Top and side stereomicroscopy images of a representative multi-layer sample.

observe that each filament consists of two parallel adjacent rods (due to the software limitation, as stated in the previous paragraph). The shrinkage of the ceramic rods during the sintering process, in some regions, caused these neighbouring rods to be

detached from each other and led to a certain free distance between them. The presence of these flaws underlines the importance of considering the right amount of overlap between two adjacent rods such that the rods squeeze into each other during consolidation.

While printing the multi-layer samples, it was observed that the capacity of the extruder capsule was not enough for printing the whole structure. Therefore, the obtained samples had smaller heights compared to the original CAD design. However, the feasibility of constructing the whole complex 3-D scaffold by robocasting technique was verified. Each sample was composed of a dense core, surrounded by four rings of different diameters. Radial filaments, extended from the external surface of the dense core to the largest ring, provided the attachment of the rings to the dense core and each other. The mean diameter of the rods was measured equal to 619 ± 21 µm. Table 5-3 collects the other physical characteristics of the sintered samples including concentric rings diameters and mean pores sizes. The diameters of the trapezoids in the X-Y plane were considered as the pore sizes and the numbering under pore sizes column in Table 5-3 represents their sequence from the core. The mean diameter of the dense core was 5.48 ± 0.11 mm, while the overall sample diameter was 15.49 ± 0.35 mm. Having these dimensions, it can be measured that the dense core consisted of 12.5% of the overall structure; therefore, most of the structure was made by the porous part, characterised by increasing pore size from inner to outer layers.

Table 5-3: Rings diameters and pore sizes of multi-layer samples.

External diameter (mm)					**Mean pore size (µm)**		
Core	1° ring	2° ring	3° ring	4° ring	1°	2°	3°
5.48±0.11	7.92±0.13	10.43±0.15	13.02±0.18	15.49±0.35	605±55	896±52	1040±31

Archimedes' measurements showed that the average final open porosity of the multi-layer structures was $27 \pm 3\%$. The density of the solid part was 2.99 ± 0.01 g/cm^3 which corresponds to 96% of the theoretical density. It can be seen that the final multi-layer structure consisted of the open pores from around 600 µm to 1.04 mm. This demonstrates the exceptional capacity of the robocasting technique in the production of the porous structure with very large tailored macropores, a quality almost impossible to be achieved by other ceramic manufacturing techniques. Furthermore, by evaluation of the image of the structure from the side view, it was observed that the constructive filaments of the largest ring spanned the distance between two radial supports, corresponding to a distance of 1.28 mm, without considerable deflection. This observation proved the high strength and shape stability of the formulated ink in supporting its own weight and the weight of the upper layers. This property is the key for printing even more complex and stable structures with high accuracy.

Figure 5-17 depicts the microstructure of the robocast samples made from as-received and WBM powders. In both cases, residual microporosities can be observed, whose size can be classified into two main ranges. Larger pores, from few micrometres to about 15 µm, correspond to the voids generated by organic

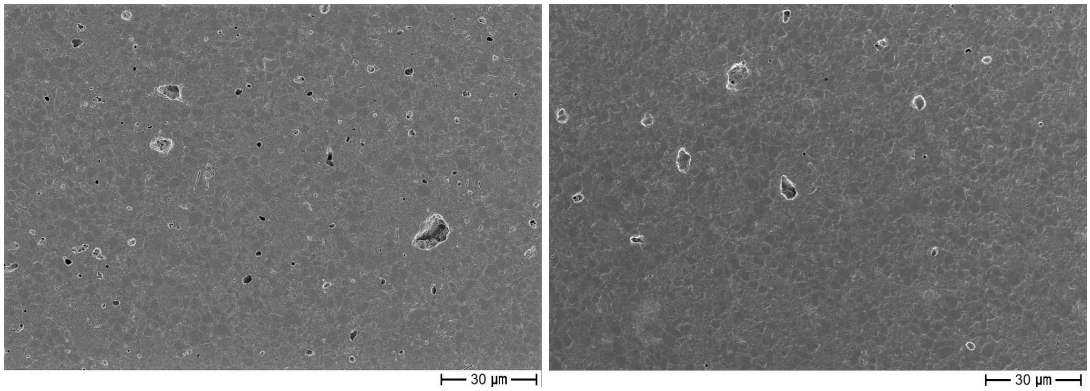

Figure 5-17: FESEM images of robocast samples produced from as-received (left) and WBM (right) powders, and showing the filament microstructure., indicating the presence of two types of microporosity.

binders burnout, as already observed in Figure 5-13 for porous samples. Smaller pores, from submicron size to a few micrometres, mainly located at the grain boundaries, which are due to the incomplete sintering process. Like gelcast samples, the higher sinterability of the WBM powder led to a lower number of intergranular micropores compared to the sample obtained from the AR powder.

Field emission scanning electron microscopy (FESEM) observation also revealed that similar to the gelcast samples made from HA-AR2, the sintered microstructure of the robocast samples were composed of grains with two distinctive sizes. As a representative, the microstructure of robocast samples made from WBM powder of HA-AR2 is presented in Figure 5-18, showing the bimodal grain size distribution. As it was discussed in chapter 3, this bimodal size distribution of the grains is the result of HA to TTCP phase transformation which took place at 1300 °C.

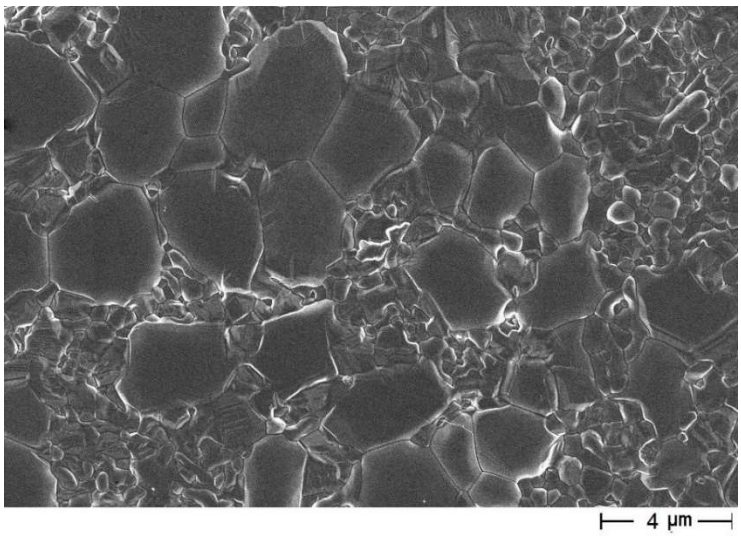

Figure 5-18: Microstructure of a robocast sample from HA-AR2 powder, showing the bimodal size distribution of the grains.

5.4.2 Mechanical tests

In order to evaluate the mechanical properties, uniaxial compressive strength tests were conducted on the porous and dense samples, using the same equipment and testing conditions used for the gelcasting samples. At least 6 samples were tested from each sample type, to get statistically reliable values. To evaluate the effect of the filament arrangement on the mechanical properties, the compressive tests on the porous samples made from AR powder were performed on two different directions: perpendicular to the printing plane (direction Z) and along with one of the two equivalent rod directions (direction X or Y).

Figure 5-19 shows a comparative summary of the mechanical data of the different scaffold types, with the error bars representing the standard deviations of the data. The compressive strength of the structure was calculated as the maximum applied load divided by the measured square section of the sample. For both dense and porous samples, we can observe the higher strength of the samples obtained from AR powders, compared to BM ones. This result is in contrast with those achieved by samples produced by the gelcasting method, where the samples made from BM powder always showed better mechanical strength. For the dense samples, this difference can be attributed to the higher open porosity of the samples obtained from BM powder (8.73%) compared to AR ones (7.29%). However, the higher resistance of the porous samples made from the AR powder is unexpected. In fact, the porous samples obtained from AR powder had higher open porosity and also less densified solid part (i.e., less densification within the filaments) than those

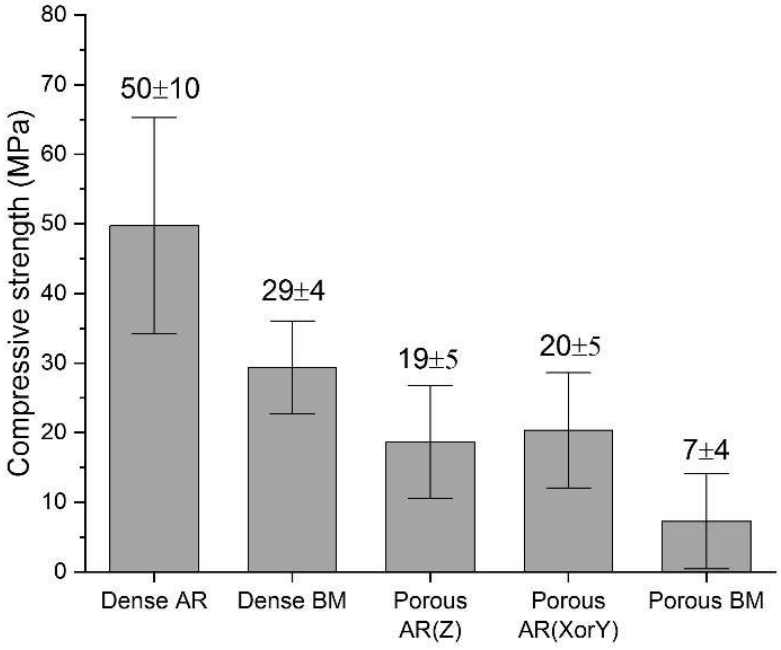

Figure 5-19: Bar chart summarizing the average compressive strength data obtained for each type of scaffold. Error bars are standard deviation.

fabricated from BM powder. Probably, the fact that the WBM inks contained a higher amount of water, and that drying was accomplished in quite short time, plays a role in lowering the mechanical properties of these samples.

Finally, we can observe a marginal role of load direction on the 3-D porous scaffolds. In fact, the average compressive strength of samples loaded along with the rod direction was slightly higher compared to the perpendicular load applied to the layers. This result was in agreement with the results already obtained by other researchers [11, 14].

The representative stress-strain curves registered during compression tests on the porous samples produced from both AR and BM powders are depicted in Figure 5-20. Several cracking events are observable from the curves. The curves reveal that at the beginning of the tests both types of the samples resisted against the external load and the applied stress increased as a function of the sample deformation. After reaching a clear initial maximum of the stress, which was much higher for the samples made from AR powders, the samples made from these powders collapsed quite soon after this point. On the other hand, the samples made from BM powders showed a significant release of the stress, followed by a subsequent recovery of the applied stress, giving rise to further peaks, and exhibiting sawtooth-like curves. The release-recovery of the stress repeated as the different layers failed (load transfer); finally, after reaching the maximum stress, which was higher than the first peak, the samples totally failed.

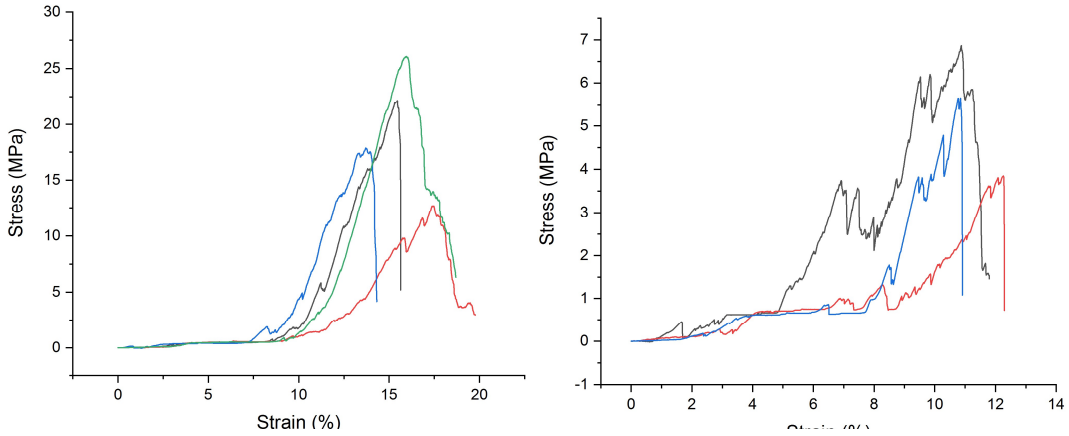

Figure 5-20: Stress-strain curves obtained during uniaxial compression tests performed on the porous samples made from as-received (left) and BM powders (right).

The stress-strain curves obtained from compression tests on the dense samples are presented in Figure 5-21, still for AR and BM powders. It can be seen that similar to the porous samples, the stress first increased to an initial maximum for both types of the samples. After this initial peak, both samples managed to recover the released stress. The stress-bearing part of the samples made from AR powder showed increasingly mechanical resistance, with the maximum stress occurring at considerably higher stress than the initial peak. On the contrary, the samples made

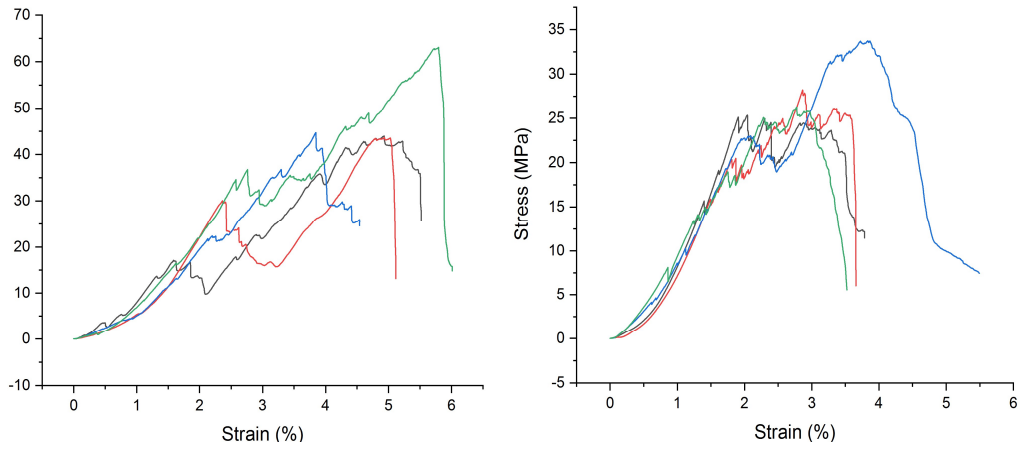

Figure 5-21: Stress-strain curves obtained during uniaxial compression tests performed on the dense samples made from as-received (left) and BM powders (right).

from BM powder exhibited a fluctuating pattern at an almost narrow range of the stress, with a very moderate stress increase before failure.

To identify the fracture modes of the porous samples, some uniaxial compression tests were performed inside an environmental scanning electron microscopy (ESEM, Quanta 450 FEG, ThermoFisher Scientific, US), at a low crosshead speed of 0.1 mm/min. A sample made by AR powder was selected for this observation. The compressive load and displacement of the load platen were monitored, and the evolution of the damage was observed in situ through one side of the specimen. Figure 5-22 shows the configuration of the samples in the test device, where the compression load was applied perpendicular to the ceramic filaments.

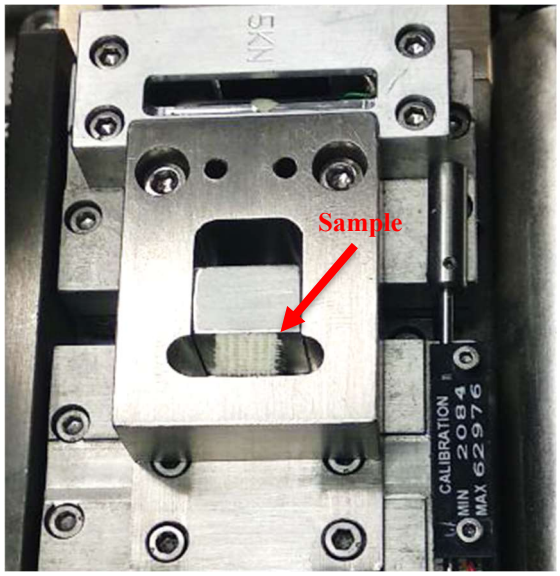

Figure 5-22: In situ compression test device, showing sample placement and test configuration.

As soon as the first drop in the load-displacement curve was observed, the loading was stopped and the sample was analysed, to observe possible cracking. As shown in Figure 5-23, the failure mode consists of longitudinal cracks running through the structure, parallel to the load axis. Fracture initiates from the external surface of the rods, close to the intersection between rods. This was probably since the area underneath two intersecting rods is under compression, while the perpendicular "free" rod fraction is probably submitted to flexural strength (with the upper parts in traction, as evidenced by the appearance of cracks indicated by white arrows in Figure 5-23). With increasing the loading, the number of longitudinal cracks increased and the cracks propagated through the layered structure.

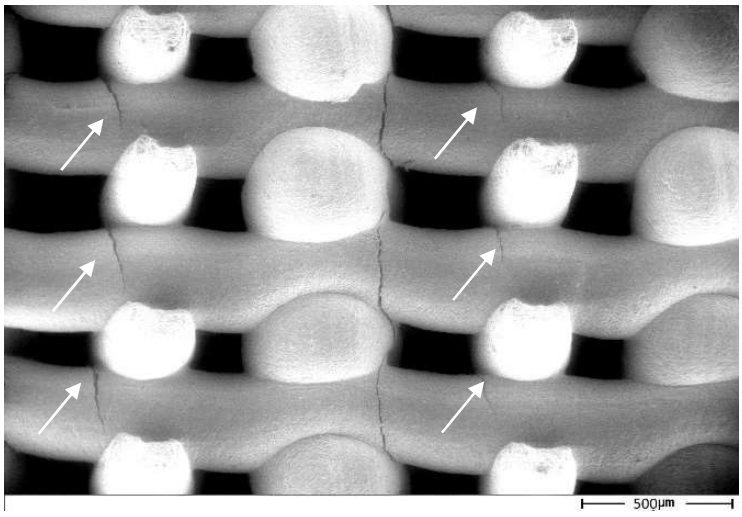

Figure 5-23: ESEM micrograph showing longitudinal cracks running through the structure of a porous scaffold, parallel to the load axis during the compression test.

Even after several longitudinal cracks had developed, the structure retained a certain mechanical resistance, as revealed by the stress-strain curves in Figure 5-20. Such residual load-bearing capacity is provided by columnar structures (Figure 5-24) that remain oriented along the load axis. Of course, when the load is removed, the columnar structure collapses with no connection between the pillars able to provide any mechanical integrity. This situation is illustrated in Figure 5-25, showing the complete failure of the porous sample within the in-situ compression test device and survived columnar structures.

Some representative micrographs illustrating the cracks propagation during the compression test inside the porous structure is illustrated in Figure 5-26. Image A was captured at the compressive loading of 2139 N. Two separate cracks close to the intersection of the rods are visible. By increasing the applied loading to 2211 N (Image B), although it seems that the opposite faces of the already initiated cracks became closer, the forward movement of the cracks tip resulting in the crack's growth is noticeable. Such a crack closure was happened because of the redistribution of the applied load due to the sample strain. The cracks grew in

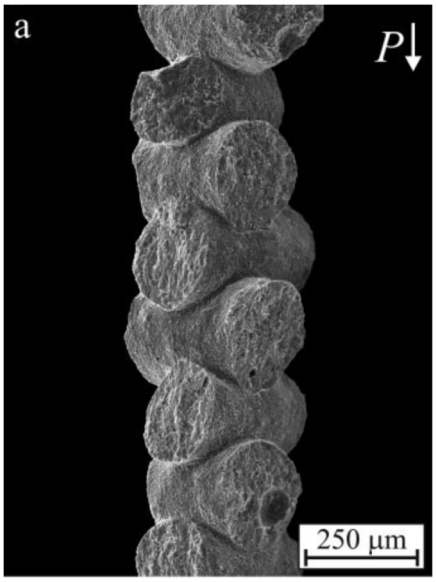

Figure 5-24: SEM micrographs showing the morphology of one of the remaining columns after a uniaxial compression test in the direction orthogonal to the rods (load, P, orientation as indicated). Reprinted from [17] with the permission of John Wiley and Sons under the license no 4771790715123.

Figure 5-25: Remaining columnar parts of a 3-D porous structure in the sample chamber after unloading of the compression test.

opposite directions but parallel to the loading direction. Image C was taken a few minutes after Image B just before the final fracture of the sample. It can be seen that the cracks grew bigger and the opposite faces of the cracks separated from each other leading to a bigger opening. Because of stress-relieving due to cracks growth,

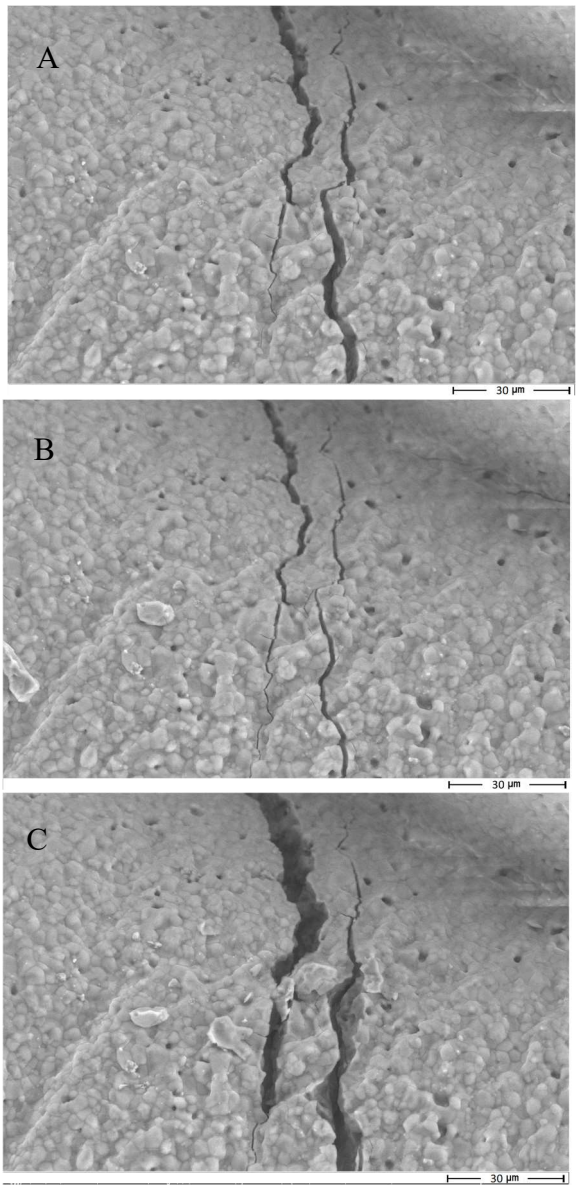

Figure 5-26: FESEM micrographs indicating crack propagation (in opposite direction) through the microstructure of a porous HA sample under compressive loading.

the final compressive loading just before the final rupture was recorded equal to 2083 N.

Another example of crack propagation during compressive loading is presented in Figure 5-27. From Image A to C the applied loading increased from 1123 to 1800 N. Crack propagation and increasing the crack length via crack tip movement is visible also for this sample. By observing the crack path within the microstructure of these two samples, both inter- and intra-granular paths can be noticed.

Due to the lack of data regarding the compression tests of robocast dense samples, it is not possible to compare the mechanical performance of the produced dense samples with literature. However, the compressive strength of 22 MPa has been reported for a dense HA sample produced by the binder-jetting method [33], significantly lower than the strength obtained in this work, which shows that the

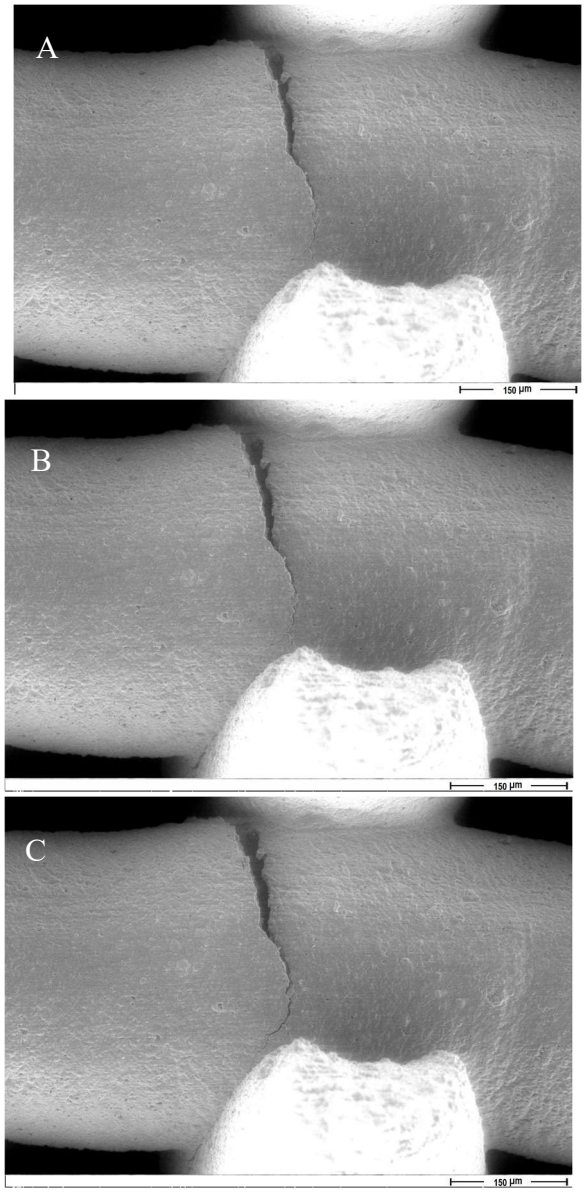

Figure 5-27: FESEM micrographs indicating crack propagation through the microstructure of a porous HA sample under compressive loading.

robocasting can be a preferred route for the production of the dense ceramic materials.

Figure 5-28 compares the compressive strength of the tetragonal 3-D porous samples obtained in current work with data reported in the literature for 3-D printed scaffolds (still by robocasting) made of HA and β-TCP. The higher strength of HA porous samples compared to β-TCP one is clear. It can be seen that the results of the AR samples obtained in the current work are positioned in the upper limit of the compressive strength of the β-TCP samples and the lower limit of the HA ones. The final composition of the scaffolds produced in current work was biphasic calcium phosphate, therefore it is reasonable to have mechanical properties between pure

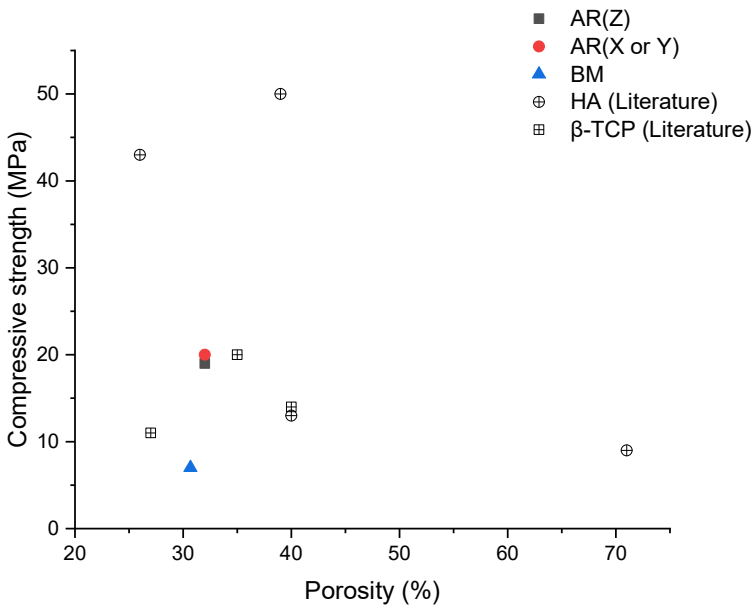

Figure 5-28: Comparative plot of compressive strength data vs porosity of robocast porous samples of this work and the literature reports of both HA and β-TCP.

HA and β-TCP samples. However, in the future, further improvements in mechanical properties can be achieved, for example by drying the samples in more controlled conditions, or even in oil bath [3,7], in order to fully exploit the potential of the BM material, as demonstrated in the case of gelcast samples

5.5 Conclusion

Robocasting is an additive manufacturing technique suitable for the fabrication of ceramic parts, able to provide customized components or parts characterised by complex architectures. In this thesis, robocasting was successfully carried out for the production of dense, porous and multilayer complex structures, starting from both AR and WBM HA powders. The multilayer samples were functionally graded structures in which the dense core part is designed to provide load-bearing function, and surrounding porous part to add biological functionality to the structure (for instance, bioactivity or bioresorbability in proper media, as will be discussed in the following chapter). In order to successfully print the different geometries, it was necessary to optimise the paste formulation as well as the printing parameters specifically. The multilayer structure demonstrated that using carefully optimised formulations and printing parameters it is possible to obtain geometrically complex parts with pore sizes of more than 1.3 mm which is not possible with other conventional methods.

The physical and microstructural characterisation demonstrated that the printed filaments were fully densified during the sintering process and the successive layers squeezed together without a noticeable boundary between them. The compressive strength tests revealed that the samples made from AR powder had higher

mechanical properties than the samples made from WBM powder, contrary to the results previously achieved by gelcast samples. Such lower mechanical strength was imputed to cracks initiated during the drying stage of the samples, which is more critical for the inks prepared from the BM powders, due to their lower solid loadings. However, further investigations will be necessary to deepen this behaviour. Moreover, the compressive tests performed on the porous samples showed that those samples achieved a higher strength when the load was applied along with the rods directions, rather than perpendicular to the layers, in agreement with previous literature results. An environmental microscope was used to identify the fracture mode of the porous samples under compression tests. The failure mode consisted of longitudinal cracks running through the structure, parallel to the load axis. The fracture initiated from the external surface of the rods, close to the intersection between rods, and led to the remaining of the individual columnar structures oriented along the load axis.

References

[1] J. A. Lewis and G. M. Gratson, "Direct writing in three dimensions," *Materials Today,* vol. 7, pp. 32-39, 2004.

[2] Z. Fu, M. Freihart, L. Wahl, T. Tobias Fey, P. Greil and N. Travitzky, "Micro- and macroscopic design of alumina ceramics by robocasting," *Journal of the European Ceramic Society,* vol. 37, pp. 3115-3124, 2017.

[3] E. Feilden, E. García-Tunón Blanca, F. Giuliani, E. Saiz and L. Vandeperre, "Robocasting of structural ceramic parts with hydrogel inks," *Journal of the European Ceramic Society,* vol. 36, no. 10, pp. 2525-2533, 2016.

[4] C. S. Marchi, M. Kouzeli, R. Rao, J. Lewis and D. Dunand, "Alumina–aluminum interpenetrating-phase composites with three-dimensional periodic architecture," *Scripta Materialia,* vol. 49, p. 861–866, 2003.

[5] A.-M. Stanciuc, C. M. Sprecher, J. Adrien, L. I. Roiban, M. Alini, L. Gremillard and M. Peroglio, "Robocast zirconia-toughened alumina scaffolds: Processing, structural characterisation and interaction with human primary osteoblasts," *Journal of the European Ceramic Society,* vol. 18, p. 845–853, 2018.

[6] L. Wahl, M. Lorenz, J. Biggemann and N. Travitzky, "Robocasting of reaction bonded silicon carbide structures," *Journal of the European Ceramic Society,* vol. 39, p. 4520–4526, 2019.

[7] S. Eqtesadi, A. Motealleh, P. Miranda, A. Lemos, A. Rebelo and J. M. Ferreira, "A simple recipe for direct writing complex 45S5 Bioglasss 3D scaffolds," *MaterialsLetters,* vol. 93, pp. 68-71, 2013.

[8] Q. Fu, E. Saiz and A. P. Tomsia, "Direct ink writing of highly porous and strong glass scaffolds for load-bearing bone defects repair and regeneration," *Acta Biomaterialia,* vol. 7, p. 3547–3554, 2011.

[9] J. E. Smay, S. S. Nadkarni and J. Xu, "Direct writing of dielectric ceramics and base metal electrodes," *International Journal of Applied Ceramic Technology,* vol. 4, no. 1, pp. 47-52, 2007.

[10] S. Michna, W. Wu and J. A. Lewis, "Concentrated hydroxyapatite inks for direct-write assembly of 3-D periodic scaffolds," *Biomaterials,* vol. 26, p. 5632–5639, 2005.

[11] P. Miranda, A. Pajares, E. Saiz, A. P. Tomsia and F. Guiberteau, "Mechanical properties of calcium phosphate scaffolds fabricated by robocasting," *Journal of Biomedical Materials Research Part A,* vol. 85, no. 1, pp. 218-227, 2008.

[12] F. J. Martínez-Vázquez, F. H. Perera, P. Miranda, A. Pajares and F. Guiberteau, "Improving the compressive strength of bioceramic robocast scaffolds by polymer infiltration," *Acta Biomaterialia,* vol. 6, p. 4361–4368, 2010.

[13] J. Franco, P. Hunger, M. Launey, A. Tomsia and E. Saiz, "Direct write assembly of calcium phosphate scaffolds using a water-based hydrogel," *Acta Biomaterialia,* Vols. 218-228, p. 6, 2010.

[14] C. Paredes, F. J. Martínez-Vázquez, A. Pajares and P. Miranda, "Development by robocasting and mechanical characterization of hybrid HA/PCL coaxial scaffolds for biomedical applications," *Journal of the European Ceramic Society,* vol. 39, p. 4375–4383, 2019.

[15] J. Roleček, L. Pejchalová, F. Martínez-Vázquez, P. Miranda González and D. Salamon, "Bioceramic scaffolds fabrication: Indirect 3D printing combined with ice templating vs. robocasting," *Journal of the European Ceramic Society,* vol. 39, p. 1595–1602, 2019.

[16] J. Cesarano III, J. G. Dellinger, M. P. Saavedra and D. D. Gill, "Customization of Load-Bearing Hydroxyapatite Lattice scaffolds," *International Journal of Applied Ceramic Technology,* vol. 2, no. 3, pp. 212-220, 2005.

[17] P. Miranda, A. Pajares, E. Saiz, A. Tomsia and F. Guiberteau, "Fracture modes under uniaxial compression in hydroxyapatite scaffolds fabricated by robocasting," *Journal of BiomedicalMaterials Research Part A,* vol. 83, no. 3, pp. 646-657, 2007.

[18] F. J. Martinez-Vazquez, F. H. Perera, I. v. d. Meulen, A. Heise, A. Pajares and P. Miranda, "Impregnation of β-tricalcium phosphate robocast scaffolds by in situ polymerization," *Journal of Biomedical Materials Research A,* vol. 101A, no. 11, pp. 3086-3096, 2013.

[19] F. Martınez-Vazquez, A. Pajares and P. Miranda, "Effect of the drying process on the compressive strength and cell proliferation of hydroxyapatite-derived scaffolds," *International Journal of Applied Ceramic Technology,* vol. 14, no. 6, pp. 1101-1106, 2017.

[20] J. Cesarano, "A review of robocasting technology," *Materials Research Society Symposium Proceeding,* 1999.

[21] J. Smay, G. Gratson, R. Shepherd, J. Cesarano III and J. Lewis, "Directed colloidal assembly of 3D periodic structures," *Advanced Materials,* vol. 14, no. 18, pp. 1279-1283, 2002.

[22] E. Saiz, L. Gremillard, G. Menendez, P. Miranda, K. Gryn and A. Tomsia, "Preparation of porous hydroxyapatite scaffolds," *Materials Science and Engineering C,* vol. 27, pp. 546-550, 2007.

[23] S. Eqtesadi, M. A. F. H. Perera, P. Miranda, A. Pajares, R. Wendelbo, F. Guiberteau and A. L. Ortiz, "Fabricating geometrically-complex B_4C ceramic components by robocasting and pressureless spark plasma sintering," *Scripta Materialia,* vol. 145, pp. 14-18, 2018.

[24] J. E. Smay, J. Cesarano III and J. A. Lewis, "Colloidal inks for directed assembly of 3-D periodic structures," *Langmuir,* vol. 18, no. 14, pp. 5429-5437, 2002.

[25] L. C. Hwa, S. Rajoo, A. Mohd Noor, A. Norhayati and M. Uday, "Recent advances in 3D printing of porous ceramics: A review," *Current Opinion in Solid State and Materials Science,* vol. 21, pp. 323-347, 2017.

[26] R. German, Handbook of Mathematical Relations in Particulate Materials Processing, John Wiley & Sons, 2009.

[27] K. Lalit Narayan, K. Mallikarjuna Rao and M. M. M. Sarcar, Computer aided design and manufacturing, New Delhi: Prentice - Hall of India, 2008.

[28] K. Brans, "3D Printing, a Maturing Technology," in *11th IFAC Workshop on Intelligent Manufacturing Systems*, São Paulo - Brazil, 2013.

[29] J. An, J. Ee Mei Teoh, R. Suntornnond and C. K. Chua, "Design and 3D printing of scaffolds and tissues," *Engineering,* vol. 1, no. 2, pp. 261-268, 2015.

[30] International Organization for Standardization, "Ceramic tiles - Part 3: Determination of water absorption, apparent porosity, apparent relative density and bulk density" (ISO 10545-3:2018), 2018.

[31] I. V. Antoniac, Handbook of Bioceramics and Biocomposites, Springer, 2016.

[32] P. Sepulveda, H. A. Bressiani, J. Bressiani, L. Meseguer and B. Konig Jr, "Synthesis and properties of ceramic foams for hard tissue repair," *Key Engineering Materials,* vol. 218, pp. 413-416, 2002.

[33] H. Seitz, W. Rieder, S. Irsen, B. Leukers and C. Tille, "Three-dimensional printing of porous ceramic scaffolds for bone tissue engineering," *Journal of Biomedical Materials research, Part B: Applied biomaterials,* vol. 74B, no. 2, pp. 782-788, 2005.

Chapter 6 Preliminary Biological Studies

Abstract

The bioactivity properties of the produced samples were tested *in vitro* by soaking the sintered samples in simulated body fluid (SBF). FESEM observations showed that all the tested samples were covered by an apatite layer confirming their osteoconductivity. While the porous samples were entirely covered by the new layer, partial coverages were observed on the dense samples. Furthermore, it was shown that the samples made from HA-AR2, obtained a thicker bioactive layer than the samples made from HA-AR1, thanks to their lower Ca/P ratio. EDX analyses showed that the new precipitated layer with Ca/P ratio of 1.33, was OCP (octacalcium phosphate) rather than HA. In fact, OCP is considered as a precursor of the formation of nonstoichiometric biological apatites and is thermodynamically more favourable phase than HA to precipitate from calcium and phosphorous solutions.

As an innovative procedure, the antibacterial functionality was also added to the produced scaffolds by casting a polymer-ceramic composite around them and obtaining multifunctional graded structures. Incorporation of a small amount of Ag^{+} ions in the composite material is demonstrated to eliminate almost 100 per cent of the Planktonic and the adhered bacteria and would be a powerful tool to prevent post-surgery infection after implantation of the orthopaedic implants.

Abbreviations

2-D	Two dimensional
3-D	Three dimensional
BM	Ball-milled
CAD	Computer-aided design
CT-scan	Computed tomography scan
ESEM	Environmental scanning electron microscopy
FESEM	Field emission scanning electron microscopy
FGM	Functionally graded material
HA	Hydroxyapatite
HA-AR2	As-received hydroxyapatite powder, batch n.2
ISO	International standard organisation
PCL	polycaprolactone
PEI	Polyethyleneimine
SBF	Simulated body fluid
TTCP	Tetracalcium phosphate
WBM	Wet ball milling
β-TCP	β-tricalcium phosphate

6.1 Bioactivity properties

When an artificial material is implanted in a living body, the essential requirement for its bonding to the living bone is the formation of bone-like apatite on its surface, called bioactivity [1, 2]. The mechanism of bone-bonding is based on the formation of a surface layer of hydroxycarbonate apatite (HCA), which mimics the chemical and crystallographic characteristics of bone [3]. In 1991, Kokubo [1] showed that the *in vivo* apatite formation can be reproduced in an acellular simulated body fluid (SBF). Analyses of the surface layer formed in SBF showed that its composition and structure was similar to the bone mineral. This means that the *in vivo* bone bioactivity of a material can be predicted from the apatite formation on its surface in SBF which has been used since then as the criteria for the bioactivity of materials [2]. However, it must be considered that other factors also govern the behaviour of the cell in the body, which are not presents in SBF test, and therefore this method might not be truly representative of the *in vivo* physiological conditions [4]. For example, upon insertion of the implant, the pH of the body fluid in the vicinity of the implant reduces from the normal value of 7.4 to 5.5, and in the course of 10 to 15 days regains neutrality, the factor that is not considered *in vitro* tests [5]. Nonetheless, a recent review on the relationship between apatite formation in SBF and *in vivo* bone-bonding stated that about 3/4 of the *in vitro* studies of apatite-forming ability successfully predicted *in vivo* performance of the same materials [6].

In this thesis, preliminary *in vitro* bioactivity tests were carried out on representative samples of dense, porous and bilayer structures made by both gelcasting and robocasting techniques. The tests were performed according to ISO 23317:2014 [7]. The SBF solutions were prepared according to a strict preparation protocol by dissolving reagent chemicals of sodium chloride (NaCl) sodium hydrogen carbonate ($NaHCO_3$), potassium chloride (KCl), dipotassium hydrogen phosphate trihydrate ($K_2HPO_4.3H_2O$), magnesium chloride hexahydrate ($MgCl_2.6H_2O$), hydrochloric acid solution, (HCl), calcium chloride dihydrate ($CaCl_2.2H_2O$) and sodium sulphate (Na_2SO_4) into deionised water. The fluid was buffered at physiological pH 7.40 at 37 °C using trishydroxymethyl aminomethane (TRIS) and 1 mol/L HCl. The ion concentration of the standardised SBF solution along with the corresponding concentrations in the blood are presented in Table 6-1.

Table 6-1: The ion concentrations of SBF and human blood plasma according to the ISO standard [7].

Ion	Concentration (10^{-3} mol)	
	SBF (pH 7.4)	Blood plasma (pH 7.2–7.4)
Na^+	142.0	142.0
K^+	5.0	5.0
Mg^{2+}	1.5	1.5
Ca^{2+}	2.5	2.5
Cl^-	147.8	103.0
HO_3^-	4.2	27.0
HPO_4^{2-}	1.0	1.0
SO_4^{2-}	0.5	0.5

Preliminary Biological Studies

Disc-shaped specimen were placed in transparent plastic bottles as shown in Figure 6-1 and were soaked in the SBF solution. The required volume of the SBF solution is a function of the apparent surface area of the specimen and is calculated according to the following formula:

$$v_s = 100mm.S_a \qquad \text{Equation 6-1}$$

where v_s and S_a are the volume of SBF in mm^3 and the apparent surface area of the specimen in mm^2, respectively. For porous samples, the volume of SBF must be greater than the calculated v_s [7].

After soaking at 37 °C for 4 weeks, the samples were washed under a gentle flow of ultrapure deionised water to remove the residual SBF ions and were dried subsequently. The lower surface of the samples was observed by field emission scanning electron microscopy (FESEM) after coating the samples with a Pt–Pd thin film. FESEM observations revealed that all of the samples were covered, partially or completely, by an almost thick and newly developed layer confirming the bioactivity properties of the samples.

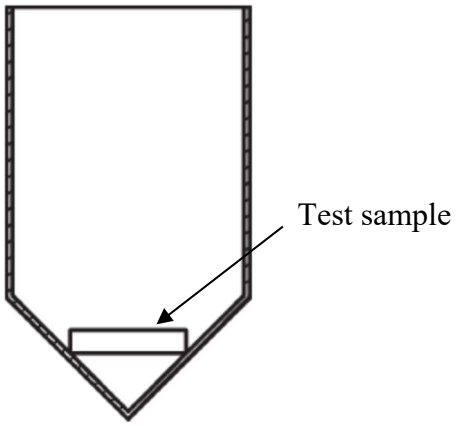

Figure 6-1: Configuration of the disc-shaped specimen in plastic bottles for SBF test.

Figure 6-2 shows the FESEM images obtained from the dense samples produced from wet ball-milled (WBM) HA-AR1 (left) and HA-AR2 (right) by gelcasting method. As discussed in chapter 3, these samples were multiphasic calcium phosphate (CaP) ceramics composed of different percentages of β-tricalcium phosphate (β-TCP) (around 28% and 62 % for WBM HA-AR1 and WBM HA-AR2, respectively). In both cases, we can observe that the newly formed apatite layers don't cover the samples surfaces entirely. Furthermore, the higher magnification images reveal different morphologies for the precipitated CaP layers, depending on the starting powder. While the sample made from HA-AR1 was covered by a homogenous layer of flakes, showing the typical flower-like morphology [8], the new layer on the sample made from HA-AR2 was in the form of spherical agglomerates of rod-shaped crystals. Both types of morphologies were

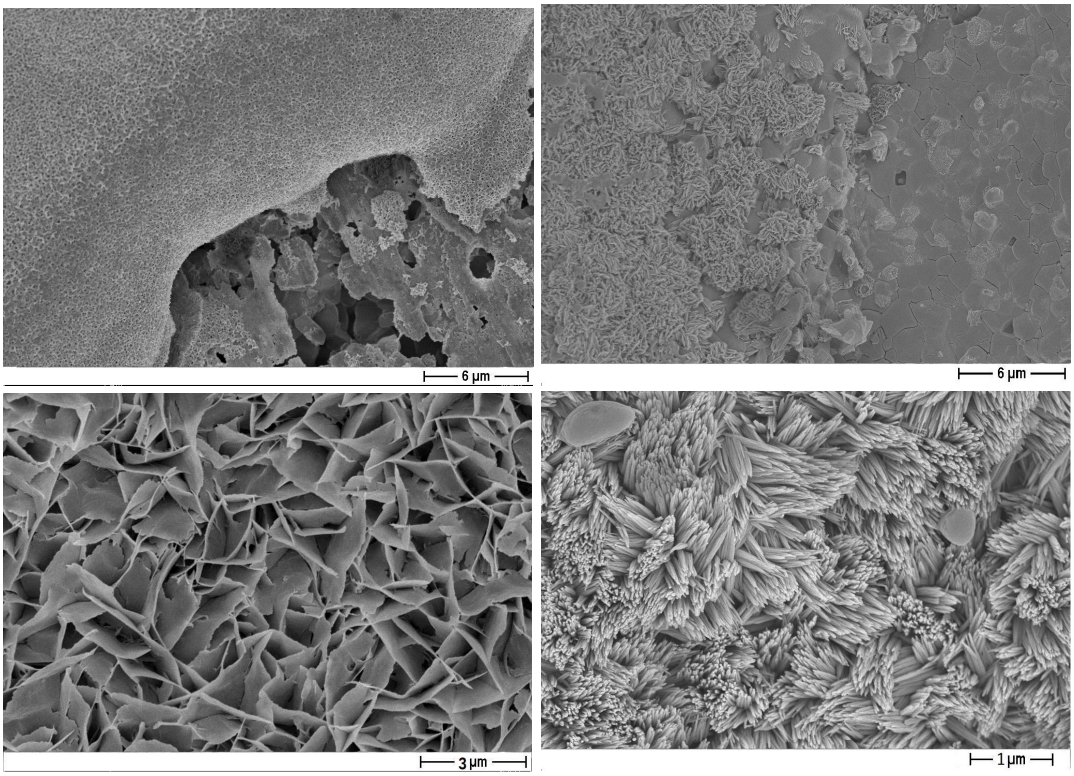

Figure 6-2: The new precipitated CaP layer on gelcast dense samples produced from HA-AR1 (left) and HA-AR2 (right), partially covering the surface of the samples. Images at higher magnification (bottom) show the different morphologies of the precipitated crystals.

already reported in the literature [1, 4, 9, 10]. It seems that the deposited layer on the HA-AR2 sample was thicker than the HA-AR1 sample which can be due to the higher amount of the β-TCP phase of the former. It has already been reported that in biphasic HA/β-TCP materials, there is a direct relationship between the rate of apatite crystal formation and the β-TCP proportion. The higher the β-TCP proportion the higher the apatite crystal formation [11, 12]. This differencecan be explained considering the higher solubility of β-TCP than that of HA, which favours the ion exchange between the material and the SBF solution. In fact, the β-TCP grains preferentially dissolve when immersed in SBF and release Ca^{2+} and PO_4^{3-} ions which can stimulate precipitation of the apatite crystals [9]. Similar observations are reported by LeGeros [13] for both *in vitro* and *in vivo* conditions in which the amount of the deposited layer is directly related to the solubility of the material. The higher the dissolution rate, the higher the new layer deposition.

In the case of gelcast porous samples produced by wet ball milled HA-AR2 powder, very high bioactivity was confirmed by FESEM observations. As it can be seen in Figure 6-3, the thickness of the new apatite layer seemed higher compared to the dense HA-AR2 sample, and the new crystals provided an entire coverage of the porous material surfaces. It can be seen that a continuous network of precipitated apatite adhered to the pore walls and, as a result, the connective windows were

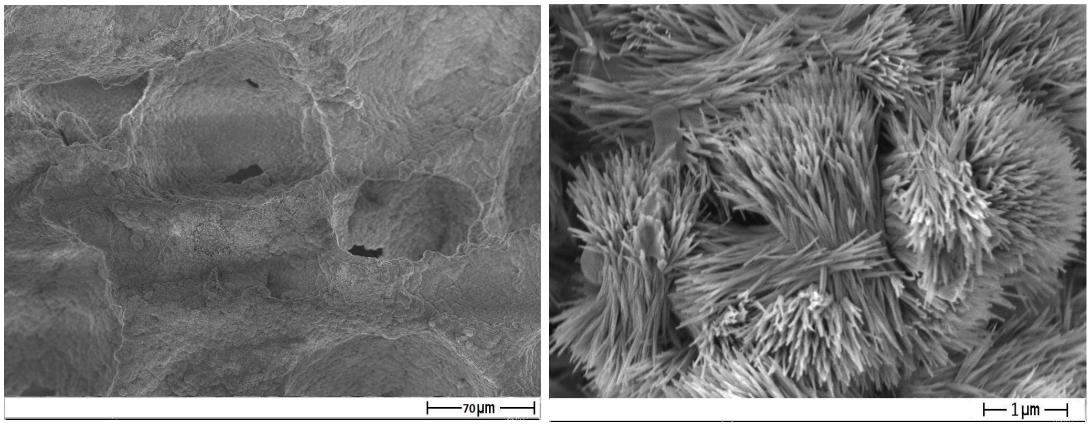

Figure 6-3: The new precipitated CaP layer on the porous gelcast parts produced from HA-AR2.

partially or completely filled by the deposited layer, reducing the porosity. The high magnification image shows that, similarly to the dense part made from HA-AR2, the participated crystals were characterised by rod-shaped morphology.

The formation of a bulky CaP layer was also observed on the surface of the bilayer sample made by robocasting technique from wet ball-milled HA-AR2, as illustrated in Figure 6-4. The precipitation of a rough layer covering the surface of the printed filaments was evident. Like gelcast samples of HA-AR2, the morphology of the deposited crystals was rod-shaped or needle-like. However, unlike spherical aggregates in the gelcast HA-AR2, they distributed evenly on the surfaces. It seems that not only the initial powder but also the production technique affects the morphology of the bioactive layers' crystals.

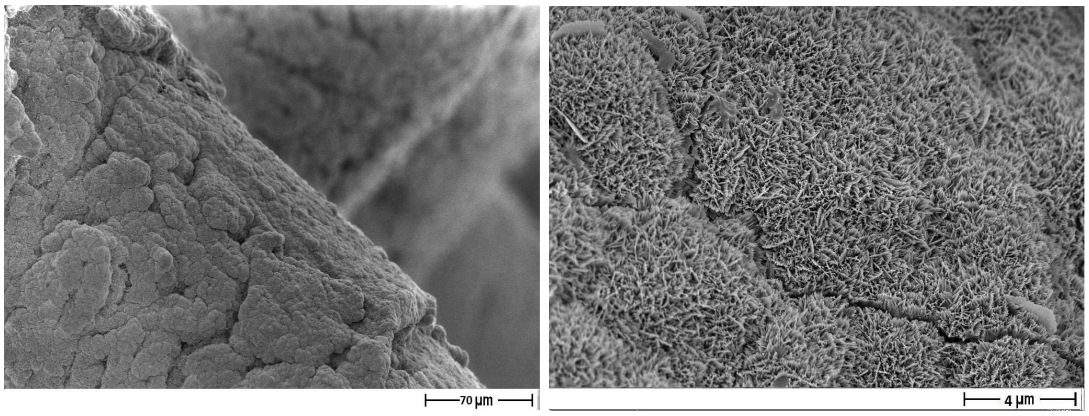

Figure 6-4: The new precipitated CaP layer on the surface of the bilayer robocast sample produced from HA-AR2.

The chemical composition of the precipitated layer formed on the bilayer robocast sample was examined by Energy-dispersive X-ray spectroscopy (EDX) analysis as a representative of the bioactivity tested samples. The results, collected

in Table 6-2, suggested a calcium to phosphorous ratio of 1.33 for the precipitated layer. Previous studies have shown that hydroxyapatite (HA) is not the most preferred precipitation phase from supersaturated calcium and phosphorous solutions, and other CaP phases such as octacalcium phosphate (OCP:$Ca_8H_2(PO_4)_6.5H_2O$, with Ca/P ratio of 1.33) and dicalcium phosphate dihydrate (DCPD) are kinetically more favoured. In fact, while HA is thermodynamically the most stable phase in SBF, theoretical studies indicated that the OCP nucleation rate is substantially higher than HA in physiological environments [10, 14]. OCP is considered as a precursor phase for the formation of nonstoichiometric biological apatites [15], and with time and by increasing the Ca/P ratio, OCP precipitation layers become more apatitic in nature and convert to HA. The gradual phase transformation from OCP to more basic apatitic CaP phases is a well-known phenomenon and several authors have reported this observation by both *in vitro* and *in vivo* tests and after long soaking periods in SBF [14, 15, 16, 17]. The conversion of OCP to HA is mostly a hydrolytic solid-state reaction and takes place according to the following reaction [17]:

$$5Ca_8H_2(PO_4)_6.5H_2O \rightarrow 8Ca_5(PO_4)_3OH + 6H_3PO_4 + 17H_2O \qquad \text{Equation 6-2}$$

Table 6-2: Chemical composition of the bioactivity deposited layer, At%.

Ca	P	O	Si	Mg	Na	Ca/P
15.44	11.63	71.4	0.32	0.56	0.65	1.33

Therefore, it can be concluded that the obtained result by EDX analyses was not surprising and the precipitated CaP layer in this work was OCP which would be transformed to HA if the bioactivity tests were conducted for longer times.

Because of structural similarity between HA and OCP, since OCP structure is composed of apatite layers separated by hydrated layers [15], there is a risk of misidentifying OCP as HA when using X-ray diffractometry (XRD) analyses. However, by transmission electron microscopy (TEM), Xin et al. [10] identified as OCP the precipitated layer produced on HA/β-TCP biphasic ceramics, either under *in vitro* (by immersing the sample in SBF) and *in vivo* (samples implanted in rabbit) test conditions. Moreover, Leeuwenburgh et al. [15] confirmed the initial presence of OCP as the precipitated layer after the in-vivo bioactivity test by means of FTIR analyses. Both of these characterisation techniques can be a subject for future work to have a deeper insight to the composition of the precipitated phases.

6.2 Antibacterial properties

Bacterial adhesion to implant surfaces which results in inflammation and infection is one of the major failure sources of the orthopaedic implants. Generally, the infection starts due to adhesion of bacteria onto the implant surface which is originating from the surgery and escaped from immunological surveillance [18]. Formation of bacterial biofilms shields bacteria from the host immune system and

also makes any antibiotic therapy ineffective leading to the consequent implant loss and revision surgery [18, 19].

The most reliable way to improve the antibacterial properties of medical devices and more specifically of the orthopaedic implants is to prevent bacterial adhesion by incorporation of heavy metals such as silver, zinc, copper, mercury, tin etc. into implant material thanks to their antibacterial properties [18, 20]. Among these elements, silver has been exploited since ancient times as an effective antimicrobial agent. The silver ions in contact with bacteria damage their RNA and DNA, thus inhibiting their replications [21]. Not only it can effectively destroy bacterial cell walls and membranes and inhibit bacterial growth, but it also shows remarkably low toxicity compared with other heavy metals [19]. Furthermore, silver has broad-spectrum antimicrobial property, which is particularly important in the case of the polymicrobial colonization associated with biomaterial related infections [22].

In our work, the antibacterial functionality was introduced into bilayer robocast samples. In a particular way, an external polymer/ceramic (HA+β-TCP) composite layer was added to the produced scaffolds, and such a polymer layer was functionalized by Ag^+ ions. The final structures were functionally graded tri-layer samples, in which each layer was designated to perform a special function: the core dense layer as the load-bearing part, the intermediate porous layer to perform osteoconductivity and osteoinductivity functions, and the outer composite layer to provide additional functionalities, which were bioresorption and antibacterial properties. The new outer layer was composed of poly(ε-caprolactone) (PCL, Mw 80000, Sigma Aldrich, Italy) as the matrix reinforced by a 70/30 mixture of HA and β-TCP (whitlockite, batch P346S OD, Plasma Biotal, UK) particles. PCL to CaP mass ratio was 60:40. Salt leaching method was exploited to obtain macroporosity in the composite layer and acetone was used as the dispersion medium. Silver was added to the composite material as $AgNO_3$ compound.

PCL is a semicrystalline and easily processable polymer which is very well-investigated regarding its mechanical properties, miscibility with a large range of other polymers, and biodegradability. The preparation of controlled drug delivery systems using PCL formulated by several polymers and copolymers has been extensively studied thanks to its native biocompatibility and biodegradability.Its permeability to a wide range of drugs enables uniform drug distribution in the matrix, assuring a long-term release up to several months [23]. In order to improve the osteoconductivity and bioactivity of the antibacterial layer, HA/β-TCP mixture (indicated as biphasic calcium phosphate, BCP) was hybridized with PCL solution to make the PCL/BCP composite material. In fact, such materials have wide clinical application in the repair of hard tissue in a variety of craniofacial, maxillofacial, and periodontal applications [24].

Figure 6-5 shows the successive steps which were followed for the production of the antibacterial composite layer. The production started by the dissolution of $AgNO_3$ in acetone, at 0.4 wt%, closed to the solubility limit [25]. The mixture was needed to be stirred for 72 hours for complete dissolution. Next, the BCP mixture

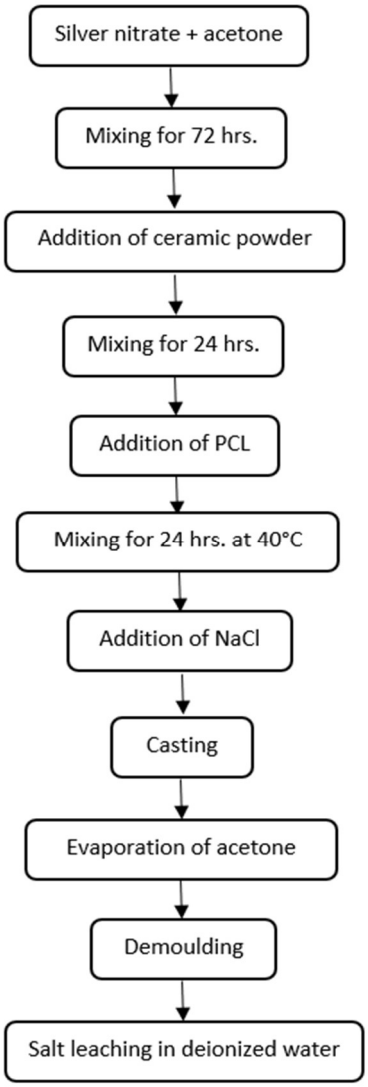

Figure 6-5: Flowchart of the salt leaching method for production of the macro-porous polymer-based layer.

was added to the solution, and the suspension was homogenized for 24 hours under magnetic stirring. After complete homogenization of the ceramic powder in acetone, PCL was added to the suspension. For complete dissolution of the PCL, the mixture was stirred for further 24 h at 40 °C. The addition of NaCl crystals was the last step before casting. NaCl granules (Sigma Aldrich, Italy) were sieved in the 125-355 μm range, as shown in Figure 6-6 (left). They are characterised by regular-shaped grains, most of them with cubic geometry. The grain size distribution (by number) and the relative cumulative distributions are collected in Figure 6-6 (right), allowing to determine an average size of about 215 μm and showing that ~ 95% of the grains were lower than 355 μm. The concentration of $AgNO_3$ was 1 wt% in the final material.

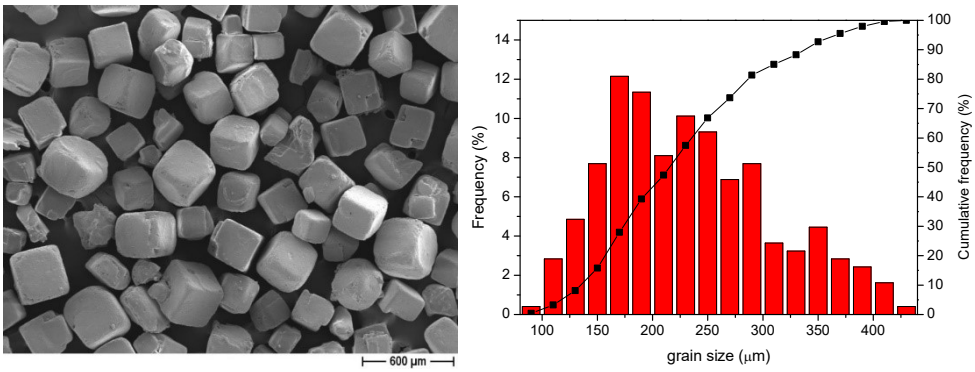

Figure 6-6: FESEM micrograph of NaCl salt, sieved in the 125-355 µm range (left) and corresponding particle size distribution (right).

The mixture was perfectly homogenized before casting, to obtain consistent and uniform mixture thoroughly. The casting was performed in order to obtain two different types of samples. In the first case, the mixture was cast in simple plastic moulds (20 mm diameter, 10 mm height) to obtain cylindrical, monolayer samples (Figure 6-7 left); in the second case, the same mixture was cast around the sintered bilayer robocast samples, in plastic moulds (30 mm diameter) to obtain trilayer samples (Figure 6-7, centre and right, for Ag-free and Ag-containing samples).

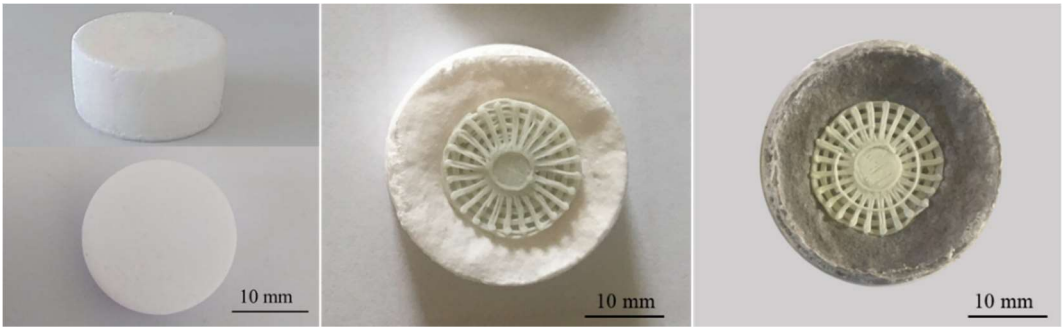

Figure 6-7: Digital photographs of a PCL/BCP monolayer sample (left) and of two representative trilayer samples, obtained by casting the PCL/BCP layer around robocast bilayer samples. Centre: Ag-free PLC/BCP layer; right: Ag-added PLC/BCP layer.

Drying was accomplished at room temperature for 24 hours, allowing the complete acetone evaporation, and then the samples demoulded and immersed in deionised water for 4 days to leach out the NaCl crystals. The water was refreshed every 24 hours. The amount of each component used in the production of this antibacterial layer is presented in Table 6-3. The PCL to BCP mass ratio was fixed at 1.5. As a reference, monolayer and trilayer scaffolds without antibacterial agent were also produced: apart from the initial silver nitrate addition, the same procedure was followed.

Table 6-3: The composition of the composite antibacterial layer, g.

Acetone	$AgNO_3$	PCL	HA/β-TCP mixture	NaCl
48	0.2	12	8	108

Preliminary Biological Studies

In Figure 6-8, the XRD pattern of the Ag-free monolayer samples is depicted. The analysis shows the main diffraction patterns of polycaprolactone, precisely the (110) plane at $2\theta \sim 21.4°$ and the (200) plane at $2\theta \sim 23.7°$, suggesting a semi-crystalline nature of the polymer [25, 26]. Besides, we can observe the main diffractions signals of both HA and β-TCP phases. In the case of Ag-added samples, no further diffraction pattern was observed, due to the low silver concentration in these samples.

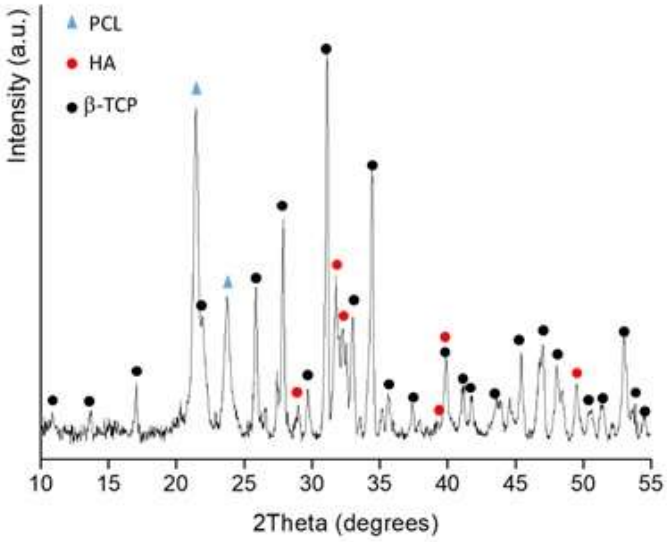

Figure 6-8: XRD pattern of the Ag-free PCL/BCP monolayer sample, showing the presence of the three expected phases.

In Figure 6-9, a representative FESEM micrograph, showing the structure of the PCL/BCP macroporous layer, is depicted (left). We can observe the irregular, square-shape of macropores left by the NaCl crystals during the leaching process. The average pore size was about 270 μm, slightly larger than the average size of NaCl granules, but still in agreement with this value. The right image is a magnified micrograph of the polymer strut between the pores, showing the presence of quite well-dispersed CaP particles within the PCL matrix, as shown by a black arrows. The size of the ceramic particles was in the range 0.5-2 μm, in good agreement with their granulometric data, thus suggesting a good dispersion of the CaP powder in the polymer solution.

The antibacterial behaviour of the samples was investigated thanks to the collaboration with the Department of Public Health and Pediatrics of the University of Torino. The antibacterial test was carried out utilizing a quantitative bacterial adhesion assay by using a sonication protocol to dislodge adherent microorganisms, as detailed in previous papers of the microbiological research group [27]

All the samples were subjected to a rigorous sterilization process before conducting the tests to remove any contamination during samples preparation and transformation stages. The sterilization was conducted by sonication of the samples in 80% ethanol (EtOH, Sigma Aldrich, Italy) medium for 10 minutes. The samples

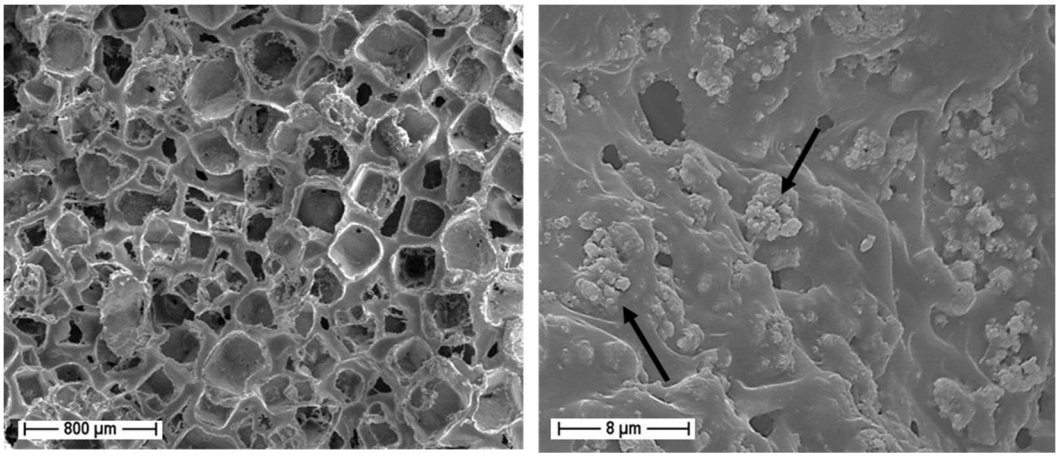

Figure 6-9: FESEM micrographs showing the macroporous PCL/BCP layer (left), while, at higher magnification (right), the CaP particles embedded in the PCL matrix are depicted.

were washed carefully with deionised water, to remove ethanol and kept in the sterile condition till antibacterial tests.

A biofilm-producing Staphylococcus aureus strain (ATCC 29213) was employed for the adhesion essay because it is one of the main pathogens involved in both orthopaedic and dental infections [29, 30].

Briefly, bacteria stored at -80°C were cultured overnight at 37°C in Mueller Hinton Broth (MHB; Becton Dickinson & Co., USA). After incubation, bacteria were re-suspended in 100 µl of MHB, harvested by 10 min centrifugation at 4000 rpm and then diluted in MHB to 10^4 CFU/mL, as confirmed by colony counts on Nutrient Agar (NA, Sigma Aldrich, Italy). The sterile samples were transferred into multiwell culture plate, covered with 7 ml of bacterial suspension and incubated by shaking for 24 h at 37 °C to allow *in vitro* bacterial adhesion. A photograph showing some monolayer and trilayer samples incubated with bacterial inoculum in the multi-well culture plate is depicted in Figure 6-10. Controls were represented by bacteria incubated in MHB with no material. After sonication (40 kHz) for 30 min at 22 °C in 10 ml of sterile physiological solution (NaCl 0.9%; Bieffe Medital S.p.A., Grosotto, Italy), the number of strongly bound bacteria on the samples after incubation was quantified. This is an ideal protocol for dislodging biofilm-producing bacteria without affecting bacterial viability [27,28,30,31]. The number of Colony Forming Units (CFU) in each sonication product was quantified, after a 10 min centrifugation at 4,000 rpm and then concentrated in 1 ml of sterile NaCl 0.9%, by serial plate counts into NA. The number of planktonic bacteria (CFU/mL) was also determined [27, 28].

All the experiments were performed simultaneously for each material, assayed in triplicate and repeated a minimum of three times.

For the adhesion assays, each sample was immersed in 5 mL of bacterial suspension in Mueller Hinton broth, containing about 107 bacteria/ml, and incubated at 37 °C for 24 h under shaking. At the end of the incubation, the samples

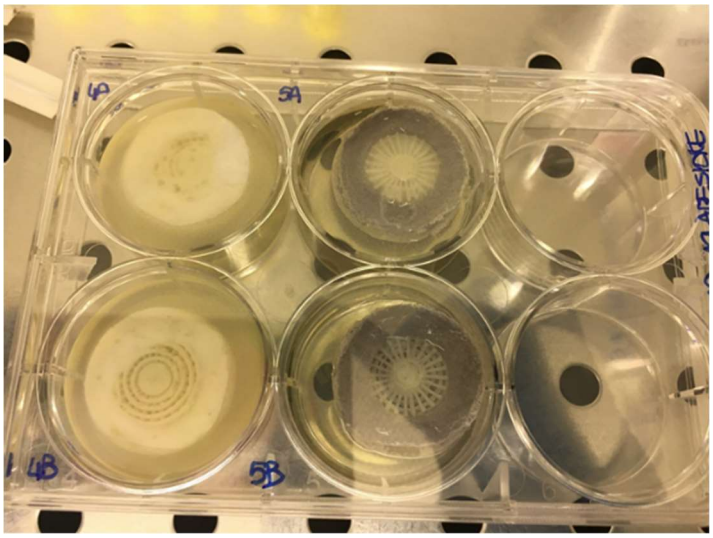

Figure 6-10: Digital photograph showing the mono- and trilayer samples incubated with bacterial inoculum in the multi-well culture plate.

were extracted from the bacterial broth, washed in sterile water, transferred into sterile plastic bags containing 1.5 mL of the same physiological solution as stated in the previous paragraph, and sonicated for 7 min at 22°C to detach adhered bacteria. Controls represented by bacteria incubated in broth, in the absence of the samples, were also prepared. Both the incubation broths and sonication solutions were serially diluted and spread on Nutrient Agar plates, to obtain, after incubation for 24h at 37 °C, the number of CFU referred to the non-adhered and adhered bacteria [29]. The adhesion experiments were assayed in triplicate and repeated a minimum of three times.

The adhesion assay results (CFU/mL) were analysed by descriptive statistics (mean ± SD). The following formula was used for the antibacterial rate calculation:

$$R = \frac{B-A}{B} \times 100\% \qquad \text{Equation 6-3}$$

where R is the antibacterial rate, A is the average recovery bacterial count of the sample (CFU) and B is the average recovery bacterial count of the control sample (CFU). The results were tested by unpaired t-tests to highlight significant differences ($p < 0.05$; 95% confidence interval) between the samples, using Graphpad Prism, Version 8 for Windows (Graphpad Software, San Diego, CA, USA).

Table 6-4 collects the results obtained from antibacterial tests. Figure 6-11 is the graphical representation of the same results. A significant number of adhered bacteria was found in the Ag-free samples (indicated as “control samples” in Table 6-4): both monolithic PCL/BCP and trilayer samples showed adherent staphylococci in the order of 10^9 CFU/mL. It can be seen that, in both samples, incorporation of Ag^+ ions in the materials was extremely effective in eradicating the studied bacteria. In fact, the addition of 1 wt% of $AgNO_3$ to PCL/BCP polymer-

Table 6-4: Bacterial count (CFU/mL) and antibacterial rate (%) obtained from antibacterial tests.

	Sample type	Ag-doped sample	Control sample	R (%)
Monolayer	Adhered bacteria	$1.90\times10^{6} \pm 9.96\times10^{5}$	$3.49\times10^{9} \pm 2.78\times10^{8}$	99.95
	Planktonic bacteria	$2.66\times10^{4} \pm 1.16\times10^{4}$	$3.18\times10^{9} \pm 2.14\times10^{8}$	100.00
Trilayer	Adhered bacteria	$7.16\times10^{4} \pm 3.5\times10^{4}$	$3.22\times10^{9} \pm 3.07\times10^{8}$	100.00
	Planktonic bacteria	$4.31\times10^{4} \pm 1.70\times10^{4}$	$2.97\times10^{9} \pm 3.82\times10^{8}$	100.00

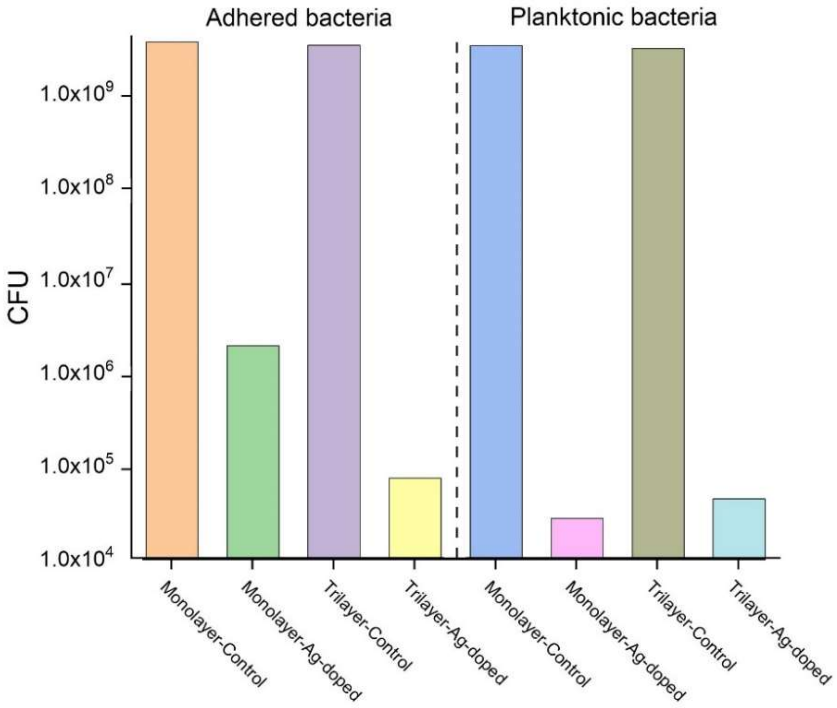

Figure 6-11: Bacterial counts of different samples obtained from microbiological tests.

ceramic composite drastically reduced the amount of adhered bacteria, and specifically to 10^6 CFU/mL in the monolayer PCL/BCP, and even lower value, 10^4 CFU/mL, in the triphasic polymer-ceramic compound. The results obtained in this work were marginally better than the average antibacterial results presented in the literature. For example Ou et al [31] used higher amount of silver (5%) as antibacterial agent and achieved 98.6% bacterial killing capability in zirconiamaterial, and in another work Yang et al. [20] used different concentrations of Ag and Zn and obtained different antibacterial levels in the range of 92.7 to 99.9%.

In order to confirm the release of silver ions from the functionalized scaffolds, and its antibacterial properties, after 24 h incubation, the planktonic bacteria (i.e., those present in the broth) were quantified as well. We can observe that the Ag-free control samples were characterised by an elevated concentration of planktonic bacteria (109 CFU/mL), which significantly decrease (to 104 CFU/mL) in the broths containing the Ag-functionalized samples, for both mono and trilayer

materials, and justify the low adhering bacteria in these materials. These results show that the Ag+ incorporation in the composite layer was markedly effective in killing bacterial, and confirm the bactericidal functionality of the produced FGMs.

The antibacterial mechanism of Ag-containing scaffolds can be considered as following steps: the released Ag^+ ions were absorbed into the surfaces of negatively charged bacterial cell walls because of the electrostatic attraction between negatively charged bacterial cells and positively charged Ag ions [31]. When the Ag ions combined with the bacterial DNA by penetrating the cell walls, they destroy bacterial cell walls and membranes causing the cytoplasm leakage and prevent cells to replicate [32].

Concerning the concentration of Ag^+ ions needed to inhibit bacteria, a minimum concentration of 30-125 ppb has been proposed [31]. However, the effectiveness of Ag incorporation in the implant material in killing the bacteria is also dependent on the bacterial release to the infected environment. On the other hand, the cytotoxicity and the toxic effect of silver on the biological systems should also be accounted for. Upon diffusion into the cell, Ag ions can trigger DNA damage and chromosomal abnormalities at different levels: molecules, organelles, and the entire cell [33]. The cytotoxicity of silver is claimed to be dependant on several parameters such as size, shape, concentration, agglomeration or aggregation [33]. Therefore, it should be mentioned that the antibacterial study conducted in this work was a preliminary study to identify the feasibility of the production of multilayer FGM materials with different functionalities including antibacterial properties, and a more detailed and comprehensive multidisciplinary study is needed to identify different aspects of the antibacterial properties of the produced samples which can be the subject of a future work.

Some of the non-sonicated samples were submitted to FESEM characterisation, in order to observe the interaction between the bacteria and the Ag-free or Ag-functionalized-materials. In Figures 6-12 we can observe the micrographs of an Ag-free monolayer sample (left and centre images): the presence of a biofilm on the surface of the porous polymer can be easily observed: the lower magnification image allows to observe the extension of such biofilm (as highlighted by the arrows), covering large portions of the scaffold, while at higher magnifications, the morphology of the film as well as some isolated bacteria, or formation of small units of two or few staphylococci. On the contrary, the Ag-functionalized sample (right image) showed ‘cleaned’ surfaces, in which no staphylococci or just a few isolated bacteria, could be observed.

A similar observation was carried out on the trilayer samples: Figure 6-13 shows the structure of the sample (centre image), while the left and right images are higher magnifications of the polymer and ceramic part, respectively. We can observe that in both cases, huge colonization of the bacteria occurred, with extended biofilms, in both parts. Once again, the Ag-functionalization resulted to be very effective, as shown in Figure 6-14, since we can observe almost entirely bacteria-free microstructures. The absence of staphylococci was observed not only in the

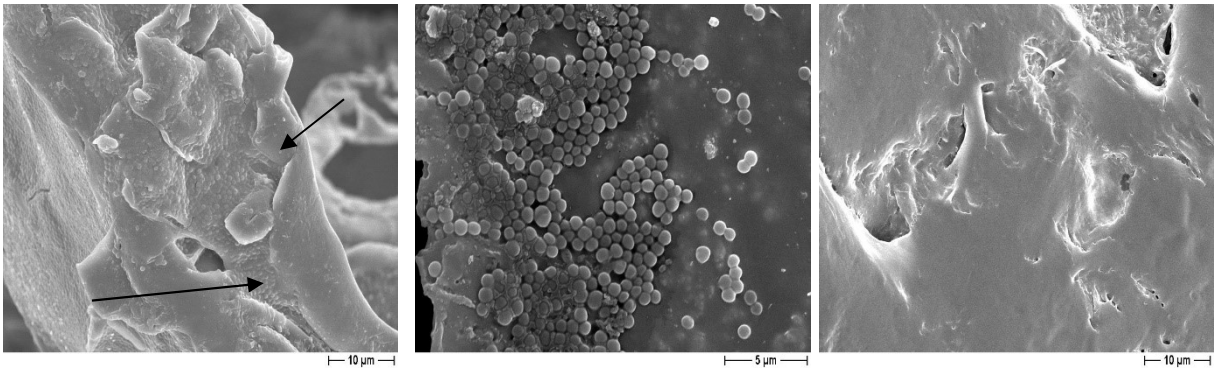

Figure 6-12: FESEM micrographs of an Ag-free (left and centre images) and of an Ag-functionalized monolayer sample (right image). Arrows in the left image show the presence of a biofilm in the former sample.

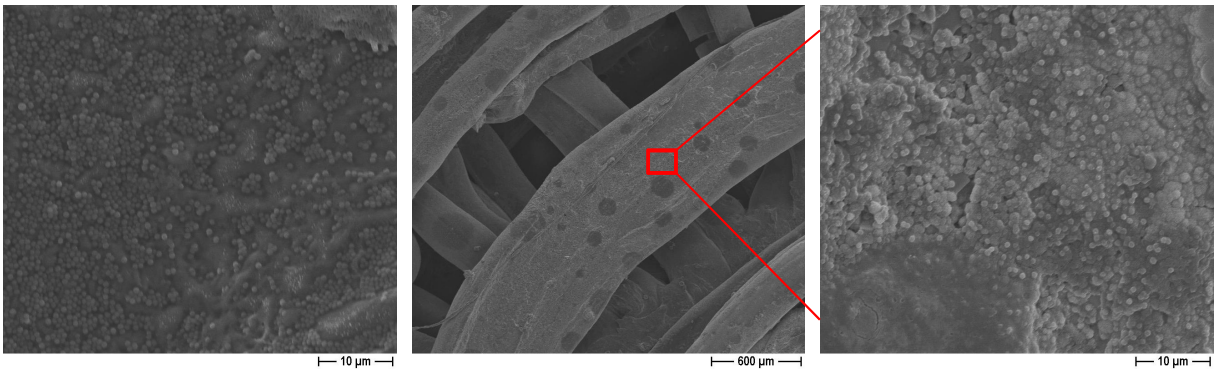

Figure 6-13: FESEM micrographs of an Ag-free multi-layer sample: left and right images are high magnification of the centre image, showing the extended biofilms observed on both polymer (left) and ceramic (right) parts .

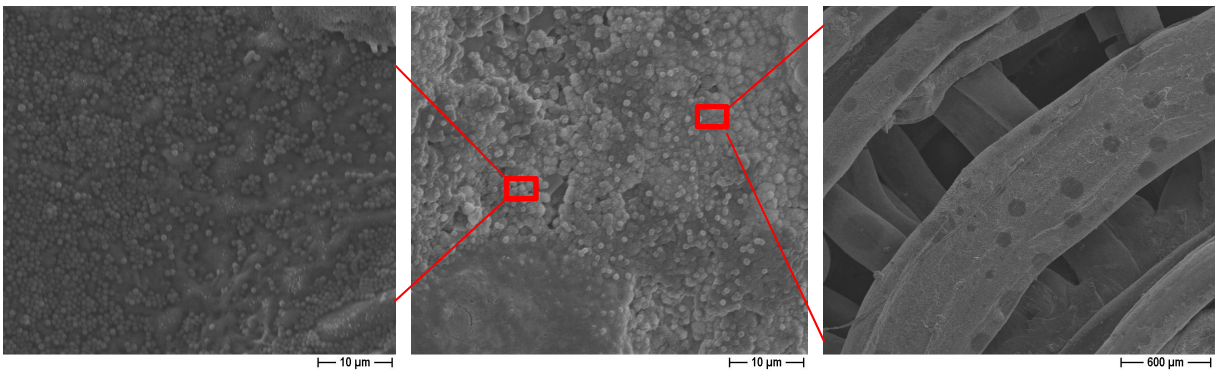

Figure 6-14: FESEM micrographs of an Ag-functionalized triphasic sample: left and right images are high magnification of the centre image, showing the bacteria-free microstructure for both the polymer (left) and ceramic (right) parts.

Ag-functionalized porous layer, but also in the ceramic part, suggesting that the Ag release in the broth, as indicated by the quantification of the planktonic bacteria,

inhibited staphylococci development, and consequently their adhesion to the scaffolds.

6.3 Conclusion

Osteoconduction is considered as an important requirement for biomaterials to be replaced for the damaged bones. The osteoconduction properties of an implant material can be predicted by soaking them *in vitro* in the SBF. The soaking of sintered samples made from ball-milled HA-AR1 and HA-AR2 with different configurations showed the coverage of the samples surfaces with new CaP layers. It was found that the porous samples covered completely by thick layers while the dense parts showed partial coverage. The new crystals morphologies were found to be different for the samples either made from different powders or fabricated with different techniques. Using EDX analyses, the new layer was identified as OCP which is considered as a precursor of biological HA.

The feasibility of the introduction of the antibacterial properties for the produced samples was studied by addition of a new PCL/CaP composite macroporous layer to the already sintered robocast bi-layer parts. The antibacterial properties were added by incorporation of Ag^{+} ions as a powerful antimicrobial agent. The antibacterial tests verified excellent antibacterial properties of the new multifunctional trilayer samples which can be very promising for a future application as an orthopaedic implant.

References

[1] T. Kokubo, “Bioactive glass ceramics: properties and applications,” *Biomaterials,* vol. 12, no. 2, pp. 155-163, 1991.

[2] T. kokubo and H. Takadama, “How useful is SBF in predicting in vivo bone bioactivity?,” *Biomaterials,* vol. 27, pp. 2907-2915, 2006.

[3] S. Ferraris, S. Yamaguchi, N. Barbani, M. Cazzola, C. Cristallini, M. Miola, E. Vernèa and S. Spriano, “Bioactive materials: In vitro investigation of different mechanisms of hydroxyapatite precipitation,” *Acta Biomaterialia,* vol. 102, pp. 468-480, 2020.

[4] H. Pan, X. Zhao, B. W. Darvell and W. W. Lu, “Apatite-formation ability – Predictor of ‘‘bioactivity”?,” *Acta Biomaterialia,* vol. 6, pp. 4181-4188, 2010.

[5] N. Eliaz and N. Metoki, “Calcium phosphate bioceramics: A review of their history, structure, properties, coating technologies and biomedical applications,” *Materials,* vol. 10, no. 4, p. 334, 2017.

[6] A. A. Zadpoor, “Relationship between in vitro apatite-forming ability measured using simulated body fluid and in vivo bioactivity of biomaterials,” *Materials Science and Engineering C,* vol. 35, pp. 134-143, 2014.

[7] International Organization for Standardization (ISO), "Implants for surgery - In vitro evaluation for apatite-forming ability of implant materials" (ISO 23317:2014), 2014.

[8] P. Li, K. Nakanishi, T. Kokubo and K. De Groot, “Induction and morphology of hydroxyapatite, precipitated from metastable simulated body fluids on sol-gel prepared silica,” *Biomaterials,* vol. 14, no. 13, pp. 963-968, 1993.

[9] M. K. Ahn, Y. W. Moon, Y. H. Koh and H. E. Kim, “Production of highly porous triphasic calcium phosphate scaffolds with excellent in vitro bioactivity using vacuum assisted foaming of ceramic suspension (VFC) technique,” *Ceramics International,* vol. 39, pp. 5879-5885, 2013.

[10] R. Xin, Y. Leng, J. Chen and Q. Zhang, "A comparative study of calcium phosphate formation on bioceramics in vitro and in vivo," *Biomaterials,* vol. 26, p. 6477–6486, 2005.

[11] C. Shuaia, P. Li, J. Liu and S. Peng, "Optimization of TCP/HAP ratio for better properties of calcium phosphate scaffold via selective laser sintering," *Materials characterization,* vol. 77, pp. 23-31, 2013.

[12] C. Piccirillo, R. Pullar, E. Costa, A. Santos-Silva, M. E. Pintado and P. Castro, "Hydroxyapatite-based materials of marine origin: A bioactivity and sintering study," *Materials Science and Engineering C,* vol. 51, pp. 309-315, 2015.

[13] R. Z. LeGeros, "Calcium phosphate-based osteoinductive materials," *Chemical reviews,* vol. 108, no. 11, p. 4742–4753, 2008.

[14] X. Lu and Y. Leng, "Theoretical analysis of calcium phosphate precipitation in simulated body fluid," *Biomaterials,* vol. 26, p. 1097–1108, 2005.

[15] S. C. Leeuwenburgh, J. G. Wolke, M. C. Siebers, J. Schoonman and J. A. Jansen, "In vitro and in vivo reactivity of porous, electrosprayed calcium phosphate coatings," *Biomaterials,* vol. 27, p. 3368–3378, 2006.

[16] Y. Lenga, J. Chenb and S. Qu, "TEM study of calcium phosphate precipitation on HA/TCP ceramics," *Biomaterials,* vol. 24, p. 2125–2131, 2003.

[17] N. Eidelman, L. C. Chow and W. E. Brown, "Calcium phosphate saturation levels in ultrafiltered serum," *Calcified Tissue International,* vol. 40, pp. 71-78, 1987.

[18] R. Sorrentino, A. Cochis, B. Azzimonti, C. Caravaca, J. Chevalier, M. Kuntz, A. A. Porporati, R. M. Streicher and L. Rimondini, "Reduced bacterial adhesion on ceramics used for arthroplasty applications," *Journal of the European Ceramic Society,* vol. 38, p. 963–970, 2018.

[19] S. F. Ou, R. J. Chung, L. H. Lin, Y. C. Chiang, C. F. Huang and K. L. Ou, "A mechanistic study on the antibacterial behavior of silver doped bioceramic," *Journal of Alloys and Compounds,* vol. 629, pp. 362-367, 2015.

[20] S. Yang, Y. Zhang, J. Yu, Z. Zhen, T. Huang, Q. Tang, P. K. Chu, L. Qi and L. H. , "Antibacterial and mechanical properties of honeycomb

ceramic materials incorporated with silver and zinc," *Materials and Design,* vol. 59, pp. 461-465, 2014.

[21] A. Balamurugan, G. Balossier, D. Laurent-Maquin, S. Pina, A. Rebelo, J. Faure and J. Ferreira, "An in vitro biological and anti-bacterial study on a sol–gel derived silver-incorporated bioglass system," *Dental Materials,* vol. 24, pp. 1343-1351, 2008.

[22] V. Guarino, G. Gentile, L. Sorrentino and L. Ambrosio, "Polycaprolactone: synthesis, properties, and applications," in *Encyclopedia of Polymer Science and Technology*, John Wiley & Sons, Inc, 2017.

[23] P. S. Poh, D. W. Hutmacher, B. M. Holzapfel, A. K. Solanki, M. M. Stevens and M. A. Woodruff, "In vitro and in vivo bone formation potential of surface calcium phosphate-coated polycaprolactone and polycaprolactone/bioactive glass composite scaffolds," *Acta Biomaterialia,* vol. 30, pp. 319-333, 2016.

[24] A. Seidell and W. F. Linke, Solubilities of inorganic and organic compounds, New York: D. Van Nostrand Company, 1919.

[25] N. Aliah and A. M. M. N, "Thermal analysis on characterization of polycaprolactone (PCL) – chitosan scaffold for tissue engineering.," *International Journal of Scientific Research Engineering & Technology,* vol. 6, no. 2, pp. 76-80, 2017.

[26] Y. Qian, Z. Zhang, L. Zheng, R. Song and Y. Zhao, "Fabrication and characterization of electrospun polycaprolactone blended with chitosan-gelatin complex nanofibrous mats," *Journal of Nanomaterials,* vol. 2014, pp. 1-7, 2014.

[27] G. Banche, V. Allizond, P. Bracco, A. Bistolfi, M. Boffano, A. Cimino, B. d. P. E. M and A. M. Cuffini, "Interplay between surface properties of standard, vitamin E blended and oxidised ultra high molecular weight polyethylene used in total joint replacement and adhesion of Staphylococcus aureus and Escherichia coli," *The Bone & Joint Journal,* vol. 96, no. 4, pp. 497-501, 2014.

[28] S. Ferraris, S. Spriano, M. Miola, E. Bertone, V. Allizond, A. Cuffini and G. Banche, "Bioactive and antibacterial titanium surfaces through a modified oxide layer and embedded silver nanoparticles: effect of reducing/stabilizing agents on precipitation and properties of the

nanoparticles," *Surface and Coatings Technology,* vol. 344, pp. 177-189, 2018.

[29] D. Campoccia, L. Montanaro and C. Renata Arciola, "The significance of infectionrelated to orthopedic devices and issues of antibiotic resistance," *Biomaterials,* vol. 27, p. 2331–2339, 2006.

[30] T. Monsen, E. Lövgren, M. Widerström and L. Wallinder, "In vitro effect of ultrasound on bacteria and suggested protocol for sonication and diagnosis of prosthetic infections," *Journal of Clinical Microbiology,* vol. 47, no. 8, pp. 2496-2501, 2009.

[31] S.F. Ou, M.S. Huang, S.Y. Chiou and K.L. Ou, "Research of antibacterial activity on silver containing yttria-stabilized–zirconia bioceramic," *Ceramics International,* vol. 39, p. 3591–3596, 2013.

[32] S.F. Ou, R.J. Chung, L.H. Lin, Y.C. Chiang, C.F. Huang and K.L. Ou, "A mechanistic study on the antibacterial behavior of silver doped bioceramic," *Journal of Alloys and Compounds,* vol. 629, pp. 362-367, 2015.

[33] T. Zhang, L. Wang, Q. Chen and C. Chen, "Cytotoxic potential of silver nanoparticles," *Yonsei Medical Journal,* vol. 55, no. 2, pp. 283-291, 2014.

Chapter 7 Conclusion

The objective of this thesis was the elaboration of dense and porous structures from hydroxyapatite bioceramic for biomedical applications. This bioceramic has been studied intensively in the past few decades to be used in bone repair and replacement applications due to its excellent biological characteristics. The most exceptional characteristic of HA is bioactivity which not only leads to the formation of direct and strong bonding between the host tissue and the bioceramic but also facilitates the formation of new bone. However, low mechanical properties such as inherent brittleness and low-reliability limit HA usage to non-load-bearing applications [1, 2].

In this work, gelcasting and robocasting, as two different advanced ceramic fabrication techniques, were optimised for the production of dense and porous HA parts. Both techniques, based on the colloidal ceramic processing, are suitable for the production of high-performance complex geometries [3]. However, on one side, gelcasting provides flawless components with higher mechanical properties; on the other side robocasting, as an additive manufacturing technique, allows to control the scaffold architecture and complexity more precisely [4]. Bilayer scaffolds made by an inner dense core and a porous external layer were also produced by both techniques.

Fabrication process started with powder characterisation and dispersion study and followed by the investigation and optimisation of the sintering behaviour of the ceramic. In the next stages, dense, porous and multi-layer functionally graded structures (FGM) were fabricated and characterised using both gelcasting and robocasting techniques. The last step was the biological studies including *in vitro* bioactivity tests and introduction of antibacterial properties via the addition of a further polymer/ceramic composite layer incorporated by antibacterial ion.

Material characterisation and sintering optimisation

Two different batches of a commercial HA (namely HA-AR1 and HA-AR2) were used for the production of HA samples which were characterised as calcium deficient HA (CD-HA). In attempts for reduction of the powders particles sizes,

although dry ball milling (DBM) was found only useful for breaking soft agglomerates, wet ball milling (WBM) effectively reduced the particle sizes. However, WBM combined with ultrasonic dispersion was found to be the most effective method in the reduction of the sizes and the distribution range of the ceramic particles. Apart from the expected decomposition of CD-HA to HA+β-TCP (β-three calcium phosphate) which took place at around 1000 °C, calcination of the powders revealed a further important and rarely reported phase transformation of HA to TTCP (tetracalcium phosphate) + α-TCP at 1300 °C. This phase transformation, later on, was found to have a significant effect on the microstructural features of the fired materials as will be described in the followings.

Dilatometry tests were used to study the sintering behaviour of the DBM and WBM powders as well as the identification of different sintering stages and phase transformations. Increasing the heating rate and reduction of the particles sizes were found to significantly improve the sinterability of the powders. Combining the effects of lower particles sizes and higher heating rates, the sinterability of the powder improved more than 15 times leading to an increase of the final density from 73 %TD to almost full densification of near to 99 %TD. While CD-HA bioceramics are characterised by poor sinterability due to different phase transformations during sintering [5, 6], the obtained density level in our work was higher than the values reported in the literature after conventional sintering of this kind of ceramics [5, 6, 7, 8, 9, 10]. Considering the fact that many of the reports used cold pressing for green sample production, which normally results in higher densities than the casting methods [11], the effectiveness of the sintering optimisation conducted in this work has key importance. However, it must be noticed that because of these phase transformations full density cannot be obtained for HA/β- or HA/α-TCP ceramics [6]. The optimum sintering conditions for DBM and WBM powders were found with the heating rate of 10 °C/min for 3 hours, and the heating rate of 5°C/min for 64 min at 1300 °C, respectively.

The effects of different heating rates and sintering times on microstructural development were also studied by analyses of the FESEM images of the WBM samples sintered at 1300 °C. Increasing the heating rate was found to induce grain coarsening at similar sintering time. The final β-TCP phase percentage of the sintered parts was independent of the heating rate.

By increasing the sintering time, different microstructural developments were detected between the samples made from HA-AR1 and HA-AR2. In the case of HA-AR1 samples grains sizes distribution continuously shifted to bigger sizes by increasing the sintering time. However, sintering of the HA-AR2 samples for more than 1 hour led to a remarkable grain refinement leading to decrease in the average grain size from 1.37 μm after 1 hour to 0.37 μm after 3 hours sintering. In fact, after 3 hours sintering, the microstructure of the HA-AR2 samples was composed of the bimodal size distribution of small and big grains and the β-TCP phase percentage increased significantly. HA to TTCP and TCP phase transformation was found responsible for the grain refinement, and the increase of the β-TCP phase percentage, as EDX analyses characterised the big and small grains as TCP and

TTCP phases respectively. This phase transformation was rarely reported in the literature for HA sintering process but sometimes for plasma-sprayed HA coatings due to the catalysing effect of the titanium substrate [12, 13, 14].

Production of dense parts by gelcasting method

Gelcasting of dense and porous HA samples were conducted using agar as the gelling agent. Agar is a non-toxic environmentally friendly biopolymer without harmful effect on nature or human and in comparison with other gelling materials [15,16,17,18,19,20], it was found very effective in the development of a strong gel network. Dense and porous samples were made from two different ranges of the initial powder particles sizes: 1.5 to 2.0 μm and 0.6 to 1.2 μm obtained from DBM WBM processes, respectively. Using a range of particles sizes made it possible to study the effect of initial powder particles sizes on different processing parameters such as green and sintered densities as well as sintering shrinkages and densifications. Sintering of the samples was performed according to the already optimised sintering conditions at two different soaking times of 1 and 3 hours. It was found that by decreasing the initial powders particles sizes the difference between the sintering shrinkages and the final densities of 1-hour and 3-hours sintered samples continuously reduced. In fact, at mean particle sizes of less than 0.78 μm the final density of the 1-hour sintered samples became higher than the 3-hours sintered samples. Based on the dependence of the final density to the initial ceramic mean particles sizes, the minimum mean particles sizes necessary to obtain dense bodies (≥95 %TD) were measured. It was found that to obtain dense part with densities more than 95 %TD by sintering for 1 hour and 3 hours at 1300 °C, the initial ceramic's mean particle size should be less than 0.88 and 0.99 μm, respectively. This finding can be considered as a key criterion for the optimisation of the sintering process of the parts made from this powder.

Uniaxial compression tests were used to study the mechanical properties of both DBM and WBM samples which showed typical compressive behaviour of CaP bioceramics. The effects of the β-TCP phase fraction, green and sintered densities, as well as microstructural characteristics on the material's strength, was identified. By increasing the green density, reduction of the initial powder particles sizes and using powder batch with a higher Ca/P ratio, the compressive strength of the produced dense samples was increased to almost 300 MPa which was in the upper limit of the HA strengths reported in the literature.

Production of porous and bilayer parts by gelcasting method

Highly porous HA samples characterised by interconnected spherical pores were produced by gelcasting of foam technique using sodium dodecyl sulphate (SDS) as the foaming agent. By changing the slurries compositions, the porosity level tailored between 63 and 87%, and more importantly, independent of the porosity level a wide range of pores and windows sizes were preserved for all of the samples. WBM HA-AR1 was found more suitable for the production of low

porosity high strength samples and samples made from DBM HA-AR2 showed the highest obtainable porosity level.

Studying the effect of the slurry constituents on the porosity and pores sizes revealed different behaviours between the samples made from HA-AR1 and HA-AR2. While the HA-AR1 samples showed a reciprocal relationship between the final porosity level and either solid loading or agar amount, it was found that the final porosity of the HA-AR2 samples was mainly related to SDS rather than agar and solid loading. For example, at low SDS concentrations, the final porosity decreased by increasing the agar amount but at high SDS concentrations, it became almost independent of the agar amount. On the other hand, the final porosity was not changed by changing the SDS amount, suggesting that the surfactant type is the most important factor in controlling the final porosity. However, as an important finding, it was found possible to tailor the pores sizes toward smaller sizes by increasing the agar amount at the same amount of SDS and solid loading. In other words, despite other reports in which decreasing the pores sizes always accompanied by a decrease in the final porosity [15, 21, 22], porous bodies with similar porosity level, but different pore sizes were produced.

Functionally graded bilayer cylindrical parts were produced combining the already optimised gelcasting techniques of the dense and porous samples. The produced bilayer structures proved the advantages of the gelcasting method in the production of multilayer multifunctional scaffolds. The outer porous part was designed to enhance interlocking with the surrounding bone under physiological conditions, while the inner dense part acts as a load-bearing region because of its superior compressive strengths. By tailoring the ratio between the two parts and their structural position, the functional diversity of the graded porous HA scaffolds can be expanded.

Production of dense, porous and bilayer parts by the robocasting method

Similar to the gelcasting technique, dense, porous and multilayer structures were produced by robocasting technique from both DBM and WBM powders. The dense and porous parts were in the shape of a cylinder and a cube composed of a network of linear struts, respectively. The multi-layer structure was a functionally graded structure designed as a dense cylinder in the centre, surrounded by concentric rings constructing pores from 600 μm up to 1 mm. In order to successful printing of each part, the inks formulations and printing parameters were specifically tailored. The outset layer was characterised by filaments spanning distances as high as 1.28 mm between two supports demonstrating the high strength and shape stability of the formulated ink in supporting its own weight and the weight of the upper layers.

The mechanical performance of the dense and porous robocast samples was analysed by the uniaxial compression test. In both cases, the DBM parts showed higher strength than the WBM parts. This unexpected result can be attributed to the higher solid loadings of the inks used for the production of the as-received samples, resulting in lower internal stresses during drying of the samples. Moreover, the

porous samples showed higher strength when the loading was applied perpendicular to the printing plane compared to the loading along with the rod directions. As an unprecedented study, the fracture modes of the porous samples were investigated using an environmental scanning electron microscope (ESEM) equipped with a compression test device. It was found that fracture initiated from the external surface of the rods, close to the intersection between rods, and propagated parallel to the load axis. The crack propagation leading to the failure of the material during the compression test was also monitored which migrated in both inter- and intra-granular paths.

Functional properties: bioactivity and antibacterial properties

The osteoconductive properties of the produced samples confirmed by the formation of the apatite layer on their surfaces after being soaked in simulated body fluid (SBF). While the porous samples were entirely covered by the new layer, there was partial coverage on the dense samples, demonstrating the higher biological performance of the porous samples. The morphology of the new layer was also found to be different between the samples either made from different powders or different fabrication techniques. On the other hand, bioactivity layers on the HA-AR2 samples were thicker than the HA-AR1 samples thanks to their lower Ca/P ratio. EDX analyses showed that the new layer was octacalcium phosphate (OCP) rather than HA which is considered as a precursor of nonstoichiometric biological apatites and kinetically precipitates earlier than HA in biological conditions [23].

Antibacterial property as a new functionality was added to multilayer robocast samples by adding a new PCL/CaP composite incorporated with Ag^{+} ions macroporous layer around them. This new layer was added using salt leaching technique and the microbiological tests confirmed its effectiveness in eradicating of different bacteria.

The final conclusion of the whole work

Due to the inherent low mechanical properties, the clinical applications of HA bioceramic are currently taking advantages of its high biological characteristics rather than mechanical properties. Therefore, the common practice is to use it as porous scaffold or as a coating on other orthopaedic implants rather than load-bearing applications. Attempts that have been made to increase the sintering densification and improve the mechanical properties of HA bioceramics have not received practical usage so far due to limitations such as using expensive equipment [24], the complexity of the production setup [25] or being limited to simple geometries and small sample sizes [11]. On the other hand, most of the papers in which high degrees of densification are reported are related to stoichiometric HA, which has significantly higher sinterability than CD-HA [6], but limited biomedical application because of lack of bone regeneration properties [26]. In this work, by optimisation of the sintering process along with the reduction of the initial powder particles sizes, we obtained a high degree of densification near to 99 %TD as well as high mechanical properties for a commercial HA bioceramic. Moreover, the

material we used was a CD-HA rather than stoichiometric HA, which resulted in sintered bodies composed of both HA and β-TCP phases, therefore benefited from both the high bioactivity of HA and the high bone regeneration properties of β-TCP at the same time. Other important advantages of this work are related to the adopted procedure: on one side, the green bodies were produced by gelcasting method, which can be used for the production of large and complex parts; on the other, the specimens were sintered by natural, pressureless sintering, still with no limitations in shape and dimensions. Despite, no advanced sintering techniques were used, through correct optimisation of the sintering cycle, high levels of sinterability, and therefore high mechanical properties, were obtained. Also, we demonstrated the suitability of agar as the gelling agent which contrary to many other gelling matters is an environmentally friendly agent and is neither considered toxic nor harmful to living organisms.

In the production of porous structures of HA, the main intention is to maximise the porosity level to increase the biological performances of the material. On the other hand, while the minimum pore size of 100 μm is needed for bone ingrowth [27], smaller pores were also found encouraging for specific aspects of new bone formation [1, 28]. In this work, gelcasting of foam technique was tailored for the production of porous structures of HA with different levels of porosity from 63 to 87% covering a wide range of compressive strengths between 2 and 15 MPa. In porous samples, the knowledge acquired on the dense samples was exploited, thus to achieve a good densification degree in the struts. At the same time, the control of the foaming procedure allowed to control both porosity level and pores sizes. Irrespective of the porosity level, a wide range of pores sizes were preserved in all of the produced parts assuring high biological performance. In other words, even if the processing parameters controlled in a way to increase the mechanical properties by reduction of the porosity level, this reduction of porosity was not accomplished by decreasing the pores sizes, therefore the biological performance of the porous part was guaranteed. Moreover, porous parts with the same porosity level but different pores sizes were also developed in which, contrary to previous reports, the porosity level was maintained although the reduction of the pores sizes [15, 21].

Production of the FGM using gelcasting method was a step forward in the utilisation of this method in the development of advanced materials. Having dual structure composed of dense and porous parts which are already optimised to their best performances, these materials benefited from both high mechanical and high biological properties at the same time. Therefore, not only it can be used in both applications of porous parts and dense parts but it can also rectify the common disadvantages of these materials: low mechanical properties of the porous parts and the low biological properties of the dense ones.

Production of dense, porous and multilayer structures from the same material using the robocasting technique allowed us to not only study the feasibility of the production of these structures using an advanced additive manufacturing technique but also to compare the advantages and disadvantages of the two different ceramic fabrication techniques. Robocasting was selected among different additive

manufacturing techniques because it is an almost simple technology without the need for expensive sophisticated equipment, and the feeding material is very similar to gelcasting slurry, with a low degree of organic matters.

Some researchers have already proved the suitability of the robocasting technique for the production of monolithic or porous structures [29,30,31,32,33], however, to the best of my knowledge, this work was the first time that the robocasting technique was used in the production of multi-layer FGM structures, and it demonstrated that with tailoring the ink formulation and printing parameters it is possible to simultaneously print dense and porous structures in one single part.

In comparison with the gelcasting method, the ability to accurately control the pores sizes and morphologies, as well as obtaining large pores more than 1 mm were the advantages of the robocasting technique. While the gelcast sample geometry is dependent on the shape of the mould which is used for the casting, there is less limitation in the designing of the robocast parts. It is possible to produce patient-specific parts with the robocasting technique which are customized specifically for the anatomy of the person who is receiving the implant. Moreover, the production of multilayer parts was found more convenient by robocasting technique. It was shown that both dense and porous parts can be printed at the same time using a suitable paste formulation and there is no limitation for the shape and the arrangement of these parts.

However, the mechanical properties of the robocast samples were lower than the gelcast ones. While in the case of dense samples, this result can be ascribed to the open porosities in the structure of the robocast samples, in the case of porous ones it can be the effect of pores morphology: the short distance between adjacent pores in the gelcast samples controlled the maximum size of the cracks to the thickness of the solid walls between pores, while in the robocast porous parts these cracks can grow to much more bigger sizes, so reduce the samples' strengths. Therefore, some measures can be proposed to increase the mechanical performance of the robocast parts: in the case of dense samples, to modify the ink formulation and the part design to decrease the open porosities, and in the case of porous parts, to use smaller nozzle sizes to limit the cracks' sizes.

Another advantage of this thesis was the usage of the drug delivery characteristics of PCL biopolymer and introduction of antibacterial functionality to the robocast multilayer samples. Practically, this anti-bacterial layer can be added to other samples regardless of their production techniques or geometries. The microbiological tests showed that the slow release of the Ag^{+} ions by resorption of the PCL in the host body can effectively prevent the bacterial infection during and after implantation surgery. In fact, this last multifunctional structure can be very promising for future applications as an orthopaedic implant by which not only antibacterial properties but also other drug deliveries can be performed to better recovery of the patient. Furthermore, in the future by using polymer impregnation method, it will be also possible to benefit from both drug delivery and improvement of the mechanical properties together, as the studies have shown the improvement of the ceramic toughness using polymer impregnation [34, 35].

References

[1] L. L. Hench, An introduction to bioceramics, second edition, Imperial College Press, 2013.

[2] T. Kokubo, Bioceramics and their clinical applications, Woodhead Publishing in Materials, 2008.

[3] M. N. Rahaman, Ceramic processing, second edition, CRC Press, 2017.

[4] S. Bose, D. Ke, H. Sahasrabudhe and A. Bandyopadhyay, "Additive manufacturing of biomaterials," *Progress in Materials Science ,* vol. 93, pp. 45-111, 2018.

[5] H. S. Ryu, K. S. Hong, J.-K. Lee, D. J. Kim, J. H. Lee, B.-S. Chang, D.-h. Lee, C.-K. Lee and S.-S. Chung, "Magnesia-doped HA/β-TCP ceramics and evaluation of their biocompatibility," *Biomaterials,* vol. 25, pp. 393-401, 2004.

[6] S. Raynaud, E. Champion and D. Bernache-Assollant, "Calcium phosphate apatites with variable Ca/P atomic ratio II. Calcination and sintering," *Biomaterials ,* vol. 23, pp. 1073-1080, 2002.

[7] O. Prokopiev and I. Sevostianov, "Dependence of the mechanical properties of sintered hydroxyapatite on the sintering temperature," *Materials Science and Engineering A,* vol. 431, pp. 218-227, 2006.

[8] C. Piccirillo, R. Pullar, E. Costa, A. Santos-Silva, M. E. Pintado and P. Castro, "Hydroxyapatite-based materials of marine origin: A bioactivity and sintering study," *Materials Science and Engineering C,* vol. 51, pp. 309-315, 2015.

[9] F. N. Oktar, Y. Genc, G. Goller, E. Z. Erkmen, L. S. Ozyegin, D. Toykan, H. Demirkiran and H. Haybat, "Sintering of synthetic hydroxyapatite compacts," *Key Engineering Materials,* Vols. 264-268, pp. 2087-2090, 2004.

[10] F. Ben Ayed, J. Bouaziz and K. Bouzouita, "Pressureless sintering of fluorapatite under oxygen atmosphere," *Journal of the European Ceramic Society,* vol. 20, pp. 1069-1076, 2000.

[11] S. Pramanik, A. K. Agarwal, K. Rai and A. Garg, "Development of high strength hydroxyapatite by solid-state-sintering process," *Ceramics International ,* vol. 33, pp. 419-426, 2007.

[12] C. Moseke and U. Gbureck, "Tetracalcium phosphate: Synthesis, properties and biomedical applications," *Acta Biomaterialia ,* vol. 6, pp. 3815-3823, 2010.

[13] W. Jie, L. Xiaoguang, Z. Xingdong and J. Xiaoyang, "Thermal decomposition of hydroxyapatite structure induced by titanium and its dioxide," *Journal of Materials Science Letters,* vol. 13, pp. 159-161, 1994.

[14] H. Guo, K. Aik Khor, Y. Chiang Boey and X. Miao, "Laminated and functionally graded hydroxyapatite/yttria stabilized tetragonal zirconia composites fabricated by spark plasma sintering," *Biomaterials ,* vol. 24, p. 6678675, 2003.

[15] P. Sepulveda, F. Ortega, M. D. M. Innocentini and V. C. Pandolfelli, "Properties of highly porous hydroxyapatite obtained by the gelcasting of foams," *Journal of American Ceramic Society,* vol. 83, no. 12, pp. 3021-3024, 2000.

[16] F. Mendonça, L. Louro, J. de Campos and M. Prado da Silva, "Porous biphasic and triphasic bioceramics scaffolds produced by gelcasting," *Key Engineering Materials,* vol. 361, pp. 27-30, 2008.

[17] B. Chen, D. Jiang, J. Zhang, M. Dong and Q. Lin, "Gel-casting of β-TCP using epoxy resin as a gelling agent," *Journal of the European Ceramic Society ,* vol. 28, pp. 2889-2894, 2008.

[18] F. S. Ortega, P. Sepulveda and V. C. Pandolfelli, "Monomer systems for the gelcasting of foams," *Journal of the European Ceramic Society ,* vol. 22, pp. 1395-1401, 2002.

[19] S. Rekha Dash, R. Sarkar and S. Bhattacharyya, "Gel casting of hydroxyapatite with naphthalene as pore former," *Ceramics International,* vol. 41, pp. 3775-3790, 2015.

[20] A. Asif, R. Nazir, T. Riaz, N. Ashraf, S. Zahid, R. Shahid, A. Ur-Rehman, A. Anwar Chaudhry and I. Ur Rehman, "Influence of processing parameters and solid concentration on microstructural properties of gel-

casted porous hydroxyapatite," *Journal of Porous Materials,* vol. 21, pp. 31-37, 2014.

[21] M. Potoczek, "Gelcasting of alumina foams using agarose solutions," *Ceramics International,* vol. 34, p. 661–667, 2008.

[22] X. Mao, S. Shimai and S. Wang, "Gelcasting of alumina foams consolidated by epoxy resin," *Journal of the European Ceramic Society ,* vol. 28, pp. 217-222, 2008.

[23] R. Xin, Y. Leng, J. Chen and Q. Zhang, "A comparative study of calcium phosphate formation on bioceramics in vitro and in vivo," *Biomaterials,* vol. 26, p. 6477–6486, 2005.

[24] A. Thuault, E. Savary, J.-C. Hornez, G. Moreau, M. Descamps, S. Marinel and A. Leriche, "Improvement of the hydroxyapatite mechanical properties by direct microwave sintering in single mode cavity," *Journal of the European Ceramic Society,* vol. 34, pp. 1865-1871, 2014.

[25] M. Mazaheri, M. Haghighatzadeh, A. Zahedi and S. Sadrnezhaad, "Effect of a novel sintering process on mechanical properties of hydroxyapatite ceramics," *Journal of Alloys and Compounds ,* vol. 471, pp. 180-184, 2009.

[26] E. B. Nery, R. Z. LeGeros, K. L. Lynch and K. Lee, "Tissue response to biphasic calcium phosphate ceramic with different ratios of HA/beta TCP in periodontal osseous defects," *Journal of Peridontology,* vol. 63, no. 9, pp. 729-735, 1992.

[27] S. Bose, M. Roy and A. Bandyopadhyay, "Recent advances in bone tissue engineering scaffolds," *Trends in Biotechnology,* vol. 30, pp. 546-554, 2012.

[28] I. V. Antoniac, Handbook of Bioceramics and Biocomposites, Springer, 2016.

[29] J. Cesarano III, J. G. Dellinger, M. P. Saavedra and D. D. Gill, "Customization of load-bearing hydroxyapatite lattice scaffolds," *International Journal of Applied Ceramic Technology,* vol. 2, no. 3, pp. 212-220, 2005.

[30] S. Michna, W. Wu and J. A. Lewis, "Concentrated hydroxyapatite inks for direct-write assembly of 3-D periodic scaffolds," *Biomaterials,* vol. 26, p. 5632–5639, 2005.

[31] P. Miranda, A. Pajares, E. Saiz, A. Tomsia and F. Guiberteau, "Fracture modes under uniaxial compression in hydroxyapatite scaffolds fabricated by robocasting," *Journal of BiomedicalMaterials Research Part A,* vol. 83, no. 3, pp. 646-657, 2007.

[32] N. Eidelman, L. C. Chow and W. E. Brown, "Calcium phosphate saturation levels in ultrafiltered serum," *Calcified Tissue International,* vol. 40, pp. 71-78, 1987.

[33] Q. Fu, E. Saiz and A. P. Tomsia, "Direct ink writing of highly porous and strong glass scaffolds for load-bearing bone defects repair and regeneration," *Acta Biomaterialia,* vol. 7, p. 3547–3554, 2011.

[34] F. J. Martínez-Vázquez, F. H. Perera, P. Miranda, A. Pajares and F. Guiberteau, "Improving the compressive strength of bioceramic robocast scaffolds by polymer infiltration," *Acta Biomaterialia,* vol. 6, p. 4361–4368, 2010.

[35] C. Paredes, F. J. Martínez-Vázquez, A. Pajares and P. Miranda, "Development by robocasting and mechanical characterization of hybrid HA/PCL coaxial scaffolds for biomedical applications," *Journal of the European Ceramic Society,* vol. 39, p. 4375–4383, 2019.

Appendix A: Experimental Procedures

A-1 Ball milling

Ball milling is the most common way to reduce the size of ceramic particles where the comminution occurs by compression, impact, and shear (friction) between the moving grinding balls and the particles. a range of particles sizes from ~10 μm to as low as a fraction of a micrometre can be obtained by ball milling and it is suitable to be conducted in wet or dry conditions. Several factors, such as the mill parameters, the properties of the grinding medium, and the properties of the particles to be ground affect the rate of grinding.

Tumbling ball milling were used in this work which consisted of a rotating horizontal cylinder partly filled with grinding balls and ceramic particle. 2 mm Ø zirconia balls were utilised as the grinding media. The ball milling was conducted in two different conditions of dry and wet ball milling where the conveying medium was demineralised water using slurries with a solid loading of 30%. The rotation speed of the mill was regulated at 75% of the critical speed, f_c, which was defined as the speed (in revolutions per unit time) required to just take the balls to the apex of revolution, where the centrifugal force just balances the force of gravity providing cataracting motion. The critical speed is calculated according to the following equation:

$$f_c = \frac{1}{2\pi}\left(\frac{g}{R_m}\right)^{0.5} \qquad \text{Equation A-1}$$

Where g is the acceleration due to gravity and R_m is the mill diameter. A schematic of a ball mill in cataracting or falling motion is shown in the following figure.

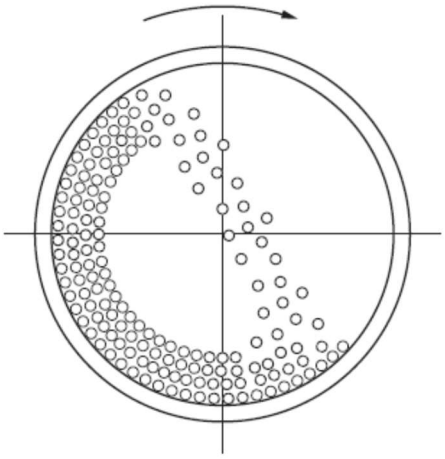

Figure A-1: Schematic of a ball mill in cataracting or falling motion.

Ultrasonic agitation is a process in which ultrasound usually from 20 – 40 kHz, was used for dispersion and deagglomeration of ceramic particles into liquids. In sonication

process, the propagating sound waves in the liquid media apply alternating high-pressure (compression) and low-pressure (rarefaction) cycles on the solid particles providing enough mechanical stress to neutralise the attracting electrostatic forces (e.g. van der Waals forces). The sonication of the slurries was conducted using Vibra-cell VC 750 US processor (Sonic and materials, Inc. Newtown, US) with the frequency of 30 kHz for 10 minutes.

Figure A-2: Vibra-cell VC 750 US processor.

A-2 Laser diffraction granulometry

Laser diffraction granulometry technique uses the principle of diffraction and scattering of a laser beam striking a particle. When a laser beam strikes the suspended ceramic particles, the intensity and diffraction angle of the diffracted rays are changed by the size of the particle. Larger particles induce smaller scattering angles. A series of well-placed photodetectors detect the scattered light known as the diffraction pattern. The sizes of the ceramic particles are measured by interpretation of the diffraction pattern using Mie or Fraunhofer theory.

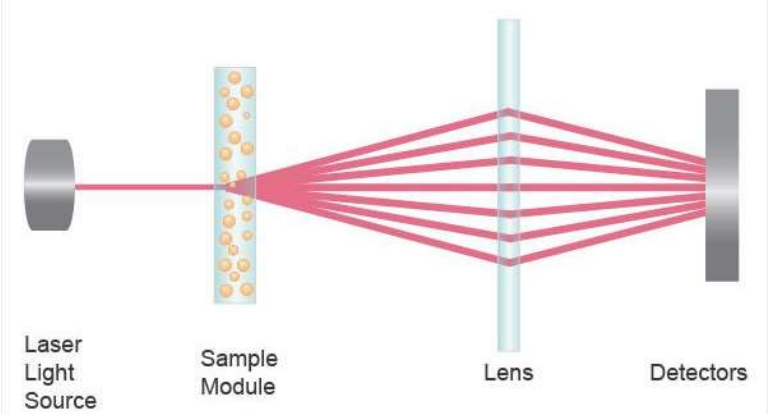

Figure A-3: Schematic of the diffraction of the laser beam after strikes ceramic particles.

Conclusion

The granulometry Malvern Mastersizer 3000 was used to evaluate the particle size distribution of the powders (dispersed in water). The particles sizes distributions were calculated using the Mie theory. The final granulometry result of each sample was the average of 5 measurements.

A-3 Scanning electron microscopy

Scanning electron microscopy (SEM) is a method for obtaining high-resolution images of materials surfaces. Instead of visible light in optical microscopes, electron beams were used for the SEM. In comparison with the optical microscopy, SEM obtains much higher magnifications (~10^6 X) and greater depth of field up to 100 times. It is also possible to conduct qualitative and quantitative chemical analysis with the SEM using an energy dispersive x-ray spectrometer (EDX).

In the SEM, a beam of incident electrons is generated and accelerated by an electron column above the sample chamber by which the sample's surface is scanned in a raster pattern. An SEM image is created by detection of the emitted electrons which are displayed in a monitor as brightness. By synchronizing the position in the image scan to that of the scan of the incident electron beam, the display represents the morphology of the sample surface area.

A-3-1 Field emission scanning electron microscopy

The Field Emission SEM (FESEM) is a type of SEM that works just like a conventional SEM but uses a different electron generation system and provides images at higher resolutions and a much greater energy range. A field emission gun that produces extremely focused high and low-energy electron beams are used as a source of electrons in the FESEM.

A Zeiss Supra 40, Jena, Germany, Field Emission Scanning Electron Microscopy was used in this project for imaging of the powders and, green and sintered samples.

Sample preparation is essential in scanning electron microscopy. Flawed sample preparations reduce the quality of results and lead to false conclusions. Sintered samples were polished using SiC abrasive papers up to grit size 2400 and then get a mirror finish by removing scratches using diamond pastes of 1 micron for final polishing. The samples were thermally etched for 30 min at temperatures which were 50 °C less than their sintering temperatures. To improve the electrical conductivity of the ceramic samples the sputtering was conducted by coating the samples surfaces with a thin layer of Pt with a thickness of about 50 μm.

Figure A-4: Zeiss Supra 40 FESEM device equipped with an Oxford EDS instrument.

A-3-2 Environmental scanning electron microscope

The environmental scanning electron microscope (ESEM) is a type of SEM which enable SEM of wet and insulating samples. the electrical conductivity is provided by a low-pressure gas in the sample chamber. Whether the gas is water or some other gas, ions formed on collisions between electrons emitted from the sample and the gaseous molecules drift back towards the sample surface helping to reduce charge build-up.

The fracture mechanism and crack propagation monitoring of robocast porous samples were carried out using ESEM, Quanta 450 FEG, FEI, Japan with a built-in compression testing instrument. No specific preparation work was needed for the samples before the test.

Figure A-5: Quanta FEG 450 ESEM device.

A-4 Energy Dispersive Spectroscopy

Energy Dispersive X-Ray Spectroscopy (EDS or EDX) is a chemical analysis technique used in conjunction with SEM. The EDX technique characterises the elemental composition of the samples by detection of the X-rays emitted from the sample. Bombardment of a sample surface by SEM's electron beam leads to the ejection of electrons from the atoms of the sample's surface. A characteristic X-ray is emitted upon filling the resulting electron vacancies by electrons from a higher state.

The detector in EDX is typically lithium-drifted silicon, solid-state device, when it strikes by an incident x-ray, it creates a charge pulse that is proportional to the energy of the x-ray. A charge-sensitive preamplifier converts the charge pulse to a voltage pulse. The signal is then sent to a multichannel analyser and from there to a computer for display and further data evaluation.

An Oxford EDS microanalysis (Oxford Instrument plc, Abingdon, UK), used to determine the chemical composition of both powder and sintered specimen.

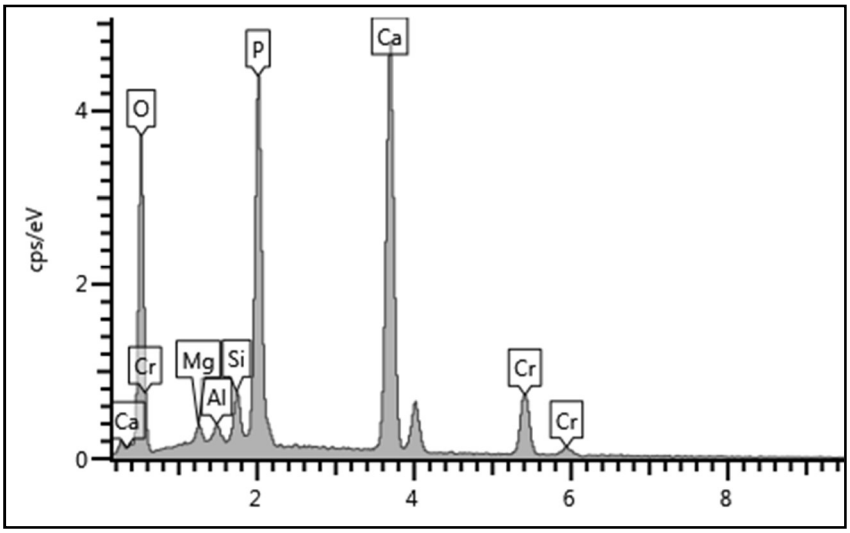

Figure A-*6*: EDS Spectrum detected for HA-AR1.

A-5 X-ray Diffraction

The X-ray diffraction technique determines the phase composition of a sample. In fact, each phase presents specific diffractions peaks based on the lattice structure and atoms positions. It is also possible to evaluate the structure of the crystalline materials and to measure the crystallite size.

X-ray diffraction analysis was carried out by using a conventional diffractometer Philips PW 3800 with Cu K_α radiation (0.154 nm) and acquired in the range 5-70° 2θ, with a step size of 0.026° and an acquisition time per step of 5 seconds.

A-6 Thermal Analyses: TG-DTA

The thermal analysis measures physical or chemical changes in a material as a function of temperature. Two common complementary techniques in this category are differential thermal analyses (DTA) and thermogravimetric analysis (TG).

In TG analysis the sample's weight as a function of temperature and time is continuously measured using a microbalance. The sample is placed in a small pan and thermally treated in a controlled manner. The atmosphere around the sample may be an inert gas, such as nitrogen, or reactive gas, such as air or oxygen. Reactions such as volatilization of sample components, decomposition, oxidation/reduction reactions can lead to the sample's weight changes. In DTA, a small portion of a sample is placed in an aluminium pan and along with a reference sample which must of the times is α-Al_2O_3, are heated in a controlled manner. The difference in temperature between the sample and the reference is monitored and recorded continuously. TG and DTA analyses were carried out on 150 mg of powder using STA 409C (Netzsch, Selb, Germany) device, up to 1400 °C with heating and cooling rates of 10 °C/min, under static air.

A-7 Dilatometry

Dilatometry is a technique for precise measurement of a sample's dimension changes during a programmed temperature change. This technique is employed for investigation of the densification of a ceramic body under a thermal cycle and the results are used for setting up the sintering treatment of the material.

The dilatometric measurements were carried out using a Netzsch 402E (Netzsch, Selb, Germany) instrument. This instrument is made of a controllable furnace and a dilatometer with an alumina tube acts as a sample holder. A small alumina bar in contact with the sample follows the length variations of the sample, allowing to evaluate expansion or shrinkage as a function of temperature.

A-8 Viscosimetry

The viscosity of a fluid is defined as its resistance to deformation at a given rate. In fact, internal friction is created when a layer of the fluid moves with respect to another layer. The viscosimetry evaluates this internal friction. The shear rate is the velocity gradient created and it measures the change in speed at which the layer moves with respect to the others. It is measured in reciprocal seconds (s^{-1}). The force required to induce motion, referred to the unit area, is measured in Pascal (Pa). The viscosity η can be then defined as the ratio between the shear stress and the shear rate; the unit is Pascal seconds (Pa.s) or milipascal seconds (mPa.s).

The viscosities of HA slurries were measured using a digital viscosimeter (Brookfield HBDV-II) at room temperature to study their viscosity behaviour.

A-9 Image analyses

ImageJ desktop program which is a java-based open-source image processing program was used for the analyses of the microstructural images taken of gelcast and robocast samples. The microstructural grains sizes of the dense samples, the pores and windows sizes in the case of the porous samples, and the filament and pores sizes in the case of robocast samples were measured by this program. The images were opened by the program, and at the first, the scale of the program was calibrated using the scale bar of each image. Then any desired distance was measured by sketching a straight line between the beginning and the end points of the distance.

A-10 Compression test

A compression test is a method for determining the behaviour of materials under a compressive load. Compression tests are conducted by loading the test specimen between two plates and then applying a force to the specimen by moving the crossheads together. By testing material in compression, the compressive

strength, yield strength, ultimate strength, elastic limit, and the elastic modulus among other parameters may all be determined.

The compression tests were performed according to ASTM C773-88(2016) under displacement control mode using an MTM Zwick/Roell Z050 (ZwickRoell AG, Ulm, Germany) machine with the displacement rate of 0.1 mm/min.

Conclusion